

RELIABILITY ANALYSIS OF DETERIORATED POST-TENSIONED CONCRETE BRIDGE DECKS

DOHA AL-MOSAWE

Thesis submitted to the University of Nottingham

for the degree of

DOCTOR OF PHILOSOPHY

January 2019

Abstract

During the last fifty years, there has been an increase in the development of pre-stressed highway bridges to accommodate the increasing of the road traffic. The construction of post-tensioned (PT) segmental concrete bridges is one of the most important developments in highway bridges since they represent a proven method for delivering durable bridges. The inspection of existing PT bridges has shown that significant corrosion can occur in tendons and, eventually, lead to tendon failure. Corrosion results from, fundamentally, two phenomena: the ingression of chloride ions into partially grouted ducts and the ingression of de-icing salts through the expansion points. Therefore, periodic on-site inspections are very important to ensure their safety and durability. However, it is very difficult to find visual evidence of corroded tendons and, in some locations, almost impossible. Accordingly, reliability analysis should be applied to assess the safety of PT concrete bridges with corroded tendons.

The primary purpose of this thesis is to establish a framework to assess the reliability of segmental PT concrete bridges, by considering a real case study in UK.

Reliability analysis methods, in particular FORM and Monte-Carlo simulation (MCS), are firstly studied and applied on a simple example of a RC beam.

Then, the non-linear behaviour of concrete beams tested experimentally were modelled numerically using the Concrete Damage Plasticity (CDP) model in ABAQUS. The results were compared with the experimental data available in the literature. This work is essential because it can be considered as a calibration

of the modelling approach. The modelling approach is then used to model the non-linear behaviour of the real case study.

Then, FORM and MCS are integrated with a numerical model using a newly developed approach to apply time-dependent reliability analysis on a simple example of a deteriorated RC beam. The developed method connects MATLAB and ABAQUS using a Python script file, to speed up the application of reliability analysis. The proposed method helps to solve one of the main limitations in reliability analysis, computational cost.

Finally, a time-dependent reliability analysis of the selected case study, Ynys-y-Gwas bridge, is carried out considering the deterioration due to corrosion of prestressing strands, which is the most concerning cause of PT concrete bridges degradation. The temporal and spatial variability of localized corrosion are considered through the existing time-dependent model and the uniform capacity length of the tendon according to Stewart (2004) method. The available data in the literature has been used to prepare the model and to identify the degree of corrosion in tendons. The adopted procedure shows that localized corrosion along the joints has strongly reduced the reliability of the bridge. Additionally, the reliability index after 32 years (the time of failure) is very low (near to zero) which is compatible with the observed bridge failure. The effect of bond degradation associated with localized and generalized corrosion is analysed and its effect is very significant in case of general corrosion.

The most relevant variables were the model uncertainties, traffic load and the resistance moment. This method can be used to assess any identical bridges after getting the most important data (chloride concentration and degree of corrosion) from inspection.

Acknowledgements

I wish to express my gratitude to some people and organisations for their support and assistance during the time spent on this thesis. First of all, I would like to express my sincere thanks to my project supervisors, Dr. Luis Neves and Dr. John Owen for their constant support, guidance and motivation. It would never have been possible for me to take this work to completion without their incredible support and encouragement. Thus, it is clear to me that without their input I would not have transitioned from a hesitant student to a self-sufficient researcher.
Special thanks are due to the University of Baghdad / Ministry of Higher Education in Iraq who sponsored the research and funded me for the study period. I would also like to thank all the members of staff at the Iraqi Cultural Attaché for supporting me to pursue my studies.
Still, I would like to thank the outstanding contributions of all of the staff and postgraduate research students in the Faculty of Engineering who have helped to make my time at Nottingham so enjoyable.
My deep appreciation goes out to the High Performance Computer (HPC) team for their cooperation in this work.
My wholeheartedly thanks also go to my friends for their love and assistance in making my PhD time balanced and enjoyable.
I am truly grateful to my parents for their immeasurable love and care. They have always encouraged me to explore my potential and pursue my dreams. They helped me a lot to reach this stage in my life. I would also like to thank my brothers for their everlasting encouragement and supports.

Finally and perhaps more importantly, I owe thanks to a very special person, my husband, Ammar Al-Atta for his continued and unfailing love, support and understanding during my pursuit of Ph.D degree that made the completion of thesis possible. He was always around at times I thought that it is impossible to continue, he helped me to keep things in perspective. I greatly value his contribution and deeply appreciate his belief in me. I appreciate my daughters, Zahraa, and my little baby girl, Sana, for abiding my ignorance and the patience they showed during my study journey. Words would never say how grateful I am to all of you. I consider myself the luckiest in the world to have such a lovely and caring family, standing beside me with their love and unconditional support.

Contents

List of Figures **ix**

List of Tables **xix**

1 Introduction **1**

1.1 Overview 1

1.2 Previous research into reliability analysis of PT concrete bridges . 4

1.3 Aim and objectives 5

1.4 Thesis organisation 6

1.5 Contributions to the research field 7

2 Principles of Reliability Analysis and Probabilistic Model **10**

2.1 Introduction 10

2.2 Basic concepts for reliability analysis 11

2.2.1 Uncertainties in engineering problems 11

2.2.2 Limit state function 18

2.3 Reliability of structural systems 19

2.4 Probabilistic models 23

2.4.1 Modelling of concrete material properties 24

2.4.2 Reinforcement and pre-stressing steel material properties modelling 28

2.4.3 Modelling of loads 29

2.4.4 Deterioration model 33

2.5 Summary 43

3 Reliability Analysis Methods **44**

3.1 Introduction 44

3.2 Probability of failure 45

3.3 First Order Reliability Method FORM 47

3.3.1 First Order Second Moment (FOSM) method or MVFOSM 50

3.3.2 Advanced First Order Second Moment (AFOSM) for normal variables (Hasofer-Lind method) 51

3.3.3 Advanced First Order Second Moment (AFOSM) for non-normal variables 55

3.4 Monte-Carlo simulation 59

3.5 Implementation of FORM and MCS methods 61

3.5.1 Beam geometry and material data 61

3.5.2 Failure mode and random variables 62

3.6 Reliability analysis and results 64

3.7 Summary 71

4 Finite Element Modelling of Reinforced Concrete Beams **73**

4.1 Introduction 74

4.2 Constitutive behaviour of plain concrete 75

4.2.1 Compressive behaviour of concrete 75

4.2.2 Tensile behaviour 76

4.3 FE-modelling of concrete nonlinear materials 78

4.4 Concrete damage plasticity model in ABAQUS 79

4.4.1 Stress-strain curve for uniaxial compression 79

4.4.2 Stress-strain curve for uniaxial tension 81

4.4.3 Plastic flow potential, yield surface and viscosity parameter 82

4.5 Finite element simulations 88

4.5.1 Numerical solver 88

4.5.2 Beams geometry and material properties details 89

4.5.3 3D beams modelling 91

4.5.4 Mesh sensitivity 94
4.5.5 Model validation 97
4.6 Summary 102

5 Computational Approach for Advanced Reliability Analysis 103
5.1 Introduction 103
5.2 Implicit performance function 104
5.2.1 Monte Carlo simulation 104
5.2.2 Response Surface Method (RSM) 105
5.2.3 Sensitivity based analysis 106
5.2.4 Artificial Neural Network method (ANN) 107
5.3 Reliability analysis of a RC beam with implicit performance function 109
5.3.1 Beam details and random variables 110
5.3.2 3D-nonlinear FE modelling 113
5.3.3 Analysis procedure and results 114
5.4 Summary 134

6 Case study: Description and Structural Modelling 136
6.1 Introduction 136
6.2 Ynys-y-Gwas bridge details 137
6.2.1 General details 137
6.2.2 Bridge geometry and material properties description 138
6.2.3 Bridge collapse 142
6.3 3D-non-linear finite element modelling 144
6.3.1 Beam modelling 144
6.3.2 Material models 145
6.3.3 Element mesh size 147
6.3.4 Modelling the boundary conditions 151
6.3.5 Bond-slip model 151
6.4 Summary 155

7 Case study: Reliability analysis and results **156**

7.1 Introduction 156

7.2 Preliminary calculations 157

7.2.1 Prestress losses 157

7.2.2 Corrosion initiation and propagation 168

7.2.3 Pitting factor 173

7.2.4 Bridge load 178

7.2.5 Bond-slip relationship 179

7.3 Limit state function 183

7.4 Random variables 185

7.5 Time dependent reliability analysis procedure 188

7.6 Results 189

7.6.1 Deterministic analysis 189

7.6.2 Time dependent reliability analysis 198

7.7 Parametric study 202

7.8 Summary 207

8 Conclusions and Recommendations **208**

8.1 Summary and main conclusions 208

8.2 Recommendations for future work 213

Bibliography **214**

.1 Appendix A 228

List of Figures

2.1 The probability distribution function: (a) Probability density function (PDF) of the random variable X. (b) Cumulative distribution function (CDP) of the random variable X 14

2.2 Probability density funcion (PDF) of normal distribution with $\mu = 0$ and different values of σ 15

2.3 Probability density funcion (PDF) of the lognormal distribution with $\lambda = 0$ and different values of ξ 16

2.4 Probability density funcion (PDF) of Extreme value ditribution type I with different means and standard deviations 17

2.5 Limit state function of two sets of random variables. It represents the boundary between the acceptable and unacceptable region (Mahadevan and Haldar, 2000) 19

2.6 Series system 20

2.7 Correlation between two failure modes or segments (Estes, 1997) . 22

2.8 Parallel system 23

2.9 Corrosion induced cracking and spalling of concrete (Daily, 1999) 33

2.10 Initiation and propagation corrosion model of reinforcement steel (Darmawan, 2010) 34

2.11 The effect of increasing mix proportion in concrete on the chloride diffusion coefficient (D) (Vu and Stewart, 2000) 35

2.12 The effect of concrete quality and cover on corrosion rate as studied by Vu and Stewart (2000) 39

2.13 Uniform loss of reinforcement due to general corrosion Darmawan (2010) 40

2.14 Configuration of pitted corroded rebar: (a) cross section of corroded rebar with P_{max} and (b) equivalent average cross section referred to the overall corroded rebar surface (Zhang et al., 2013) 40

2.15 Non-uniform loss of reinforcement due to localized (pitting) corrosion (Val and Melchers, 1997) 40

3.1 Three dimensional representation of a possible joint density function ($f_{RS}(r,s)$) for two random variables with marginal density functions $f_R(r)$ and $f_S(s)$ (Schneider, 2006) 46

3.2 The two dimensional case of a linear limit state function and standardized normally distributed variables X_i' (Faber, 2005) 48

3.3 The linearisation of the non-linear failure surface in standard normal space proposed be Hasofer and Lind (1974) from Faber (2005) 49

3.4 Hasofer-Lind Method for linear limit state function (a) original coordinates (b) reduced coordinates (Mahadevan and Haldar, 2000) 52

3.5 Hasofer-Lind Method reliability index for non-linear limit state function (Mahadevan and Haldar, 2000) 53

3.6 Algorithm for finding β_{HL} (Mahadevan and Haldar, 2000) 55

3.7 Principle for simulation of a random variable (Faber, 2005) 60

3.8 Simply supported RC beam section 62

3.9 Total area of steel reduced with the time due to localized corrosion for the two cases 65

3.10 The direction cosine values of i_{corr} with the time for case 2 66

3.11 Reliability indices differences between case 1 and case 2, β is lower in case 2 due to the conidration of the uncertainty of i_{corr} 66

3.12 Reliability index reduction due to increasing the standard deviation of i_{corr} 67

3.13 Influence of different values of i_{corr} standard deviation on the value of $\alpha_{i_{corr}}$ 67

3.14 Sensitivity factors α at design points that gives the importance of each random variable 68
3.15 The effect of using model uncertainties (θ_E and θ_R) on the values of reliability index along the years 69
3.16 Reliability index comparison between using 4 and 8 reinforcement bars. Increasing the number of bars will lead to increase the capacity of the beam and subsequently increase the reliability index of the beam 69
3.17 Fixed ended beam 70
3.18 Variation in reliability index with age for the support and middle moments 70
3.19 The probability of failure of the simply supported beam shows a good agreement between the FORM and MCS methods 71

4.1 Concrete compressive stress-strain diagram according to Eurocode2 (Eurocode-2, 2004) 76
4.2 Concrete tension stress-strain diagram (Belarbi et al., 1996) . . . 77
4.3 Methods of modelling concrete cracks in FE analysis(Pankaj, 1990) 78
4.4 Definition of inelastic strains for the concrete compressive behaviour of the CDP model (ABAQUS, 2013) 80
4.5 Definition of inelastic strains for the concrete tensile behaviour of the CDP model (ABAQUS, 2013) 82
4.6 Plastic potential surface and yield surface in the deviatory plane (ABAQUS, 2013) 83
4.7 Dilation angle (Ren et al., 2015) 84
4.8 Dilation angle and eccentricity in the meridian plane (ABAQUS, 2013) 84
4.9 (a) stress-strain relation for a material undergoing hardening and (b) the initial and subsequent yield surfaces in the deviatoric plane (Carstensen, 2011) 85

4.10 Drucker-Prager yield criterion in the deviatoric plane for $K_c = 1$ and $K_c = 2/3$ (ABAQUS, 2013) 86
4.11 Yield surface under biaxial stress in the CDP model (ABAQUS, 2013) 86
4.12 Detailing of the simply supported reinforced concrete beam (Barros and Fortes, 2005) 89
4.13 The cross section of the simply supported reinforced concrete beam (Barros and Fortes, 2005) 89
4.14 Stress strain relation for the steel bars (Barros and Fortes, 2005) . 90
4.15 Ideal situation of element deformation under bending effect 91
4.16 Reduced integration element deformation under bending effect . . 91
4.17 Full integration element deformation under bending effect 92
4.18 3-D finite element modelling of $V1$: (a) concrete section. (b) reinforcement steel 93
4.19 Mesh sensitivity study 95
4.20 Uniaxial stress strain curve of concrete in compression for beam model $V1$ 96
4.21 Uniaxial stress strain curve of concrete in tension for beam model $V1$ 96
4.22 Uniaxial stress strain relationship for reinforcement steel of beam model $V1$ 97
4.23 Experimental vs. FE load deflection curves using different values of viscosity parameters μ (Model $V1$) 98
4.24 Experimental vs. FE load deflection curves using different values of viscosity parameters μ (Model $V2$) 99
4.25 Experimental vs. FE load deflection curves using different values of viscosity parameters μ (Model $V3$) 99
4.26 Experimental vs. FE load deflection curves using different values of viscosity parameters μ (Model $V4$) 100

4.27 Crack distribution near the concrete beam tension zone: (a) $\mu = 10^{-2}$, (b) $\mu = 10^{-3}$, (c) $\mu = 10^{-4}$ and (d) $\mu = 10^{-5}$ 101

5.1 Multi-layer neural network (Chojaczyk et al., 2015) 107
5.2 Simply supported RC beam section 111
5.3 The three dimensional view of meshing the RC simply supported beam 113
5.4 Beam cracks due to bending 114
5.5 Reliability analysis procedure flowchart 116
5.6 Model of steel corrosion (a) Increasing of pit depth with the time; (b) Reduction of the steel cross sectional area due to pitting corrosion 120
5.7 Load displacement curves at each year. The figure shows the deterioration of beam ultimate load capacity over the years due to corrosion 121
5.8 Reduction of the resistance moment mean value with the time due to corrosion 121
5.9 Histogram of flexural strength for no corrosion case (t = 0) 122
5.10 The effect of corrosion on the distribution of the beam resistance moment along the years 122
5.11 (a) Beam reliability indices reduction along the years. (b) Beam probability of failure increasing along the years 126
5.12 Direction cosines at design points as a function of time 127
5.13 Structure of ANN 128
5.14 Predicted and target limit state function (year 1) 130
5.15 Predicted and target limit state function (year 11) 130
5.16 Predicted and target limit state function (year 21) 131
5.17 Predicted and target limit state function (year 31) 131
5.18 Predicted and target limit state function (year 41) 131
5.19 Predicted and target limit state function (year 51) 132
5.20 Predicted and target limit state function (year 61) 132

5.21 Predicted and target limit state function (year 71) 132
5.22 Predicted and target limit state function (year 81) 133
5.23 Predicted and target limit state function (year 91) 133
5.24 Comparison between the two methods: MCS with FORM and ANN-based FORM: (a) Reliability index (b) Probabilty of failure 134

6.1 Cross section of the Ynys-y-Gwas bridge (Woodward and Williams, 1988) 139
6.2 The longitudinal tendons profile in each precast beam 139
6.3 Longitudinal section of I-beams, segments $1-3$ (Woodward and Williams, 1988) 140
6.4 Ynys-y-Gwas bridge, plan view of deck (Woodward and Williams, 1988) 141
6.5 The top and side view of Ynys-y-Gwas bridge collapse showing the failure of all the beams (Woodward and Williams, 1988) 143
6.6 Tendon localized corrosion near joints (Woodward and Williams, 1988) 143
6.7 The cardboard tube that has been seen around the longitudinal tendons accross the transverse joints (Woodward and Williams, 1988) 144
6.8 3-D finite element model of the concrete beam with the five curved tendons 145
6.9 The uniaxial compressive model of concrete that is applied in this study for the Ynys-y-Gwas bridge according to Eurocode-2 (2004) 146
6.10 The uniaxial tensile model of concrete that is applied in this study for the Ynys-y-Gwas bridge according to Eurocode-2 (2004) . . . 146
6.11 Prestressing steel stress strain relation considered in this study for the Ynys-y-Gwas bridge 147
6.12 The uniform capacity length L_u and the spatial capacity of corroded reinforcing bar (Stewart and Al-Harthy, 2008) 148

6.13 Effect of using different values of uniform capacity length (steel element size) on the ultimate capacity of Ynys-y-Gwas bridge. The figure shows that using element length with 800 and 900 mm provides the closest solutions to the theoretical calculations 149
6.14 Distribution of pitting corrosion along the tendon modelled in ABAQUS. The figure shows the corrosion is assumed to be within the elements near the joints 149
6.15 Beam section and stress 150
6.16 Connector element type: (a) Cartesian and (b) Rotation (ABAQUS, 2013) 153
6.17 Connector elements in the finite element model 154

7.1 Sum of angular displacement (θ) at each tendon. 161
7.2 Percentage losses of the prestress force due to friction for the five tendons. Losses are arranged from high to low values according to the profile of the tendon 161
7.3 Anchorage losses. (a) Anchorage draw-in effect along distance. (b) pre-stress loss near the anchorage (Gilbert et al., 2017) 162
7.4 Comparison between losses due to friction effect only and losses due to friction + anchorage draw-in effect. 163
7.5 The increase of the drop in the prestressing force with distance from the jacking ends due to the effect of anchorage draw-in. . . . 163
7.6 Remaining prestressing force at each tendon. 164
7.7 Losses in prestress force due to concrete creep 165
7.8 Losses in prestress force due to concrete shrinkage 166
7.9 Losses in prestress force due to tendon relaxation 166
7.10 Total pre-stress losses: short term losses + long term losses 166
7.11 Final remaining prestress along the length of tendon 1 over time . 167
7.12 Chloride diffusion process of corrosion initiation through the transverse joint in Ynys-y-Gwas bridge 168

7.13 Vertical profile of chloride concentraion in Ynys-y-Gwas bridge at different levels from the soffit (Woodward and Williams, 1988) . . 169
7.14 Progress of chloride concentration with the time for Ynys-y-Gwas bridge 171
7.15 Progress of the corrosion rate with the time for Ynys-y-Gwas bridge 172
7.16 Probability of bridge failure along the years, when the statistical parameters of the pitting factor were considered according to Equation 2.46 174
7.17 Degree of corrosion in longitudinal tendons near joints for beams J, H and G and segments 1, 2 and 3 (Woodward and Williams, 1988) 175
7.18 The probability of loss of cross sectional area according to the corrosion assessment of the longitudinal tendons near joints 175
7.19 Histogram of loss of cross sectional area at year 1 176
7.20 Histogram of loss of cross sectional area at year 11 176
7.21 Histogram of loss of cross sectional area at year 21 177
7.22 Histogram of loss of cross sectional area at year 31 177
7.23 Histogram of loss of cross sectional area at year 41 177
7.24 Histogram of loss of cross sectional area at year 51 178
7.25 HA loading includes the unifomly distributed load (UDL) and the knife edge load (KEL) on one notional lane 179
7.26 Bond stress-slip relationship according to Model Code (CEB, 1992) 181
7.27 Improved local bond stress-slip relationship between strand and concrete (Wang et al., 2016) 181
7.28 Deterioration of the maximum normalized bond strength (R_b) with increasing corrosion (Wang et al., 2016) 183
7.29 Method of testing joints to find their capacities 184
7.30 Bending moment diagram of the simply supported beam 185
7.31 The progress of corrosion level with the time for the deterministic analysis with using pitting factor $R = 6$ 190

7.32 The deterioration of maximum normalized bond strength with increasing corrosion loss, used in this study for determinstic analysis 190
7.33 The deterioration of beam capacity due to corrosion only 191
7.34 Bond-slip relationshp input to the model 191
7.35 The input and output bond-slip model for years 1 and 11 192
7.36 The input and output bond-slip model for year 21 192
7.37 The input and output bond-slip model for year 31 192
7.38 The input and output bond-slip model for year 41 193
7.39 The input and output bond-slip model for year 51 193
7.40 The input and output bond-slip model for year 61 193
7.41 The input and output bond-slip model for year 71 194
7.42 The input and output bond-slip model for year 81 194
7.43 The input and output bond-slip model for year 91 194
7.44 The input and output bond-slip model for year 101 195
7.45 Deterioration of the beam ultimate loads along the years in case of considering general corrosion 196
7.46 Flextural crack distribution according to the experimental test carried out by Zhang et al. (2017) where (a) Crack distribution when η=12% and (b) Crack distribution when η=60% 196
7.47 Flextural crack distribution of the Ynys-y-Gwas bridge according to the finite element analysis, where (a) Crack distribution when η=11% and (b) Crack distribution when η=51% 197
7.48 Deterioration of the beam ultimate load, due to localized corrosion, for case 2 (area reduction) and case 3 (area and bond reduction) . 198
7.49 Probability of failure (P_f) and reliability index (β) as a function of time for the three cases considering the exhibition of brittle and ductile behaviour of strands 199
7.50 Direction cosine values of M_R with the time for the original case (rate 1) 201

7.51 Sensitivity factors α at the design points that give the importance of each random variables for the original case (rate 1) 201

7.52 Probability of failure P_f for a spatial and mid-section analysis . . 202

7.53 Comparison of the probability of failure P_f of each joint 202

7.54 Reduction of corrosion rates with the time used in this study . . . 205

7.55 Probability of failure P_f for different corrosion rates 205

7.56 Direction cosine values of M_R with the time for the four rates considered. The figure shows the influence of M_R uncertainty on reliability analysis 206

7.57 Sensitivity factors α at the design points that gives the importance of each random variables for the four rates considered 206

List of Tables

2.1 Statistical parameters of Y parameter according to JCSS (2001) . 26

2.2 Statistical parameters of the concrete cylinder compressive strength f_{c0} according to JCSS (2001) 26

2.3 Probabilistic models of the concrete compressive strength according to the literature (the most common used in reliability of structures) 27

2.4 Probabilistic models of the concrete tensile strength according to the literature (the most common used in reliability of structures) . 27

2.5 Probabilistic models of the concrete modulus of elasticity according to the literature 28

2.6 Statistical parameters of steel reinforcement properties 28

2.7 Statistical parameters of pre-stressing steel properties 29

2.8 Statistical parameters of dead load according to Nowak and Szerszen (1998) 30

2.9 Statistical parameter of pre-stress losses according to (JCSS, 2001) 31

2.10 Statistical parameter of pitting factor (R) 42

3.1 Statistical parameters of random variables for ultimate limit state analysis 63

4.1 Concrete material properties of the tested beams (Barros and Fortes, 2005) 90

4.2 Steel reinforcement properties of the tested beams (Barros and Fortes, 2005) 91

4.3 Results from mesh sensitivity parameter study for beam $V1$ . . . 94

4.4 Concrete damage plasticity input parameters 95
4.5 Comparison between the experimental data and FE results for beam model $V1$ 98

5.1 Deterministic values of beam geometry, material properties and load parameters 110
5.2 Statistical parameters of random variables for ultimate limit state analysis 112
5.3 Ultimate load capacity of the beam corresponding to different values of corrosion loss 119
5.4 Estimated reliability index (β) 128
5.5 Performance of ANN model 129

7.1 Friction coefficient (μ) for post-tensioned tendons (Eurocode-2, 2004) 160
7.2 Chloride concentrations obtained for different positions of TRRL segments according to Woodward and Williams (1988) 170
7.3 Classification of corrosion (Woodward and Williams, 1988) 174
7.4 Loss of tendon area percentage along the years for Ynys-y-Gwas bridge 178
7.5 Statistical parameters of random variables used in time dependent reliability analysis 187
7.6 Cosines direction of M_R along time for each corrosion rate considered in this study 204

Chapter 1

Introduction

1.1 Overview

Since the mid twentieth century, the development of pre-stressed concrete became a popular choice for bridge construction around the world (Nguyen et al., 2013) as they can be used for short and long spans up to 450 m. From the mid-1970s, the increasing road traffic and the rapid growth of many major cities led to increase in demand of new highways bridges within a short period of time (Hewson, 2003). According to the Highway Agency, there are about 3000 post-tensioned bridges in the UK. The first post-tensioned bridge built in the UK was the Nunns bridge which was completed in 1947 with a span of 22.5 m (Das and Frangopol, 2001). Das and Frangopol (2001) stated that the construction of post-tensioned concrete bridges was the preferred method in the 1950s because they offered many benefits to the economy and the construction industry of bridges. However, these structures could be most at risk due to the presence of voids, caused by the poor grouting, which increases the availability of oxygen and moisture in ducts. For segmental post-tensioned bridges, the joints between segments can increase the chance of chloride penetration through the deck. Therefore, corrosion will increase and that will lead to tendon rupture and bridge failure.

During the 1980s, a significant number of post-tensioned concrete bridges had to

be replaced in the UK due to tendon corrosion (Pearson-Kirk, 2014). In 1985, the most serious event happened in Wales when the single span segmental post-tensioned Ynys-y-Gwas bridge collapsed without warning. Collapse of the bridge was due to the penetration of water and salts through the transverse joints leading to corrosion of the longitudinal tendons (Woodward and Williams, 1988). In September 1992, the UK Department of Transport banned the construction of any new post-tensioned grouted duct bridges until the construction standards were improved. Although the moratorium was lifted in 1996, there were still reservations about the corrosion protection of the tendons where they crossed the joints and the moratorium remained in place for pre-cast segmental constructions with internal tendons (Woodward, 2001). Therefore, periodic on-site inspections are very important to ensure their safety and durability. However, the results of these inspections are usually poor and have a high degree of uncertainty since there is little or no visual evidence if anything is wrong as it is only possible to inspect a small sample of ducts. In consequence, it is recognized that the inspection assessment is not effective (Frangopol and Hearn, 1996). Hence, decision making regarding existing bridges is done in UK according to BD54/15 (2015) method. It is a risk based method, mostly qualitative and based on bridge exposure conditions and definitions of critical sections followed by inspection and non-destructive testing. The approach followed in this thesis is similar to the method of BD54/15 (2015) but tries to quantify risk using reliability analysis methods. Reliability analysis methods are increasingly used for the evaluation, quantification, monitoring and assessment of risk for concrete structures (JCSS, 2001). Reliability analysis methods can assess the condition of the existing bridge structure depending on information concerning the actual bridge condition which is unknown in the design phase. The material properties, measurements of actual bridge geometry, collection load data and the results of the periodic inspections performed within the lifetime of the bridge are the major sources of this information.

The results of the application of reliability analysis can be used to determine appropriate maintenance and repair measures. The reliability analysis methods are used to evaluate the safety of concrete structures by evaluating the limit state function $g(X_i)$ which represents the boundary between the safe and unsafe region. The limit state function is a mathematical equation representing the condition beyond which a structure exceeds a specific design requirement. Hence, the limit state function can be regarded as the difference between the resistance of a structural component (R) and the action load (S). The system failure condition occurs when $g(X_i) < 0$, where X_i is a vector of random variables represent the uncertainties on material, load, geometry and corrosion of the structure, while $g(X_i) > 0$ indicates that the system has not failed. The probability of failure (P_f) for a system can be defined as the probability event occurrence $g(X_i) < 0$.

Up to now, the great majority of reliability analysis studies are related with the assessment of RC bridges, such as Bastidas-Arteaga et al. (2009); Stewart (2009); Stewart (2010); Bastidas-Arteaga et al. (2010); Stewart (2012); Strauss et al. (2012); Hackl and Kohler (2016); Zhu et al. (2016); and Hajializadeh et al. (2016). Less research has been dedicated to the time dependent reliability analysis of deteriorated pre-stress concrete bridges especially for segmental post-tensioned type, such as Guo et al. (2010); Guo et al. (2016); Tu et al. (2017); Pillai et al. (2010) and Pillai et al. (2014). Therefore, this thesis is seen as a contribution to this work by considering a real case study of bridge that is deteriorated due to corrosion. This requires the use of accurate methods to represent the actual behaviour.

1.2 Previous research into reliability analysis of PT concrete bridges

After more than four decades since its potential was first applied, a considerable amount of research has been published on the assessment of RC bridges using reliability analysis methods. However, applicability to pre-stress concrete in particular post-tensioned bridges remains in its infancy. This section provides an overview of the previous research into reliability analysis of post-tensioned concrete bridges to highlight the limitations of the work.

Few works aiming to assess the reliability of deteriorated post-tensioned concrete bridges have been found in the literature. Pillai et al. (2010) developed an analytical framework to predict the time variant service reliability index of PT segmental concrete bridges subjected to various structural loading and corrosive exposure conditions by considering an example of PT concrete bridge. For the considered application example, Pillai et al. (2010) assumed that only the external tendons were exposed to corrosive conditions, while all internal tendons were assumed to be intact and free from corrosion.

The American Association of State Highway and Transportation Officials (AASHTO) specification presents reliability-based design procedures which ensure high reliability for new PT bridges. However, these design procedures do not consider long-term losses in reliability due to the potential corrosion of strands; and therefore may not guarantee sufficient reliability during the desired life of the bridge. Therefore, Pillai et al. (2012) proposed a reliability based design approach to ensure long-term reliability of PT concrete bridges based on an extensive experimental program that tested 536 strand specimens under various environmental conditions. The design approach involves the assessment of long-term structural reliability during the preliminary design phases of PT bridges.

Pillai et al. (2014) developed an analytical framework to predict the flexural reliability index of PT segmental concrete bridges subjected to various structural and environmental loading conditions by considering a typical PT bridge. It has

been also assumed that the corrosion attacks the external tendons only, while the internal tendons were assumed to be intact. The moment capacity of the PT girder is formulated using probabilistic models for the tension capacity of corroding PT strands exposed to various voids and environmental conditions. The research indicates that the flexural reliability index reaches a value below the recommended value within a relatively short period of time when moisture and chlorides infiltrate the tendons. These findings emphasize the critical need for new inspection, assessment and repair methods for these kind of bridges.
The major absence of the existing studies is a general framework that can be used to assess the safety of any existing PT segmental concrete bridges. This can be done by using a more realistic modelling approach using three dimensional models to simulate the actual case . Furthermore, the existing studies did not consider the effect of i) corrosion in the internal tendons ii) long term losses of pre-stress force due to creep and shrinkage iii) bond deterioration due to corrosion, on the reliability of these bridges. Therefore, the work presented in this thesis focuses on these main limitations by considering a real case study of segmental PT bridge that has been failed due to the corrosion of the tendons near the joints.

1.3 Aim and objectives

The aim of this project is to establish a framework to assess the reliability of existing post-tensioned concrete bridges. A real PT bridge that failed due to corrosion is considered as a case study to assess its reliability at the time of failure. The objectives to tackle this aim can be summarised as follows:

1. Develop detailed understanding of reliability analysis and methods based on detailed literature review.

2. Characterise the properties of the Ynys-y-Gwas bridge including the geometry, load, material properties and corrosion process by using data on the bridge available in the literature.

3. Develop a three dimensional model for the Ynys-y-Gwas bridge using finite element software. Finite element method is a tool that has became widely used for structural analysis due to its ability to consider complex material non-linearity and the 3D structural behaviour.

4. Define the limit state functions and the probabilistic models for all relevant random variables. These variables include mechanical properties of materials, geometry in particular concrete cover and area of steel, dead load and live load and corrosion model

5. Define the reliability model by combining the finite element model (objective 3) with the probabilistic models (objective 4).

6. Use Monte-Carlo simulation to estimate the flexural resistance of the bridge and fit a distribution to the obtained results.

7. Use FORM analysis method to estimate the reliability index of the bridge over time.

1.4 Thesis organisation

The thesis consists of seven chapters. Chapter 1 presents a general introduction to the problem, the previous research on reliability analysis of PT bridges, the aim and objectives and the outline of the thesis.
Chapter 2 aims at introducing the principles of reliability analysis by providing a theoretical background to the relevant literature. The chapter presents the basic concept of reliability analysis and the existing probabilistic models of the variables related to reinforced concrete structures.
Chapter 3 introduces the reliability analysis methods, MCS and FORM. The chapter also presents an application for the two methods to an example of a simply supported RC beam deteriorating over time due to corrosion.
Chapter 4 discusses the constitutive behaviour of concrete and describes the meth-

ods that can be used to model this behaviour in finite element analysis. The chapter also presents an application for modelling reinforced concrete beams in finite element, describing the approach, the material and the modelling parameters used. The modelling application aims at establishing a better understanding of the modelling approach to be used in Chapter 6

Chapter 5 presents an application of reliability analysis for a deteriorated simply supported beam with implicit performance function. This is done by combining the methods used in Chapters 3 and 4. To achieve this, a connection between MATLAB and ABAQUS Python script file is used in order to speed up the reliability analysis processing.

Chapter 6 presents the description and structural finite element modelling of the case study, i.e., of the Ynys-y-Gwas bridge.

Chapter 7 applies the procedure presented in Chapter 5 on the real bridge case study. The analysis studied the effect of corrosion on the bridge behaviour in terms of load deflection curves, cracking pattern and bond deterioration. The analysis results also show the effect of pitting corrosion on the bridge probability of failure.

Finally, Chapter 8 presents the conclusions from this work and gives recommendations for future work.

1.5 Contributions to the research field

Several contributions for this research can be highlighted as a result of this thesis, namely:

- **Establish a framework for reliability analysis of segmental PT concrete bridges**

  The previous research were focused on applying reliability analysis for RC structures, while few research have been dedicated for pre-stress concrete structures especially for segmental PT concrete bridges such as Pillai et al.

(2010); Pillai et al. (2012) and Pillai et al. (2014).

In the UK, there are significant number of existing segmental PT concrete bridges since this kind of concrete represent a proven method for delivering a durable bridges. However, they have witnessed a high risk due to the corrosion of strands which can lead to whole bridge collapse. Therefore, a reliability framework has been established in this thesis to ensure the long term safety of segmental PT concrete bridges. This has been done by considering a real case study with its collected data.

The developed reliability framework has taken into account the series reliability for spatial pitting corrosion variation using Ditlevsen (1979) bounds and the uncertainties in material properties, pre-stress losses, dead load and live load. The method proposed in this thesis can be used for any identical bridges to give the decision about the condition of the bridge.

- **Consider the effect of bond deterioration in reliability analysis**

  The bond between steel and concrete is usually affected by corrosion products. The expansive nature of the corrosion products that build up at the interface exerts a radial pressure on the surrounding concrete, which leads to cracking and spalling. Spalling will reduce the bond by removing the concrete cover, which in turn will reduce the confinement of the steel tendons and expose the concrete to further corrosion activity.

  The effect of bond deterioration in reliability analysis study has not been considered yet. Therefore, in this thesis the effect of bond deterioration due to corrosion was considered for the first time in reliability analysis. Furthermore, apart from reliability analysis, the effect of bond deterioration in post-tensioned concrete beam is also considered for the first time in this study. By using ABAQUS/Standard, connector elements were used to simulate the interface layer between the steel and the concrete. The effect of uniform and localized corrosion on the bond deterioration were both considered.

- **Develop a new approach to speed up the reliability analysis**

  In this thesis, the reliability analysis has been applied using a newly developed approach which depends on the connection between the MATLAB and ABAQUS using Python script file. This method has been developed and exploited to produce a novel combined process that can speed up the reliability analysis for non-linear structures.

- **Develop a new method for estimating the statistical parameter of the pitting factor (R)**

  The pitting facto is an important parameter that can be used to measure the extent of pitting corrosion along the tendons length. The statistical parameter of the pitting factor is usually computed according to Equation 2.46. However, using this equation can underestimate the results by giving an inaccurate estimation for the probability of failure (3% at the time of failure) since this equation did not take into account the effect of the degree of corrosion. Therefore, in this study the statistical parameters of the pitting factor were calculated according to the degree of corrosion in the bridge as it has been explained in details in Section 7.2.3. This developed method gives more accurate results for estimating the bridge probability of failure by getting more than 40% at the time of failure which is reasonable.

Chapter 2

Principles of Reliability Analysis and Probabilistic Model

This chapter describes the principles of reliability analysis by providing the theoretical background according to the relevant literature. This includes a description of the basic concept of reliability analysis, followed by a brief review of the reliability system. Then the literature on probabilistic models for material properties, load and corrosion will present.

2.1 Introduction

Structures shall be designed, constructed and maintained in such a way that they are suited for their use during the design working life and in an economic way, Joint Committee on Structural Safety (JCSS) model code (JCSS, 2001). Therefore, structures should have an appropriate level of reliability, which means that the degree of reliability should be adopted to suit the use of the structure. The reliability of a structure describes its ability to function under stated conditions for a specific period of time (Leitch et al., 1995). Moreover, the reliability is expressed as the probability that the structure will not fail. Therefore, reliability analysis forms the basis of the assessment of probabilities of occurrence of uncer-

tain events, and thus constitutes a cornerstone in risk and decision analysis. The development of probabilistic models are considered as the main task in reliability analysis. Therefore, this chapter will briefly describe the basic concept of reliability analysis including uncertainties, random variables, probability distributions and the existing probabilistic models for the uncertainties that are associated with reinforced and pre-stressed concrete structures.

2.2 Basic concepts for reliability analysis

2.2.1 Uncertainties in engineering problems

Generally, engineering experiments or systems contain a certain amount of uncertainty. In other words, repeated measurements will not necessarily give the same results, and different outcomes can be obtained. According to that, the uncertainty can be defined as the occurrence of different results without any patterns (Mahadevan and Haldar, 2000). The uncertainties in engineering problems are quantified by using probabilities.

The uncertainties in engineering problems may result from three different sources which are classified according to Faber (2005), Malkawi et al. (2000), Melchers and Beck (2017) and Benaissa et al. (2015) as follows:

- Inherent random variability.
- Uncertainties due to inadequate knowledge (model uncertainties).
- Statistical uncertainties.

Faber (2005) considers that the first type of uncertainty is further divided into two sub-categories: the uncertainties that are influenced by human activities and the uncertainties that are influenced by the natural environment factors. The first category is, e.g., the uncertainties of strength values and concrete dimensions. The second one is concerned with the applied forces, e.g., wind speed and

earthquake. The Inherent random uncertainty can be decreased by using more advanced production and quality control methods. However, this will increase the cost.

The second type of uncertainty also can be divided into two sub-categories: the first one is associated with the predictive accuracy of calculation models used (theory errors or the inaccurate assumptions). The second one is associated with the prediction of future developments such as the future evolution of traffic loads on bridges.

The last type of uncertainties is associated with the statistical evaluation of test results or observations that result when the design decisions are based on a small sample of observations. The small number of observations can cause uncertainties in the estimation of the statistical parameters such as mean and standard deviation. Moreover, the uncertainties of statistical evaluation can result from neglecting the systematic variations of the observed variables such as the climate variables. However, the statistical uncertainties can be decreased by increasing the efforts of observations and testing.

Traditionally, in reliability analysis the uncertainties that should be taken into consideration are denoted as *Random Variables (X)*. The basic random variables should be able to represent all types of uncertainties that are included in the analysis. Each random variable should be described with a particular type of *a probability distribution function* and its *statistical parameters*. The probability distribution function is a function that can be used to define a particular probability distribution. The probability distribution function is described by the cumulative distribution function, CDF, $F_X(x)$ or the probability density function, PDF, $f_X(x)$. The CDF defines the probability that a variable X is equal or less than a certain value x as shown in Figure 2.1 and it is given by:

$$F_X(x) = P(X \leq x) \tag{2.1}$$

The PDF describes the variation of the parameter X and it is given by the following equation:

$$f_X(x) = \frac{dF_X(x)}{dx} \tag{2.2}$$

The statistical parameter of a specific distribution describes the properties of the variable and it is represented by the mean (μ_X) and standard deviation (σ_X). The mean and standard deviation of a probability distribution are:

$$\mu_X = \int_{-\infty}^{+\infty} x f_X(x) dx \tag{2.3}$$

and

$$\sigma_X = \sqrt{\sigma_X^2} \tag{2.4}$$

where σ_X^2 is the variance of X:

$$\sigma_X^2 = \int_{-\infty}^{+\infty} (x - \mu_X)^2 f_X(x) dx \tag{2.5}$$

The coefficient of variation (COV) denoted by V_X is defined as:

$$V_X = \frac{\sigma_X}{\mu_X} \tag{2.6}$$

In structural reliability, different probability distributions have been used for different variables including the Normal, Lognormal, Uniform, Gamma, Beta, and Extreme type I, II and III. In this section, the normal, lognormal, and the extreme type I distributions will be introduced since they are further used in this thesis.

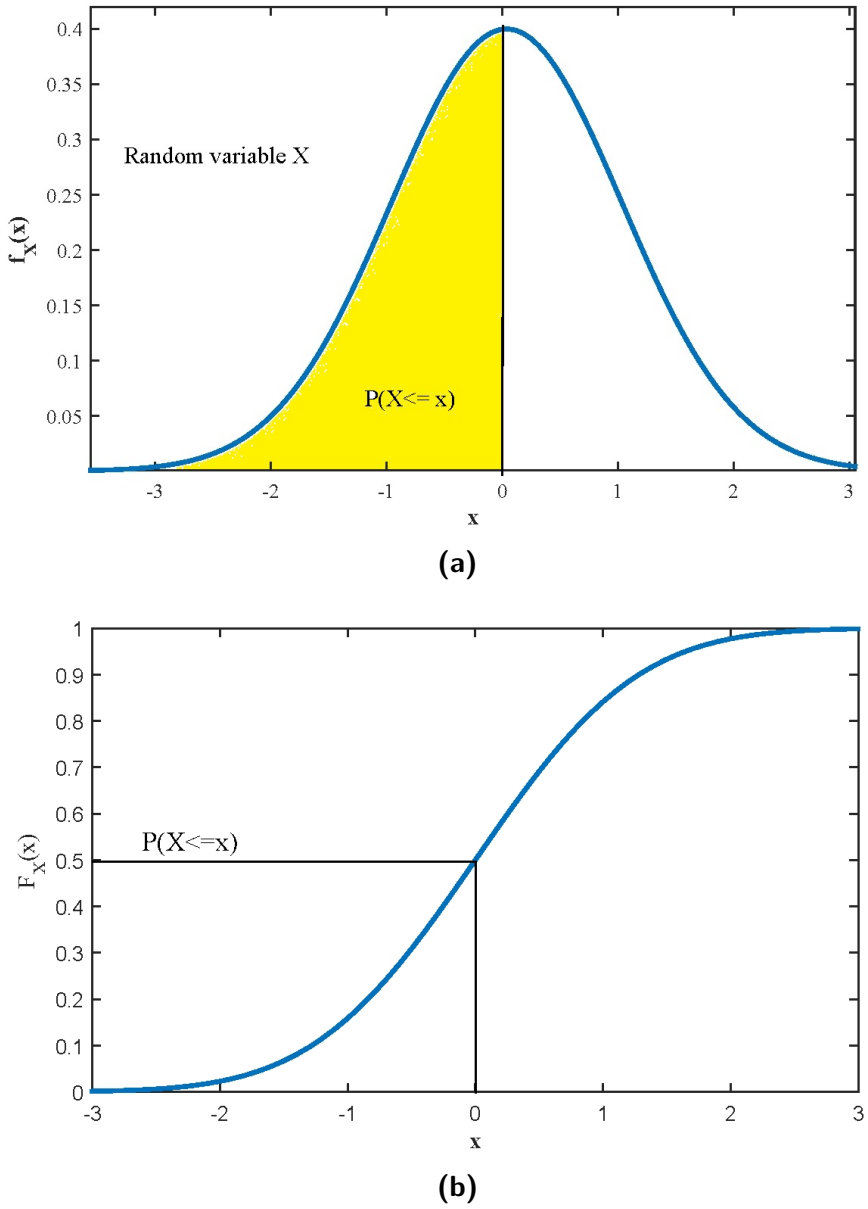


Figure 2.1: *The probability distribution function: (a) Probability density function (PDF) of the random variable X. (b) Cumulative distribution function (CDP) of the random variable X*

Normal distribution

The normal distribution is the most common distribution used in the probability theory of engineering problems (Mahadevan and Haldar, 2000). The normal distribution is applicable for random variables that are possible in range $-\infty$ to $+\infty$ and is denoted as $\mathcal{N}(\mu, \sigma)$. The probability distribution function (PDF) of

the normal distribution is symmetrical around its mean value as shown in Figure 2.2. The normal distribution with zero mean and unit standard deviation is called Standard normal distribution. The PDF of the normal distribution can be expressed as:

$$f_X(x) = \frac{1}{\sigma_x\sqrt{2\pi}} exp\Big[-\frac{1}{2}\Big(\frac{x-\mu_x}{\sigma_x}\Big)^2\Big] \tag{2.7}$$

where μ_x and σ_x are the mean and standard deviation of the normal distribution.

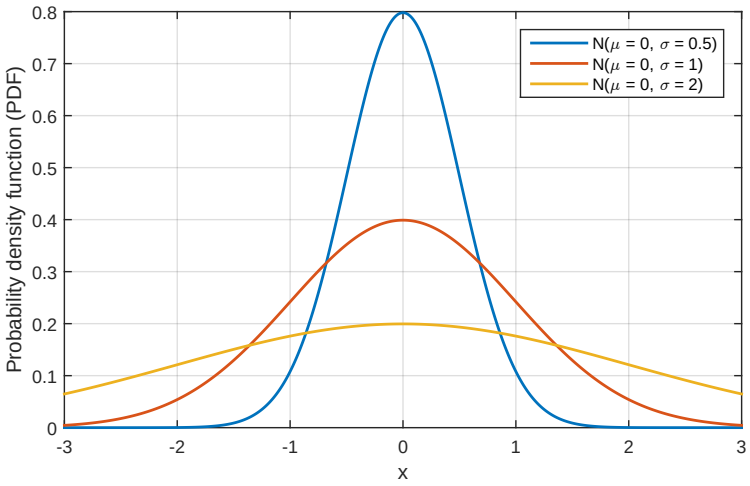


Figure 2.2: *Probability density funcion (PDF) of normal distribution with $\mu = 0$ and different values of σ*

Lognormal distribution

A lognormal distribution is a probability distribution of a random variable whose logarithm is normally distributed. This distribution is applicable for random variables with values between 0 and $+\infty$. Therefore, it is used widely in structural reliability when the random variables cannot have negative values such as the weight of people. The lognormal distribution is not symmetric around its mean, unlike the normal distribution, and it is skewed to the right as shown in Figure 2.3. The PDF of the lognormal distribution can be expressed as:

$$f_X(x) = \frac{1}{\xi_x\sqrt{2\pi}} exp\Big[-\frac{1}{2}\Big(\frac{ln(x)-\lambda_x}{\xi_x}\Big)^2\Big] \tag{2.8}$$

where ξ_x and λ_x are the parameters of the distribution that are related to the mean μ_x and standard deviation σ_x of the random variables as follows:

$$\mu_x = exp\Big(\lambda_x + \frac{\xi_x^2}{2}\Big) \tag{2.9}$$

$$\sigma_x = \mu_x \sqrt{exp(\xi_x^2) - 1} \tag{2.10}$$

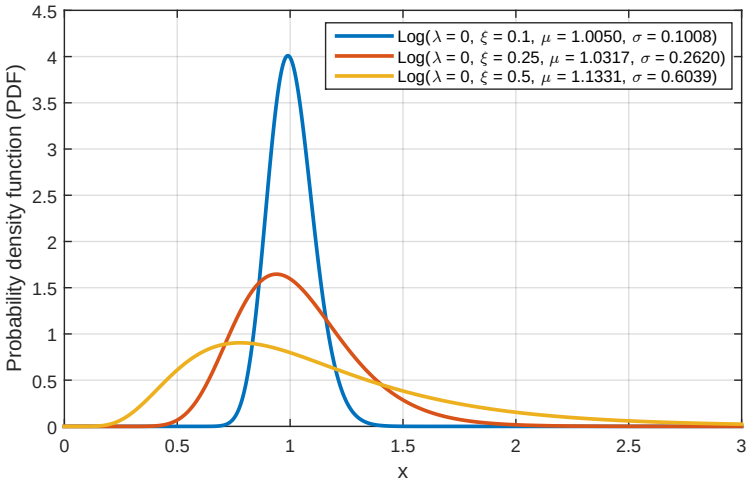


Figure 2.3: *Probability density funcion (PDF) of the lognormal distribution with* $\lambda = 0$ *and different values of* ξ

Extreme value type I distribution

The extreme value distribution is commonly used in engineering applications to model the maximum or minimum value of a random variable, such as the maximum wind speed, maximum load on bridges, minimum material properties and time to failure etc. (Mahadevan and Haldar, 2000). Three types of extreme value distribution have been classified according to Gumbel (1958): type I, type II and type III. In this section, the type I will be introduced since it is used in this thesis. The details of the other types can be found in Mahadevan and Haldar (2000) and Melchers and Beck (2017). The PDF and the CDF of the distribution

are expressed as:

$$f_X(x) = \alpha_n exp(-\alpha_n(x-u_n))exp[-exp(-\alpha_n(x-u_n))] \quad -\infty < x < +\infty \tag{2.11}$$

$$F_X(x) = 1 - exp[-exp(\alpha_n(x-u_n))] \tag{2.12}$$

where α_n and u_n are related to the mean and standard deviation of the extreme value variable X as:

$$\mu_x = u_n + \frac{\gamma}{\alpha_n} \tag{2.13}$$

where $\gamma \cong 0.57722$ (Euler constant)

$$\sigma_x = \frac{\pi}{\sqrt{6}\alpha_n} \tag{2.14}$$

The extreme value distribution has an exponential tail as shown in Figure 2.4.

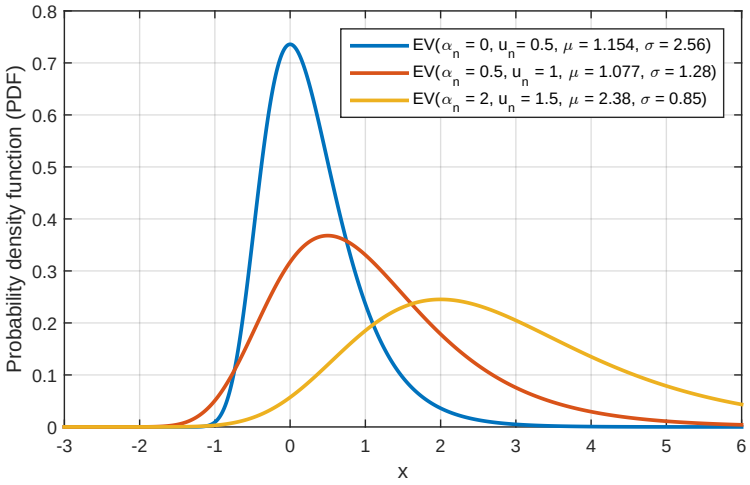


Figure 2.4: *Probability density funcion (PDF) of Extreme value ditribution type I with different means and standard deviations*

2.2.2 Limit state function

The reliability of a structure is described by a set of limit states representing a specific condition of a structure beyond which the structure no longer fulfils the relevant criterion on its function. The limit state can be defined according to JCSS (2001) as the border that separates the desired states (acceptable) from the adverse states (unacceptable) (see Figure 2.5) such as collapse, buckling and deflection. JCSS (2001) states that the limit states can be divided into two categories: the Ultimate limit states and the Serviceability limit states. The first category concerns the safety of people and structures which correspond to the loss of structural equilibrium, rupture or excessive deformation that result from the attainment of maximum resistance capacity and the rupture of members (e.g. bending, shear and fatigue failure modes). The second category concerns the functioning of the structure under normal use, the gradual deterioration and the comfort of people which correspond to the reduction of structure durability and efficiency that result from the local damage (e.g. cracking, excessive stresses that lead to permanent deformation). In order to quantify the reliability of a structure with respect to a particular limit state, this limit state should be formulated via a mathematical model describing it in terms of a function, called the limit state function, whose value depends on all relevant design parameters.

Each limit state function considered should contain a specific set of basic variables (S and R) that are the physical quantities representing the actions and environmental influences, material and geometrical quantities. The limit state function can be expressed as:

$$g(S, R) = 0 \tag{2.15}$$

where S and R are the basic variables modelling the effects of loads and resistance respectively, and they can be represented by a random vector X. Then Equation 2.15 can be written as $g(X_i) = g(X_1, X_2, ..., X_n) = 0$.

While the limit state function returns a negative value under system failure conditions $g(X_i) < 0$ and a positive value when the system is not failing $g(X_i) > 0$.

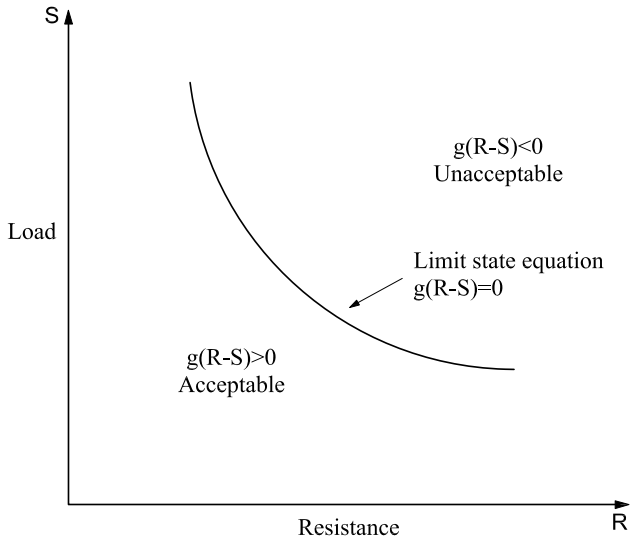


Figure 2.5: *Limit state function of two sets of random variables. It represents the boundary between the acceptable and unacceptable region (Mahadevan and Haldar, 2000)*

Therefore, it can be viewed as the difference between resistance R and effect of loads S.

$$g(X_i) = R - S \tag{2.16}$$

The probability of failure represents the probability of the system being under failure condition can be expressed as:

$$P_f = Prob\{g(X_i) \leq 0\} = P(R \leq S) = P(R - S \leq 0) \tag{2.17}$$

2.3 Reliability of structural systems

System reliability is the reliability of a structural system that is composed of several structural elements in which individual or combined failure can lead to the failure of the whole system (Schneider, 2006). The system reliability can also be defined as the reliability of a structure that has several failure modes such as bending, shear etc. with same importance (Faber, 2005). System reliability can be simplified into two extreme cases:

- **Series system**

  In the series system, (Figure 2.6), the local failure of the weakest component will rapidly lead to the failure of the whole structure. Therefore, the safety series system is defined by the weakest segment. For the series system, the

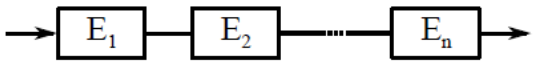


Figure 2.6: *Series system*

probability of failure can be expressed as:

$$P_f = 1 - \prod_{i=1}^{n}(1 - p_{fi}) \tag{2.18}$$

where p_{fi} is the probability of failure of the i^{th} segment. This equation can be used when all elements or components of the structure are statistically independent. For perfectly correlated elements, the probability of failure can be expressed as:

$$P_f = max[p_{fi}] \tag{2.19}$$

The probability of failure for partially correlated elements falls between the two limits:

$$max[p_{fi}] \leq P_f \leq 1 - \prod_{i=1}^{n}(1 - p_{fi}) \tag{2.20}$$

Narrower bounds have been proposed by Ditlevsen (1979) to estimate the probability of failure for the series system by taking into account the correlation between the components:

$$max[p_{fi}] + \sum_{a=2}^{n} max\left(p_{fa} - \sum_{b=1}^{a-1} p_{fa} \cap p_{fb}; 0\right) \leq P_f \leq \sum_{a=1}^{n} p_{fa} - \sum_{a=2,b<a}^{n} max(p_{fb} \cap p_{fa}) \tag{2.21}$$

According to Ditlevsen (1979), the upper and lower bounds are considered the individual and the joint (combination between two segments) probability of failure $p(f_a)$ and $p_{fa} \cap p_{fb}$ respectively. For simplicity, the joint

probability of failure involving three or more segments is neglected due to its complex calculations.

The individual probability of failure can be estimated using the reliability methods such as First Order Reliability Method (FORM) or Monte Carlo Simulation (MCS) as will be explained in detail in Sections 3.3 and 3.4. The joint probabilities are calculated using the integral of the bivariate normal distribution:

$$P(p_{f1} \cap p_{f2}) = \int_{\beta 1}^{\infty} \int_{\beta 2}^{\infty} \frac{1}{2\pi\sqrt{1-\rho_{sysab}^2}} e^{-1/2(1-\rho_{sysab}^2)(\beta_a^2\beta_b^2 - 2\rho_{sysab}\beta_a\beta_b)} d\beta_a d\beta_b \tag{2.22}$$

where β_a and β_b are the reliability indices (as to be explained in Section 3.3) for segments a and b respectively, ρ_{sysab} is the correlation between segments a and b, which represents the cosine of the angle between the two reliability vectors associated with segment a and b as shown in Figure 2.7. The correlation factor is calculated according to the direction cosine of each random variable of each segment or failure mode as:

$$\rho_{sysab} = \frac{Cov(a,b)}{\sigma_a \sigma_b} = \sum_{k=1}^{n} \alpha_{ak}^* \alpha_{bk}^* \tag{2.23}$$

and the system correlation matrix can be written as:

$$\begin{bmatrix} \rho_{sys11} & \rho_{sys12} & \cdots & \rho_{sys1z} \\ \rho_{sys21} & \rho_{sys22} & \cdots & \rho_{sys2z} \\ \vdots & \vdots & \ddots & \vdots \\ \rho_{sysz1} & \rho_{sysz2} & \cdots & \rho_{syszz} \end{bmatrix}$$

The reliability of the series system can be estimated as the average between the upper and lower bounds (Ditlevsen, 1979):

$$\beta_{sys} = \frac{\beta_{lower} + \beta_{upper}}{2} \tag{2.24}$$

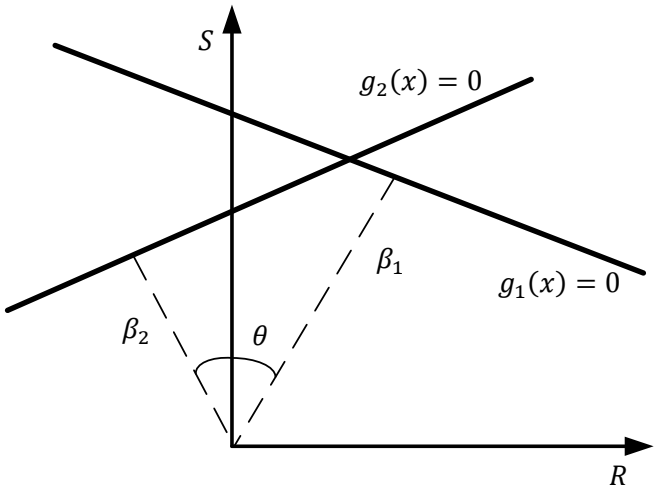


Figure 2.7: *Correlation between two failure modes or segments (Estes, 1997)*

- **Parallel system**

  In a parallel system, the local failure of one component does not lead to failure of the structure only. Hence, the components are fail safe because the whole structure fails when all components have failed (see Figure 2.8). For a parallel system, when all elements of the structure are statically independent, the probability of failure can be expressed as:

$$P_f = \prod_{i=1}^{n} p_{fi} \tag{2.25}$$

  where p_{fi} is the probability of failure of the i^{th} components. For perfectly correlated elements, the probability of failure can be expressed as:

$$P_f = min[p_{fi}] \tag{2.26}$$

  The probability of failure for partially correlated elements falls between the two limits:

$$min[p_{fi}] \leq P_f \leq \prod_{i=1}^{n} (p_{fi}) \tag{2.27}$$

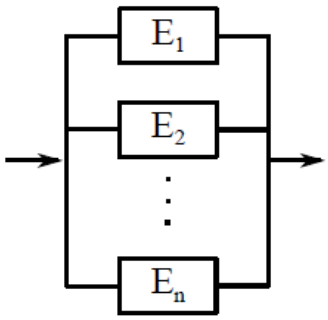


Figure 2.8: *Parallel system*

2.4 Probabilistic models

As mentioned in Section 2.2.1, the uncertainties related to an engineering system can affect the performance requirements for buildings and engineering works. These uncertainties should be described by probabilistic models. The development of probabilistic models for the basic random variables (uncertainties) is considered as the main task in reliability analysis. Mahadevan and Haldar (2000) presents the essential steps to develop the probabilistic models for uncertainties. They showed that the histograms are used to describe the characteristics of uncertainty and these identify the probability density function (PDF). Faber (2005) divides probabilistic modelling into: assessment and statistical quantification of the available data, selection of distribution function, estimation of distribution parameters e.g., and model verification. Certain parameters, that are called statistics, need to be estimated in order to describe the probability density function. The estimation of these parameters, the mean and standard deviation, is the major component of the uncertainty analysis. According to that, the randomness in the performance function can be quantified using these statistics.

The JCSS code part I (JCSS, 2001) notes that to select the distribution type of the physical uncertainties of a basic random variables, the following procedure should be followed:

- Select a set of distribution types that may be possible depending on expe-

rience from similar types of variables.

- Obtain a reasonable sample of observations and avoid systematic variation within the sample (assume the material is homogeneous along the sample).
- Select an appropriate distribution and corresponding parameters.
- Compare the sample data with the resulting distribution by using the fit tests.
- Choose the distribution that gives the smallest reliability if there are more than one distribution that fit equally well.

The JCSS Model Code (JCSS, 2001) and the literature present different probabilistic models for load and resistance covering many engineering application areas. The following sections will present the available probabilistic models of reinforced and prestressing concrete material properties, geometry, load and deterioration due to corrosion.

2.4.1 Modelling of concrete material properties

The mechanical properties of concrete have a significant variation due to three different reasons. The first is the variation of the material properties of concrete constitutes such as the material properties of cement, fine and coarse aggregate. The second is the manufacturing which includes the concrete composition (variation in components, water content, cement and aggregate) and execution that include mixing, transporting, temperature, etc. The last reason involves testing which includes, e.g., sampling, specimen preparation, curing and test procedure and equipment.

Different probabilistic models have been developed in the literature for the mechanical properties of concrete according to observations and testing. The majority of academic researchers focused on the concrete compressive strength (f_{cm}),

tensile strength (f_t) and the modulus of elasticity (E_{cm}). According to (JCSS, 2001), the concrete compressive stress can be modelled based on the concrete cylinder compressive strength after 28 days, while the other concrete properties are related to the concrete compressive strength as measured in-situ according to the following equations:

$$f_{cm} = \alpha(t,\tau) f_{c0}^{\lambda} Y_1 \qquad [MPa] \tag{2.28}$$

$$f_t = 0.3 f_{cm}^{2/3} Y_2 \qquad [MPa] \tag{2.29}$$

$$E_{cm} = 10.5 f_{cm}^{1/3} Y_3 (1 + \beta_d \phi(t,\tau))^{-1} \quad [GPa] \tag{2.30}$$

$$\varepsilon_{cu1} = 6.10^{-3} f_{cm}^{-1/6} Y_4 (1 + \beta_d \phi(t,\tau))^{-1} \quad [m/m] \tag{2.31}$$

where: f_{cm} is the concrete compressive strength as measured in-situ; $\alpha(t,\tau)$ is a deterministic function, which takes into account the concrete age at the loading time in days and the duration of loading τ in days; f_{c0} is the concrete cylinder compressive strength after 28 days; λ is a lognormal variable with mean 0.96 and COV 0.005 (this parameter can be considered deterministic); f_t is the tensile strength of concrete; E_{cm} is the modulus of elasticity; ε_{cu1} is the ultimate strain of concrete; Y_1 is a lognormal variable representing additional variation due to the placing, curing and hardening condition of in-situ concrete; Y_2, Y_3 and Y_4 are variables representing variations due to factors not well accounted for by concrete compressive strength (e.g., gravel type and size, chemical composition of cement and other ingredients). The statistical parameters of Y_{1-4} are shown in Table 2.1); β_d is the ratio of the permanent load to the total load and depends on the type of the structure (β_d is between 0.6 and 0.8); $\phi(t,\tau)$ is the creep coefficient according to the JCSS (2001), which is assumed to be a deterministic value.

The concrete cylinder compressive strength f_{c0} is usually modelled by a lognormal distribution and the statistical parameters for C15, C25, C35 and C45 ready mix concrete grade proposed by JCSS (2001) are shown in Table 2.2.

In addition to the JCSS (2001), several probabilistic models for concrete mechan-

ical properties have been proposed in the literature such as Mirza et al. (1979), Stewart (1995), Attard and Stewart (1998), Pham (1985) and Wiśniewski (2007) as presented in Tables 2.3, 2.4 and 2.5.

Table 2.1: *Statistical parameters of Y parameter according to JCSS (2001)*

Variable	Dist.	λ(MPa)	COV	Related to
Y_1	Lognormal	1.0	0.06	compression
Y_2	Lognormal	1.0	0.3	tension
Y_3	Lognormal	1.0	0.15	modulus of elasticty
Y_4	Lognormal	1.0	0.15	ultimate strain

Table 2.2: *Statistical parameters of the concrete cylinder compressive strength f_{c0} according to JCSS (2001)*

Concrete grade	Dist.	λ(MPa)	ξ(MPa)
C15	Lognormal	3.4	0.1917
C25	Lognormal	3.65	0.1643
C35	Lognormal	3.85	0.123
C45	Lognormal	3.98	0.0958

Table 2.3: *Probabilistic models of the concrete compressive strength according to the literature (the most common used in reliability of structures)*

Parameter	μ (MPa)	COV	σ (MPa)	Dist.	Source
f_{creal}	$f_{cm}^{'}$+7.5	-	6	Lognormal	(Stewart, 1995) and (Attard and Stewart, 1998)
f_{creal}	$1.03 f_{cm}$	0.18	-	Normal	(Pham, 1985)
f_{creal}	$0.675 f_{cm} + 7.7$	0.12-0.20	-	Normal or Lognormal	(Mirza et al., 1979)
f_{creal} (site cast)	$f_{cm} \times 1$	0.12	-	Lognormal	(Wiśniewski, 2007)
f_{creal} (plant cast)	$f_{cm} \times 1$	0.09	-	Lognormal	(Wiśniewski, 2007)

f_{creal} is the real concrete compressive strength in the structure.
f_{cm} is the nominal concrete compressive strength.

Table 2.4: *Probabilistic models of the concrete tensile strength according to the literature (the most common used in reliability of structures)*

Parameter	μ(MPa)	COV	Dist.	Source
f_t	$0.69\sqrt{f_{cm}}$	0.2	Normal	(Mirza et al., 1979)
f_t	$0.53\sqrt{f_{cm}}$	0.13	Normal	(Mirza et al., 1979)
f_t	$0.3 f_{cm}^{2/3}$	0.2	Normal	(Eurocode-2, 2004)

Table 2.5: *Probabilistic models of the concrete modulus of elasticity according to the literature*

Parameter	μ(MPa)	COV	Dist.	Source
E_{cm}	$4600\sqrt{f_{cm}}$	0.12	Normal	(Mirza et al., 1979)
E_{cm}	$4400 f_{cm}^{0.516}$	0.15	Normal	(Attard and Stewart, 1998)
E_{cm}	$22000 f_{cm}^{0.3}$	0.08	Normal	(Eurocode-2, 2004)

2.4.2 Reinforcement and pre-stressing steel material properties modelling

The properties of reinforcement and pre-stressing steel in structural engineering is investigated in terms of its mechanical properties including the yield strength (f_y), ultimate strength (f_u) and strain (ε). The construction environment and the variation in composition of the steel can affect the steel material properties. In the literature, several probabilistic models for reinforcement and pre-stressing steel have been developed. In this section some of commonly used models (for reinforcement and pre-stressing steel) in the literature have been summarized in Tables 2.6 and 2.7 respectively.

Table 2.6: *Statistical parameters of steel reinforcement properties*

Parameter	μ(MPa)	COV	σ(MPa)	Dist.	Source
f_y	$S_{nom.} + 2\sigma$	-	30	Normal	(JCSS, 2001)
f_y	$S_{nom.}$	0.1	-	Beta	(Mirza et al., 1979)
E_s	$1.005 E_{snom}$	0.033	-	Normal	(Mirza et al., 1979)

S_{nom} is the steel grade e.g. S300 and S400.
E_{snom} is the nominal value of steel modulus of elasticity.

Table 2.7: *Statistical parameters of pre-stressing steel properties*

Parameter	μ	COV	σ	Dist.	Source
f_{py}	$0.88f_{pk}$ MPa	0.025	-	Normal	(Mirza et al., 1980)
f_{py}	$1.04f_{pk}$ or $f_{pk}+66$ MPa	0.025	-	Normal	(JCSS, 2001)
f_{py}	$f_{pk}+1.645\times 40$ MPa	-	40 MPa	Normal	(Jacinto et al., 2012)
E_p	195 GPa	-	40 MPa	Normal	(Mirza et al., 1980)
E_p	wire 200 GPa strand 195 GPa bar 200 GPa	0.02	-	Normal	(JCSS, 2001)
E_p	195 MPa	0.025	-	Normal	(Jacinto et al., 2012)
ε_u	0.05	-	0.0035	Normal	(JCSS, 2001)
ε_u	0.05	-	0.004	Normal	(Jacinto et al., 2012)

2.4.3 Modelling of loads

The term load refers to forces and imposed displacements acting on structural components and systems. The JCSS model code (JCSS, 2001) and Faber (2005) show that a complete load model should describe its magnitude, position, direction, duration etc. In addition, it should be divided according to the time variation of the load (permanent and variable).

2.4.3.1 Permanent load

Permanent loads are usually due to the self weight of structural and non-structural elements. Although there is insignificant variation of permanent load over time, its intensity is uncertain (Faber, 2005). Faber (2005) also states that the uncertainties in the self weight of a steel component depends mostly on the uncertainty in the cross sectional area, whereas in case of concrete or timber, the uncertainty depends on the variations of the geometry and density. Therefore, the JCSS code assumes that the conservative coefficient of variation for the total permanent load is equal to 0.10 (due to the small COV of the dimensions and density of concrete). The code also assumes that the mean of the permanent load is equal to the nominal value. Moreover, the permanent load is assumed to be distributed normally. Scholten et al. (2004) suggested the use of a normal distribution for the permanent load with COV of 0.05 and 0.1 for the structure self weight and

the superimposed dead load respectively.

For highway bridges, Nowak (1993), Nowak and Szerszen (1998) and Nowak and Collins (2012) classify the dead load into three different components due to their different degrees of variation. The three components are: the weight of off-site built elements (weight of steel and precast concrete), weight of cast in place concrete members and the weight of asphalt. They considered the dead load as normally distributed with coefficient of variation for the three dead load components equal to 8%, 10% and 25% respectively as listed in Table 2.8. The bias factors, which represent the ratio of the measured (actual) load to the corresponding predicted (nominal) load (Bathurst and Javankhoshdel, 2017), are also used for each bridge permanent load components as shown in Table 2.8.

Melchers (1999) stated that the dead load is commonly treated to be normally distributed with a mean equal to the nominal value and a coefficient of variation of $0.05 - 0.1$. However, Ellingwood (1980) observed that there are some human errors when estimating the dead load and therefore, it is recommended to use a mean value of 5% higher than the nominal.

Table 2.8: *Statistical parameters of dead load according to Nowak and Szerszen (1998)*

Component	Thickness	Bias	COV
Factory made members	-	1.03	0.08
Cast in place members	-	1.05	0.1
Asphalt	75mm	-	0.25

The permanent load is not due to the self weight only but also for the load due to pre-stress. Usually, the pre-stressing force should be available all throughout the life of a structure. However, there are some losses in pre-stress force due to the short ($t = 0$) and long ($t = \infty$) term losses (explained in detail in Chapter 7).

$$P(x,t) = P_o - \Delta P(x,t) \tag{2.32}$$

where P_o is the jacking force; $\Delta P(x,t)$ is the losses of pre-stress and $P(x,t)$ is the remaining pre-stress forces after short and long term losses.

According to JCSS (2001), there are different design codes that can be used to estimate the pre-stress losses depending on different parameters such as the type of pre-stress, properties of pre-stressing steel and concrete, environmental condition etc. Therefore, there is no exact value of the pre-stress losses. According to that, the variability of the pre-stress losses should be considered in reliability analysis. Pre-stress losses can be treated as a normal distribution and their statistical parameters are shown in Table 2.9 (JCSS, 2001). The uncertainty in losses is constant over time, but as the mean force decrease, this leads to an in crease in the COV.

Table 2.9: *Statistical parameter of pre-stress losses according to (JCSS, 2001)*

Parameter	μ	COV Immediate, $t = t_o$	COV Long term, $t = \infty$
Pre-stress losses, $\Delta P(x,t)$	$\Delta P(x,t)$	0.3	0.3
Pre-stress force $P(x,t)$	$P(x,t)$	$0.04 - 0.06$	$0.06 - 0.09$

2.4.3.2 Live load

The live load in buildings is the load imposed by weight of people, furniture, equipments and stored objects. Live load in buildings can be divided in sustained and transient load. The sustained load represents, for example, furniture which tends to be constant over long periods, while the transient load represents short term loads such as weight of people and vehicles. The JCSS code suggests that the combined total live load is represented by a Gumbel distribution (EV-type I) because the important random variables are the magnitude of the largest extreme load that occurs during a specified reference period for which the probability of failure is calculated.

For highway bridges, the live load covers the static and dynamic effects produced by vehicles (Nowak, 1993). Different factors can affect bridges live load such as the span length, truck weight, axle load, axle configuration, position of the vehicle (transverse and longitudinal), number of vehicles and girders spacing and stiffness. Generally, bridges live load are modelled according to the static load which represents the weight of the truck (W) factored by the dynamic load factor (DLF) which take into consideration the effect of bridge vibration due to the dynamic load. Nowak (1993) observed that the dynamic load factor decreases for heavier trucks according to the survey of truck load over 75 years. Additionally, the load dynamic factor depends on the road surface roughness, bridge dynamics and vehicle dynamics. For multiple lane bridges, the critical load effect generally occurs when heavily loaded trucks occur side by side and have fully correlated weights. The distribution of the load of the heaviest truck in a given period is (Nowak, 1993):

$$F_n(w) = \left[\Phi\left(\frac{w-\mu_w}{\mu_w V_w}\right)\right]^N \tag{2.33}$$

where Φ is the cumulative distribution function of the standard normal distribution; N is the number of trucks in this period; w is the static and dynamic component of the truck load (random variable) $w = (1 + DLF)W$; DLF has a mean value of 0.15 for single truck and 0.1 for two trucks and coefficient of variation of 0.8 (Nowak, 1993) and μ_w and V_w are the mean and COV of the truck weight. Based on a survey data comprising 9250 trucks in the US, Nowak (1995) computed the mean truck weight as 250 kN and its coefficient of variation as 0.4. Nowak (1993) describes the bridge loads using a normal distribution, however, the extreme value type I is commonly used (Scholten et al., 2004) due to the fact that the traffic load model has to represent the maximum load in which a bridge is going to experience during its lifetime. Therefore, in this work Gumbel distribution is used to model the live load.

2.4.4 Deterioration model

The corrosion of reinforcing bars is one of the main causes of deterioration of concrete structures, leading to reduction in their service life, their durability or even to failure. Normally, reinforcing steel does not corrode because of the generation of a passive film on the steel surface due to the initial corrosion reaction. The high alkalinity developed from cement hydration in freshly placed concrete fixes the film on the steel surface and the passive film slows further corrosion by isolating the steel from the environment. Nevertheless, there are two aggressive agents that can cause the corrosion of reinforcement in concrete structures: carbonation and chloride contamination. When these two aggressive agents reach the reinforcement bar, corrosion may start, affecting the cross sectional area and the mechanical properties of steel reinforcement, causing concrete cover cracking due to the expansion of corrosion products and reducing the bond between steel and concrete (see Figure 2.9) (Rodriguez et al., 1997). Consequently, the safety and serviceability of the concrete structure will be affected.

The deterioration of reinforced concrete structures due to corrosion comprises two stages: corrosion initiation and corrosion propagation (see Figure 2.10) as will be explained in the following subsections.

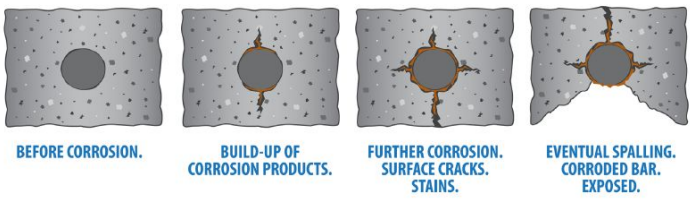


Figure 2.9: *Corrosion induced cracking and spalling of concrete (Daily, 1999)*

2.4.4.1 Corrosion initiation

Corrosion is initiated mainly by chloride ion contamination, often in conjunction with poor concrete quality or inadequate concrete cover. Chloride contamination

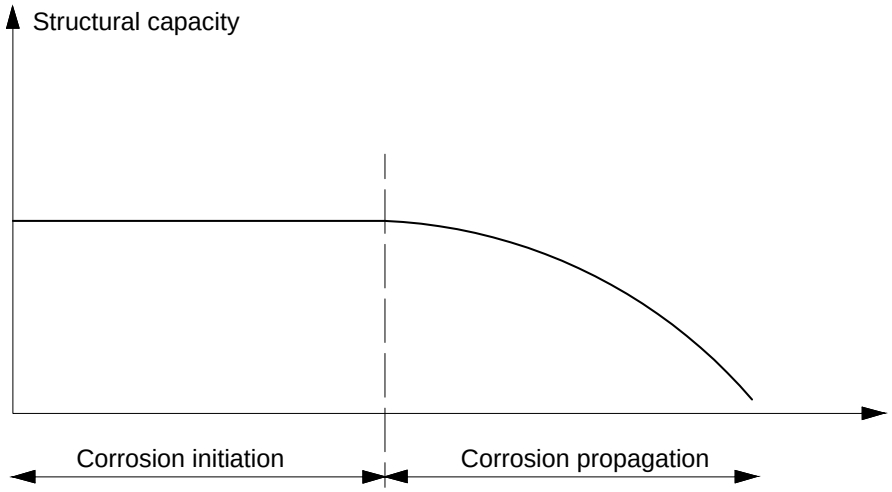


Figure 2.10: *Initiation and propagation corrosion model of reinforcement steel (Darmawan, 2010)*

is considered to be the major cause of reinforcement corrosion in concrete structures and may occur due to different sources, e.g., the application of de-icing salts, exposure to sea-spray in marine environments, and, in some rare cases, from chloride contaminated concrete admixtures. The chloride ions can disrupt the passive film and cause reinforcement corrosion if present in sufficient quantity (Daily, 1999). Daily (1999) also shows that the concentration of chloride ions that is needed to initiate corrosion (break down the passive film) is extremely low (about 0.026% by weight of concrete). Darmawan (2010, 2009) indicate that chloride contamination will reduce the service life, strength and serviceability of concrete structures by reducing the cross-sectional area of steel and increasing the cracking and spalling of concrete.

The initiation stage involves the movement of chlorides through concrete cover until the steel passive layer is destroyed. That can happen when the chloride ions at steel surface exceed a threshold limit. The time that is needed for chloride ions to reach the threshold chloride concentration is called the time to corrosion initiation.

According to Stewart and Rosowsky (1998), Fick's second law of diffusion can be

used to simulate the chloride ingress into concrete pores, which is expressed as:

$$\frac{\partial C}{\partial t} = D\frac{\partial^2 C}{\partial x^2} \tag{2.34}$$

where C is the chloride concentration at a distance x from the surface at time t and D is the diffusion coefficient. According to Vu and Stewart (2000), the diffusion coefficient represents the concrete permeability, which can be affected by different factors such as the water cement ratio, cement type, curing and environment. Several models have been proposed in the literature (Hobbs, 1998; Papadakis et al., 1996; Stewart and Rosowsky, 1998) considering the effect of water cement ratio on the chloride diffusion coefficient. All the models developed show that increasing the water cement ratio leads to the increasing of the capillary porosity of concrete and subsequently increased diffusion coefficient (see Figure 2.11).

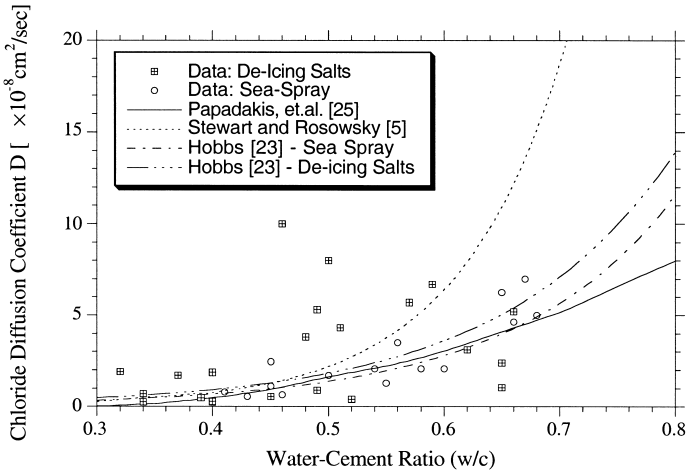


Figure 2.11: *The effect of increasing mix proportion in concrete on the chloride diffusion coefficient (D) (Vu and Stewart, 2000)*

For typical water cement ratios (0.35-0.5), the models exhibit the same trend. According to Vu and Stewart (2000), the model developed by Papadakis et al. (1996) gives the best fit to the available data in the literature and it can be

expressed as:

$$D = D_{H2O} 0.15 \frac{1 + \rho_c \frac{c}{w}}{1 + \rho_c \frac{w}{c} + \frac{\rho_c a}{\rho_a c}} \left(\frac{\rho_c \frac{w}{c} - 0.85}{1 + \rho_c \frac{w}{c}} \right)^3 \qquad (cm^2/s) \qquad (2.35)$$

where D_{H2O} is the chloride diffusion coefficient in an infinite solution ($=1.6 \times 10^{-5}$ cm^2/s for NaCl); ρ_c and ρ_a are the mass densities for cement and aggregates respectively; a/c is the aggregate to cement ratio and w/c is the water cement ratio which can be estimated from Bolomey's formula:

$$\frac{w}{c} = \frac{27}{f_{c0} + 13.5} \qquad (2.36)$$

where f_{c0} is the concrete compressive strength of a standard test cylinder in MPa. Hoffman and Weyers (1994) estimated the diffusion coefficient in each state in the US and found a mean value of $2 \times 10^{-8} (cm^2/s)$ and coefficient of variation between 0.3 to 1.6, with a mean value equal to 0.75, and lognormal distribution. The chloride content $[C(x,t)]$ at time t and distance x can be calculated according to the following equation:

$$C(x,t) = C_o \text{erfc} \left[\frac{x}{2\sqrt{D_o t}} \right] \qquad (2.37)$$

where erfc is the complementary error function and C_o is the surface chloride concentration, which is independent of time, and it is related to the environment aggressiveness. The reference values of the surface chloride concentration can be estimated according to experimental results, such as Hoffman and Weyers (1994) who studied a number of samples taken from 321 concrete bridges in the United States. Hoffman and Weyers (1994) found that the surface chloride concentration does not accumulate over the time. Alternatively, they found that the surface chloride concentration is in equilibrium with the concentration of chlorides in the saturated de-icing salts solution. So, according to Hoffman and Weyers (1994), the surface chloride concentration is modelled (in the US) with a lognormal distribution with mean and coefficient of variation $3.5 Kg/m^3$

and 0.5 respectively. From Equation 2.37, the time to corrosion initiation can also be evaluated by assuming the chloride concentration $C(x,t)$ to be equal to the chloride concentration threshold over which the steel corrosion is triggered. The critical threshold chloride concentration tends to lie within the range 0.6-1.2 Kg/m^3 with a mean and COV of 0.9 and 0.19 respectively and distributed uniformly (Cady and Weyers, 1983; Mehta, 1991).

2.4.4.2 Corrosion propagation

In the second stage, the corrosion propagation happens when the reinforcement corrodes causing metal loss, loss of area and bond, and therefore reduces structural capacity (Darmawan, 2009; Stewart and Rosowsky, 1998). Corrosion propagation is usually described in terms of corrosion rate in mm/year, which represents the loss of metal per unit of surface per unit of time. Hence, the corrosion rate can be quantified by removing the steel from structures and measuring the weight differences with reference to its surface area exposed to corrosion. However, this method can not be used for structures during their service life. Therefore, a non-destructive method is currently used based on electrochemical measurements to estimate the corrosion rate in terms of corrosion current density $i_{corr}[\mu A/cm^2]$ (Andrade and Alonso, 1996; Broomfield, 1994).

Studies show that the corrosion rate is one of the most important parameters in the corrosion induced deterioration model for reinforced concrete structures (Li et al., 2006; Otieno et al., 2011). The availability of water and oxygen at the reinforcement surface can have a large effect on the corrosion rate. Yalcyn and Ergun (1996) mentioned that the corrosion rate is affected by the oxygen on the cathode that is increased with increasing humidity. Vu and Stewart (2000) shows that the oxygen availability at the steel surface depends on concrete quality (water cement ratio w/c), concrete cover and environmental conditions (temperature and humidity). Vu and Stewart (2000) found the effect of concrete cover and water cement ratio on the corrosion rate for a typical humidity and temperature 75% and 20°C (see Figure 2.12), and they proposed an equation for the corrosion

rate as a function of concrete quality and cover as follows:

$$i_{corr}(1) = \frac{37.8(1 - w/c)^{-1.64}}{Cover} \qquad (\mu A/cm^2) \tag{2.38}$$

where $i_{corr}(1)$ is the corrosion rate at the start of corrosion propagation. Earlier studies (Liu and Weyers, 1998; Yalcyn and Ergun, 1996) suggested that the corrosion rate reduces with time rapidly during the first few years after initiation but then will reduce slowly. Vu and Stewart (2000) expect that the production of rust on the steel surface will reduce the diffusion of iron ions away from the steel surface. They also used the data of corrosion rate reduction with time from Liu and Weyers (1998) to develop a relationship between time since initiation and corrosion rate which is expressed empirically as:

$$i_{corr}(t_p) = i_{corr}(1).0.85.t_p^{-0.29} \tag{2.39}$$

where t_p is the time since corrosion initiation and $i_{corr}(1)$ is given by Equation 2.38. In general, corrosion may be expressed as a time dependent variable such that:

$$i_{corr}(t - t_i) = i_{corr}(1).\alpha.(t - t_i)^{\beta} \quad \left(\mu A/cm^2\right) \quad where(t - t_i) \geq 1year \tag{2.40}$$

where t_i is the time to corrosion initiation and α and β are constants equal to 0.85 and -0.29 respectively.

For general corrosion, it is assumed that the corrosion process will lead to a uniform reduction in the area of steel over the whole exposed surface of the rebar as shown in Figure 2.13. The general corrosion is a simplified assumption used by several researchers such as Thoft-Christensen and Hansen (1993) and Stewart and Rosowsky (1998) in which they ignore the spatial variability of pitting corrosion along the rebar. Under this assumption, the corrosion rate is assumed to be constant according to the Faraday's law and the remaining area of steel after t

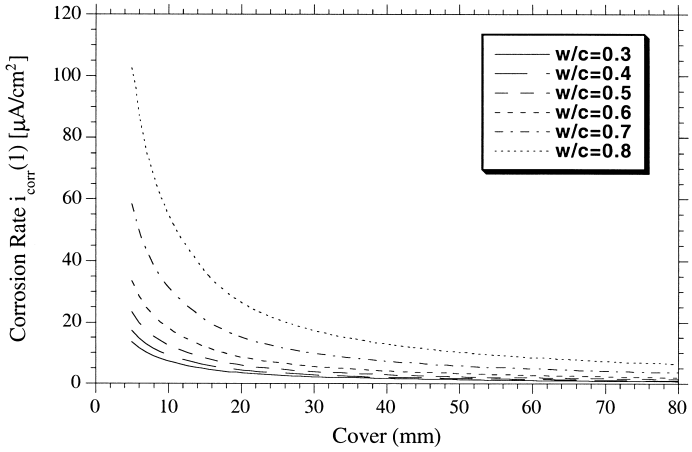


Figure 2.12: *The effect of concrete quality and cover on corrosion rate as studied by Vu and Stewart (2000)*

years can be estimated from:

$$A_s(t) = \begin{cases} n\frac{\pi D_o^2}{4}, & t \leq t_i \\ n\frac{\pi[D_o - \Delta D(t)]^2}{4}, & t > t_i \end{cases} \tag{2.41}$$

where D_o is the initial diameter of the rebar, n is the number of bars, t_i is the time in years to corrosion initiation and $\Delta D(t)$ is the reduction in bar diameter that estimated as (Thoft-Christensen and Hansen, 1993):

$$\Delta D(t) = D_o - 0.0232(t - t_i)i_{corr} \tag{2.42}$$

The mean current density (i_{corr}) is estimated to be $i_{corr} = 1\mu A/cm^2$ based on a study carried out by Dhir et al. (1994) where uncracked concrete specimens were exposed to salt spray conditions. However, Darmawan (2010) illustrates that this approach is not accurate when the concrete structure is subjected to chloride attack, which usually results in pitting corrosion. Val and Melchers (1997) proposed an alternative model for pitting corrosion, based on accelerated corrosion test carried out by Gonzalez et al. (1995), by assuming a non-uniform reduction in reinforcement bar diameter as shown in Figure 2.14. The maximum penetration of pitting in localized corrosion is about four to eight times the average

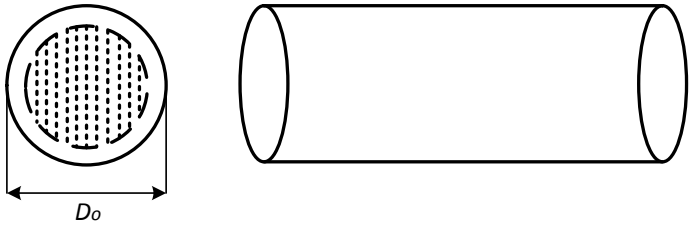


Figure 2.13: *Uniform loss of reinforcement due to general corrosion Darmawan (2010)*

penetration and for simplicity, Val and Melchers (1997) assumed the pit form to be hemispherical as shown in Figure 2.15.

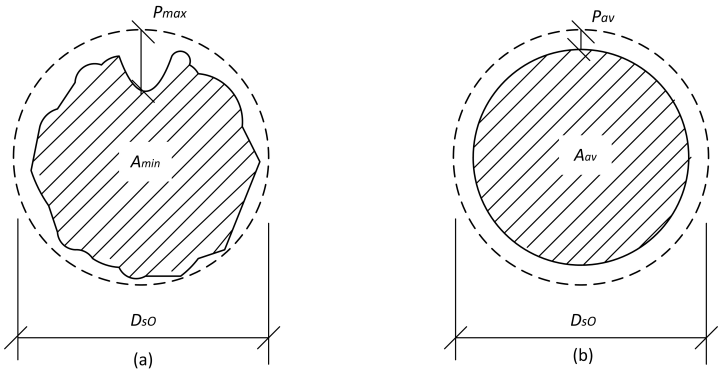


Figure 2.14: *Configuration of pitted corroded rebar: (a) cross section of corroded rebar with P_{max} and (b) equivalent average cross section referred to the overall corroded rebar surface (Zhang et al., 2013)*

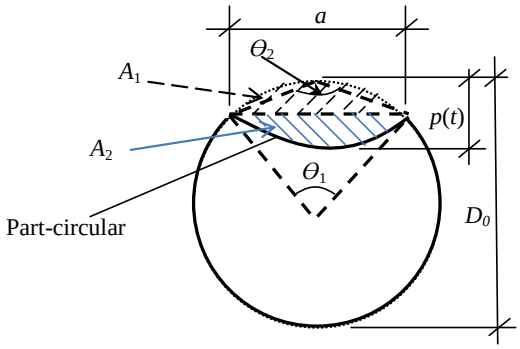


Figure 2.15: *Non-uniform loss of reinforcement due to localized (pitting) corrosion (Val and Melchers, 1997)*

The maximum pit depth at time t along a reinforcing bar is estimated from:

$$P(t) = 0.0116(t - t_i)i_{corr}R \tag{2.43}$$

where R is the pitting factor representing the extent of pitting corrosion as the ratio between the maximum and average corrosion penetration as follows:

$$R = P(t)/P_{av}(t) \tag{2.44}$$

$$P_{av}(t) = 0.0116i_{corr}(t - t_i) \tag{2.45}$$

Tuutti (1982) suggested that the pitting factor varies between 4 and 10 for reinforcing bar of 5 and 10 mm diameter and 150 to 300 mm in length. Similarly, Gonzalez et al. (1995) found that the pitting factor varies between 4 and 8 according to experimental test for specimens with 8 mm diameter reinforcing bars with 125 mm length. According to the information of the previous researchers, Stewart (2004) proposed a statistical model for pitting factor depending on an accelerated corrosion test for 10 mm diameter and 100 mm length of reinforcement bar. The maximum pit depth is measured for each 100mm length. Stewart (2004) used a Gumbel distribution (EV type I) to fit the data of maximum pit depth and that seems reasonable as the extreme value is used widely to characterise pitting of steel plates and pipes and pre-stressing wires (Darmawan and Stewart, 2007; Hawn, 1977). Furthermore, Stewart and Al-Harthy (2008) developed a probabilistic model for pitting factor according to an accelerated corrosion test of two RC slabs with 16 and 27mm diameters, the maximum pit depth is also measured at each 100mm length and they are well fitted with Gumbel distribution. Table 2.10 summarises the statistical parameters of the pitting factor for $L_o = 100$mm.

To predict the distribution of maximum pit depth for increased length of bar (L_u), the Gumbel statistical parameters can be modified according to the follow-

Table 2.10: *Statistical parameter of pitting factor (R)*

Specimen	L_o (mm)	Diameter (mm)	μ	COV	μ_o	α_o	Source
Y10	100	10	5.65	0.22	5.08	1.02	(Stewart, 2004)
Y16	100	16	6.2	0.18	5.56	1.16	(Stewart and Al-Harthy, 2008)
Y27	100	27	7.1	0.17	6.55	1.07	(Stewart and Al-Harthy, 2008)

ing (Sheikh et al., 1990):

$$\mu = \mu_o + \frac{1}{\alpha} ln(\frac{L_u}{L_o}) \qquad \alpha = \alpha_o \tag{2.46}$$

where μ_o and α_o are the Gumbel parameters derived from statistical analysis of pitting data for reinforcement of length L_o as explained above.

The remaining area of the corroded steel at time t after pitting corrosion is then calculated as the following equations (Val and Melchers, 1997):

$$A_r(t) = \begin{cases} \frac{\pi.D_o^2}{4} - A_1 - A_2, \; if & P(t) \leq \frac{\sqrt{2}}{2} D_o \\ A_1 - A_2, if & \frac{\sqrt{2}}{2} D_o < P(t) \leq D_o \\ 0, if & P(t) > D_o \end{cases} \tag{2.47}$$

where

$$A_1 = 0.5\Big[\theta_1.(\frac{D_o}{2})^2 - a.|\frac{D_o}{2} - \frac{P(t)^2}{D_o}|\Big] \tag{2.48a}$$

$$A_2 = 0.5\Big[\theta_2 P(t)^2 - a.\frac{P(t)^2}{D_o}\Big] \tag{2.48b}$$

$$a = 2P(t)\sqrt{1 - [\frac{P(t)}{D_o}]^2} \tag{2.48c}$$

$$\theta_1 = 2\text{arcsin}\big(\frac{a}{D_o}\big) \quad and \quad \theta_2 = 2\text{arcsin}\big(\frac{a}{2P(t)}\big) \tag{2.48d}$$

2.5 Summary

In this chapter, the theoretical background on the principles of reliability analysis have been reviewed. The background included the explanation of types of uncertainties in engineering problems. Some principles definitions were also included such as the probability distribution function of the normal. lognormal and extreme value type I, as well as, the limit state function and the system reliability. This followed by a survey of the most common probabilistic models used in reliability of structures. This included the probabilistic models of concrete, reinforced and prestressed steel material properties. The last part of this chapter presented the deterioration and load probabilistic models. This background is used in the next chapters (3, 5 and 7) in which reliability analysis has been applied.

Chapter 3

Reliability Analysis Methods

This chapter aims at applying the methods of reliability analysis to a reinforced concrete beam deteriorating over time. Two methods, First Order Reliability Method (FORM) and Monte-Carlo Simulation (MCS), have been applied using a MATLAB code. The MATLAB code is then used to find the probability of failure of the real case study, as described in Chapter 7.

This chapter is organised in eight sections. Section 3.1 gives a small introduction to reliability analysis. Section 3.2 defines the probability of failure. Section 3.3 presents the historical traceability of FORM method and the procedure of its application. Section 3.4 describes MCS method. Section 3.5 and 3.6 presents an application of FORM and MCS methods on a simply supported reinforced concrete beam and discuss the analysis results. Finally, Section 3.7 summarises the findings of this chapter.

3.1 Introduction

Generally, reliability analysis of technical components became an important issue during the Second World War. During this period significant problems were encountered especially in regard to the performance of electrical systems (Faber, 2005). Nowadays, reliability analysis has been developed for different applications and in a wide range of different industries such as the nuclear industry,

chemical industry and building industry. Therefore, the application of reliability analysis received a worldwide acceptance from the engineering profession. Reinforced concrete structures can deteriorate due to the environmental effects and over loading. Therefore, periodic on-site inspections are very important to ensure their safety and durability. However, the results of these inspections are usually poor and have a high degree of uncertainty. Consequently, it is recognized that a deterministic approach is not effective for assessment (Frangopol and Hearn, 1996).

Nowadays, the practical probabilistic method or the reliability analysis is increasingly used for the evaluation, quantification, monitoring and assessment of risk for concrete structures (JCSS, 2001). In addition, the reliability analysis methods are used to make appropriate decisions about the performance of a structure (Frangopol et al., 1997; Vu and Stewart, 2000). Furthermore, these methods are also used for the structures that are at the design stage, under construction or in actual use. This chapter will introduce the most common techniques of structural reliability analysis, namely, First Order Reliability Methods (FORM)and Monte-Carlo simulation. Firstly, the basic idea and steps of FORM method will be explained in detail. Secondly, the basic concepts of Monte-Carlo simulation will be clarified. The last part of this chapter will present the application of the two methods on a deteriorated simply supported reinforced concrete beam.

3.2 Probability of failure

As mentioned in Chapter 2, the performance function (limit state function) is described as $g(X_i) = 0$, where X is the vector of the basic random variables. The basic random variables are usually represented the resistance (R) and action (S) variables. Therefore, the limit state function can be written as $g(R, S) = 0$.

Generally, when the action effect is larger than the resistance, the failure occur. Therefore, the probability of failure can be defined as the probability of limit

state violation, and it can be written as:

$$P_f = P\big(g(X_i) < 0\big) = P\big(g(R,S) < 0\big) \tag{3.1}$$

Or it can be written as:

$$P_f = P\big(R < S\big) = P\big(R - S < 0\big) \tag{3.2}$$

The two random variables R and S have a marginal density functions $f_R(r)$ and $f_S(s)$, respectively, that are combined together to generate a joint density function $f_{RS}(r,s)$ as shown in Figure 3.1. When only two random variables are considered (r and s), the probability of failure can be determined from the following equation:

$$P_f = \int\int_{G(r,s)<0} f_{R,S}(r,s)drds \tag{3.3}$$

The integration of Equation 3.3 is illustrated in Figure 3.1 which is corresponds to the grey volume.

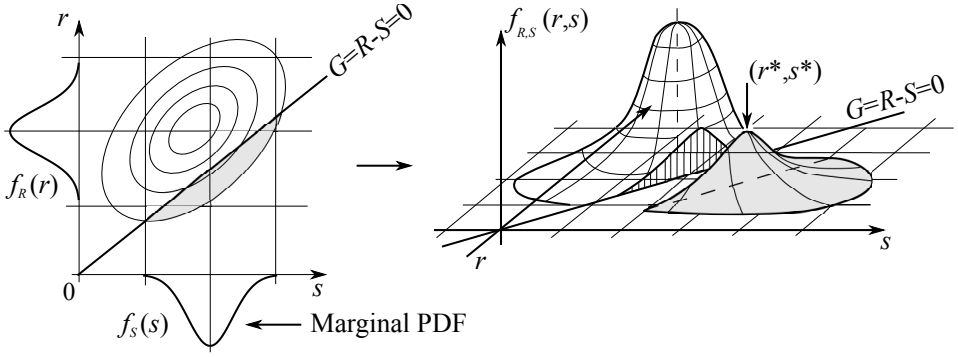


Figure 3.1: *Three dimensional representation of a possible joint density function ($f_{RS}(r,s)$) for two random variables with marginal density functions $f_R(r)$ and $f_S(s)$ (Schneider, 2006)*

In case of independent random variables, Equation 3.3 can be re-written as:

$$P_f = \int_{-\infty}^{+\infty} F_R(x) f_s(x) dx \tag{3.4}$$

where $F_R(x)$ is the CDF of structural resistance and $f_s(x)$ is the PDF of load demands. Equation 3.4 can be generalized to N dimensions, however, it is difficult to solve multiple integrals equation analytically and the reliability methods should be used to solve it. In the following sections, the direct focus is on the First Order Reliability Method (FORM) and Monte-Carlo simulation that can be used to solve Equation 3.4.

3.3 First Order Reliability Method FORM

The First Order Reliability Method (FORM) was first developed more than four decades ago (Faber, 2005). After that, the method has been refined and developed significantly, to be the most important method for reliability evaluation in structural reliability theory. The first order name is derived from its dependence on the first order Taylor series to approximate the limit function.

The basic concept of FORM analysis method is to transform the original set of random variables X_i into a set of standardized normally distributed random variables $(X_i^{'})$ (standard Gaussian distribution) as:

$$X_i^{'} = \frac{X_i - \mu_{X_i}}{\sigma_{X_i}} (i = 1, 2, ..., n) \tag{3.5}$$

such that, the random variables $X_i^{'}$ have zero means and unit standard deviations. Noting that, Equation 3.5 can be used just when X_i are distributed normally. This equation is also used to transform the original limit state function $g(X_i) = 0$ to the reduced limit state function $g(X_i^{'}) = 0$ as shown in Figure 3.2. The X coordinate system is referring to the original coordinate system and $X^{'}$ refers to the transformed or reduced coordinate system. Note that since X_i is normal, $X_i^{'}$ are standard normal with zero mean and unit standard deviation.

In the FORM method, the probability of failure is obtained by the value of *reliability index* (β) which represent the smallest distance from the origin to the limit state function in the normalized space as shown in Figure 3.2. The minimum dis-

tance point on the limit state function is called the design point or the checking point, which is represented by a vector x^* in the original coordinate system, and by a vector $x^{'*}$ in the reduced coordinate system.

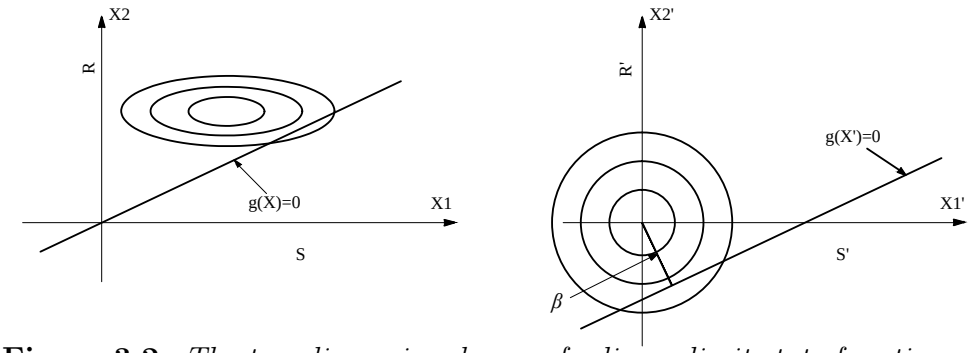


Figure 3.2: *The two dimensional case of a linear limit state function and standardized normally distributed variables* $X_i^{'}$ *(Faber, 2005)*

.

For the linear limit state function, if the random variables have a normal distribution, then the limit state function will have the same distribution with mean ($\mu_{g(X_i)}$) and standard deviation ($\sigma_{g(X_i)}$) defined as:

$$\mu_{g(X_i)} = \mu_R - \mu_S \tag{3.6}$$

$$\sigma_{g(X_i)} = \sqrt{\sigma_R^2 + \sigma_S^2} \tag{3.7}$$

According to that, the probability of failure can be expressed by the following equations:

$$P_f = P\Big(g(X_i) < 0\Big) = \Phi\left(\frac{0 - \mu_{g(X_i)}}{\sigma_{g(X_i)}}\right) = \Phi\left(\frac{-\mu_{g(X_i)}}{\sigma_{g(X_i)}}\right) = \Phi(-\beta) \tag{3.8}$$

where Φ is the standard normal distribution function with zero mean and unit standard deviation. According to Equation 3.8, the reliability index as expressed by Cornell (Cornell, 1969) is:

$$\beta = \frac{\mu_{g(X_i)}}{\sigma_{g(X_i)}} \tag{3.9}$$

By substituting Equations 3.6 and Equations 3.7 in Equation 3.9 the Cornell reliability index will be expressed from the following equation:

$$\beta_c = \frac{\mu_R - \mu_S}{\sqrt{\sigma_R^2 + \sigma_S^2}} \tag{3.10}$$

For non-linear limit state function, it is more difficult to find the reliability index compared to the procedure outlined above. Therefore, Hasofer and Lind (1974) proposed a linearisation of the failure surface $g(X_i')$ in the design point x'^* as shown in Figure 3.3.

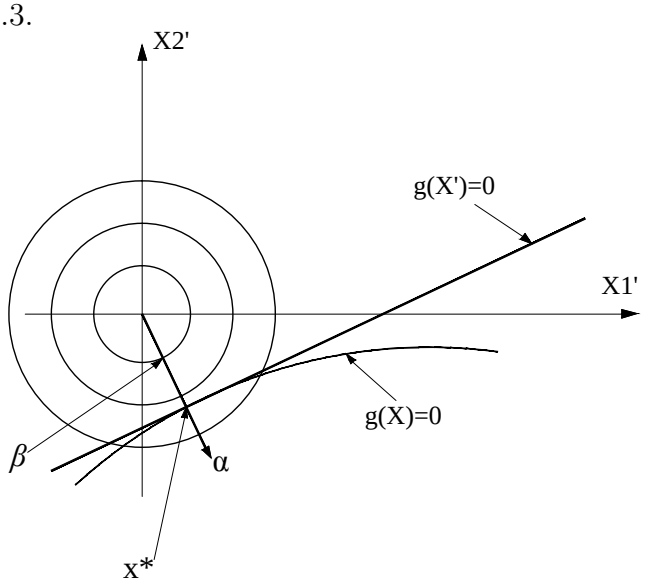


Figure 3.3: *The linearisation of the non-linear failure surface in standard normal space proposed be Hasofer and Lind (1974) from Faber (2005)*

.

The vector α is the direction cosines vector to the failure surface in the design point x'^*.

FORM method is traced historically to second-moment methods which are the First Order Second Moment (FOSM) and Advanced First Order Second Moment (AFOSM) methods.

3.3.1 First Order Second Moment (FOSM) method or MVFOSM

The FOSM method is also referred to MVFOSM (mean value first order second moment) method. The name of this method is derived from its dependence on the first-order Taylor series approximation of the limit state function. In addition to that, this method uses only second moment statistics (mean and variance) of the random variables.

In this method, if the performance is written as:

$$Z = g(X_i) = g(X_1, X_2, ..., X_n) \tag{3.11}$$

the Taylor series of the limit state function is given by:

$$Z = g(\mu_X) + \sum \frac{\partial g}{\partial X_i}(X_i - \mu_{X_i}) + \frac{1}{2}\sum\sum \frac{\partial^2 g}{\partial X_i \cdot \partial X_j}(X_i - \mu_{X_i})(X_j - \mu_{X_j}) + ... \tag{3.12}$$

where the derivatives are evaluated at the mean of the random variables μ_{X_i}. Truncating the series at the linear terms, results in:

$$\mu_Z = g(\mu_{X_1}, \mu_{X_2}, ..., \mu_{X_n}) \quad and \quad \sigma_Z^2 = \sum (\frac{\partial g}{\partial X_i})^2 var(X_i) \tag{3.13}$$

The reliability index is then calculated depending on the ratio of the mean value of Z to its standard deviation as given in Equation 3.9. Again the probability of failure is obtained depending on reliability index from $P_f = \Phi(-\beta)$.

Although this approach is easy to use and it does not require knowledge of the random variables distribution, it has some disadvantages:

- The reliability index is calculated assuming a limit state function is linear, and the method introduces an error for non-linear performance criteria.
- The results are inaccurate if the distributions of random variables are not normal.

Therefore, to tackle these problems of FOSM method, Hasofer and Lind (1974) suggest an advanced method (AFOSM) in which the distribution information of the random variables are used. Moreover, this method is used for the non-linear limit state function.

3.3.2 Advanced First Order Second Moment (AFOSM) for normal variables (Hasofer-Lind method)

The AFOSM method is considered to be the best method for reliability analysis because it gives the most accurate approximation of risk (Li et al., 2007). Ganji and Jowkarshorijeh (2012) state that because the AFOSM solution does not vary with the form of limit state function expression, it can be considered as an invariant reliability analysis method as compared with FOSM method. Furthermore, the AFOSM method can be applied when the random variables are distributed non-normally. AFOSM method has been previously used to study the reliability of reinforced concrete structures subjected to deterioration (Capra et al., 2003; Val and Melchers, 1997).

For random variables with normal distribution, the procedure of the Hasofer-Lind method (AFOSM) for the linear and nonlinear limit state limit state function has been described below. The Hasofer-Lind method (AFOSM) depends on transformation the random variables to the standard Gaussian variables with zero mean and unit standard deviation. For linear limit state function, Figure 3.4 demonstrates the AFOSM method by considering the two variables R and S. In this method, the limit state function can be written as:

$$Z = R - S = 0 \tag{3.14}$$

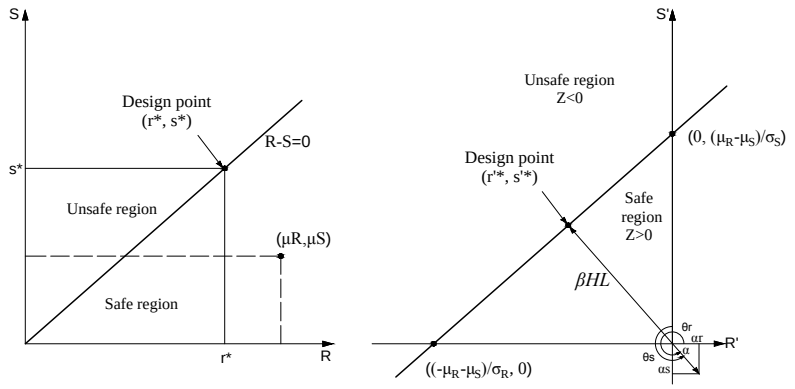
The reduced variables are obtained from

$$R^{'} = \frac{R - \mu_R}{\sigma_R} \quad and \quad S^{'} = \frac{S - \mu_S}{\sigma_S} \tag{3.15}$$

The reduced limit state function is obtained by substituting Equation 3.15 in Equation 3.14 as

$$g(X_i) = \sigma_R R^{'} - \sigma_S S^{'} + \mu_R - \mu_S = 0 \tag{3.16}$$

Figure 3.4b shows that if the limit state function line is closer to the origin, then the unsafe region will become larger, while if it is farther away from the origin then the unsafe side will be smaller. Hence, the position of the limit state surface in the reduced coordinate system indicates the reliability of the system.



(a) Original coordinates (b) Reduced coordinates

Figure 3.4: *Hasofer-Lind Method for linear limit state function (a) original coordinates (b) reduced coordinates (Mahadevan and Haldar, 2000)*

.

The distance of the limit state function from the origin (reliability index) can be calculated from:

$$\beta_{HL} = \frac{\mu_R - \mu_S}{\sqrt{\sigma_R^2 + \sigma_S^2}} \tag{3.17}$$

This equation is the same as the Cornell reliability index (β_c) in FOSM method for random variables with normal distribution. Although the reliability index in Hasofer-Lind method is obtained in different way from that obtained in the FOSM method, both methods will give an identical reliability index for normal variables and linear limit state function.

In most cases, for many random variables $X = (X_1, X_2, ..., X_n)$ and reduced random variables $X' = (X_1', X_2', ..., X_n')$, the limit state function $g(X_i') = 0$ is a non-linear function of the reduced variables coordinates as shown in Figure 3.5. From this figure, the Hasofer-Lind reliability index β_{HL} represents the minimum distance from the origin to the limit state function while x'^* represents the design point or the point of minimum distance from the origin to the limit state. The reliability index is an invariant value because regardless of the form in which the limit state function is written, its geometric shape and distance from origin remain constant.

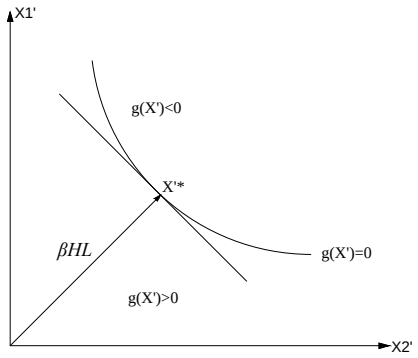


Figure 3.5: *Hasofer-Lind Method reliability index for non-linear limit state function (Mahadevan and Haldar, 2000)*

.

For non- linear limit state functions, the optimization problem is to calculate the reliability index β_{HL}. Rackwitz (1976) cited in Mahadevan and Haldar (2000) formulates an algorithm to compute the reliability index as follows:

1. Define the appropriate limit state function.

2. Assume the initial design point x_i^*. Typically, the initial design point is assumed to be the mean of the random variables.

3. Calculate the design point in the reduced coordinates from $x_i'^* = \dfrac{x_i^* - \mu_{X_i}}{\sigma_{X_i}}$.

4. Evaluate $(\dfrac{\partial g}{\partial X_i'})^*$ from the reduced limit state function, and then calculate

α_i at $x_i'^*$ from

$$\alpha_i = \frac{\left(\frac{\partial g}{\partial X_i'}\right)^*}{\sqrt{\sum \left(\frac{\partial g}{\partial X_i'}\right)^{2*}}} \tag{3.18}$$

where $\left(\frac{\partial g}{\partial X_i'}\right)^*$ is the partial derivative evaluated at the design point. α_i (the direction of the design point) is the cosine along the coordinates axis X_i'.

5. Obtain the new design point in the reduced coordinates in terms of β_{HL}

$$x_i'^* = -\alpha_i \beta_{HL} \tag{3.19}$$

6. Substitute the new $x_i'^*$ in the limit state equation $g(X_i'^*) = 0$ and solve for β_{HL}.

7. Using the β_{HL} value obtained in step 6 and re-evaluate $x_i'^* = -\alpha_i \beta_{HL}$.

8. Repeat step 4 through 7 until β_{HL} converges.

This algorithm is shown geometrically in Figure 3.6. The algorithm constructs a linear approximation to the limit state at every search point and finds the distance from the origin to the limit state.

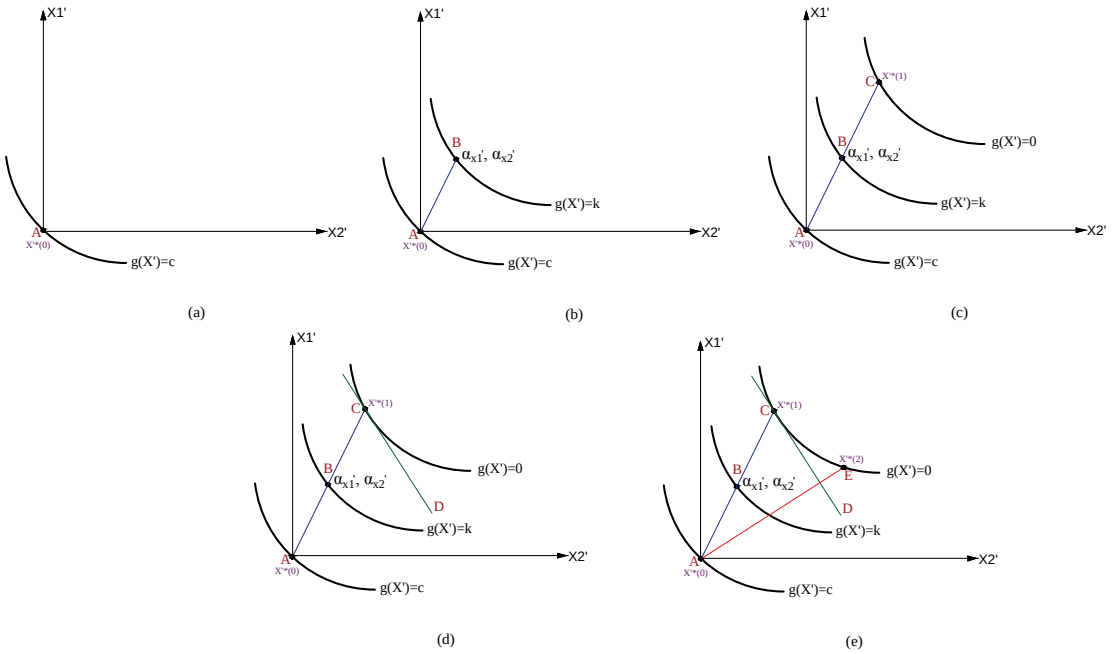


Figure 3.6: *Algorithm for finding β_{HL} (Mahadevan and Haldar, 2000)*

.

3.3.3 Advanced First Order Second Moment (AFOSM) for non-normal variables

The previous method of Hasofer-Lind reliability index is exactly related to the failure probability $P_f = \Phi(-\beta)$ if all the variables are normally distributed. However, the Hasofer-Lind method gives an incorrect results if the distribution of the random variables are non-normal. Therefore Rackwitz and Fiessler (1978) corrected this method and included information on the distribution of random variables in cases of both linear and non-linear limit state functions. The AFOSM method for non-normal variables includes the estimation of the equivalent normal mean and standard deviation at the design point as will be clarified in the next section.

3.3.3.1 Equivalent normal variables

Most of random variables in engineering problems are not distributed normally. In order to consider the problem of non-normal distribution of random variables in the context of limit state equation, it is necessary to transform the non-normal

variables into equivalent normal variables. The transformation is used to obtain a set of statistically independent standard normal variables for which the joint CDF of all random variables are available. The Rackowitz-Fiessler method is used for this purpose. Rackwitz and Fiessler (1978) estimate the parameters of the equivalent normal distribution $\mu_{X_i}^N$ and $\sigma_{X_i}^N$ by using two appropriate conditions. The cumulative distribution function (CDF) and the probability density function (PDF) for the actual variable and the equivalent normal variables should be equated at the design point $(x_1^*, x_2^*, ..., x_n^*)$ on the failure surface. The approximation is introduced by:

$$F_{x_i}(x_i^*) = \Phi\Big(\frac{x_i^* - \mu_{X_i}^N}{\sigma_{X_i}^N}\Big) \tag{3.20}$$

where $F_{x_i}(x_i^*)$ is the cumulative distribution function (CDF) of the original non-normal variables, $\mu_{X_i}^N$ and $\sigma_{X_i}^N$ are the mean and standard deviation of the equivalent normal variables at the design point. From Equation 3.20, the mean of the equivalent normal variable is found as:

$$\mu_{X_i}^N = x_i^* - \Phi^{-1}[F_{x_i}(x_i^*)]\sigma_{X_i}^N \tag{3.21}$$

Equating the PDF_s of the original variables and the equivalent variables at the design point is:

$$f_{x_i}(x_i^*) = \frac{1}{\sigma_{X_i}^N}\phi\Big(\frac{x_i^* - \mu_{X_i}^N}{\sigma_{X_i}^N}\Big) \tag{3.22}$$

where $f_{x_i}(x_i^*)$ is the pdf of the original non-normal variables and ϕ is the PDF_s of the equivalent standard normal variables. From Equation 3.20 it can be found:

$$\Big(\frac{x_i^* - \mu_{X_i}^N}{\sigma_{X_i}^N}\Big) = \Phi^{-1}[F_{x_i}(x_i^*)] \tag{3.23}$$

and by substituting this Equation in Equation 3.22

$$f_{x_i}(x_i^*) = \frac{1}{\sigma_{X_i}^N}\phi\Big[\Phi^{-1}[F_{x_i}(x_i^*)]\Big] \tag{3.24}$$

Then, the standard deviation of the equivalent normal variable is found as:

$$\sigma_{X_i}^N = \frac{\phi\Big[\Phi^{-1}[F_{x_i}(x_i^*)]\Big]}{f_{x_i}(x_i^*)} \tag{3.25}$$

To calculate the design point and the reliability index in this case (non-normal variables), two algorithms are commonly used. The first method, referred to as FORM method 1, requires a solution of the limit state function during the iteration (Rackwitz and Fiessler, 1978). This method is easy to apply and estimate, as a small computer programme can be written to complete the calculations. However, this method is not efficient for complex cases with non-linear limit state functions, such as found in many practical problems. Therefore, the second method referred to as FORM method 2 (Rackwitz and Fiessler, 1978) uses a Newton-Raphson type recursive formula to find the design point for complicated performance functions.

3.3.3.2 FORM method 2

In the case of a complex non-linear limit state function, a Newton-Raphson type recursive algorithm, FORM method 2, is used to find the design point. In this method, instead of solving the limit state function explicitly for β, the derivatives are used to find the next iteration point. The method can be decomposed in the following steps:

1. Define the appropriate limit state function.

2. Assume the initial design point x_i^* where $i = (1, 2, .., n)$; the initial design point is usually equal to the mean of the random variables, and then compute the corresponding value of the limit state function $g(X_i)$.

3. Compute the mean and standard deviation at the design point of the equivalent normal distribution for the non-normal random variables. The coor-

dinates of the design point in the equivalent standard normal space are:

$$x_i^{'*} = \frac{x_i^* - \mu_{X_i}^N}{\sigma_{X_i}^N} \tag{3.26}$$

4. Compute the partial derivatives $\frac{\partial g}{\partial X_i}$ evaluated at the design point x_i^*.

5. Compute the partial derivatives $\frac{\partial g}{\partial X_i'}$ in the equivalent standard normal space

$$\frac{\partial g}{\partial X_i'} = \frac{\partial g}{\partial X_i} \cdot \frac{\partial X_i}{\partial X_i'} = \frac{\partial g}{\partial X_i} \cdot \sigma_{X_i}^N \tag{3.27}$$

6. Compute the directions cosines α_i at the design point as:

$$\alpha_i = \frac{\left(\frac{\partial g}{\partial X_i}\right)^* \cdot \sigma_{X_i}^N}{\sqrt{\sum \left(\frac{\partial g}{\partial X_i}\sigma_{X_i}^N\right)^{2*}}} \tag{3.28}$$

Note that Equation 3.18 and Equation 3.28 are identical. In Equation 3.18, α_i is evaluated in the reduced coordinates when the standard deviation of the reduced variables are unity. However, in Equation 3.28, if the random variables are normal, then their standard deviation can be used directly, otherwise, the equivalent standard deviations at the design point need to be used.

7. Obtain the new design point $x_i^{'*}$ in terms of β

$$x_i^{'*} = -\alpha_i \times \beta \tag{3.29}$$

8. Apply the new design point $x_i^{'*}$ in the recursive formula to calculate β

$$g(X_i) = g_{x_i}^* + \frac{\partial g}{\partial x_i^{'*}}(x_{i+1}^{'*} - x_i^{'*}) \tag{3.30}$$

9. Calculate the new design point $x_i^{'*} = -\alpha_i\beta$.

10. Compute the new values for the design point in the original space (x_i^*)

$$x_i^* = \mu_{X_i}^N + \sigma_{X_i}^N x_i'^* \tag{3.31}$$

11. Repeat step 3 through step 10 until β converges.

3.4 Monte-Carlo simulation

In the previous sections, different methods that are used to estimate the probability of failure are explained. Most of these methods are applicable only when the limit state function is defined explicitly. However, for both implicit and explicit limit state function, the simulation technique is a possible method to calculate the probability of failure (Mahadevan and Haldar, 2000). The implicit limit state function is defined for the very complicated problems as long as an algorithm is available to compute the structural response (e.g. non-linear finite element analysis). Modern computer software makes the process of simulation very efficient. In the simplest form of the basic simulation, each random variable in a problem is generated many times to estimate its distribution depending on its statistical characteristics.

In this approach, the most important task is to generate random samples of the random variables in order to simulate a large number of experiments. The generation of random numbers according to a specific distribution is the heart of Monte-Carlo simulation.

In structural reliability, a large number of samples are generated (simulated). For each sample outcome, the value of the limit state function is computed. The probability of failure after N simulations is estimated through

$$P_f = \frac{n_f}{N} \tag{3.32}$$

where n_f is the number of simulations in which the failure is occurred ($g(X_i) < 0$) and N is the total number of simulations. By using a large number of simulations, the estimation of the probability of failure becomes close to the exact solution. This means that the estimation will converge to the correct answer when N is near ∞. Therefore, this method is less suitable for complex structures because large simulations are required to estimate the probability of failure and that requires many time consuming numerical calculations. In chapter 5, MCS based FORM analysis is used to reduce the time required for the probability of failure estimation.

The simulation of the N outcomes of the joint density function in Equation 3.32 is in principle simple and may be seen as consisting of two steps as shown in Figure 3.7. In the first step, a uniformly distributed random number, z_{ji}, is generated between 0 and 1 for each component of $\hat{x}_j$ using pseudo random number generator (PRNG). In the second step the outcomes of the pseudo random numbers z_{ji} are transformed to outcomes of $\hat{x}_{ji}$ by:

$$x_{ji} = F_{X_i}^{-1}(z_{ji}) \tag{3.33}$$

where $F_{X_i}^{-1}()$ is the CDF for the random variable X_i.

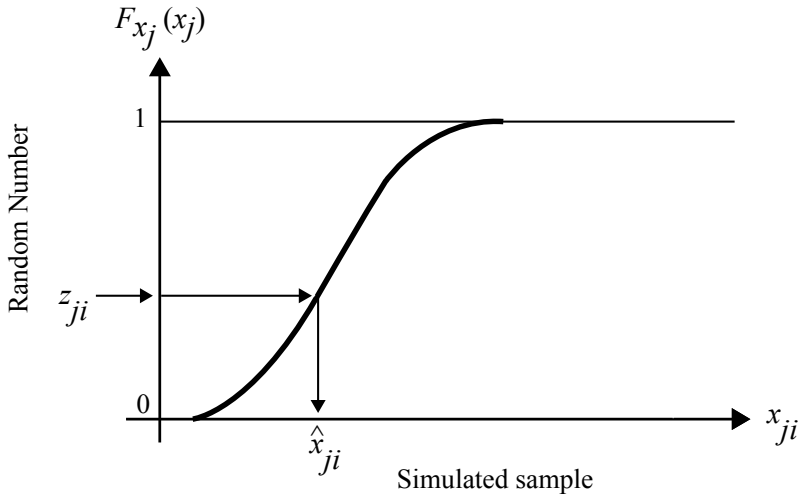


Figure 3.7: *Principle for simulation of a random variable (Faber, 2005)*

3.5 Implementation of FORM and MCS methods

This section will present the application of the theory covered in the previous sections. An example problem of a reinforced concrete beam deteriorating in time due to localized corrosion, is considered. The beam is modelled analytically using a MATLAB code. The reliability index for this beam is estimated with time, considering bending failure only. FORM method 2 is used in this study due to its efficiency for the complex non-linear limit state functions and the non-normal variables. The analysis has been repeated using MCS and the results have been compared with FORM. The beam details, failure mode and the random variables considered will be presented in the following subsection.

3.5.1 Beam geometry and material data

A corroded simply supported reinforced concrete beam with uniformly distributed load is considered in this study to estimate the reliability of the beam. The service life of the beam considered in this study is taken as 70 years.

The beam has a span length of 9.5 m. The nominal values of concrete compressive strength f_{ck} and steel yield stress f_{yk} are 30 and 500 MPa respectively. The nominal values of the permanent load g_k and live load q_k are equal to 4 and 6 kN/m respectively. The beam is designed in bending using Eurocode 2 reinforced concrete design (Mosley et al., 2012). The beam depth is $d = 0.4$ m and the width is $b = 0.25$ m. Four reinforcement bars are embedded in the beam with diameter 16 mm as shown in Figure 3.8.

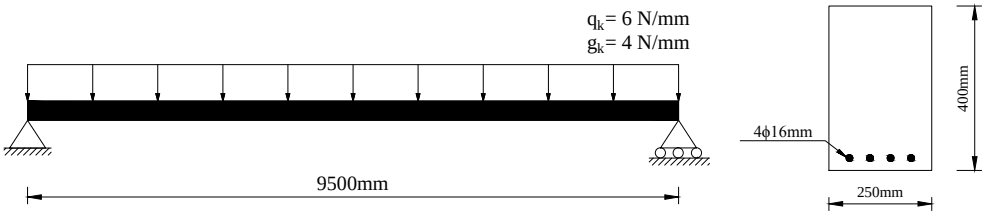


Figure 3.8: *Simply supported RC beam section*

3.5.2 Failure mode and random variables

In this example, the limit state occurs when $M_R \leq M_S$, then the limit state function is written as:

$$g(X_i) = M_R - M_S = 0 \tag{3.34}$$

where M_R is the resistance moment and it is equal to (according to Eurocode 2 (Mosley et al., 2012)):

$$M_R = A_s.f_y.\Big(d - \frac{A_s.f_y}{0.85bf_c \times 2}\Big) \tag{3.35}$$

and M_S is the action moment at the mid span of the beam as follow:

$$M_S = wl^2/8 \tag{3.36}$$

where $w = g_k + q_k$. Then the limit state function is written as:

$$g(X_i) = A_s.f_y.\Big(d - \frac{A_s.f_y}{0.85bf_c \times 2}\Big) - \frac{l^2}{8}(g_k + q_k) = 0 \tag{3.37}$$

In reliability analysis, the compressive strength of the concrete and the yield stress of the reinforcement are treated as lognormal and normal random variables, respectively and their mean and coefficient of variation are adopted from Wiśniewski (2007) and (JCSS, 2001), respectively as described in Chapter 2. The dead load is treated as a normal random variable and its mean value represents

the nominal permanent load (self weight) of the beam and the coefficient of variation is 10% according to JCSS (2001). The live load is treated as a Gumbel (EV-type I) random variable with coefficient of variation of 0.4 (Nowak, 1993). According to the corrosion model described in Chapter 2, the loss of cross sectional area of the reinforcement bars due to pitting corrosion depends on the corrosion rate (i_{corr}), time to corrosion initiation (T_i) and the pitting factor (R). In this study, the time to corrosion initiation is assumed to be zero (it is assumed that the corrosion starts immediatly after construction) and the pitting factor is assumed, for simplicity, to be a deterministic value ($R = 4$). The corrosion rate is assumed similar to the assumption of Val and Melchers (1997) to have a normal distribution with mean value = $3\mu A/cm^2$ and coefficient of variation 0.3, which represents an aggressive environmental condition according to Middleton and Hogg (1998). The probabilistic models of the load and resistance model uncertainties θ_L and θ_R are adopted from JCSS model code (JCSS, 2001), in which they have a lognormal distribution with mean value = 1 and coefficient of variation = 0.1 and 0.15 respectively. The statistical parameters of these random variables are summarized in Table 3.1. The other properties of the simply supported beam such as the geometric dimensions (L, b and d) are considered as deterministic values.

Table 3.1: *Statistical parameters of random variables for ultimate limit state analysis*

R.V	Units	Nominal value	μ	σ	COV	distribution
Yield stress (f_y)	MPa	500	560	30	0.05	Normal
Concrete compressive strength (f_c)	MPa	30	30	5.8	0.12	Lognormal
Permanent load (g)	N/mm	4	4	0.4	0.1	Normal
Live load (q)	N/mm	6	3.37	1.01	0.4	Gumbel
Corrosion rate (i_{corr})	$\mu A/cm^2$	-	3	0.9	0.3	Normal
Load model uncertainty (θ_L)	-	-	1	0.1	0.1	Lognormal
Resistance model uncertainty (θ_R)	-	-	1	0.15	0.15	Lognormal

3.6 Reliability analysis and results

The reliability analysis of the simply supported RC beam is based on FORM method 2 according to the flexural limit state function (Equation 3.37). A MATLAB code has been written to apply reliability analysis using FORM method 2. The random variables have been identified first with their statistical parameters, and the initial design point assumed to be equal to the mean values of the random variables ($x_i^* = \mu$). After that, the limit state function is computed at the design point g_{xi}^*. Next, the equivalent mean $\mu_{X_i}^N$ and standard deviation $\sigma_{X_i}^N$ in the normal space are calculated according to Equations 3.21 and 3.25 respectively. This is followed by computing the partial derivative of the limit state function at the design point ($\frac{\partial g}{\partial X_i^*}$) and in the equivalent standard normal space ($\frac{\partial g}{\partial X_i'^*}$). After this step, the direction cosine for the second design point can be calculated according to Equation 3.28. Next, the new design point in terms of β has been found according to Equation 3.29. Subsequently, this new design point need to be substituted in the limit state function to find β. Ten iterations have been used until β has been converged.

Two cases for corrosion rate and area of steel variability are considered. In the first case (case 1), corrosion rate and area of steel are considered to be deterministic values ($i_{corr} = 3\mu A/cm^2$ and $A_s = 201.06mm^2$). For the second case (case 2), corrosion rate is considered as a random variable for which the variability is independent for the four bars. The area of steel in this case will be an implicit random variable depending on the variability of i_{corr}. The loss of cross sectional area of the reinforcement steel due to pitting corrosion with the time is calculated according to the geometric model proposed by Val and Melchers (1997) (see Chapter 2 from Equation 2.45 to 2.48).

The reduction in steel area are similar for the two cases, since the corrosion rate is the same. The results show that the total area of steel reduced with the time, and after seventy years the total area is decreased by more than half as shown

in Figure 3.9. The influence of the uncertainty of corrosion rate on the beam reliability can be illustrated by the use of the sensitivity factor α. The zero value of sensitivity factor present an irrelevant impact on the analysis, whereas cosines close to -1 or 1 have respectively a significant negative or positive impact. The uncertainties with negative impact can significantly decrease the safety, while the uncertainties with positive impact increases the safety of the structures. Hence, the material properties are usually have a positive sign since they can increase the safety. On the contrary, the loads have a negative sign since they have an adverse effect on the structure.

Figure 3.10 shows the importance of the uncertainty of corrosion rate for the two cases with the time.

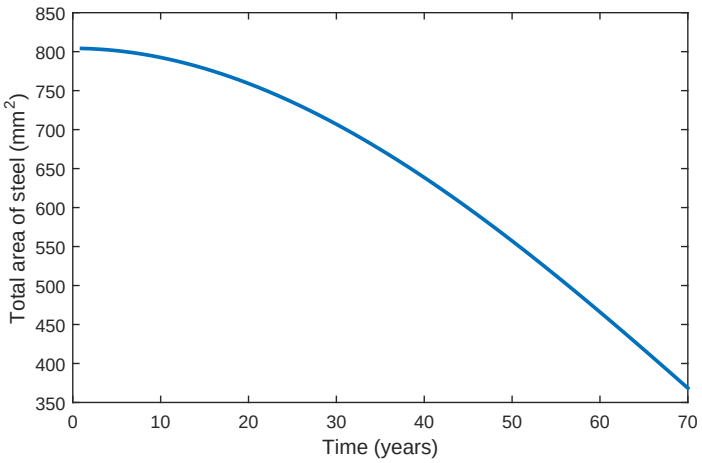


Figure 3.9: *Total area of steel reduced with the time due to localized corrosion for the two cases*

For case 2, the weight of i_{corr} is small at the first few years and the importance increases with the time as corrosion increases. Considering the uncertainty of i_{corr} is more significant to reduce the reliability index of the beam as shown in Figure 3.11. However, reliability index for the first and last few years for the two cases are similar and that is because at the first few years the structure is quite new and the area of steel is fixed due to $\alpha_{i_{corr}} = 0$. Therefore, the effect of corrosion rate is very similar in the two cases. For the last few years, the area of

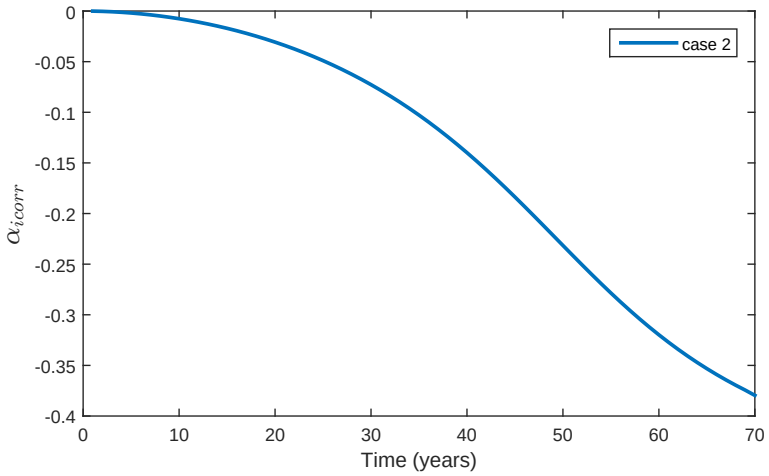


Figure 3.10: *The direction cosine values of i_{corr} with the time for case 2*

steel is very small (less than half its value (Figure 3.9), therefore, the corrosion rate has very little influence.

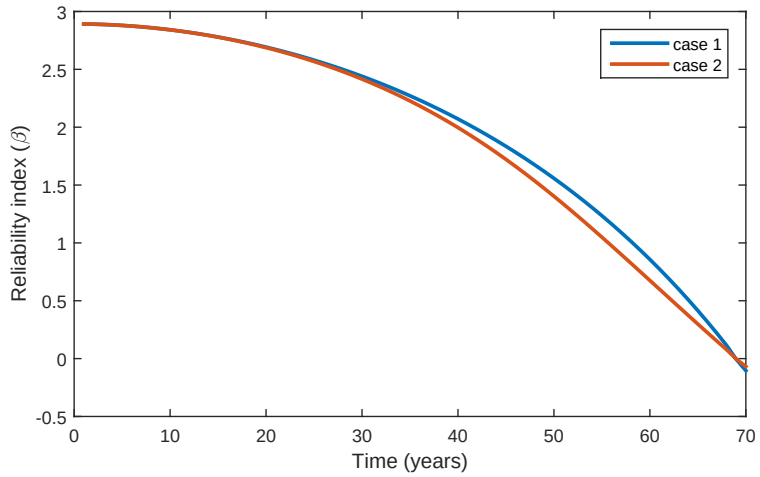


Figure 3.11: *Reliability indices differences between case 1 and case 2, β is lower in case 2 due to the conidration of the uncertainty of i_{corr}*

Figure 3.12 shows that increasing the standard deviation of i_{corr} (1.8 and 2.7) leads to a decrease in the reliability index. This implies that increasing the standard deviation means increasing the uncertainty as shown in Figure 3.13. Again, the reliability index of the last few years is not influenced by the raising of i_{corr} weight due to the large reduction of the area of steel.

The direction cosines at design point of individual random variables as a function

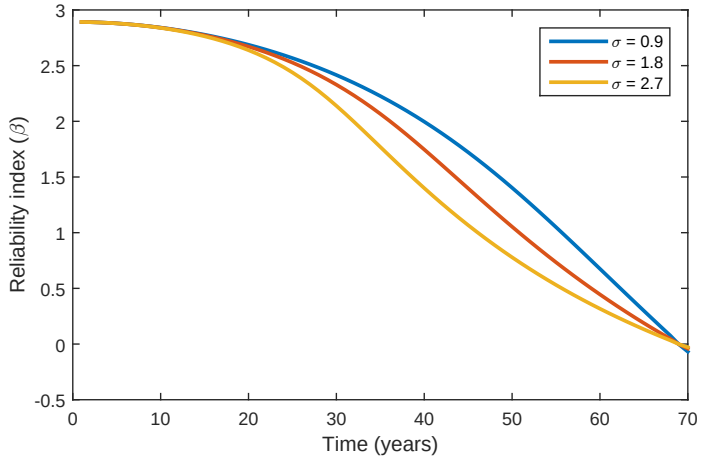


Figure 3.12: *Reliability index reduction due to increasing the standard deviation of* i_{corr}

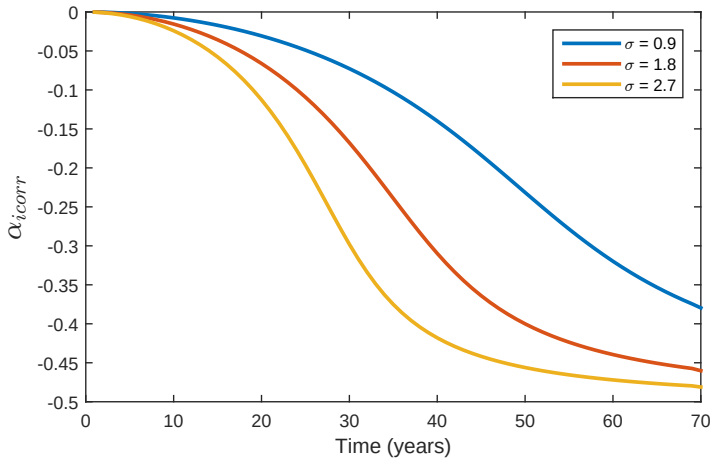


Figure 3.13: *Influence of different values of* i_{corr} *standard deviation on the value of* $\alpha_{i_{corr}}$

of time are presented in Figure 3.14. The figure shows that the live load q_k has the highest weight in the analysis reaching a value of -0.7 and exhibiting a reduction of its importance as the deterioration increases. The resistance and load models uncertainties, θ_R and θ_E, have a large influence on reliability index as shown in Figure 3.15 due to their high weight in the analysis, -0.37 and 0.55 respectively. The figure shows that ignoring the uncertainties of load and resistance increases the reliability index of the beam. This can be explained by the reduction in load

and increase in material properties (f_c and f_y) due to the ignoring of θ_L and θ_R respectively. However, the two curves in Figure 3.15 converge to zero at time 70 due to the significant reduction of steel area which lead to a high reduction in the weights of θ_L and θ_R. The influence of the uncertainties associated with other parameters (f_c, f_y, g_k) are insignificant since their sensitivity factors are less than 0.2 (Val and Melchers, 1997).

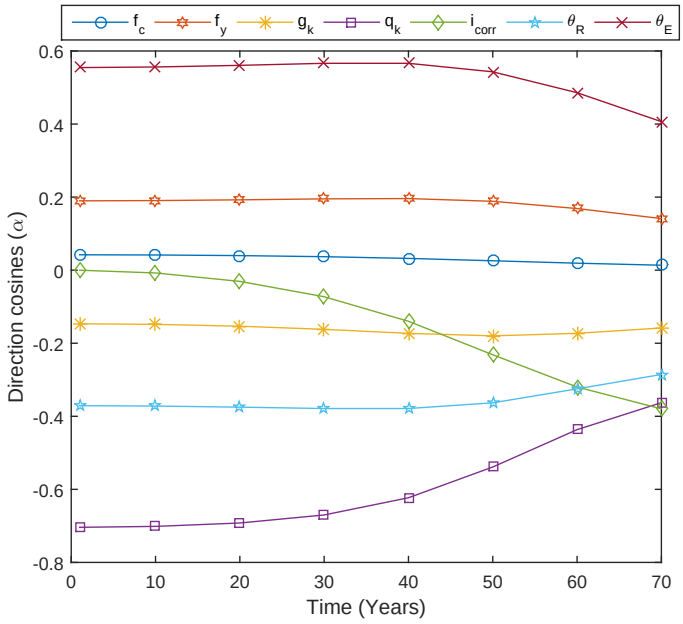


Figure 3.14: *Sensitivity factors α at design points that gives the importance of each random variable*

Increasing the number of reinforcement bars (amount of steel) also affects the reliability of the beam (see Figure 3.16).

Case 2 analysis is repeated for a fixed ended reinforced concrete beam as shown in Figure 3.17. In this condition, the reliability analysis is performed in two stages due to the support and middle moment. The two limit state functions in this situation are written as:

$$g(X_i) = A_s.f_y.\left(d - \frac{A_s.f_y}{0.85bf_c \times 2}\right) - \frac{l^2}{12}(g+q) = 0 \tag{3.38}$$

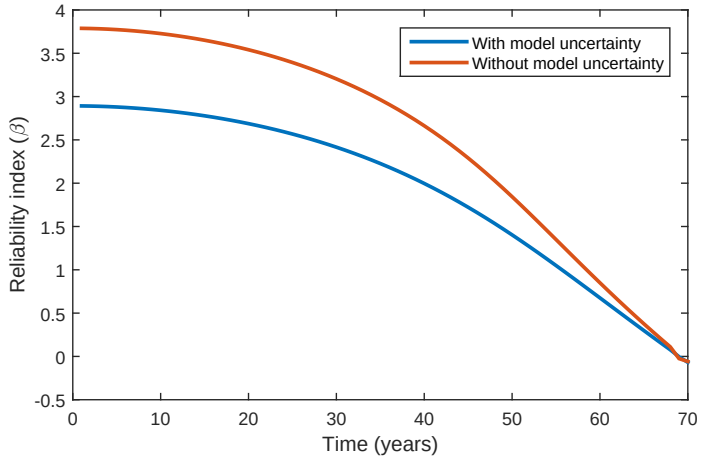


Figure 3.15: *The effect of using model uncertainties (θ_E and θ_R) on the values of reliability index along the years*

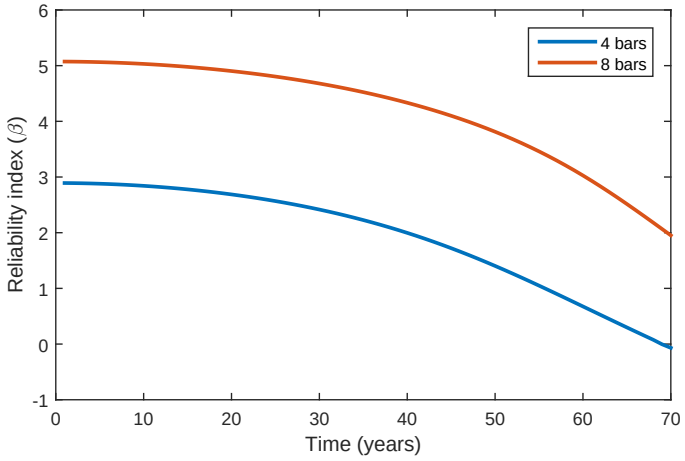


Figure 3.16: *Reliability index comparison between using 4 and 8 reinforcement bars. Increasing the number of bars will lead to increase the capacity of the beam and subsequently increase the reliability index of the beam*

and

$$g(X_i) = A_s.f_y.\left(d - \frac{A_s.f_y}{0.85bf_c \times 2}\right) - \frac{l^2}{24}(g+q) = 0 \tag{3.39}$$

The results show that the probability of failure is higher at the end supports than at the middle of the beam due to the maximum moment at the fixed support (Figure 3.18). Furthermore, the reliability index in this case is higher as compared

with the case of simply supported beam due to the lower bending moment.

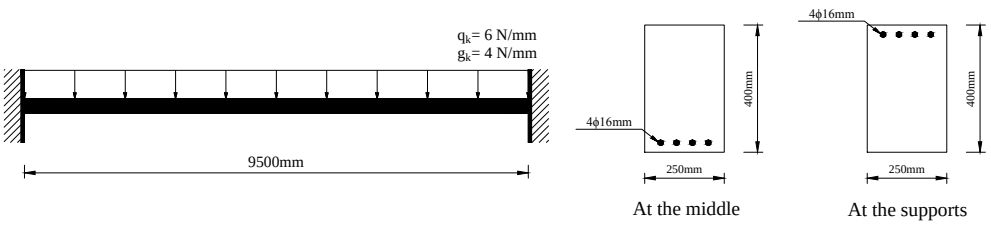


Figure 3.17: *Fixed ended beam*

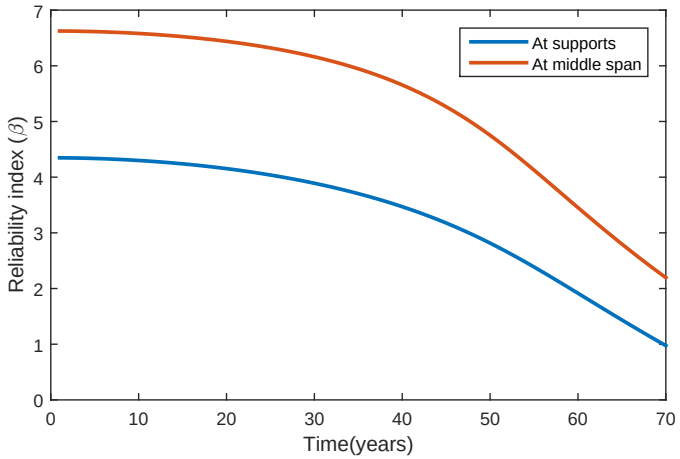


Figure 3.18: *Variation in reliability index with age for the support and middle moments*

Monte Carlo simulation is also performed in this study for case 1 in order to compare the results with FORM method. A large number of samples (10^6) have been generated for all random variables considered in case 1 depending on their statistical parameters (see Table 3.1). The probability of failure is calculated according to Equation 3.32. The results show a very good agreement between the two methods as shown in Figure 3.19. Finally, the two methods show their capability and simplicity to estimate the reliability of structures when the limit state function is defined explicitly.

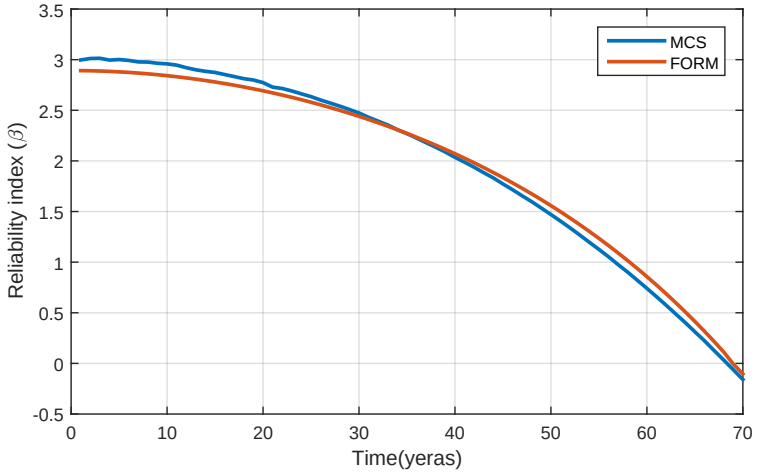


Figure 3.19: *The probability of failure of the simply supported beam shows a good agreement between the FORM and MCS methods*

3.7 Summary

In this chapter, it can be seen that FORM method is traced historically to FOSM and AFOSM methods. FOSM method is easy to apply, however, it is adequate for linear limit state function and it introduces an error for non-linear limit state functions. In addition, the results of FOSM method is inaccurate if the distribution of the random variables are non-normal. AFOSM method is used for the normal and non-normal variables as well as for the non-linear limit state functions. For the non-normal variable case, there are two algorithms are commonly used, FORM method 1 and FORM method 2. FORM method 1 is easy to apply and estimate and a small computer programmes can be written to complete the calculations. However, this method is not efficient for complex non-linear limit state functions such as found in many practical problems. FORM method 2 is used for the more complex performance function by using Newton-type recursive formula. However, FORM method 2 can not be used for any type of realistic applications, because the derivative of the limit state function can be impossible to compute accurately, in particular for implicit limit state functions.

Monte-Carlo simulation is likely to be used in practical problems, however, a large number of simulations are required to estimate the probability of failure

and that could be take a very long time to complete. Furthermore, MCS can be used with implicit and explicit limit state function. The last part of this chapter focuses on the application of the two methods on a simply supported reinforced concrete beam example considering the two cases. In the first case, the corrosion rate and the area of steel are treated as deterministic values while in the second case, the corrosion rate and the area of steel are considered to be random variables. From the two cases, it have been found that the area of steel and the reliability index are reduced sharply with the time due to the aggressive environment. The second case shows that including the variability of i_{corr} and A_s affected the reliability of the beam. Beam reliability analysis is repeated for case 1 using MCS method and the results show a good agreement with FORM. The next two chapters will focus on applying reliability analysis for implicit limit state function using a combination between FORM and MCS.

Chapter 4

Finite Element Modelling of Reinforced Concrete Beams

This chapter presents work done to model four RC beams tested experimentally by Barros and Fortes (2005). The concrete damage plasticity model (CDP) is used and hence, a sensitivity analysis study on the model parameters in particular the viscosity parameter, is presented. The finite element results compare well with the published experimental data, demonstrating the effectiveness of the CDP model and its capability for use in the subsequent chapters. The chapter is organized as follows:

Section 4.1 provides a brief justification for using finite element modelling in this thesis. Section 4.2 reviews the constitutive behaviour of concrete in compression and tension. Section 4.3 reviews the methods that are used to model concrete behaviour in ABAQUS. Section 4.4 describes the CDP model including the stress strain curves for compression and tension. Section 4.5 presents details of the beams and the the 3D nonlinear finite element model and discusses the results. Finally, section 4.6 summarises the findings of the chapter.

4.1 Introduction

Reinforced concrete structures are exposed to aggressive environmental conditions which lead to corrosion of the embedded steel reinforcement. As a result, the safety and durability of concrete structures will be reduced (Ožbolt et al., 2012). Billions of dollars are needed to repair the damaged structures (Elfergani et al., 2013). Prediction of structural safety can lead to a significant reductions in maintenance costs by maximising the impact of investments.

As the aim of this chapter is to provide an accurate prediction of the four beams ultimate capacity, finite element analysis is used in this study to build an appropriate model and to predict the capacity of the beams in order to capture the failure mechanism. Finite element method is a tool that has become widely used for analysis of structures since its much more effective than other methods (e.g. theoretical modelling) in dealing with the complexities of material nonlinearity and the 3D structural behaviour.

Reinforced concrete is made up from steel and concrete. Steel is a homogeneous material and its properties can be defined easily. However, concrete has a different non-linear behaviour in tension and compression that makes it more complex to define its properties (Kwak and Filippou, 1990). The non-linear response of reinforced concrete structures is caused by several major effects such as: concrete cracking and crushing due to the tensile and compressive stresses, yielding of reinforcement, complex behaviour of bond slip between steel and concrete, shrinkage and temperature effects. Moreover, due to the complicated material properties of concrete, the finite element method cannot represent reinforced concrete easily unlike an elastic material (Kwak and Filippou, 1990; Xiaogang, 1999). However, considerable efforts have been made to understand the behaviour of concrete structures (Buyukozturk and Shareef, 1985).

In this chapter ABAQUS/Standard is used as a tool of finite element analysis due to its availability. The concrete damage plasticity model is used to model the nonlinear behaviour of concrete since it has the possibility to represent the

complete inelastic behaviour in tension and compression.

4.2 Constitutive behaviour of plain concrete

Understanding the behaviour of concrete is important to understand the response of RC structures under loading. Tension and compression stresses lead to cracking and crushing respectively. Typically, concrete has a higher resistance in compression than tension; the latter can lead to cracking and separation of the concrete. Concrete exhibits a large number of micro cracks that develop during loading due to the difference in stiffness between aggregate and cement. In addition, micro cracks can also be formed, even before any load is applied, due to shrinkage and thermal expansion of cement. The presence of these micro cracks has a very big effect on the mechanical behaviour including contributing to the non-linearity of concrete (Kwak and Filippou, 1990). To understand these details, it needs to look into the concrete compressive and tensile behaviour as follows:

4.2.1 Compressive behaviour of concrete

According to Eurocode-2 (2004), the stress strain curve for concrete in compression is as shown in Figure 4.1. The complete stress strain curve is defined as:

$$\sigma_c = \left(\frac{k\eta - \eta^2}{1 + (k-2)\eta}\right) f_{cm} \tag{4.1}$$

with:

$$\eta = \frac{\varepsilon_c}{\varepsilon_{c1}} \tag{4.2}$$

$$k = 1.05 E_{cm} \frac{\varepsilon_{c1}}{f_{cm}} \tag{4.3}$$

$$\varepsilon_{c1} = 0.7 (f_{cm})^{0.31} \tag{4.4}$$

$$E_{cm} = 22 (0.1 f_{cm})^{0.3} \tag{4.5}$$

where σ_c is the compressive stress at any point along the elastic region, f_{cm} is the maximum compressive strength (MPa), k is the plasticity number, ε_c is the compressive strain in the concrete at any point along the stress-strain curve, ε_{c1} is the concrete compressive strain at the maximum stress (f_{cm}) and E_{cm} is the elastic modulus (GPa).

Figure 4.1 shows that a linear approximation was assumed up to 40% of the ultimate compressive strength (f_{cm}). Above this point, the stress increases gradually up to the maximum compressive strength. After it reaches the maximum compressive strength (f_{cm}) at ε_{c1}, a softening region causes the curve to descend and eventually crushing failure occurs at an ultimate strain ε_{cu1}=0.0035.

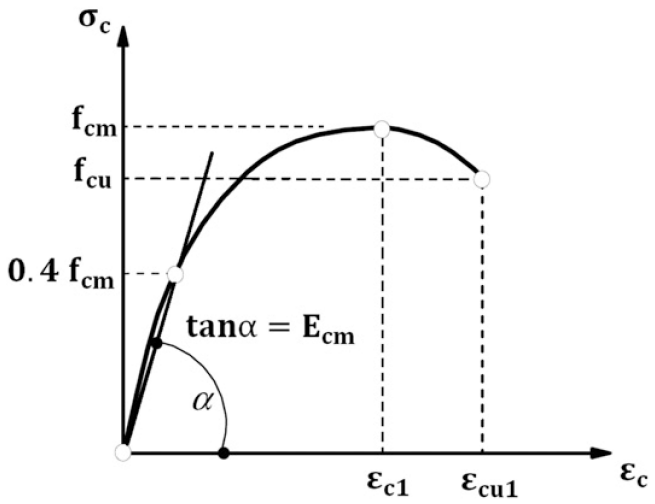


Figure 4.1: *Concrete compressive stress-strain diagram according to Eurocode2 (Eurocode-2, 2004)*

Equations 4.1 to 4.5 can be used to estimate the stress strain values of concrete if the maximum compressive strength is available and there are no uniaxial compression test results.

4.2.2 Tensile behaviour

The tensile strength of concrete (f_t) is about $8-15\%$ of the compressive strength (f_{cm}). The uni-axial stress-strain curve for concrete is approximately linear elastic

up to the maximum tensile strength (f_t), which can be calculated from Equation 4.6. After this point, the concrete cracks and the strain softening starts so that the strength decreases gradually to zero at a total strain ε_{tu} of about ten times ε_{to} (Eurocode-2, 2004).

$$f_t = 0.3(f_{ck})^{2/3} \tag{4.6}$$

$$f_{ck} = f_{cm} - 8(MPa) \tag{4.7}$$

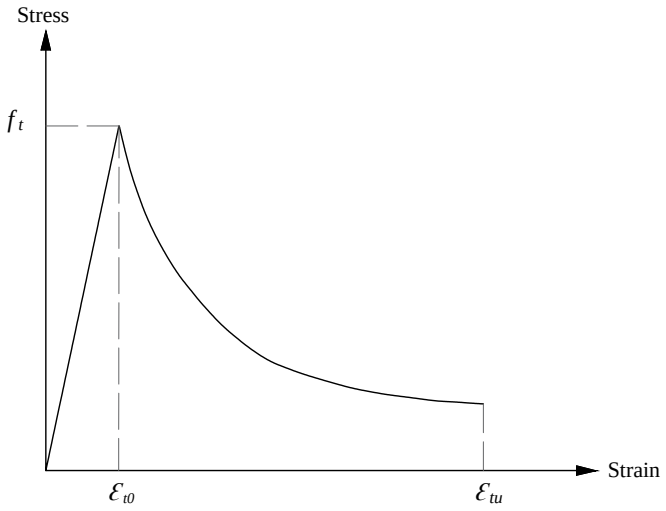


Figure 4.2: *Concrete tension stress-strain diagram (Belarbi et al., 1996)*

For this behaviour, the stress strain values of concrete can be obtained from the available equations in the literature such as the equation that is proposed by Belarbi and Hsu (1994):

$$\sigma_t = \begin{cases} E_{cm}.\varepsilon_t, & for \quad \sigma_t \leq f_t \\ f_t.\left(\dfrac{\varepsilon_{t0}}{\varepsilon_t}\right)^{0.4}, & for \quad \sigma_t > f_t \end{cases} \tag{4.8}$$

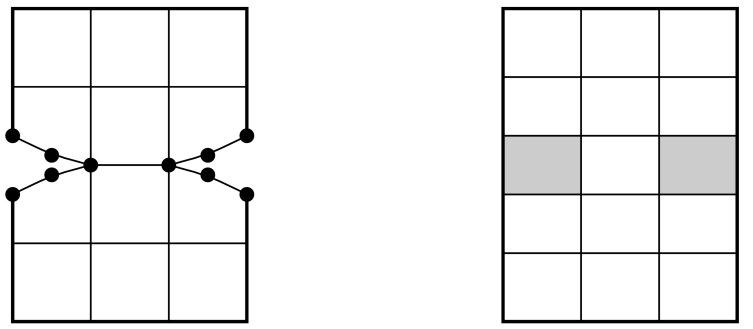
where ε_t is the tensile strain in the concrete at any point along the stress strain curve; ε_{t0} is the tensile strain at the maximum tensile stress (f_t).

It is important that this different behaviour in tension and compression is included within a model of RC structures. Finite element model should include some

approach to consider the behaviour of concrete as it will describe in the next section.

4.3 FE-modelling of concrete nonlinear materials

There are different finite element software packages that can be used to model reinforced concrete structures such as ANSYS (Barbosa et al., 1998), ABAQUS (Kmiecik and Kamiński, 2011) and DIANA (Rots et al., 1985). In this work ABAQUS is adopted because of its availability and capabilities for modelling the nonlinear behaviour of concrete. The elastic behaviour of concrete can be simulated using the elastic model available in ABAQUS by defining the modulus of elasticity (E_{cm}) and Poison's ratio (υ). For the plastic behaviour, some approaches need to be considered in finite element analysis to consider the change in concrete stiffness due to cracking. Two different approaches are available in ABAQUS (ABAQUS, 2013); the discrete crack and the smeared crack as shown in Figure 4.3.



(a) Discrete crack model (b) Smeared crack model

Figure 4.3: *Methods of modelling concrete cracks in FE analysis(Pankaj, 1990)*

In the discrete crack approach, the nodes are separated during crack propagation and each crack is considered separately. The separation of nodes takes place at each element and therefore, it requires a very fine mesh to get a high level

of accuracy. This method is difficult to implement and it requires an extensive computational time.

In the smeared crack model, the cracks of concrete are modelled by adjusting the material properties in the regions of cracking or strain localisation. In this model, the material properties calculations are performed independently at each integration point in the finite element model. The presence of cracks is included in these calculations by the way in which the cracks affect the stress and material stiffness associated with the integration points.

The concrete damage plasticity model (CDP) is a smeared crack model in the sense that it does not take an individual macro cracks. The CDP model uses a smeared crack approach to represent the sudden change in stiffness caused by a crack.

In this study, the CDP model is used, as this model has the possibility to represent the complete inelastic concrete behaviour in tension and compression by including damage parameters. Furthermore, this model can also be used for analysing structures that are subjected to any loading combinations including static, dynamic and cyclic. The CDP model will be described in the following sections:

4.4 Concrete damage plasticity model in ABAQUS

The CDP model has the ability to model any brittle material including concrete. As mentioned in section 4.3, the CDP model assumes that the two main failure mechanisms are tensile cracking and compressive crushing. The required parameters for stress analysis in CDP model are described in the following sections:

4.4.1 Stress-strain curve for uniaxial compression

In uniaxial compression, the stress strain relation is assumed to be linear until the value of initial yield σ_{c0}, and after this point the response of concrete is char-

acterized by strain hardening to the ultimate stress f_{cm}, followed by softening (ABAQUS, 2013). The parameters of stress-strain defining the curve of concrete can be obtained from a uniaxial test or estimated based on concrete class. After the stress-strain curve is obtained, the strain should be transformed to the inelastic strain ε_c^{in} by deducting the elastic part (corresponding to the undamaged material) from the total strain which is obtained from the test or equations.

$$\varepsilon_c^{in} = \varepsilon_c - \varepsilon_c^{el} \tag{4.9}$$

where:

$$\varepsilon_c^{el} = \frac{\sigma_c}{E_{cm}} \tag{4.10}$$

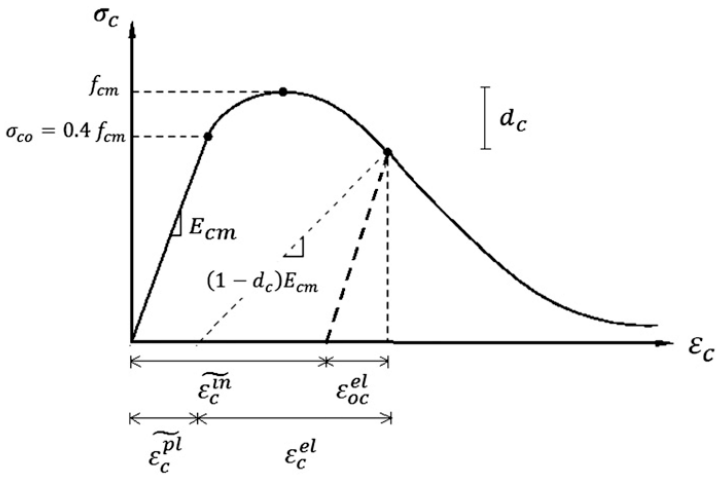


Figure 4.4: *Definition of inelastic strains for the concrete compressive behaviour of the CDP model (ABAQUS, 2013)*

The CDP model also requires scalar damage parameters to represent the degradation of the concrete stiffness with the increase of inelastic deformation. In other words, the compressive damage parameter d_c is used to determine the differences in slope between the unloading line and the initial modulus E_{cm} (see Figure 4.4). The damage parameter values ranges between zero and one to represent the undamaged and fully damaged materials, respectively (ABAQUS, 2013).

The following equations are used to calculate the compression damage parameter

(d_c):

$$d_c = \begin{cases} 0, & for \quad \varepsilon_c < \varepsilon_{c1} \\ 1 - \dfrac{\sigma_c}{f_{cm}}, & for \quad \varepsilon_c \geq \varepsilon_{c1} \end{cases} \tag{4.11}$$

When the unloading data (damage parameter) is available, ABAQUS automatically calculates the concrete stress and strain when unloading from any point on the curve, according to the following equations:

$$\sigma_c = (1 - d_c) E_{cm} (\varepsilon_c - \varepsilon_c^{pl}) \tag{4.12}$$

$$\varepsilon_c^{pl} = \varepsilon_c^{in} - \frac{d_c}{(1 - d_c)} \cdot \frac{\sigma_c}{E_{cm}} \tag{4.13}$$

where E_{cm} is the initial undamaged elastic stiffness; ε_c^{pl} is the equivalent plastic strain and the subscript and c refers to compression.

4.4.2 Stress-strain curve for uniaxial tension

For the uniaxial tension, the stress strain relationship is assumed to be linear-elastic up to the tensile strength f_t. After this point, the stress-strain response is defined by the softening which represents the descending part of the curve (ABAQUS, 2013) (Figure 4.5). The stress-strain values of concrete can also be obtained from a uniaxial tensile test or estimated based on its compressive strength. After the stress-strain curve is defined, the strain should be transformed to the inelastic strain ε_c^{in}, which represent the difference between the total strain (that is obtained from the test or equations) and the elastic strain for the undamaged material as follow:

$$\varepsilon_c^{in} = \varepsilon_t - \varepsilon_c^{el} \tag{4.14}$$

where:

$$\varepsilon_c^{el} = \frac{\sigma_c}{E_{cm}} \tag{4.15}$$

The stress and plastic strain ε_t^{pl} when unloading from any point on the curve are

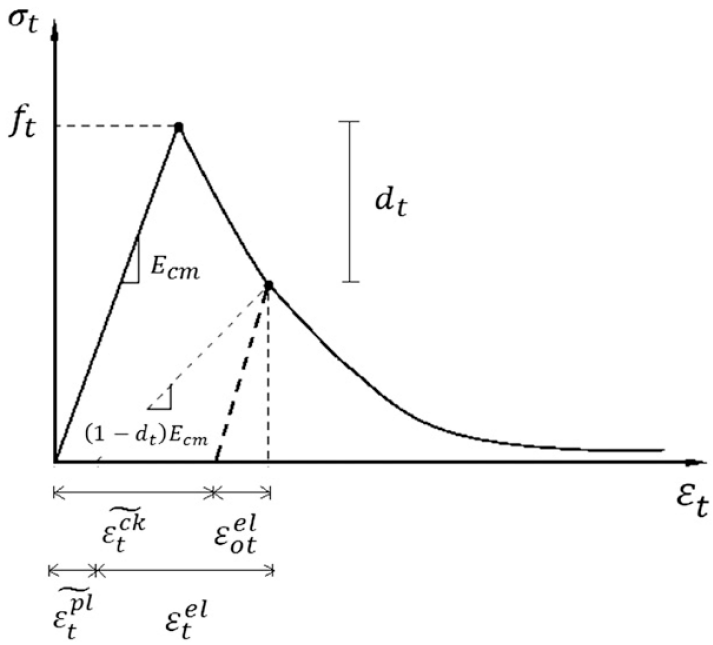


Figure 4.5: *Definition of inelastic strains for the concrete tensile behaviour of the CDP model (ABAQUS, 2013)*

then calculated in a similar way to the compression case using:

$$\sigma_t = (1 - d_t)E_{cm}(\varepsilon_t - \varepsilon_t^{pl}) \tag{4.16}$$

$$\varepsilon_t^{pl} = \varepsilon_t^{in} - \frac{d_t}{(1 - d_t)} \cdot \frac{\sigma_t}{E_{cm}} \tag{4.17}$$

where:

$$d_t = \begin{cases} 0, & for \quad \varepsilon_t < \varepsilon_{t0} \\ 1 - \dfrac{\sigma_t}{f_t}, & for \quad \varepsilon_t \geq \varepsilon_{t0} \end{cases} \tag{4.18}$$

4.4.3 Plastic flow potential, yield surface and viscosity parameter

The CDP model requires other constitutive parameters in order to identify the shape of the plastic flow potential function and the yield surface. The plastic flow potential describes the increment of plastic strain after yielding while the yield

surface determines the stress state when yielding occurs. Figure 4.6 shows the difference between the plastic potential surface and the yield surface, the figure also shows that the plastic strain increment $d^p_{\in}$ is normal to the plastic potential surface.

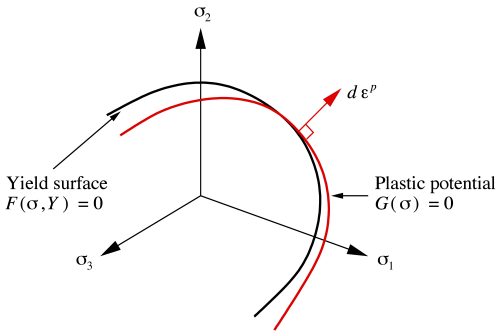


Figure 4.6: *Plastic potential surface and yield surface in the deviatory plane (ABAQUS, 2013)*

The CDP model is based on the Drucker-Prager hyperbolic function to define the plastic flow potential function ($G(\sigma)$) as given in Equation 4.19

$$G(\sigma) = \sqrt{(f_c - \epsilon.f_t\ tan\ \psi)^2 + \bar{p}^2} - \bar{q}\ tan\ \psi - \sigma \tag{4.19}$$

where ψ is the dilation angle that shows the direction of the plastic strain increment vector ($d^p_{\in}$) to define the inelastic volumetric change occurring when the material is under shear (see Figure 4.7). Lee and Fenves (1998) found that when the concrete is subjected to uniaxial compressive and tensile loading in both monotonic and cyclic tests, a dilation angle of 31° produces results in good agreement with the experimental data. f_c and f_t are the uniaxial compressive and tensile stress at failure; ϵ is the flow potential eccentricity which expresses the eccentricity of the plastic potential surface as shown in Figure 4.8. According to ABAQUS (2013), the default value of ϵ is 0.1 which shows that the concrete has the same dilation angle through a wide range of confining pressure stresses. $\bar{p}$ and $\bar{q}$ are two stress invariants of the effective stress tensor ($\bar{p}$ is the hydrostatic pressure stress and $\bar{q}$ is the von Mises equivalent effective stress).

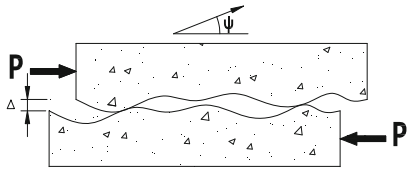


Figure 4.7: *Dilation angle (Ren et al., 2015)*

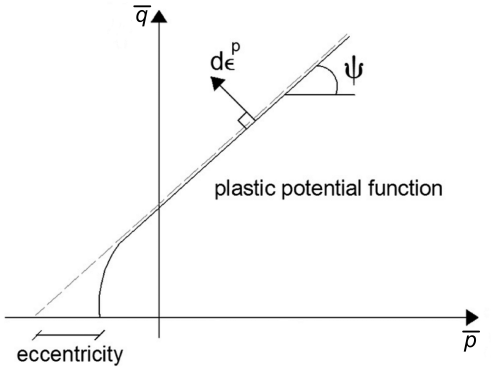


Figure 4.8: *Dilation angle and eccentricity in the meridian plane (ABAQUS, 2013)*

In order to know if the material has yielded or not, the stresses in the material need to be compared with the yield surface criteria. If the stress in the material has reached the yield surface it is clear that the subsequent deformation is inelastic. The yield surface is the surface in the stress space enclosing the volume of the elastic region. In other words, the stress inside the surface is elastic while the states of the stress on the surface have reached the yield point. It is possible for the yield surface to change in size and shape as plastic deformation occurs. This is necessary in order to account for hardening or softening behaviour in a model as shown in Figure 4.9.

This figure shows the stress-strain relation and the yield surfaces of the initial and the subsequent yield points.

The hypothesis of Drucker-Prager is most often applied to concrete which assumes a conical shape for the yield surface. However, this hypothesis is not fully consistent with the actual behaviour of concrete (Kmiecik and Kamiński, 2011).

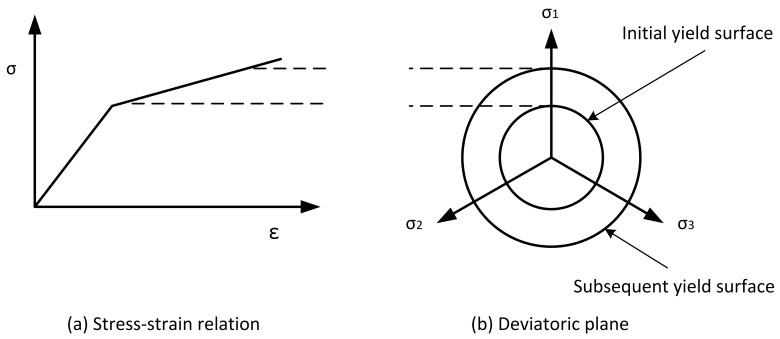


Figure 4.9: *(a) stress-strain relation for a material undergoing hardening and (b) the initial and subsequent yield surfaces in the deviatoric plane (Carstensen, 2011)*

Therefore, the CDP model uses a modification of the Drucker-Prager hypothesis that was proposed by Lubliner et al. (1989) and Lee and Fenves (1998). According to this modification, the failure surface in the deviatoric plane needs not to be a circle and its governed by the parameter K_c. K_c is the ratio of the second stress invariant on the tensile meridian ($q_{(TM)}$) to that on the compressive meridian ($q_{(CM)}$) at initial yield for any given value of pressure invariant p (see Figure 4.10). This ratio is in the range of 0.5 to 1 and when it assumes the value of 1, the deviatoric cross section of the failure surface becomes a circle (as in the classic Drucker-Prager strength hypothesis). However, the typical value of K_c is 2/3 (Lubliner et al., 1989) in which the failure surface has a triangular shape as shown in Figure 4.10. This shape is similar to the strength criterion (a combination of three mutually tangential ellipses) formulated by William and Warnke (1975) as shown in Figure 4.11. This is a theoretical-experimental criterion based on triaxial stress test results. The CDP model recommends to use $K_c = 2/3$.
The yield function in terms of the effective stresses $\bar{p}$ and $\bar{q}$ as given in Equation 4.20 is used in ABAQUS. This equation is proposed by Lubliner et al. (1989) and modified by Lee and Fenves (1998):

$$F = \frac{1}{1-\alpha}\Big(\bar{q} - 3\alpha\bar{p} + \beta(\varepsilon^{pl})\langle\sigma_{max}\rangle - \gamma\langle\sigma_{max}\rangle\Big) - \sigma_c(\varepsilon^{pl}) = 0 \qquad (4.20)$$

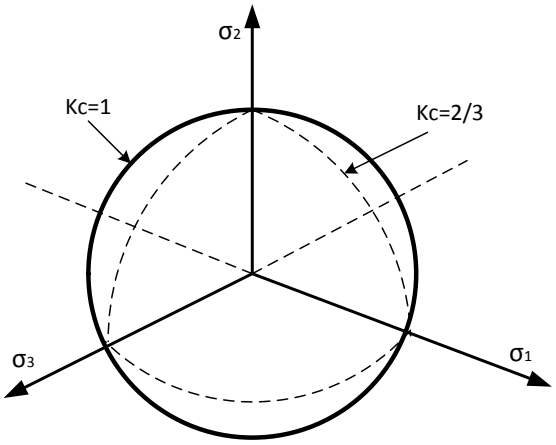


Figure 4.10: *Drucker-Prager yield criterion in the deviatoric plane for* $K_c = 1$ *and* $K_c = 2/3$ *(ABAQUS, 2013)*

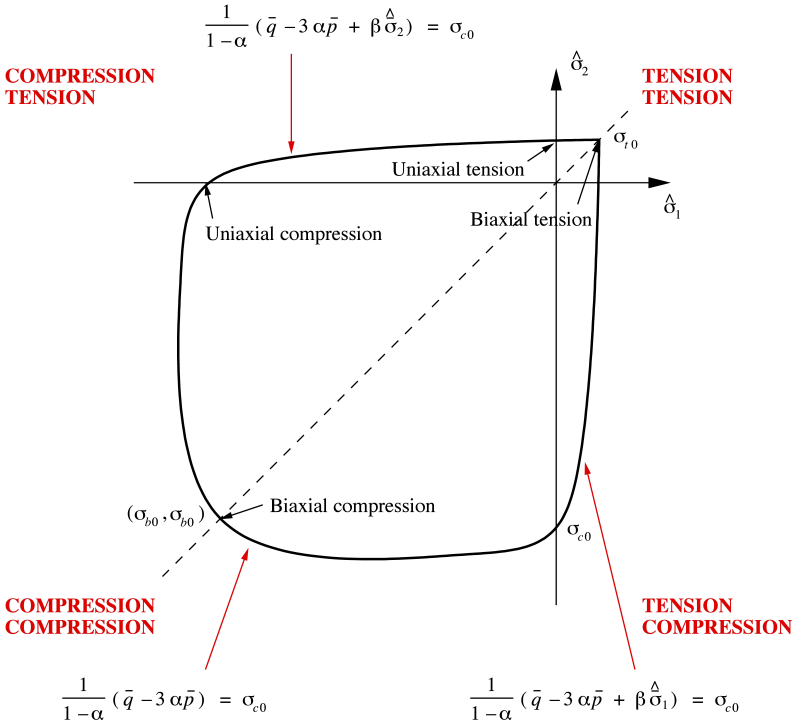


Figure 4.11: *Yield surface under biaxial stress in the CDP model (ABAQUS, 2013)*

where:

$$\alpha = \frac{(\sigma_{b0}/\sigma_{c0}) - 1}{2(\sigma_{b0}/\sigma_{c0}) - 1} \qquad 0 \leq \alpha \leq 0.5 \tag{4.21}$$

$$\beta = \frac{\sigma_c(\epsilon_c^{pl})}{\sigma_t(\epsilon_t^{pl})}(1-\alpha) - (1+\alpha) \tag{4.22}$$

$$\gamma = \frac{3(1-K_c)}{2K_c - 1} \tag{4.23}$$

From these equations, it can be seen that K_c and σ_{b0}/σ_{c0} are needed to define the shape of the function where K_c is the yield surface factor as described above and σ_{b0}/σ_{c0} is the ratio of initial biaxial compressive yield stress to initial uniaxial compressive yield stress (ABAQUS, 2013). Previous experimental investigation showed that the ratio of σ_{b0}/σ_{c0} lies between 1.1 and 1.16 (Lubliner et al., 1989). The default value of this parameter is 1.16 in ABAQUS ABAQUS (2013).

ABAQUS requires another parameter to be defined in the CDP model called the viscosity parameter μ. The viscosity parameter (μ) can help to avoid convergence difficulties in ABAQUS analysis. Problems with solution convergence may arise when increasing the non-linearity of the material. Furthermore, softening materials are associated with negative tangent stiffness which causes serious convergence difficulties (Ren et al., 2015). Simple finite element techniques, consisting in reducing the size of stress increments or increasing the maximum number of steps when solving the problem by means of the Newton-Raphson method, may prove to be insufficient. Therefore, the CDP model uses the viscosity parameter μ which allows the plastic strain to be updated and the damage is deduced using additional relaxation time in order to regularize the constitutive equation as follows:

$$\dot{\varepsilon_v^{pl}} = \frac{1}{\mu}(\varepsilon^{pl} - \varepsilon_v^{pl}) \tag{4.24}$$

where $\dot{\varepsilon_v^{pl}}$ is the strain rate with visco-plastic regularisation. The viscosity parameter in reinforced concrete problems in ABAQUS can be considered as a term related to the velocity of cracks opening or damaged area movement. In ABAQUS/Standard it is necessary to try different values of $\mu > 0$ in order to find out how big an influence it has on the problem solution result and to choose an appropriate value of this parameter.

The next section shows the results of using CDP model by simulating four reinforced concrete beams, tested experimentally by Barros and Fortes (2005), in ABAQUS. Furthermore, different values of viscosity parameter (μ) have been used in this study to see how it can affect the capacity of the beams.

4.5 Finite element simulations

Barros and Fortes (2005) tested four series of beams under four point bending in order to assess the efficacy of using a new strengthening technique using carbon fibre reinforced polymer (CFRP). They aimed to double the load carrying capacity of reinforced concrete beams failing in bending. Barros and Fortes (2005) used four reference beams (without strengthening) in order to verify the capability of their proposed technique.

In this study the four reference beams of Barros and Fortes (2005) have been considered and modelled in ABAQUS. This section highlights the details used to achieve suitable models.

4.5.1 Numerical solver

For the main simulations, ABAQUS/Standard (implicit) from ABAQUS (2013) was used in this study. The non-linear analysis that includes the non-linearities of material and geometry requires an incremental load or displacement steps. The incremental approach breaks the problem into a solution of many linear problems. At the end of each time increment the structure changes due to the material deterioration at the area of the plastic hinge. Subsequently, stiffness matrix needs to be upgraded. For implicit analysis, in each step increment, the Newton-Raphson algorithm is applied to find the equilibrium through iteration. To achieve equilibrium, the internal forces have to be equal to the external forces. Therefore, this method is accurate since the equilibrium is strictly enforced. In this study, the maximum number of increments has been used equal to 1×10^7, while the initial,

minimum and maximum increment size were 0.001, 1×10^{-20} and 0.1 respectively.

4.5.2 Beams geometry and material properties details

The four reference beams named $V1$, $V2$, $V3$ and $V4$ had a rectangular cross section of 100mm (width) and different heights of 178, 173 and 175mm with total length of 1600mm and clear span of 1500mm as shown in Figure 4.12. All beams had a top reinforcement consisted of two steel bars with diameter of 8mm, while the bottom reinforcement was composed of two steel bars for $V1$ and three steel bars for $V2$, $V3$ and $V4$ with diameter of $6mm$ and $8mm$ as shown in Figure 4.13. For shear, stirrups of $6mm$ and $3mm$ diameter were used. The distribution of stirrups and the spacing between them are shown in Figure 4.12.

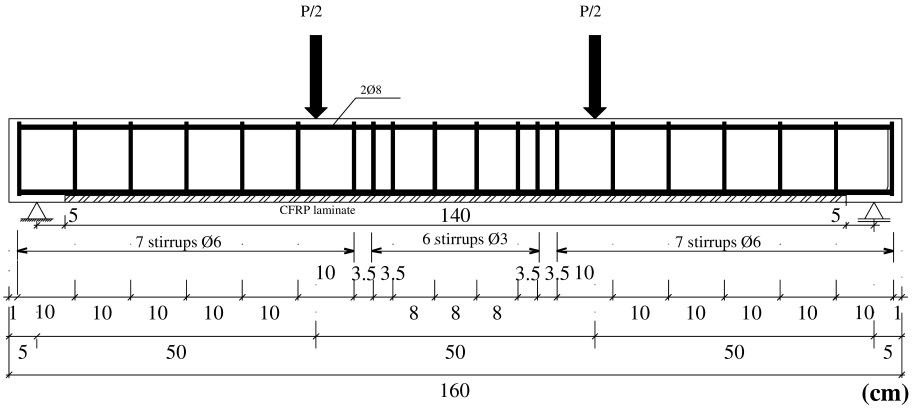


Figure 4.12: *Detailing of the simply supported reinforced concrete beam (Barros and Fortes, 2005)*

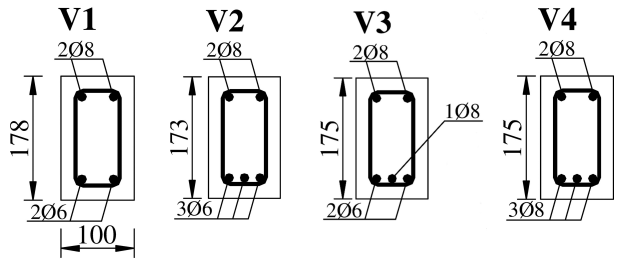


Figure 4.13: *The cross section of the simply supported reinforced concrete beam (Barros and Fortes, 2005)*

For the material properties, the concrete compressive strength was determined

from uniaxial compression test carried out on cylinders of 150 mm diameter and 300 mm height at the age of 90 days, when the beams were tested. Table 4.1 summarises the material properties of concrete for the four beams. The stress-strain curve shape for the reinforcement steel that is used in this study is shown in Figure 4.14. Table 4.2 summarises the material properties for the longitudinal and shear reinforcement.

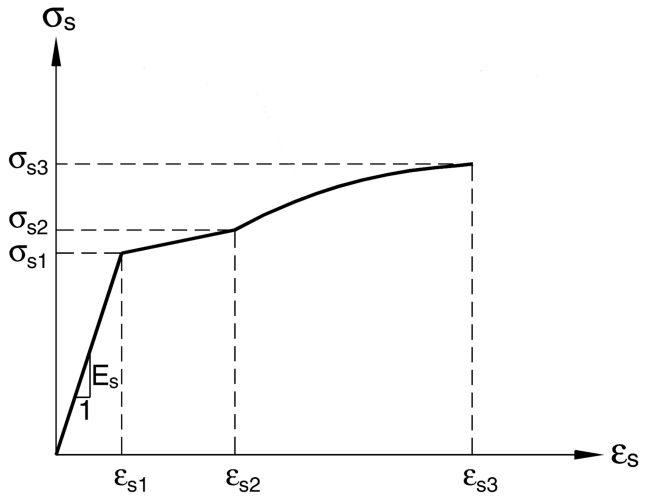


Figure 4.14: *Stress strain relation for the steel bars (Barros and Fortes, 2005)*

Table 4.1: *Concrete material properties of the tested beams (Barros and Fortes, 2005)*

Beam ref. no.	Width, Height, length (mm)	f_{cm} (MPa)	E_{cm}(GPa)	f_t(MPa)
V1	100·178·1600	45.33	33.35	3.37
V2	100·173·1600	48.9	36.5	3.58
V3	100·175·1600	42.75	34.89	3.21
V4	100·175·1600	46.4	35.86	3.43

Table 4.2: *Steel reinforcement properties of the tested beams (Barros and Fortes, 2005)*

Bar dia.(mm)	E_s (GPa)	ε_{s1} (mm/mm)	σ_{s1} (MPa)	ε_{s2} (mm/mm)	σ_{s2} (MPa)	ε_{s3} (mm/mm)	σ_{s3} (MPa)
6	200	0.00365	730	0.004	730	0.045	800
8	200	0.00262	524	0.03	554	0.15	613.5

4.5.3 3D beams modelling

Solid, 8 node, brick elements (C3D8R) were used for the concrete sections of the beams. A reduced integration was specified, which means that each element has only one integration point. Using reduced integration elements can prevent shear locking when the element is under bending. Shear locking is a numerical problem caused by the overly stiff element in bending applications and consequently, the element deformation shape will be different from the ideal situation (see Figure 4.15).

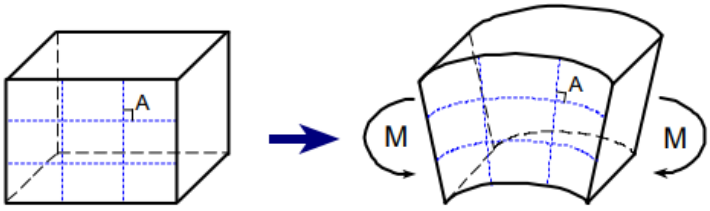


Figure 4.15: *Ideal situation of element deformation under bending effect*

The reduced integration element can represent the correct shape of element deformation, in which the vertical and horizontal line stay constant keeping $A = 90$ (see Figure 4.16), unlike the fully integrated elements.

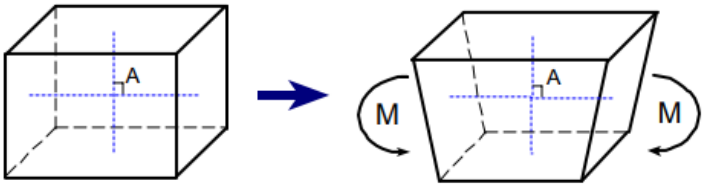


Figure 4.16: *Reduced integration element deformation under bending effect*

The fully integrated elements have four integration points with two integration

points in each direction, vertical and horizontal. The vertical and horizontal edges of the fully integrated element can not curve to represent the correct shape of deformation ($A \neq 90$) as shown in Figure 4.17. This will cause a shear deformation at the integration points with much larger stiffness and consequently, a wrong estimation for strains, stresses and displacements. Therefore, to address the shear locking and to increase the computational efficiency, the reduced integration scheme is used in this study. However, the reduced integration element can cause hourglassing effects due to the horizontal and vertical lines, which means that the normal and shear stresses are zero at the integration point and there is no strain energy generated by the deformation. This problem can happen when using a coarse mesh, however, reducing the mesh size overcomes this problem.

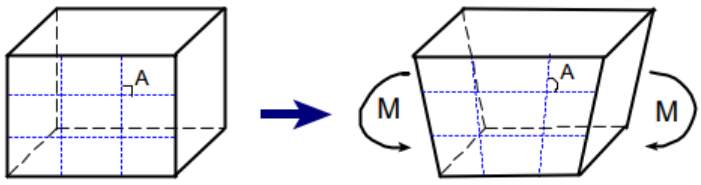
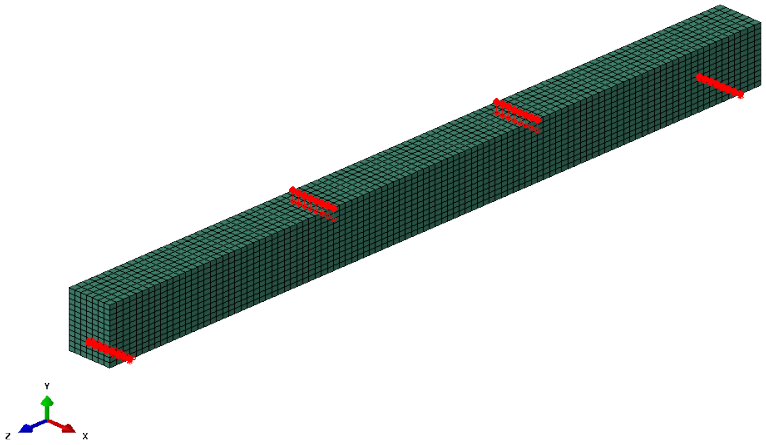


Figure 4.17: *Full integration element deformation under bending effect*

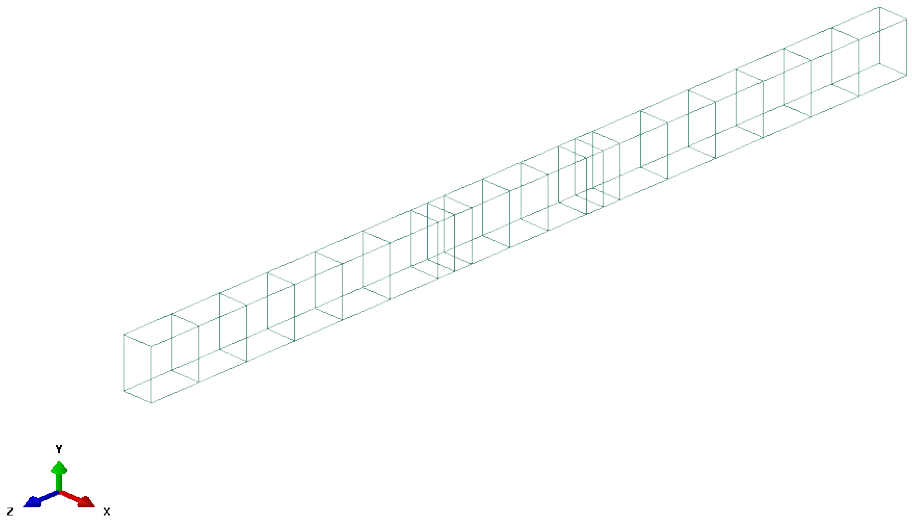
The steel reinforcement was modelled with Truss elements (T3D2), contained two nodes, with a circular cross sectional area. The bond between reinforcement steel and concrete was simulated by using ABAQUS embedded region feature. The embedded region according to ABAQUS (2013) is used to model a set of truss or beam elements embedded in a set of three-dimensional solid elements. The embedded region constrains the translational degree of freedom of the truss element nodes (steel nodes) to the interpolated values of the corresponding degree of freedom of the solid element nodes (concrete nodes). Using an embedded region in ABAQUS simulates a full bond between steel and concrete. Simulating the de-bonding effect of steel that results from the high level of stress is quite complicated in ABAQUS. Therefore, a full bond condition between the steel and the concrete using the embedded region is used in this study. Nevertheless, the

effect of bond using connector elements is considered in the real case study as the application method will be explained in details in Chapter 6.

For the boundary conditions, the beam is simply supported and therefore, the movement is eliminated in x and y direction for the hinge and in y direction for the roller. A displacement control method is used to test the beams under four point bending. The 3-D modelling of the beams is shown in Figure 4.18.



(a)



(b)

Figure 4.18: *3-D finite element modelling of V1: (a) concrete section. (b) reinforcement steel*

4.5.4 Mesh sensitivity

Mesh sensitivity analysis has been performed in this study for beam model $V1$ to identify a suitable mesh. Although the coarse mesh solution can be obtained with low computational cost, it might give an inaccurate result. However, using a very fine mesh could be too time consuming, even if it gives more accurate results. Therefore, mesh size consideration or mesh sensitivity analysis is very important task for any finite element analysis.

In this study, five different mesh sizes have been considered for beam model $V1$ as shown in Table 4.3. The comparison of the mesh sizes was made for the ultimate load of the tested beam, where the ultimate loads are plotted against the number of concrete elements used, as shown in Figure 4.19. The converged mesh appear if the reduction in the mesh size causes a negligible difference in results. Figure 4.19 shows that as the number of elements decreased (coarse mesh), the ultimate load increased. This is due to the fact that the coarse mesh does not replicate the true stress gradients across the beam section. Therefore, the local reduction due to yielding or cracking will not be exhibited, and that will result in a higher beam stiffness. This means that using coarse mesh will reduce the opportunity of assessing the state and the damage of the structures.

Based on this study, using 9360 and 12450 elements gave a close prediction to the ultimate load results from experimental test (28.2kN as shown in Table 4.5). However, 9360 number of elements is used in this study since it requires less computational time.

Table 4.3: *Results from mesh sensitivity parameter study for beam $V1$*

Number of elements	Ultimate load (F.E)
500	48 kN
3132	36.4 kN
5530	31.2 kN
9360	28 kN
12450	27.9 kN

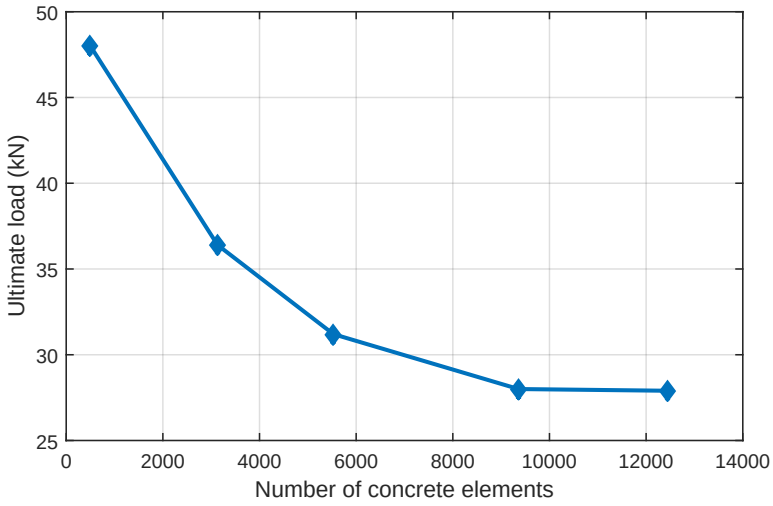


Figure 4.19: *Mesh sensitivity study*

4.5.4.1 Material models

The constitutive model for concrete is modelled according to the CDP model equations for compression and tension (Equations 4.1 to 4.8). Figure 4.20 and 4.21 respectively show the stress strain relationship of concrete in compression and tension. Figure 4.21 shows that the last point in the softening part of the tensile stress curve has been taken as 30% from the maximum tensile stress to avoid any convergence problem.

The damage parameters (d_c and d_t) are not used in this study because there is no cyclic relation in this analysis. For the CDP parameters, different values of viscosity parameter are used to study the sensitivity of this parameter on the capacity of the beams. The values of μ used are: $10^{-2}, 10^{-3}, 10^{-4}$ and 10^{-5} while the remaining parameters (dilation angle ψ, eccentricity ϵ, yield surface factor K_c and the ratio of initial biaxial compressive yield stress to initial uniaxial compressive yield stress f_{b0}/f_{c0}) are presented in Table 4.4.

Table 4.4: *Concrete damage plasticity input parameters*

Dilation angle (ψ)	Eccentricity (ε)	f_{b0}/f_{c0}	K_c
31°	0.1	1.16	2/3

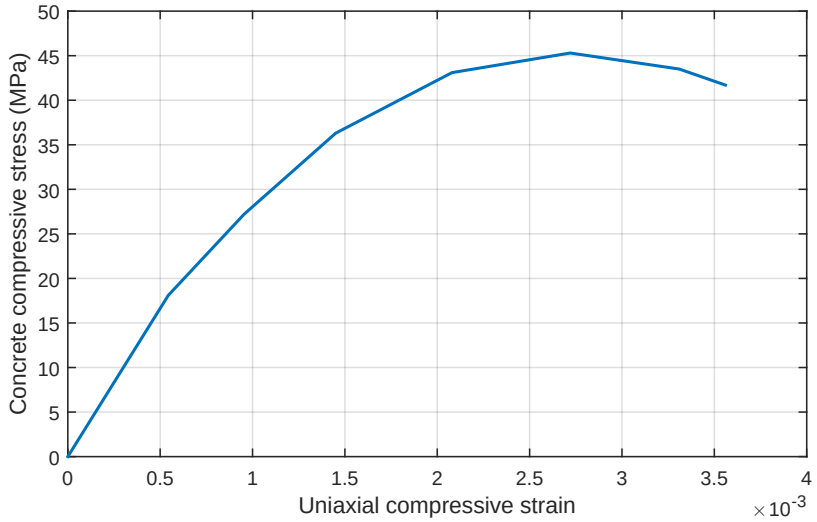


Figure 4.20: *Uniaxial stress strain curve of concrete in compression for beam model $V1$*

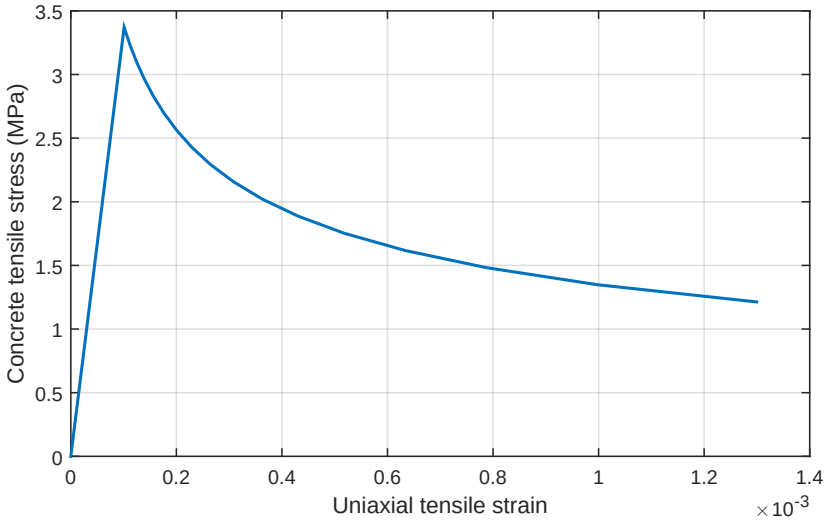


Figure 4.21: *Uniaxial stress strain curve of concrete in tension for beam model $V1$*

The reinforcement steel was modelled using a bi-linear stress strain relationship based on the values presented in Table 4.2. Poisson's ratio was specified as 0.3, as is usual for reinforcement steel. Figure 4.22 shows the bilinear stress strain curve used in this study for beam $V1$.

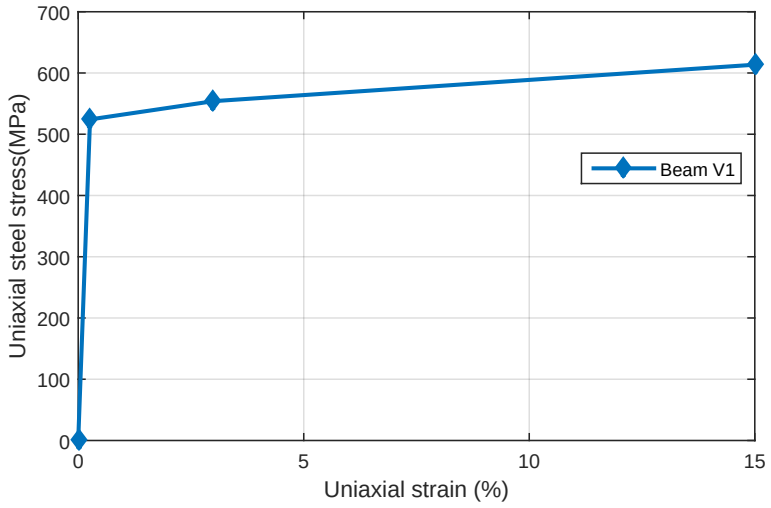


Figure 4.22: *Uniaxial stress strain relationship for reinforcement steel of beam model V1*

4.5.5 Model validation

In this section, the results of the finite element analysis for the four beams are compared with the experimental results in order to validate the modelling assumptions. The comparison is carried out on the load deflection curves to compare the ultimate load (P_u) and the vertical displacement (U_y). Figures 4.23 to 4.26 show comparisons between the experimental and the FE results for the four tested beams. The general patterns of the load deflection curves show a good correlation between the experimental and the finite element results. It can be clearly seen that the finite element simulations using the CDP model capture the experimentally observed loading trends and magnitudes for the loading range. Table 4.5 compares the experimental ultimate load and deflection corresponding to the ultimate load and deflection with those obtained from the finite element analysis for the four beams. The comparisons show a good agreement (small differences with less than 10%) between the experimental and finite element results. However, the results of finite element analysis shows that the beams are slightly more stiffer than the experimental and that may be because of the full bond assumptions. Furthermore, the results of FEA shows that there is no descending

branch in the curves which is may be because of the method that has been used to represent the concrete tensile behaviour (the last value of the tensile stress in the softening part is relatively high (see Section 4.5.4.1)). This can cause a residual strain which is not exist in reality.

From this study, it can be found that the finite element analysis using the CDP model proves its capability to predict the load-deflection curves of the reinforced concrete beam.

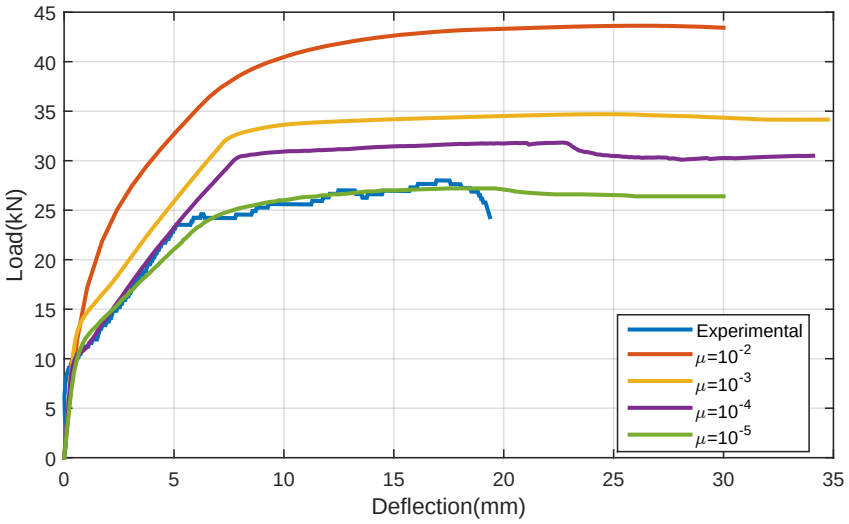


Figure 4.23: *Experimental vs. FE load deflection curves using different values of viscosity parameters μ (Model $V1$)*

Table 4.5: *Comparison between the experimental data and FE results for beam model $V1$*

Beam	$V1$		$V2$		$V3$		$V4$	
	P_u	U_y	P_u	U_y	P_u	U_y	P_u	U_y
Experimental	28.2	17	41	22	41.3	19	48.5	19.06
Finite Element	27.7	18	40	20	45.1	18.6	51.3	15.5
Differences(%)	1.7	5.5	2.4	9	8.4	2.1	5.4	18.6

Note: P_u in kN and U_y in mm.

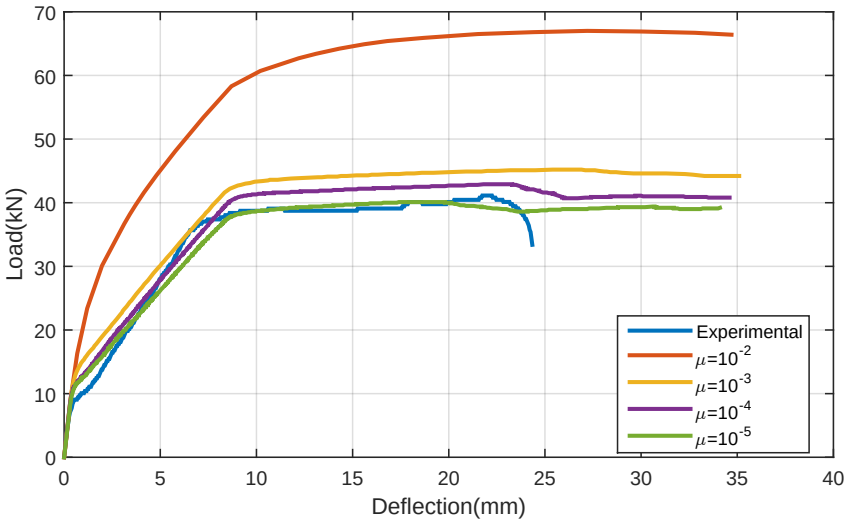


Figure 4.24: *Experimental vs. FE load deflection curves using different values of viscosity parameters μ (Model V2)*

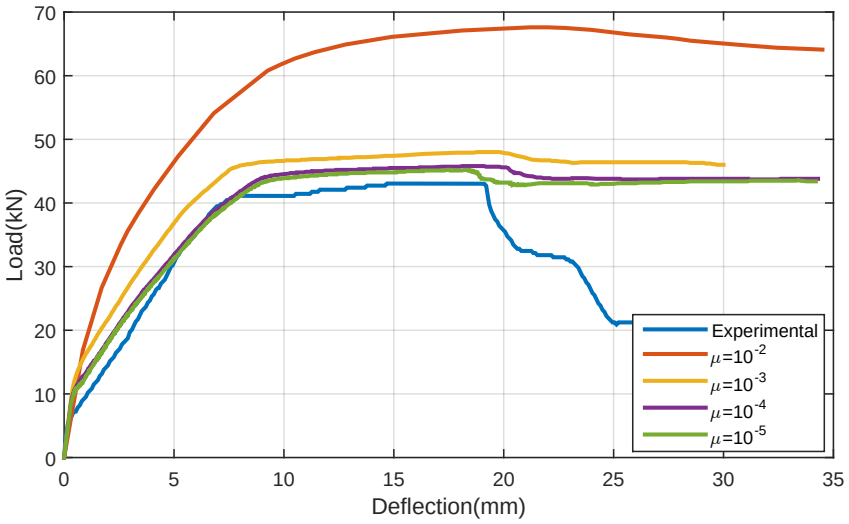


Figure 4.25: *Experimental vs. FE load deflection curves using different values of viscosity parameters μ (Model V3)*

Four different values of viscosity parameter have been used: 10^{-2}, 10^{-3}, 10^{-4} and 10^{-5}. The results show that for the all tested beams, a viscosity parameter between 10^{-4} and 10^{-5} shows a good agreement with the experimental results. However, using a higher values of viscosity parameter increases the ultimate capacity of the beams. This can be explained according to the crack distribution

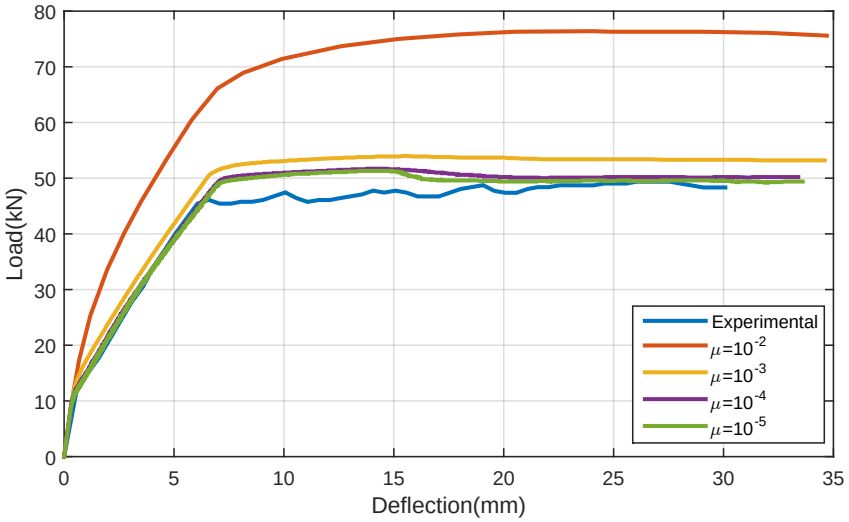


Figure 4.26: *Experimental vs. FE load deflection curves using different values of viscosity parameters μ (Model V4)*

near the tension zone of the beams as shown in Figure 4.27. Figure 4.27 shows the difference of beam crack distribution with using of different values of μ. Increasing μ will lead to spread the damage zone to more finite elements leading to diffuse pattern of cracking and limiting crack propagation. Consequently, non-accurate results are resulted from using high viscosity parameter. In accordance with the numerical tests that carried out by Szczecina and Winnicki (2015), they recommended a viscosity parameter of 0.0001. In addition, Szczecina and Winnicki (2015) found that increasing viscosity parameter led to increase the ultimate capacity of the tested specimen as well as, the damage zone takes a circular form (when using μ=0.01) and that does not represent the reality.

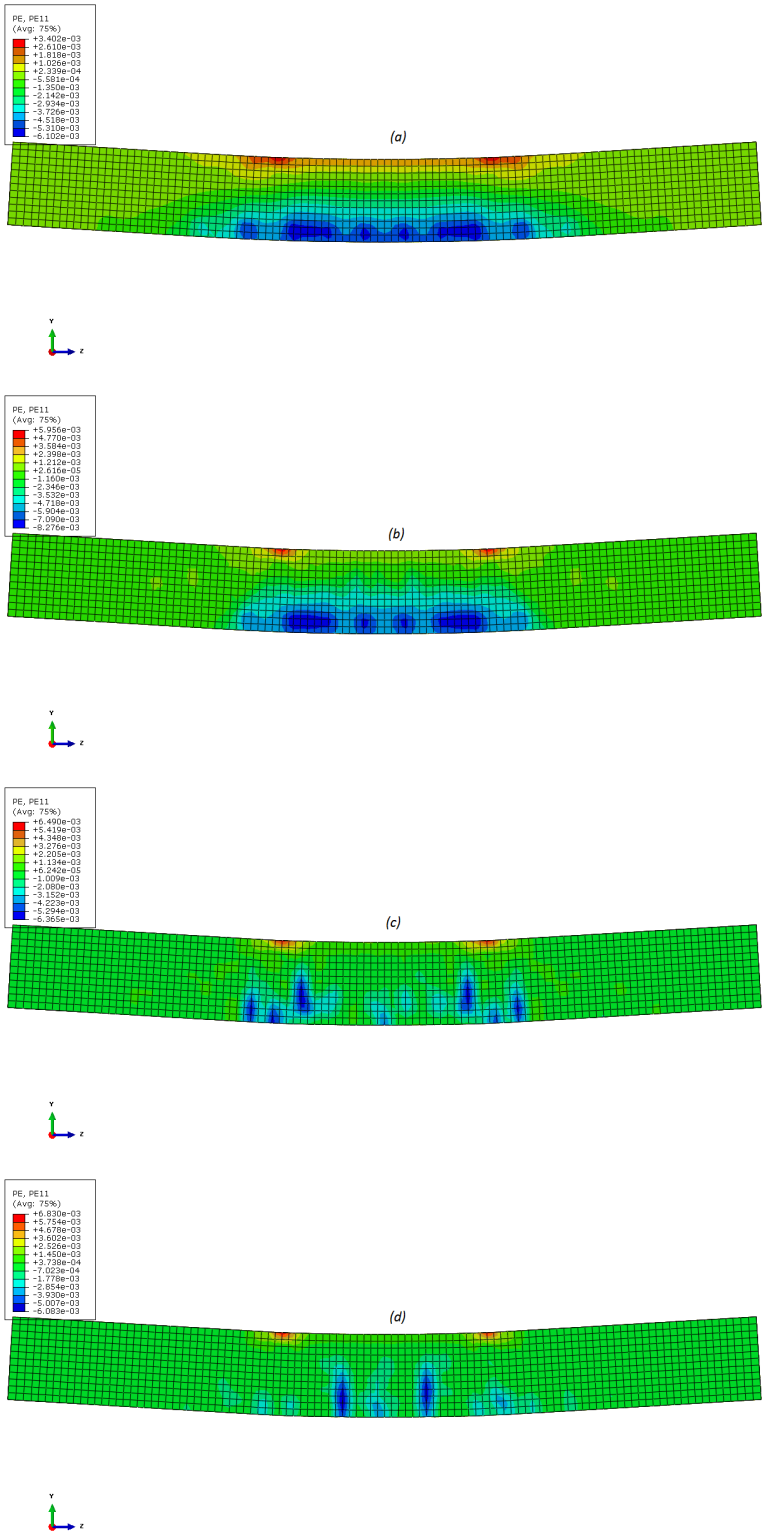


Figure 4.27: *Crack distribution near the concrete beam tension zone: (a)* $\mu = 10^{-2}$*, (b)* $\mu = 10^{-3}$*, (c)* $\mu = 10^{-4}$ *and (d)* $\mu = 10^{-5}$

4.6 Summary

This chapter has introduced the numerical approach that is used to simulate four reinforced concrete beams, in particular the CDP model. The description of the models covering the geometry and the material details is presented. The 3-D finite element nonlinear modelling of the reinforced concrete beams have been described with the use of elements. Then, mesh sensitivity analysis has been performed in order to use the suitable mesh size. Finally, the results of finite element are compared with the experimental to ensure that the simulations are provided reliable results.

The presented models are based on recognised theory and good modelling practice that make it suitable for modelling such events. The modelling approach will use in the next chapter, where a simple finite element model is used to apply advanced reliability analysis, before being used for the real case study in Chapter 7.

Chapter 5

Computational Approach for Advanced Reliability Analysis

In Chapter 3, the methods of applying reliability analysis for problems with explicit performance function have been presented. However, these methods can not be used for problems with an implicit limit state function, in which case advanced methods are needed. Therefore, the first part of this chapter focuses on presenting the available advanced reliability methods, in the literature, that have been used to estimate the reliability of a system with an implicit limit state function. The second part of this chapter presents an example application for a deteriorated simply supported beam with implicit performance function.

5.1 Introduction

Reliability analysis methods are used to evaluate the safety of reinforced concrete structures by evaluating the limit state function $g(X_i)$, which represents the boundary between the safe and unsafe regions. Since the structure should be designed so that its strength or resistance is greater than the effects of the applied load, the limit state function can be regarded as the difference between the resistance and the load acting on a structural component.

The limit state function in many reliability analysis problems can be expressed explicitly and, as mentioned in Chapter 4, the FORM method can be used to estimate the safety of structure for explicit limit state function. However, for applications to realistic structures, e.g., when the structure behaves non-linearly due to cracking and crushing of concrete, yielding of reinforcement etc., the limit state function is not available in an explicit form. In such cases, the derivative of $g(X_i)$, with respect to the random variables X, that is required in searching for the minimum distance point on the $g(X_i)$ is not available. Therefore, more advanced reliability methods are needed. Mahadevan and Haldar (2000) stated that three different approaches can be used to apply reliability analysis of structures with implicit $g(X_i)$: Monte Carlo simulation (MSC), response surface method and the sensitivity based analysis. This chapter will describe briefly these three methods and an application for MCS for a simply supported beam with implicit $g(X_i)$ will be presented. Furthermore, a new method that links MATLAB and ABAQUS has been developed and exploited to produce a novel combined process that can speed up the reliability analysis for non-linear structures.

5.2 Implicit performance function

5.2.1 Monte Carlo simulation

Monte Carlo simulation is one of the methods that is used to calculate the probability of failure for any limit state function. This method is applicable when the limit state function is defined explicitly or implicitly (when limit state function obtained from finite element analysis). The steps that are needed to apply this technique as mentioned in Mahadevan and Haldar (2000) are as follows:

- Define the failure mode $g(X_i) = 0$ with all random variables (X_i) that are needed to consider.
- Define the statistical parameters for all random variables in terms of their

distribution, mean and standard deviation.

- Generate the random numbers (samples) for each of these random variables.
- Evaluate the $g(X_i)$ for each of theses samples.
- For each outcome, $g(X_i)$ should be checked whether the failure $g(X_i) \leq 0$ has been occurred.
- estimate the P_f after N simulations through $P_f = \frac{n_f}{N}$ where n_f is the number of $g(X_i)$ that are failed and N is the total number of samples.
- Check the accuracy of the simulation by increasing the number of samples and verifying that the final conclusion is robust and meets a certain level of accuracy.

This method is the most common method that is used for structural reliability analysis due to its simplicity. However, this method is less suitable for complex structures because large simulations are required to estimate the probability of failure and that requires many time consuming numerical calculations. Therefore, Artificial Neural Network (ANN) method can be used in conjunction with MCS to overcome this problem. This method is used to reduce the time required for the intensive computations that are needed to approximate the limit state function.

5.2.2 Response Surface Method (RSM)

The Response Surface method is also used in structural reliability analysis in conjunction with the FORM and Monte-Carlo simulation. Mahadevan and Haldar (2000) refer to the main idea of the RSM method, which is to use a polynomial model (first order or second order) to replace the limit state function $g(X_i)$ through a small number of deterministic analyses. The following steps represent the methodology of this approach:

- select different sets of random variables (usually two or three values of each random variables used). In general, the values of the random variables are

selected as low and high values if two values are used. While in case of using three values, the values are supposed to be low, medium and high. The low value is represented by $\mu - k\sigma$ and the medium is represented by μ, while $\mu + k\sigma$ represents the high value, where k is integer and μ and σ are the mean and standard deviation respectively.

- Estimate the performance function $g(X_i)$ for the different selected sets values of the random variables by using a deterministic non-linear finite element analysis.

- Find the design point on the reduced limit state function (in the normalized space) by using a regression analysis for the different values of the limit state functions that are evaluated in step 3.

- Evaluate the probability of failure by using FORM or Monte-Carlo simulation methods.

Although this method is easy to estimate and apply, its application for a highly non-linear limit state function is inaccurate because it deals with a small number of samples. Moreover, the Response Surface method gives an approximation for the limit state function and that means it gives inaccurate results for the reliability index.

5.2.3 Sensitivity based analysis

As mentioned in Chapter 3, the limit state function $g(X_i)$ in FORM method can be evaluated according to deterministic analysis and, the sensitivity analysis is used to compute the gradient of $g(X_i)$ to find the design point after multiple iterations. This method is very simple to apply when the gradient is computed for an explicit performance function (analytical or numerical differentiation $g(X_i)$). However, for complex structures when finite element is needed to analyse the structure, it is not easy to evaluate the gradient of the implicit performance function. Therefore, the other possible method of structural reliability analysis is the

sensitivity based analysis (Mahadevan and Haldar, 2000).

The sensitivity based analysis can be computed through a finite difference approach and perturbation method to compute the gradient of the $g(X_i)$ at each iteration during the search for the design point at the minimum distance (Mahadevan and Haldar, 2000). Although the sensitivity based analysis is more elegant and more efficient than MCS and RSM, it requires a specialized program that are not adaptable for practical applications (Wiśniewski, 2007).

5.2.4 Artificial Neural Network method (ANN)

The ANN is a numerical algorithm introduced by McCulloch and Pitts (1943) by proposing a mathematical model to simulate neuron behaviour. The ANN model consists of multiple neurons linked together and situated in three or more layers: Input layer, Output layer and one or more hidden layers as shown in Figure 5.1.

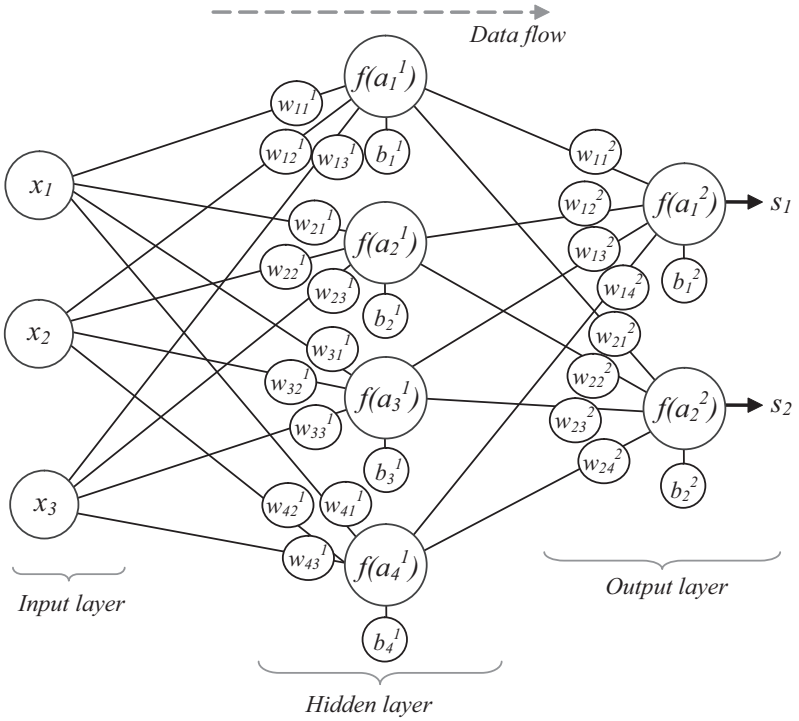


Figure 5.1: *Multi-layer neural network (Chojaczyk et al., 2015)*

Each neuron in the input layer will receive an input component of a signal vector

that represents the input random variables $X_i = x_1, x_2, ...x_n$. After that, each random variable will be multiplied by a coefficient w_{mk} which reflecting the importance of the input channel k. The activation of neuron a_m is then calculated from Equation 5.1.

$$a_m = \sum_{k=1}^{n} w_{mk}.x_k + b_m \tag{5.1}$$

where b_m is the bias, which is a constant corrective term that allows having a non-negative activation a_m. The output signal s_m of neuron is the numerical value that results from the computation of an activation hyperbolic tangent sigmoid function $f(a_m)$, which is the common choice used for this purpose, and it can be calculated from Equation 5.2.

$$f(a_m) = s_m = \frac{2}{1 + e^{-2a_m}} - 1 \tag{5.2}$$

The number of neurons on the input layer is equal to the number of input variables while the number of outputs it depends on the number of limit state functions that need to be approximated. The number of hidden layers and also the number of neurons in the hidden layers can be changed and there are no applicable general rules to choose them. Trial and error is usually used to find the suitable number of hidden layers.

The basic idea of ANN is to train a neural network model which can be used later on other values. The training of a network is an iterative process which consists of obtaining the unknown coefficients w_{mk} and b_m required to approximate the prescribed function. The most common training process, called *Back Propagation* training algorithm, consists in generating random values for the initial weights and biases and then adjusting values using a training algorithm to minimize the error between the predicted output produced by the ANN and the exact value of the function. Therefore, to perform this training test, a training data set, which includes input and target values, should be previously prepared. The iterative training algorithm performs an error minimization procedure that is repeated until the network outputs converges to the target value. The error is evaluated

using the following equation (Mean Squared Error):

$$MSE = \frac{1}{N}\sum_{i=1}^{N}(t_i - s_i)^2 \tag{5.3}$$

where N is the number of training samples, s_i is the network output values and t_i is the target output.

The ANN method has been used in reliability analysis by several researchers such as Gomes and Awruch (2004), Elhewy et al. (2006), Cardoso et al. (2008) and Chojaczyk et al. (2015). Cardoso et al. (2008) examine a methodology for computing the probability of structural failure by combining ANN and MCS. They applied this methodology to different three examples and they concluded that the application of ANN in conjunction with MCS is a versatile methodology that can approximate accurately highly nonlinear functions with very good precision. Chojaczyk et al. (2015) use the ANN-based MCS to approximate the limit state function of a ship stiffened panel subjected to uniaxial compression loads modelled using FEA. They found that this methodology is easy to implement and has a very good accuracy.

5.3 Reliability analysis of a RC beam with implicit performance function

In this section, an example application of reliability analysis of a deteriorated RC beam with implicit performance function will be presented. Two methods have been used and compared:

- Combining MCS and FORM.
- ANN-based FORM.

The details of the beam considered, the limit state function, the finite element

model and the relevant random variables will be presented in the following subsections.

5.3.1 Beam details and random variables

A simply supported reinforced concrete beam subjected to corrosion is considered in this study to assess the effect of corrosion and material strength variability on beam resistance and probability of failure over 90 years of the beam service life. The beam is designed in bending using Eurocode 2 reinforced concrete design (Mosley et al., 2012). The deterministic values of beam geometry, material properties and loads are listed in Table 5.1.

Table 5.1: *Deterministic values of beam geometry, material properties and load parameters*

Parameter	Value	Units
Length (L)	9.5	m
Clear span (L_{cs})	9	m
Height (h)	0.4	m
Width (b)	0.25	m
Effective depth (d)	0.38	m
Compressive strength (f_{ck})	30	MPa
Steel yield strength (f_{yk})	500	MPa
Permanent load (g_k)	4	kN/m
Live load (q_k)	6	kN/m

Four reinforcement bars are embedded in the beam with diameter 16 mm as shown in Figure 5.2.

As the beam is tested under bending, the failure mode criteria is flexural and the ultimate limit state function occurs when the beam resistance is less than or equal to the bending action. Therefore, the limit state function is written as:

$$g(X_i) = \theta_R.M_R - \theta_E.M_S \tag{5.4}$$

where θ_R and θ_E are the resistance and load model uncertainties. M_R is the beam resistance moment that can be evaluated from ABAQUS. M_S is the beam action

moment which can be calculated according to the applied dead and live load from the following equation:

$$M_S = wl^2/8 \tag{5.5}$$

where $w = g + q$. Then the limit state function is written as:

$$g(X_i) = \theta_R.M_R - (\frac{l^2}{8}(g+q)).\theta_E = 0 \tag{5.6}$$

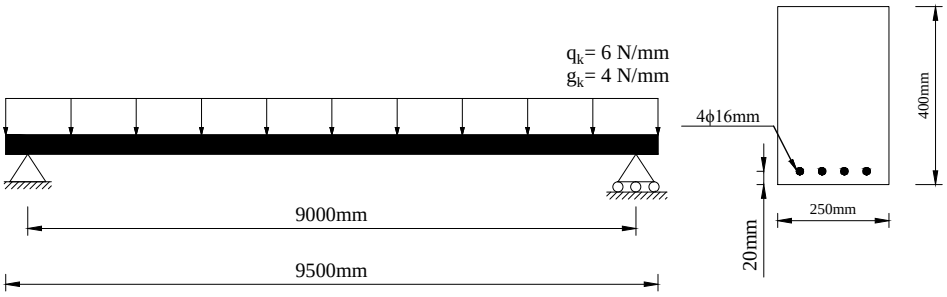


Figure 5.2: *Simply supported RC beam section*

In the reliability analysis, the compressive strength of concrete (f_c), the tensile strength of concrete (f_t), the yield stress of reinforcement steel (f_y), dead load (g), live load (q), the concrete modulus of elasticity (E_c), the resistance model uncertainty (θ_R) and the load model uncertainty (θ_E) are treated as random variables and their distribution, mean and standard deviation are presented in Table 5.2.

The analysis assumes deterministic values for corrosion rate ($i_{corr} = 3\mu.A/cm^2$) and pitting factor ($R = 4$) for simplicity. Furthermore, time to corrosion initiation (t_i) is assumed to be zero. According to the classification of corrosion rate in Middleton and Hogg (1998), $i_{corr} > 1.0$ represents a high corrosion rate typical of aggressive environments such as surfaces exposed to sea-spray.

The other relevant parameters for the mechanical properties for steel and concrete are included as implicit random variables.

Table 5.2: *Statistical parameters of random variables for ultimate limit state analysis*

Variables	Units	μ	σ	COV	Distribution	Source
Concrete compressive strength (f_c)	MPa	f_{cnom}	-	0.15	Lognormal	JCSS (2001)
Concrete tensile strength (f_t)	MPa	$0.3(f_c)^{2/3}$	-	0.2	Normal	Spaethe(1992) cited in Wiśniewski (2007)
Yield stress (f_y)	MPa	$S_{nom} + 2\sigma$	30	-	Normal	JCSS (2001)
Modulus of elasticity (E_c)	GPa	$22(0.1f_c)^{0.3}$	-	0.08	Normal	Eurocode-2 (2004)
Dead load (g)	kN/m	4	-	0.1	Normal	Nowak (1993)
Live load (q)	kN/m	6	-	0.4	Gumbel	Nowak (1993)
Load uncertainty (θ_E)	-	1	0.1	0.1	Lognormal	JCSS (2001)
Resistance uncertainty(θ_R)	-	1	0.15	0.15	Lognormal	JCSS (2001)

5.3.2 3D-nonlinear FE modelling

Figure 5.3 shows the 3D FE mesh for the nonlinear model for the RC simply supported beam. The model includes eight-node Solid elements (C3D8R) for concrete and Truss elements (T3D2) for reinforcement steel (details have been described in Section 4.5.3). The truss elements are embedded in the concrete element using embedded constraint, which means a perfect bond is assumed between concrete and steel. Elastic steel plattens are also added at the load positions and near the supports to avoid the stress concentration in the concrete. A tie constraint (surface based tie) is used to define the fully constrained contact behaviour between elastic strips and the concrete beam.

The CDP model as described in Chapter 4 has been used to model the concrete in tension and compression. The material behaviour of reinforcement steel is represented using an elastic perfectly plastic constitutive model. The default values of the CDP parameters as described in Chapter 4 have been used in this study and a 10^{-5} viscosity parameter is used.

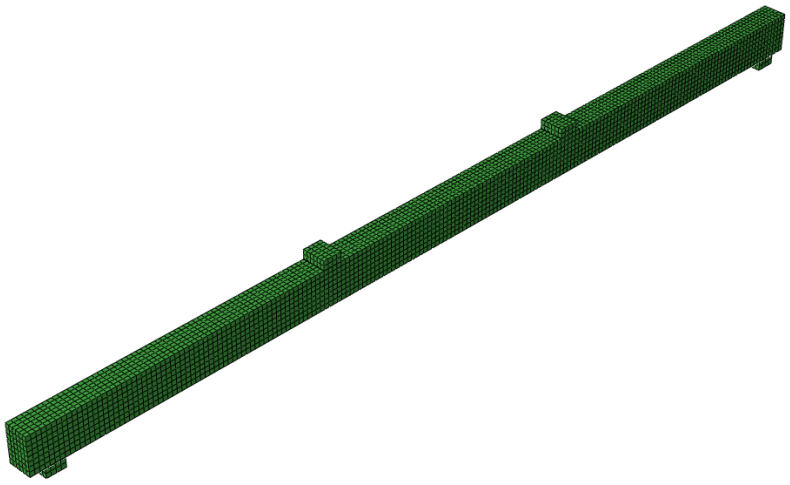


Figure 5.3: *The three dimensional view of meshing the RC simply supported beam*

The beam is loaded under four point bending using a displacement control method by applying a target displacement value of 0.3 m. As vertical displacement increased, cracks due to bending were generated in the middle span of the beam

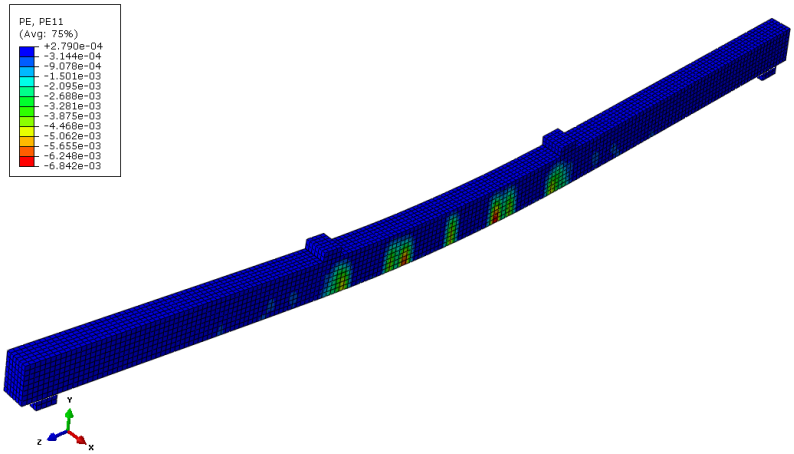


Figure 5.4: *Beam cracks due to bending*

as shown in Figure 5.4. The resistance moment at the middle section of the beam is calculated by finding the integration point stress for each element at the middle beam section and then these stresses are converted to moment by multiplying each element stress by its area and the distance from element center to the bottom of the beam.

5.3.3 Analysis procedure and results

After defining the limit state function and the relevant random variables, time dependent reliability analysis procedure according to Figure 5.5 has been applied. The procedure can be summarized in the following steps:

1. By using MCS, a large number of samples for the resistance random variables (f_c, f_y, f_t and E_c) have been generated for each time interval. However, later on it was realized that the model can be simplified by using the same generated samples for the first year.

2. For each of the generated samples in step 1, the finite element beam model is prepared and analysed.

3. The resistance moment is obtained after each finite element analysis for the beams in step 2.

4. The statistical parameters of the resistance moment are found at each time interval.

5. FORM method is used to evaluate the probability of failure (P_f).

Performing the steps listed above is quite complicated because they require a very long time to prepare the models and analyse them. For example, in this study MCS is used to generate 150 samples in step 1, which means 150 finite element models (for each time interval) need to be prepared and analysed in ABAQUS. So, if 10 years considered in time dependent reliability analysis, then 1500 finite element models need to be prepared and analysed. Doing that is impossible with the Graphical User Interface (GUI). Therefore, the ABAQUS Python script file is used in conjunction with MATLAB to reduce the time required for that, as will be explained in the next sections. Noting that, this is the first time that such method is used in structural reliability analysis to speed up the analysis via automating the processing. In conjunction with the above described method, the files have been prepared and submitted to the High Performance Computers (HPC) to complete several files at a time and to reduce the time required for each FEA.

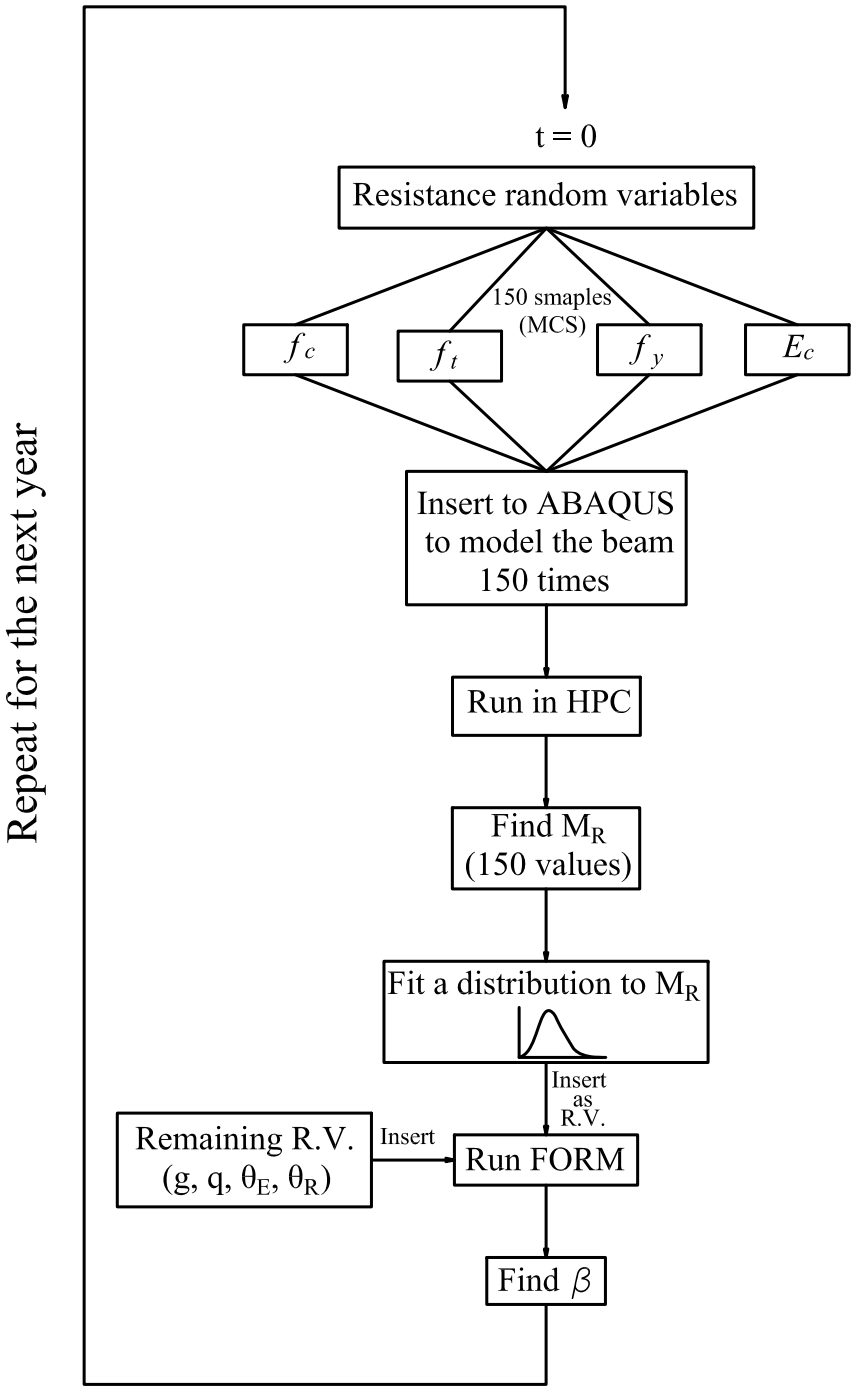


Figure 5.5: *Reliability analysis procedure flowchart*

5.3.3.1 ABAQUS Python script file

Python scripting language is a powerful tool used to communicate between modules like Graphical User Interface (GUI) in ABAQUS and ABAQUS/viewer. Python is embedded within ABAQUS software products. In some cases, using ABAQUS GUI to analyse a task can be considered as too time consuming or practically impossible, as is the case in this reliability analysis. For example, if a load is applied on a cantilever beam and the bending moment needs to be calculated as increasing the beam length then the beam should be recreated several times and if the model is complex then the sections, load, mesh and boundary conditions should be changed every time also. In this case, a Python script is a more efficient way to perform this task by considering e.g. length and load as a variables and rerunning the script in a loop for several times.
Therefore, Python script is used in this study to automate the repetitive tasks that result from the uncertainty of material properties and geometry. In addition, using the script can help to extract information from large output databases.
The way that can be used to generate the Python script file for the model database (mdb) in ABAQUS is by the following procedure:

- Create the finite element model using ABAQUS/GUI and complete the analysis.
- Save the model in a specified work directory.
- Open the journal file (*.jnl*) and save it as a Python file (*.py*). The journal file is usually generated during model creation in ABAQUS and it records all the actions of model creation.

From these steps the model database Python script file (*mdb.py*) is generated from ABAQUS which contains the whole input data such as model dimensions, material properties, mesh size and so on. In order to generate the Python file for the output database (*odb.py*) the following steps can be used:

- Open the *.odb* file (created in the same directory) and specify the results that are needed.
- Save the results in *.rpt* file and exit.
- Open the replay file (*.rpy*) and save it as a Python file (*.py*). The replay file is usually generated during extracting results from the *.odb* and it records all the actions of extracting the results from ABAQUS/viewer.

The *odb.py* file can be used to avoid the repetition of extracting the data from ABAQUS/viewer (*.odb* file). According to that, calculating the resistance moment in step 3 in Section 5.3.3 has been found one time, and then the steps of extracting these results are transformed to *odb.py* file.

5.3.3.2 ABAQUS and MATLAB connection

The two software applications ABAQUS and MATLAB can be connected together using Python file. The connection can help to automate the analysis, generate multiple simulations easily and minimize the time.
After preparing the *mdb.py* and the *odb.py* files, they were combined together in one file (See Appendix A) to accelerate the analysis. In MATLAB, the following steps are needed to complete the connection:

1. Generate the resistance random variables samples, 150 samples for each year using MCS.
2. Create a new Python file in terms of the resistance variables samples values generated in step 1.
3. Execute the file prepared in step 2 in the model data base using execfile('filename.py').
4. Run ABAQUS through MATLAB using **System** command. After this step, MATLAB will firstly read the *mdb.py* to create the model and secondly the *odb.py* to extract the results.

5.3.3.3 Resistance moment and beam capacity

The pitting corrosion is assumed to be distributed uniformly along the reinforcement bars. The pit configuration and its geometric model equations that are proposed by Val and Melchers (1997) is used in this study to predict the cross-sectional area of the pit (A_{pit}) (see Figure 2.15 and Equations 2.43, 2.47 and 2.48). According to this, the reinforcement corrosion is regarded through the steel bar area reduction as a function of time (Figure 5.6b) when the pit depth (Figure 5.6a) is generated over the reinforcement length.

Figure 5.7 shows the deterioration in beam ultimate load capacity due to corrosion along the years. The ultimate load capacity of the beam corresponding to the corrosion loss over the years has been listed in Table 5.3. The table shows that the percentage reductions in ultimate capacity were in accordance with the findings of Malumbela et al. (2010), who found that for every 1% mass loss of steel, there was a corresponding 0.7% reduction in the ultimate capacity of the beam.

Table 5.3: *Ultimate load capacity of the beam corresponding to different values of corrosion loss*

Years	Corrosion loss	Ultimate load(kN)	Perecentage reduction in ultimate capacity
1	0	104.24	0
11	0.0175	102.81	0.013
21	0.0615	99.13	0.048
31	0.128	93.89	0.099
41	0.215	86.70	0.16
51	0.318	78.12	0.25
61	0.432	68.97	0.33
71	0.554	58.32	0.44
81	0.678	46.34	0.55
91	0.798	35.50	0.65

For the resistance moment, a lognormal distribution has been fitted and the mean value is also reduced as the corrosion progressed as shown in Figure 5.8. For the no corrosion case, the resistance moment histogram is shown in Figure

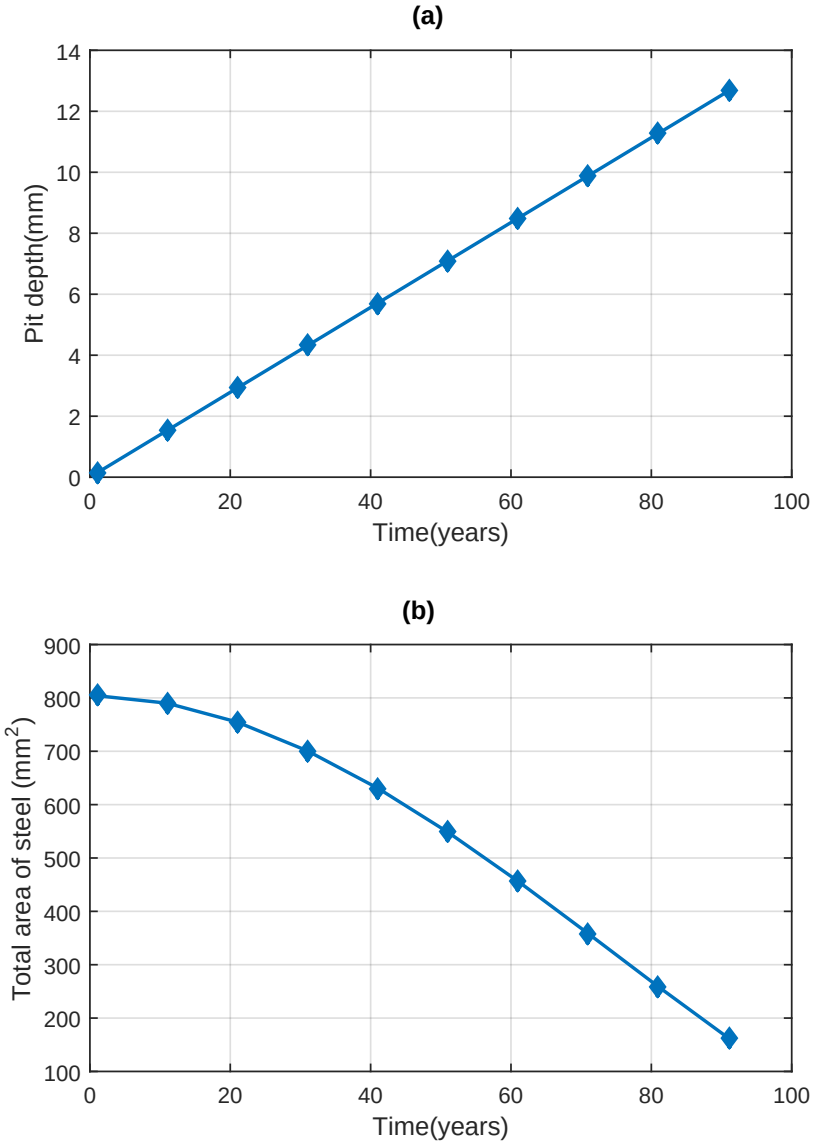


Figure 5.6: *Model of steel corrosion (a) Increasing of pit depth with the time; (b) Reduction of the steel cross sectional area due to pitting corrosion*

5.9, which shows that the mean value of the resistance moment is 176 kN.m with 9.1 kN.m standard deviation. Figure 5.10 demonstrates the effect of corrosion has on flexural strength capacity of the RC beam. The figure shows that with time the flexural strength of the beam decreases considerably. For example, after 51 years since corrosion initiation, the probability that the flexural resistance is less than 132 kN.m is around 50%. While for no corrosion case in the first year of the beam service life, the probability of getting a resistance moment less than 132

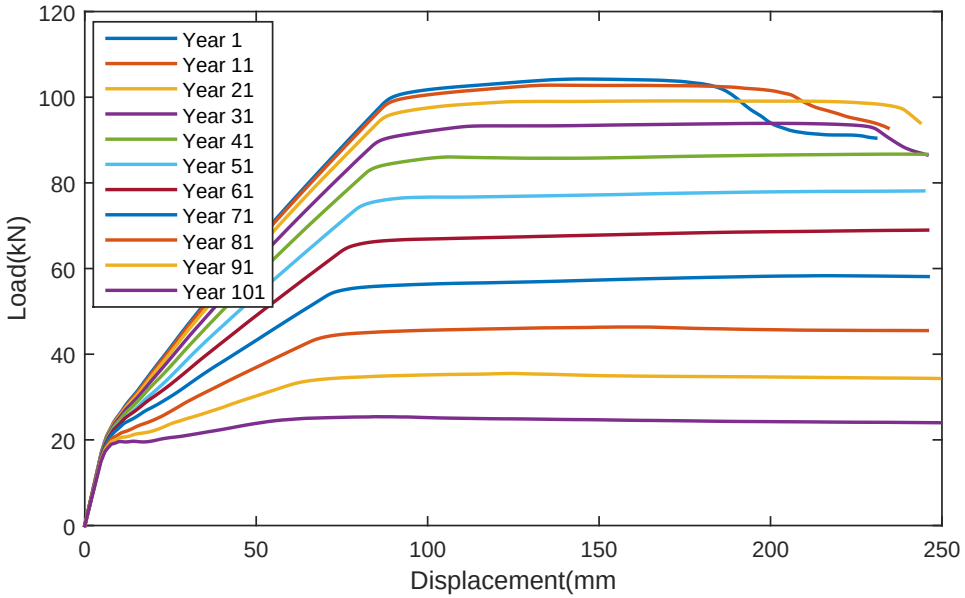


Figure 5.7: *Load displacement curves at each year. The figure shows the deterioration of beam ultimate load capacity over the years due to corrosion*

kN.m is zero. This indicates that corrosion has significant effect on the flexural resistance of the RC beams.

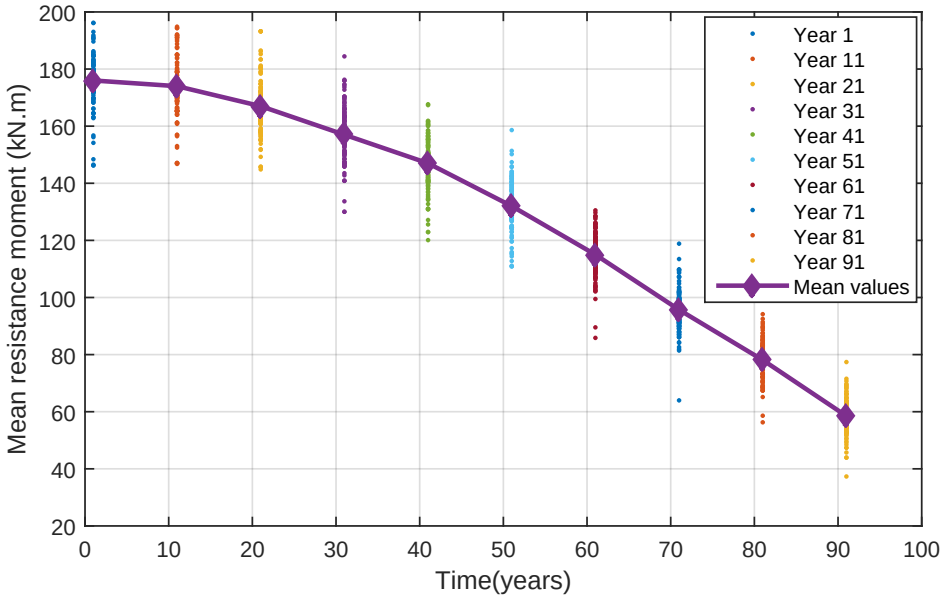


Figure 5.8: *Reduction of the resistance moment mean value with the time due to corrosion*

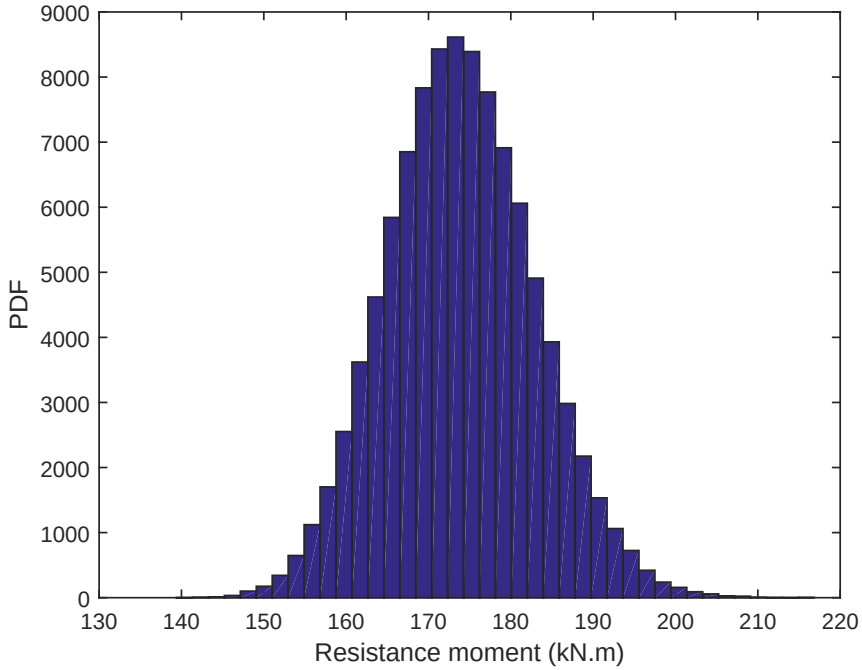


Figure 5.9: *Histogram of flexural strength for no corrosion case (t = 0)*

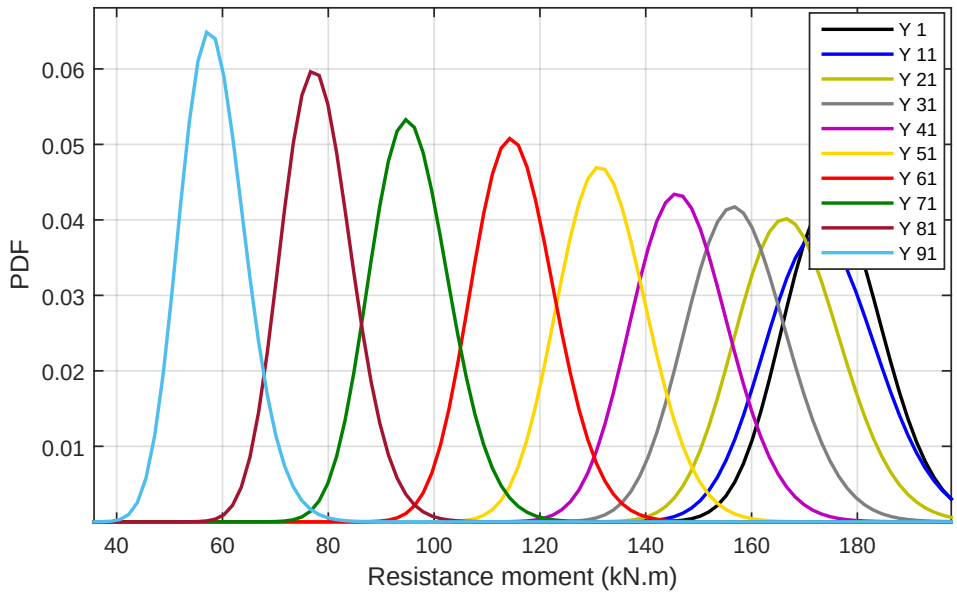


Figure 5.10: *The effect of corrosion on the distribution of the beam resistance moment along the years*

5.3.3.4 Probability of failure evaluation

After computing the resistance moment, the next step is to evaluate the probability of failure. As mentioned before, the probability of failure can be estimated using MCS by finding the ratio between the number of samples for which the

limit state function indicates failure to the total number of samples. However, the number of the generated samples in this study was small (150 samples) and accordingly, the direct estimation of the P_f will not be accurate and it might be underestimated by the results. Therefore, two methods have been used and compared in this study to estimate the P_f.

The first method is a combination between MCS and FORM analysis, while the second one which is proposed by Elhewy et al. (2006) is by training an ANN model (as described in Section 5.2.4) and connect it with the reliability methods (FORM or MCS). The following sections explain and show the details and results of the two methods.

- **MCS with FORM**

  In this method, at each time interval, the values of the resistance moments are used in conjunction with FORM analysis to estimate the limit state function and the probability of failure. According to Equation 5.6, the random variables that are considered in FORM method are the resistance moment (M_R), resistance model uncertainty (θ_R), permanent load (g), the variable load (q) and the load model uncertainty (θ_E).

  The initial design points representing the mean values of each random variable were set for the first iteration. After solving a constrained optimization problem, when the reliability index β converged, the design points and the limit state function will be obtained as described in Chapter 3. According to this approach, the reliability index and the probability of failure for each time interval are shown in Figure 5.11 *a* and *b* respectively. The results show that for the first year, when there was no corrosion, the reliability index was 3.45 which is lower than the target reliability index (β_T). The standard CEN (1990) recommends $\beta_T = 4.7$ for a one year reference period assuming no deterioration. That means the beam has not achieved the intended safety requirements since the reliability index is lower than the target one. This might be due to the absence of reinforcement at the top of the beam.

  The reliability index decreased from 3.45 in the first year to more than half this value after 60 years of the beam service life, and that looks reasonable comparing with the remaining area of steel after 60 years, which is also reduced by half due to the aggressive environmental condition used in this study ($i_{corr} = 3\mu.A/cm^2$).

  A reliability analysis should be accompanied by a sensitivity analysis. Figure 5.12 shows the direction cosines at the design points of the random variables as a function of time. The direction cosines of each variables gives

a measure of the impact that each random variable has on the estimated reliability index. The figure shows that the variable load (q) plays a fundamental role in the analysis with the largest sensitivity reaching -0.72 and exhibiting a reduction of its importance as the deterioration increase. This is followed by the resistance and load model uncertainties (θ_R and θ_E) with weights equal to 0.52 and -0.36 respectively. The influence of the resistance moment was insignificant for the first few years since the corrosion level was low, however, its importance increased considerably with the time as the corrosion level increase. The sensitivity coefficient of the resistance moment depends on the material properties and the corrosion rate.

- **ANN-based FORM**

  In this method, ANN models were prepared and used to predict the limit state function $g(X_i)$ and the probability of failure P_f that are obtained from the previous method. 10 ANN models (for each time interval) have been trained in this study. The ANN models are trained according to training data sets which include the input and the output (target) values. The training data sets considered in this study are represented by the 150 samples that are analysed using finite element analysis to get the limit state function. However, these training data sets should cover a sufficient number of samples to make sure that the network can approximate the function successfully in the entire domain. Therefore, the training data sets are prepared again by repeating the FEA for the beam with the same random variables, but increasing the standard deviation for each of them. That means, the variables that are considered in Table 5.2 are considered again with the same mean and twice their standard deviation (μ, 2σ).

  After the models have been trained, they will be connected with the reliability method (FORM) to predict the $g(X_i)$ and then P_f. The procedure that is used to tackle this method is as follows:

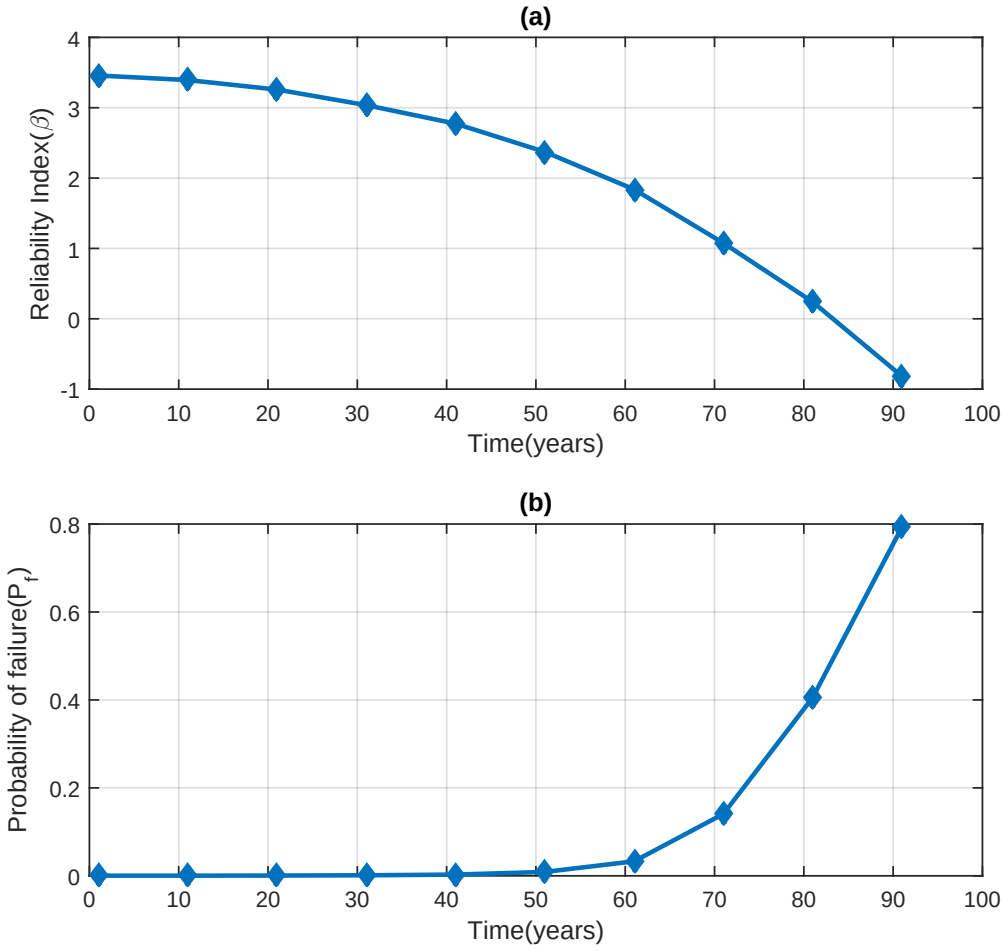


Figure 5.11: *(a) Beam reliability indices reduction along the years. (b) Beam probability of failure increasing along the years*

– *Establish ANN model*

To establish an ANN model two stages are needed: ANN model construction and ANN training and testing. In the first stage, the number of hidden layers and neurons number should be specified. Tarefder and Zaman (2005) stated that the accuracy of ANN depends on the network structure; however, there is no definite rule for choosing the hidden layers and the number of neurons at each layer. According to that, no rule has been depended in this study to select the number of hidden layers and neurons. Trial iterations were made to select the

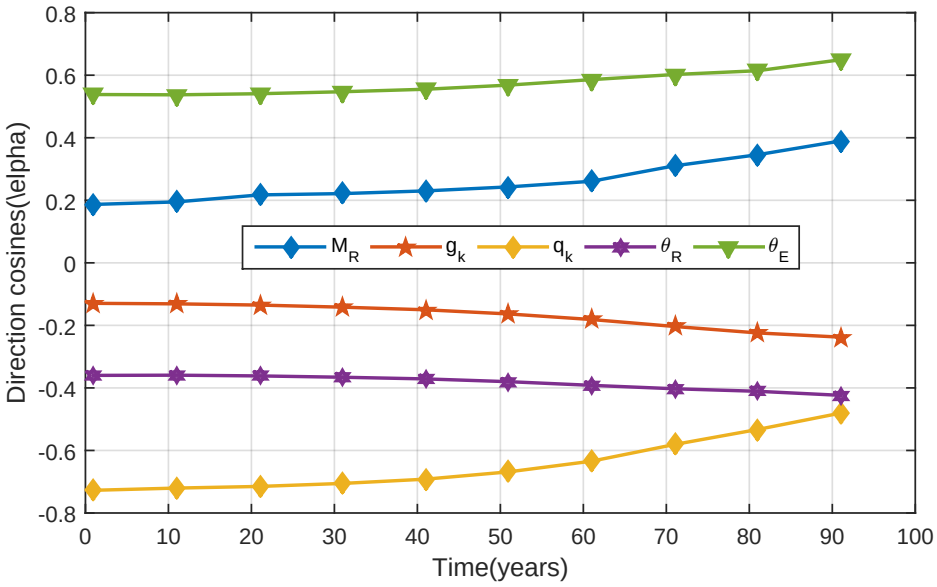


Figure 5.12: *Direction cosines at design points as a function of time*

suitable number of layers and neurons for the hidden layer. To begin with, one layer with 3 and 5 neurons have been used, however, good results were not achieved as shown in Table 5.4. Then, ANN model was built again with using two hidden layers with 3 and 5 neurons at each layer respectively. The results were worth noticing that a greater number of layers and neurons can increase the accuracy of estimating the probability of failure as shown in Table 5.4. The table shows that using two hidden layers with 5 neurons at each of them resulted in closer value of reliability index to the one that is obtained from FORM method. According to that, the structure of ANN model used in this study consists of one input layer with 5 neurons (5 random variables: M_R, g, q, θ_E and θ_R), one output layer with one neuron ($g(X_i)$) and two hidden layers with 5 neurons at each layer, as shown in Figure 5.13.

At the second stage (training and testing), the initial weight and biases are randomised. The models have been trained in this study us-

Table 5.4: *Estimated reliability index (β)*

Number of hidden layers	Number of neurons	β (NN) for year 1	β (FORM) for year 1	Difference(%)
1	3	3.63	3.45	4.7
1	5	3.50	3.45	1.2
2	3	3.55	3.45	2.6
2	5	3.45	3.45	2.90E-03

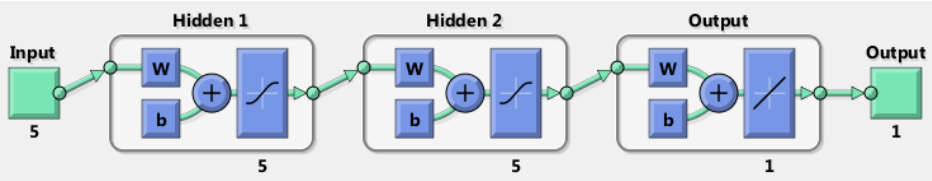


Figure 5.13: *Structure of ANN*

ing back propagation training algorithm which is a supervised learning algorithm that allows for training and adjusting the network by minimizing the error between the target and ANN output (as explained in Section 5.2.4). At each network training, the data set is processed many times as the connection weights and biases are adjusted by back propagation. At some desired level of accuracy, which can be evaluated by using an R^2 value and MSE, the training stops. R^2 represents the correlation factor between the target and the predicted values, while the MSE represents the difference between the desired and the predicted output. Therefore, a good prediction is achieved with higher value of R^2 and lower value of MSE.

In this study, 70% of the input and output data are used to train the model while 30% are used to test the model. Table 5.5 summarises the R^2 and the MSE for the ten trained ANN models. The best results are obtained with a very small MSE (near to zero) and a high R^2 (larger than 98%). According to this, the predicted limit state functions $g(X_i)$ by ANN are very close to the target or original values of $g(X_i)$ that are obtained from finite element analysis. Figures 5.14 to

5.23 show a comparison between the predicted and the original values of $g(X_i)$.

Table 5.5: *Performance of ANN model*

Years	R^2-Training	R^2-Testing	R^2-All data	MSE
1	1	0.99539	0.998	2.66E-21
11	1	0.99595	0.99878	1.52E-21
21	1	0.99571	0.99884	1.91E-21
31	1	0.99674	0.99923	1.29E-21
41	1	0.99651	0.99902	1.21E-21
51	1	0.99616	0.99884	4.977E-22
61	1	0.98834	0.99423	1.09E-21
71	1	0.99338	0.9977	1.09E-21
81	1	0.98516	0.99272	1.09E-21
91	1	0.99045	0.99744	5.54E-22

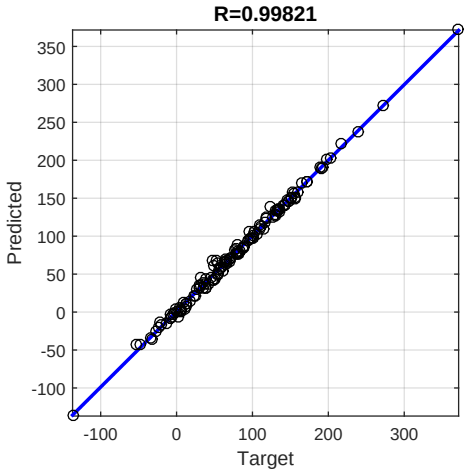


Figure 5.14: *Predicted and target limit state function (year 1)*

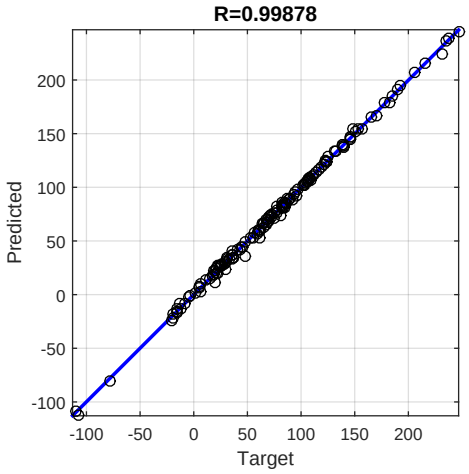


Figure 5.15: *Predicted and target limit state function (year 11)*

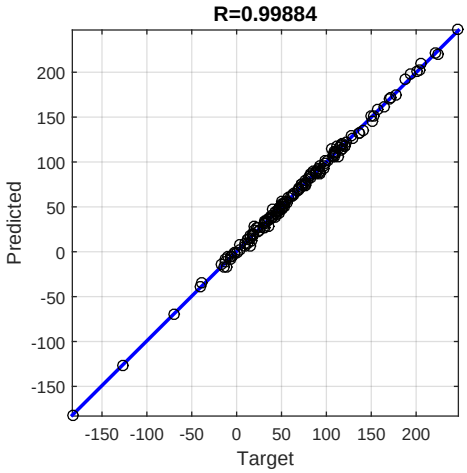


Figure 5.16: *Predicted and target limit state function (year 21)*

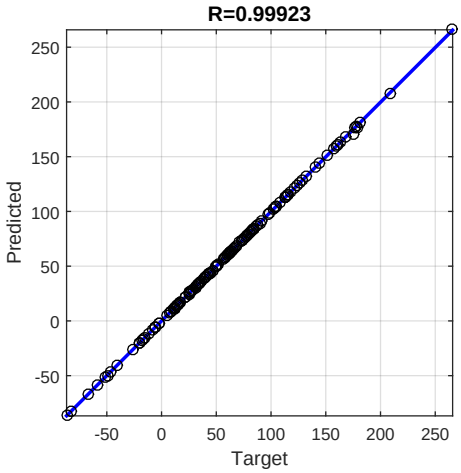


Figure 5.17: *Predicted and target limit state function (year 31)*

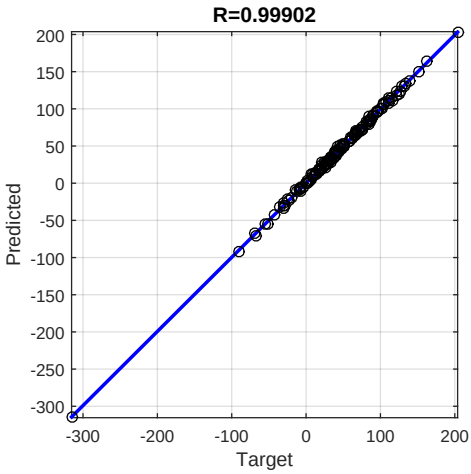


Figure 5.18: *Predicted and target limit state function (year 41)*

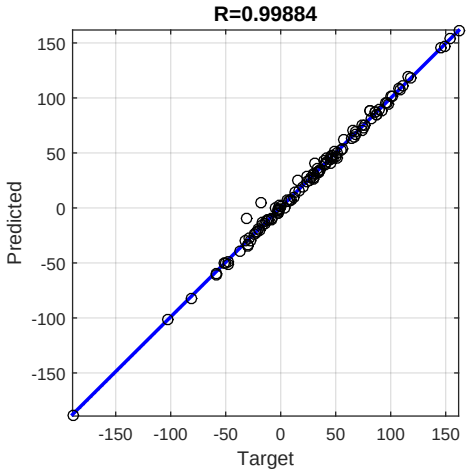


Figure 5.19: *Predicted and target limit state function (year 51)*

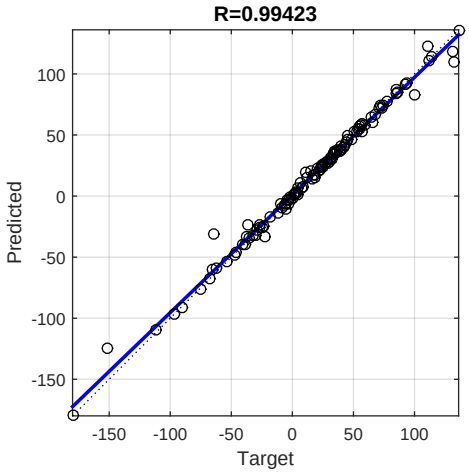


Figure 5.20: *Predicted and target limit state function (year 61)*

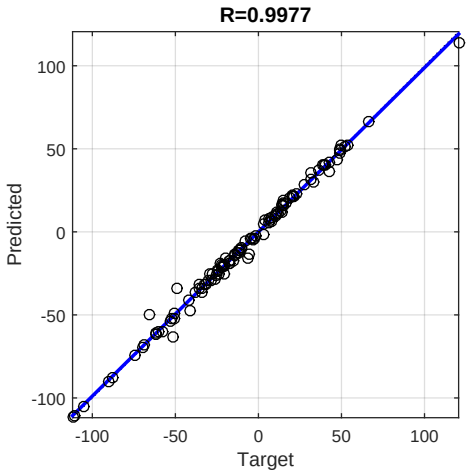


Figure 5.21: *Predicted and target limit state function (year 71)*

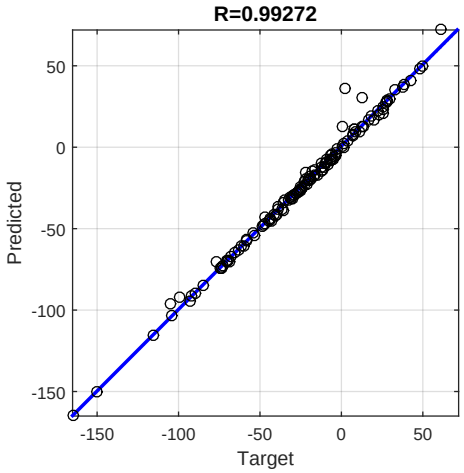


Figure 5.22: *Predicted and target limit state function (year 81)*

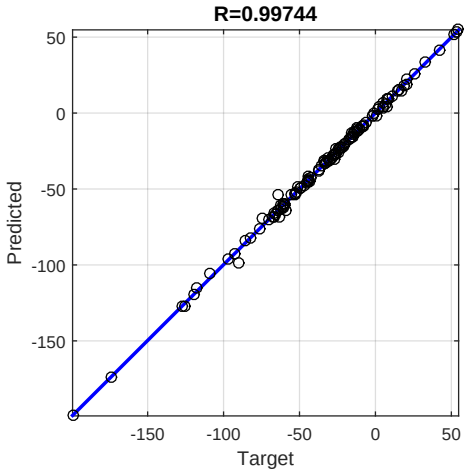


Figure 5.23: *Predicted and target limit state function (year 91)*

– *Linking ANN to reliability method (FORM)*

After all weights factors are fixed for the ANN models, they were linked to FORM method to estimate the probability of failure for each year and compare the results with that getting from the previous method (MCS and FORM). The simple way to link ANN with FORM is by setting the initial design points, the mean values of the random variables, at the first iteration. The trained ANN model will be called to estimate the limit state function at the given design point, then the calculation will be repeated until the reliability index converged as it is has been described in Chapter 3. Figure 5.24 shows the comparison

between the two methods. ANN-based FORM shows its efficiency to predict the probability of failure in which the results are very comparable between the two methods.

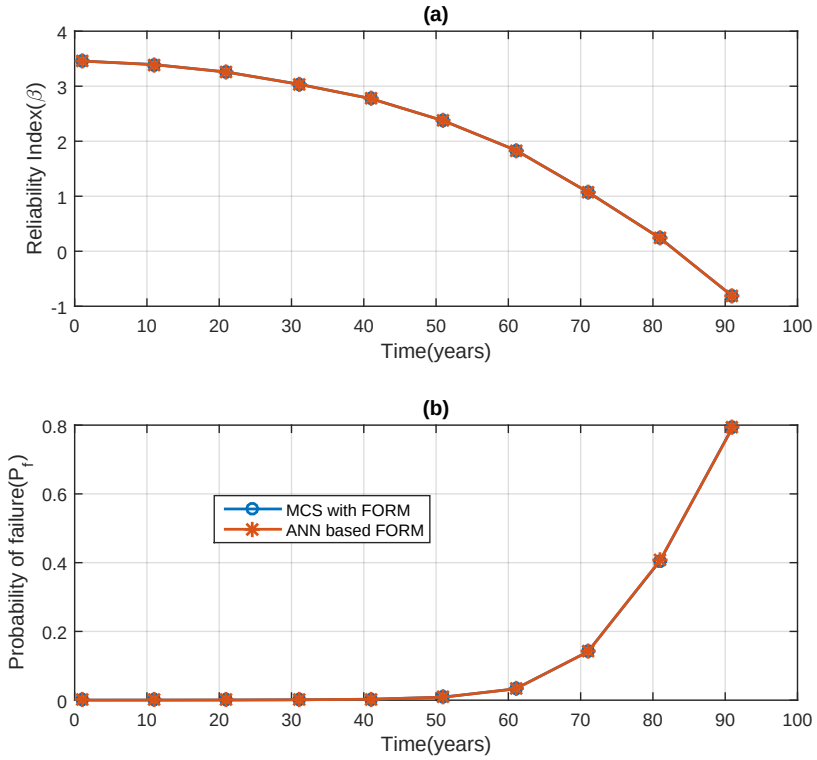


Figure 5.24: *Comparison between the two methods: MCS with FORM and ANN-based FORM: (a) Reliability index (b) Probabilty of failure*

5.4 Summary

This chapter presents an application of reliability analysis for a deteriorated simply supported RC beam with implicit performance function. As the beam is modelled in ABAQUS and the nonlinear analysis is numerically costly, applying reliability analysis will be exhausted and a time consuming process. Therefore, ABAQUS and MATLAB connection (using Python script file) has been exploited to produce a novel combined process which can speed up the reliability analysis. Two methods have been used to estimate the probability of failure: i) MCS with FORM and ii) ANN-based FORM. The two methods have been successfully es-

timated the reliability of the beam and they show a good agreement.

The presented method is suitable for applying reliability analysis of such events and it will be used for the case study in Chapter 7.

Chapter 6

Case study: Description and Structural Modelling

As the aim of this research is to establish a framework to assess the reliability of post-tensioned concrete bridges, a real case study, Ynys-y-Gwas bridge, will be considered in this chapter. To apply reliability analysis for this case study, the method proposed in Chapter 5 will be used. The proposed method in Chapter 5 consists of two parts i.e. finite element modelling and applying reliability analysis. This chapter deals with the first part which includes the description of the bridge and the method of modelling it in ABAQUS. The description of the bridge includes some general details, geometry, material properties and the cause of collapse.

6.1 Introduction

Pre-stressed concrete is widely used in different applications for structures such as bridges, buildings and long span floors where light weight is needed and to improve the performance in bending. The permanent state of tension for the pre-stressing wires can help to improve the inadequate tensile strength of concrete. Pre-stressed concrete structures are more stronger and lighter than ordinary re-

inforced concrete structures (Elfergani et al., 2013).

Concrete structures are exposed to aggressive environmental conditions that lead to corrosion of the embedded reinforcement and pre-stressing steel. During the 1980s, a significant number of post-tensioned concrete bridges had to be replaced in the UK because of corrosion of their tendons (Pearson-Kirk, 2014). In 1985, the most serious event happened in Wales when the single span segmental post-tensioned Ynys-y-Gwas bridge collapsed without warnings. Collapse of the bridge was due to the penetration of water and salts through the transverse joints and resulting longitudinal tendons corrosion (Woodward and Williams, 1988). In September 1992, the UK Department of Transport banned the construction of any new post-tensioned bridges with grouted duct until construction standards were improved. Although the moratorium was lifted in 1996, but there were still reservations about the corrosion protection of the tendons where they crossed joints and the moratorium still remains in place for precast segmental constructions with internal tendons (Woodward, 2001). Therefore, predicting of the safety of these types of bridges using reliability methods is very important to reduce the cost required for failure or maintenance, as well as, to determine the important time for monitoring and maintaining.

This chapter focuses on describing the details of Ynys-y-Gwas bridge and the method of modelling it in ABAQUS. The main cause of failure of this bridge was corrosion of tendons, making it a relevant case study to evaluate the effect of corrosion on bridge safety.

6.2 Ynys-y-Gwas bridge details

6.2.1 General details

The Ynys-y-Gwas bridge was a single span segmental post-tensioned structure. It was constructed in 1953 and collapsed in December 1985. The bridge was located in South Wales and carried an unclassified road over the river Afan approximately

6 km upstream from Port Talbot (Woodward and Williams, 1988).

The bridge was on one of the local primary gritting routes and despite its low classification, it was heavily used. However, the loads were designed according to HA loading to ensure that they do not exceed the maximum allowable normal traffic in the United Kingdom.

The bridge was inspected regularly including soffit and foundation examination and there were no warning signs that the bridge might collapse, such as beam deflections, cracking or rust staining (Woodward and Williams, 1988). Furthermore, there were no unexpected observations when 50 tonnes of concrete beams passed over the bridge.

6.2.2 Bridge geometry and material properties description

The bridge was simply supported with 19.6 m length and a clear span of 18.3 m. The cross section of the bridge shows that it composed of nine longitudinal I-beams, two box edge beams and two 1.52 m slabs spanned the gap between the I-beams and edge beams as shown in Figure 6.1. The beams consisted of eight segments, with 2.45 m length (see Figure 6.4), post-tensioned together longitudinally and transversely with Freyssinet tendons in-situ. Each tendon has twelve wires with 5 mm diameter. Five tendons were used to post-tension the I-beams while ten were used for the edge beams. The tendons had a parabolic profile, starting from different levels near the supports and then they had the same level at the mid span of each beam as shown in Figure 6.2.

The beams were 0.915 m deep and 0.61 m wide. The slabs were also made up of eight segments but were not pre-stressed in the longitudinal direction.

The transverse tendons ran through the top and bottom flanges of each I-beam at the diaphragms and near the anchorages and through the top flange near the center of each segments (see Figure 6.3). The top transverse tendons were an-

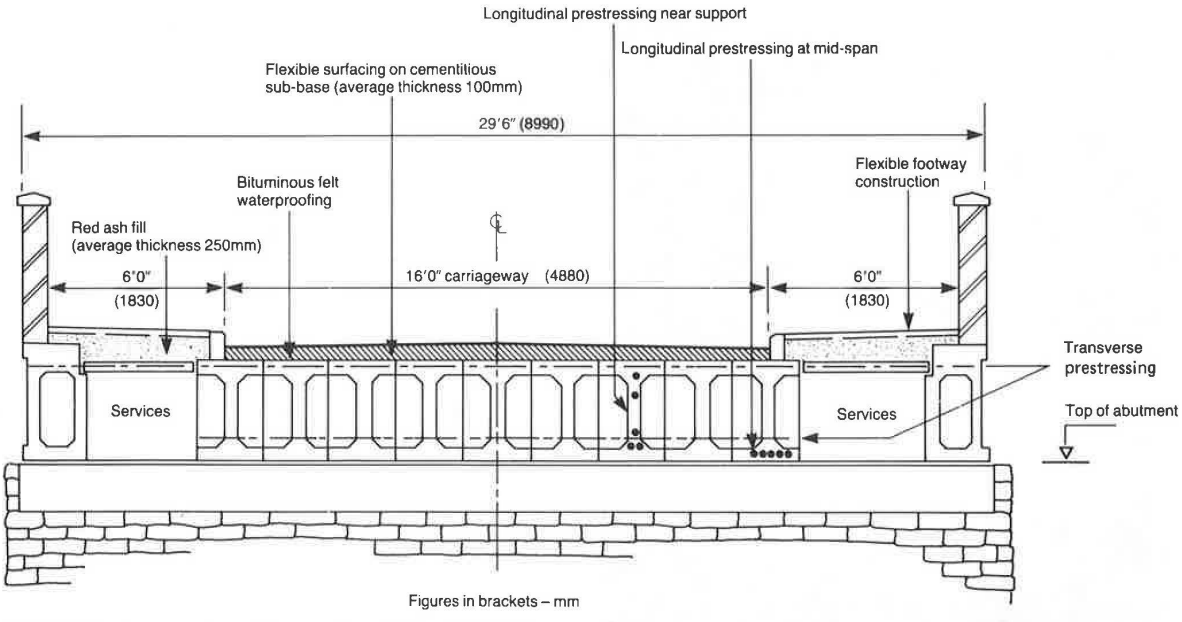


Figure 6.1: *Cross section of the Ynys-y-Gwas bridge (Woodward and Williams, 1988)*

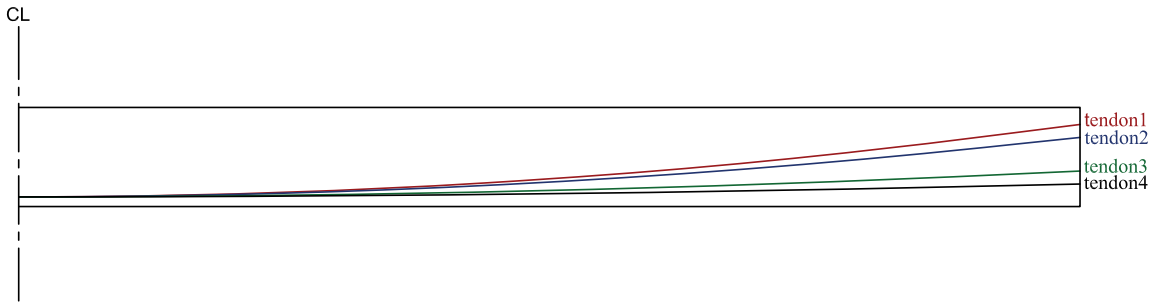


Figure 6.2: *The longitudinal tendons profile in each precast beam*

chored to the edge beams while the bottom ones were anchored in the outer I beams.

The transverse joints (25 mm) were filled with mortar cement before post-tensioning and the longitudinal ducts that were passed through the joints were covered with cardboard to prevent grout leaking out of the cable ducts at the joints. The longitudinal joints (19 mm) were not filled with mortar but asbestos has been inserted at the transverse pre-stressing tendons to soften the face to face contact and seal the ducts to facilitate grouting (Woodward and Williams, 1988).

The mix of concrete in the precast units was 1 : 1.5 : 3, which represents the ratios of cement, sand and aggregate respectively (Kaylor, 1954). The character-

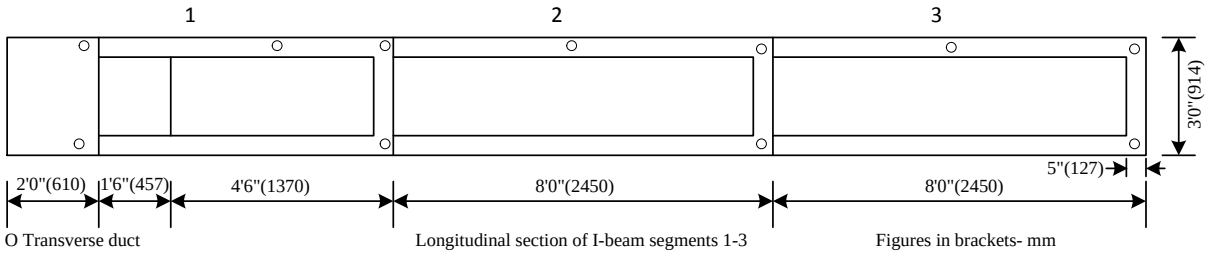


Figure 6.3: *Longitudinal section of I-beams, segments* $1-3$ *(Woodward and Williams, 1988)*

istic compressive strength of concrete cube at 28 days was 50 MPa and the high tensile steel used had an ultimate tensile strength of 1600 MPa (Kaylor, 1954). The preliminary prestress in the wire was 1000 MPa and an allowance of 20% was made for the short and long term losses, as will be discussed in Section 7.2. The tensioning of the cables was carried out on opposite banks simultaneously and each cable was tensioned separately. The cable diameter was 17.32 mm and the cable ducts were 50 mm.

After completing the tensioning of the tendons, grout was injected into the cable ducts using a mechanical air compressor. Three different mixes of grout were tried. The first mix consisted of a wet mix of cement while the second mix was a creamy mix of cement and sand with ratios of $1:1$ respectively. The two mixes was not satisfactory because the first one caused leakage from the joints while the second caused blockage in the ducts. Therefore, the third mix was used which was similar to the second mix, but using half the amount of sand (Kaylor, 1954).

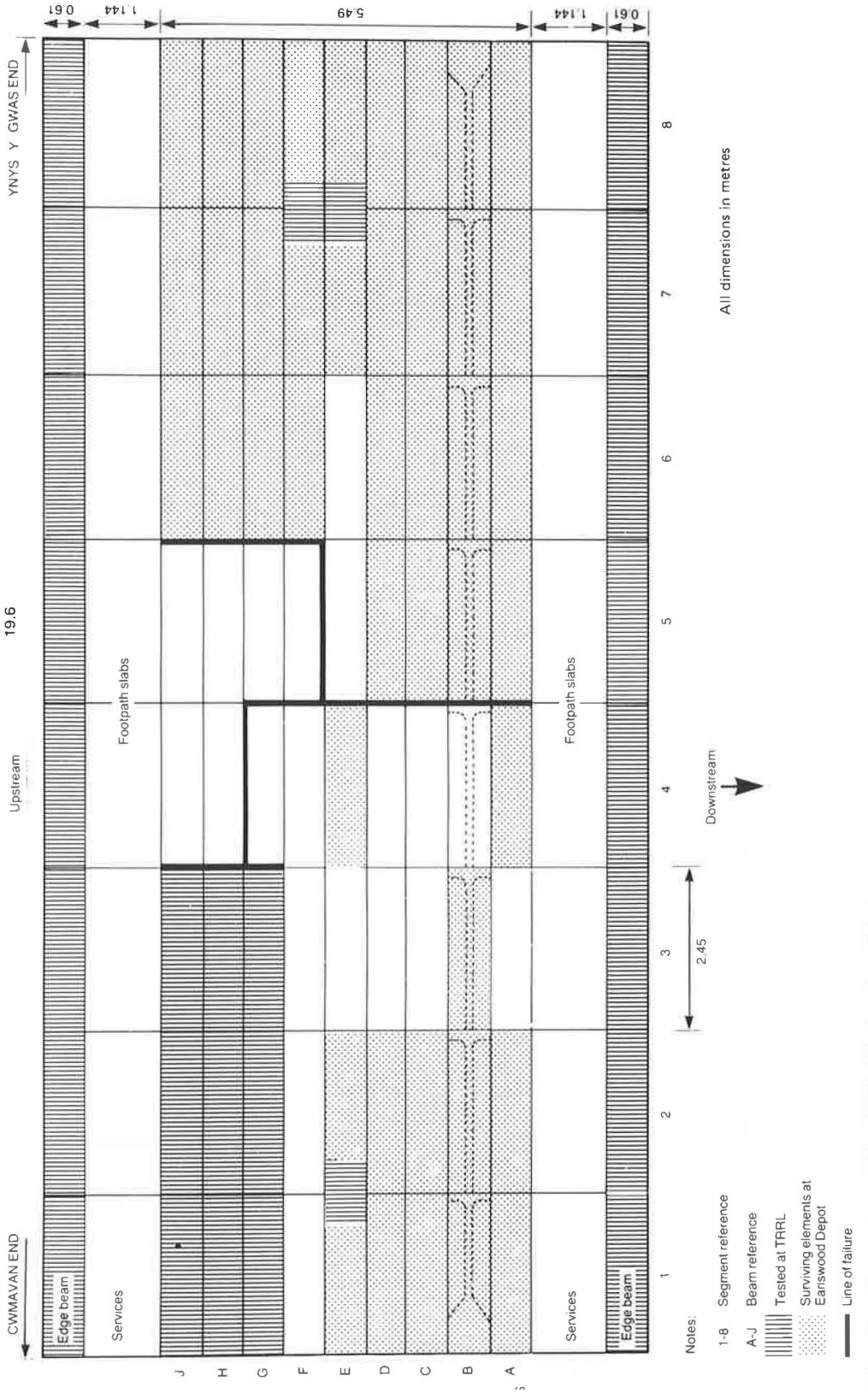


Figure 6.4: *Ynys-y-Gwas bridge, plan view of deck (Woodward and Williams, 1988)*

6.2.3 Bridge collapse

The bridge deck collapsed when there was no traffic load on it. As shown in Figure 6.5, all beams failed. Some of bridge segments were taken to the Transport and Road Research Laboratory (TRRL) (see Figure 6.4) in order to examine the condition of the beam and identify the cause of collapse (Woodward and Williams, 1988). After the inspection, it was found that the major cause of the bridge collapse was the severe localized corrosion of the tendons at the longitudinal and transverse joints due to the penetration of chloride. The severe corrosion lead to high reduction in tendon area near the joints (see Figure 6.6) and the bridge collapsed when it could no longer carry the permanent load. The high reduction in tendons area leads to reduce the pre-stressing force and subsequently reducing the capacity of the bridge.

According to Woodward and Williams (1988), the severe corrosion of tendons near joints resulted from several factors:

- The bad protection near the joints where most tendons near the transverse joints were surrounded with cardboard (see Figure 6.7) which provided a poor protection. Furthermore, the asbestos that was positioned between beams along the longitudinal joints, offered a damp environment around the transverse ducts and acted as a sponges soaking up any moisture that penetrated the waterproofing layer.

- The absence of an in-situ reinforced concrete deck slab that caused an increase in the chloride penetration through joints.

- Bridge location near the river that provided a damp environment.

- The poor grouting that increased the likelihood of corrosion along the length of tendons near the joints.

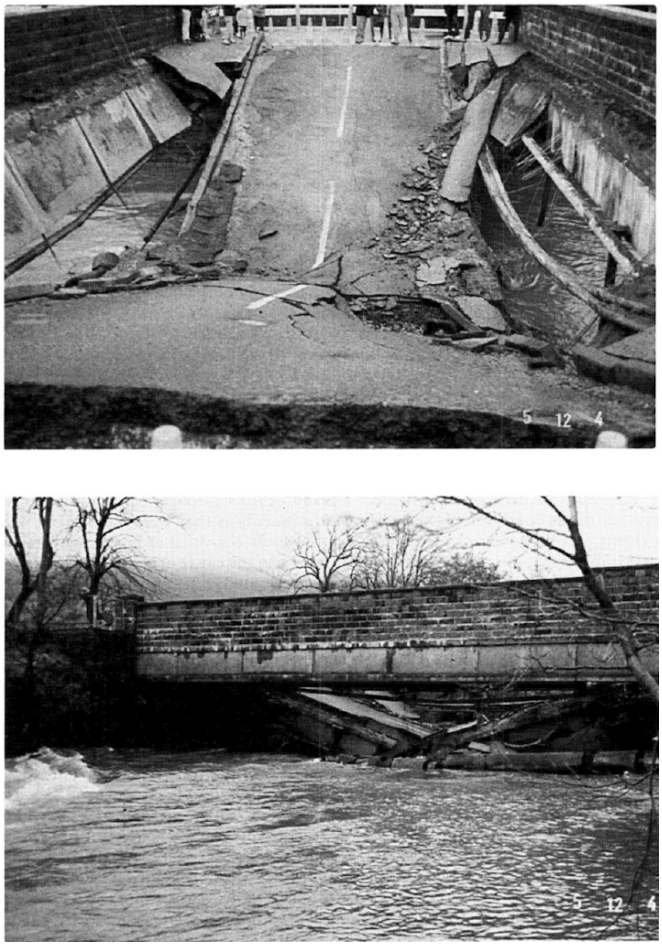


Figure 6.5: *The top and side view of Ynys-y-Gwas bridge collapse showing the failure of all the beams (Woodward and Williams, 1988)*



Figure 6.6: *Tendon localized corrosion near joints (Woodward and Williams, 1988)*



Figure 6.7: *The cardboard tube that has been seen around the longitudinal tendons accross the transverse joints (Woodward and Williams, 1988)*

6.3 3D-non-linear finite element modelling

In this section the details of modelling the bridge will be described. This will include the geometry, material, steel element mesh size, load application and the bond-slip model.

6.3.1 Beam modelling

As described in Section 6.2.2, the bridge consisted of nine internal beams. In this study, the most loaded beam was used to model the bridge, reducing the computational time required for finite element analysis. The beam was simply supported with a clear span 18.3 m, consisting of eight segments post-tensioned together by five curved tendons. Because of the post-tensioning, the eight segments behave as one segment and therefore, the beam was modelled in ABAQUS as a one segment with five curved tendons as shown in Figure 6.8. The concrete beam was modelled using Solid elements C3D8R with reduced integration to avoid shear locking when element is under bending as explained in Section 4.5.3.

The five tendons were modelled with beam elements B31 with circular cross sec-

tion and diameter of 17.32 mm. Each beam element contained two nodes and used a linear shape formulation.

Four elastic steel plattens have been used near the load and support positions to provide a stiff area to distribute loading and to avoid stress concentration. These plattens were modelled as solid elements with elastic material properties (Young's modulus and poisson's ratio of 200 GPa and 0.3 respectively). Tie constraint are used to define the fully constraint contact behaviour between elastic steel plattens and concrete beam.

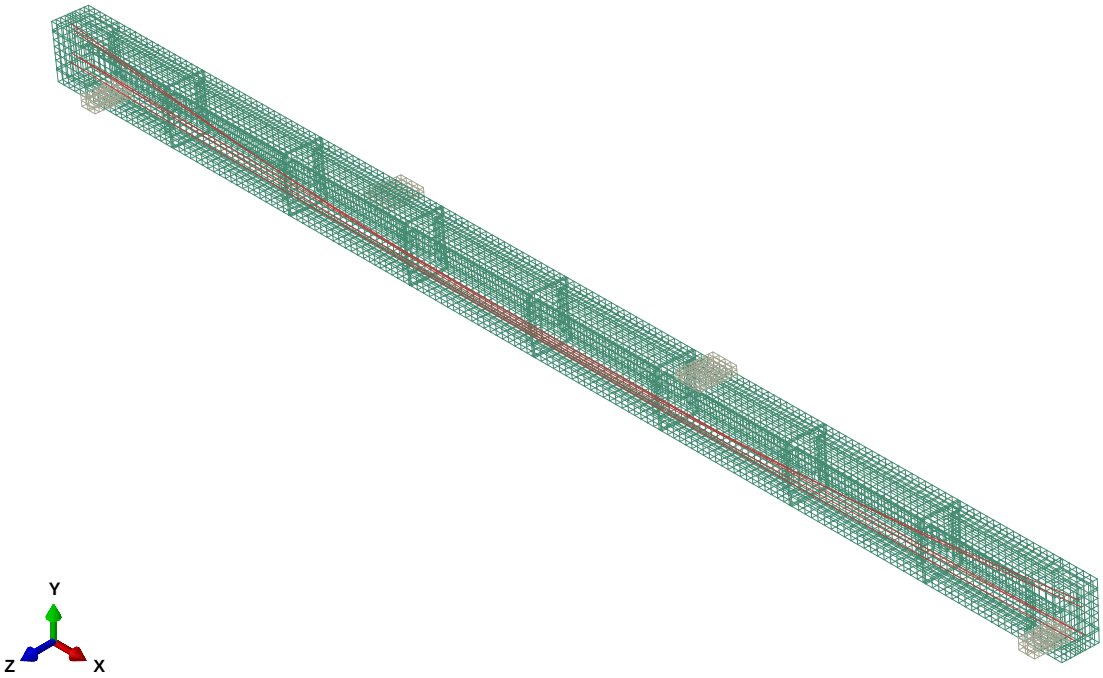


Figure 6.8: *3-D finite element model of the concrete beam with the five curved tendons*

6.3.2 Material models

Concrete

The concrete behaviour in tension and compression has been modelled using the concrete damage plasticity model described in Chapter 4. The concrete in tension and compression are modelled by following the equations of Eurocode2 (Eurocode-2, 2004) explained in Sections 4.2.1 and 4.2.2. Figures 6.9 and 6.10

show the stress strain relationship of concrete in tension and compression. Figure 6.10 shows that the last point in the softening part of the tensile stress curve has been taken as 30% from the maximum tensile stress to avoid any convergence problem.

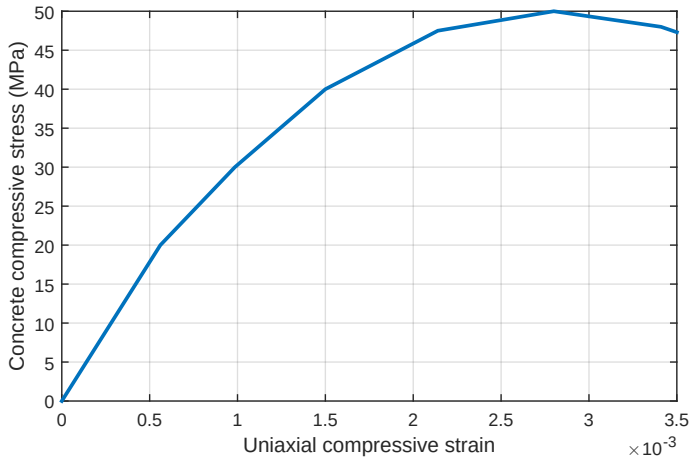


Figure 6.9: *The uniaxial compressive model of concrete that is applied in this study for the Ynys-y-Gwas bridge according to Eurocode-2 (2004)*

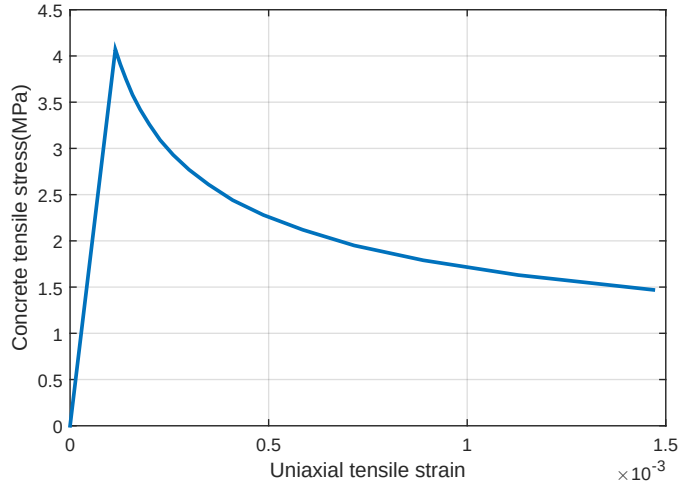


Figure 6.10: *The uniaxial tensile model of concrete that is applied in this study for the Ynys-y-Gwas bridge according to Eurocode-2 (2004)*

Pre-stressing steel

The pre-stressing steel is modelled by an idealized bilinear stress strain curve as shown in Figure 6.11 with Young's modulus of 200 GPa. The yield stress was taken as 1440 MPa, poisson's ration was specified as 0.3, as is usual for steel. After yielding, a hardening law was used up to the ultimate stress 1600 MPa and 5% ultimate strain.

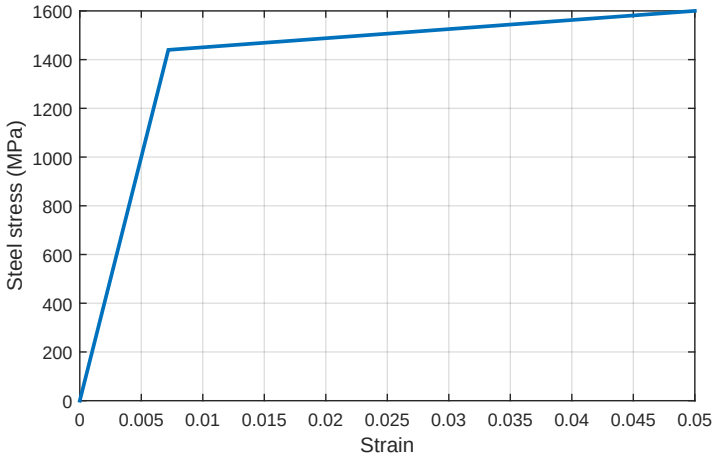


Figure 6.11: *Prestressing steel stress strain relation considered in this study for the Ynys-y-Gwas bridge*

6.3.3 Element mesh size

As mentioned in Section 6.2.3, the bridge failed due to the severe pitting corrosion near the joints. Hence, the spatial variability of tendons pitting corrosion has been considered near joints. The spatial variability of pitting corrosion was considered following the proposal of Stewart (2004). This method depends on subdividing the reinforcement bar into several segments with equal lengths (see Figure 6.12) known as the uniform capacity length (L_u). This length refers to the distance along a structural member in which localized corrosion will have a harmful effect on structural capacity. The uniform capacity length represents the element length in finite element analysis.

The tensile capacity of these segments will be reduced due to pitting corrosion

and this reduction can be calculated, according to Du et al. (2005) as:

$$f_y = (1 - 0.005\eta) f_{y0} \tag{6.1}$$

where f_{y0} is the yield stress of an uncorroded reinforcing bar and η is the percentage of corrosion loss.

The uniform capacity length depends on several factor including the ability of corroded reinforcement steel to redistribute stresses to the adjacent reinforcement, the mechanical behaviour of reinforcement, the development length of reinforcement and the geometry of reinforcement. Stewart (2012) reported that

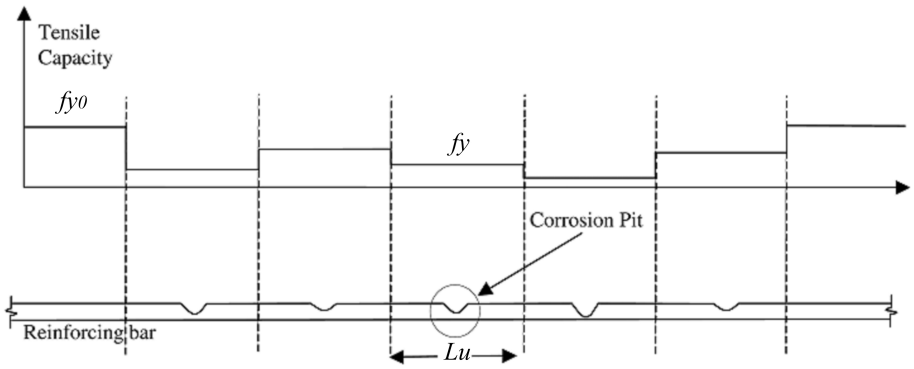


Figure 6.12: *The uniform capacity length L_u and the spatial capacity of corroded reinforcing bar (Stewart and Al-Harthy, 2008)*

the phenomena of the uniform capacity length, L_u, is incomplete and needs for further research since the recent reliability studies assumed the uniform capacity length varies between 100 and 1000 mm. According to Vu and Stewart (2005), the size of elements (L_u) should be chosen properly, not too large to avoid underestimation of spatial variability or too small to avoid the numerical instabilities. Therefore, in this study different finite element length of the tendons (100 to 1000 mm) have been used to select the optimal discretized element. The results show that for L_u less than 400 mm, the analysis suffered from convergence problems, which may be due to the small transmission length which is insufficient to transfer the tensile forces from steel to concrete. For the remaining element sizes, the ultimate capacity of the beam with each element size used was compared with

the theoretical calculations as shown in Figure 6.13. The analytical calculations were performed according to Figure 6.15 and the following equations:

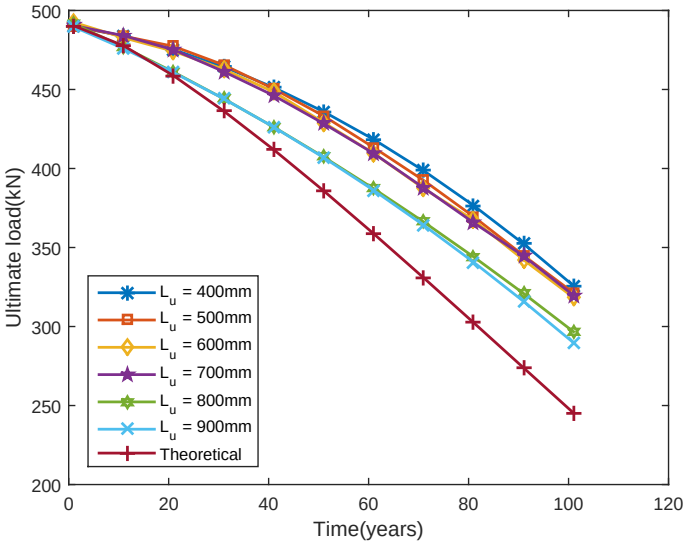


Figure 6.13: *Effect of using different values of uniform capacity length (steel element size) on the ultimate capacity of Ynys-y-Gwas bridge. The figure shows that using element length with 800 and 900 mm provides the closest solutions to the theoretical calculations*

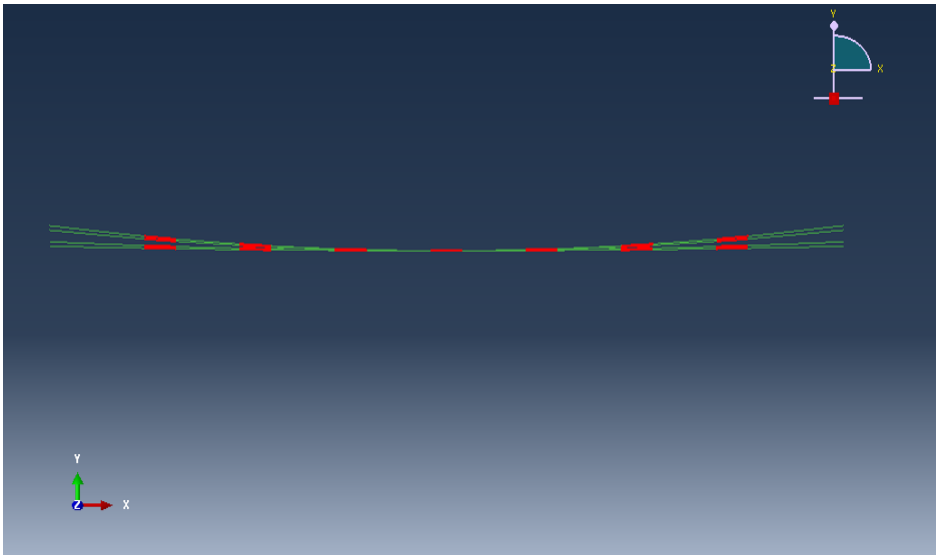


Figure 6.14: *Distribution of pitting corrosion along the tendon modelled in ABAQUS. The figure shows the corrosion is assumed to be within the elements near the joints*

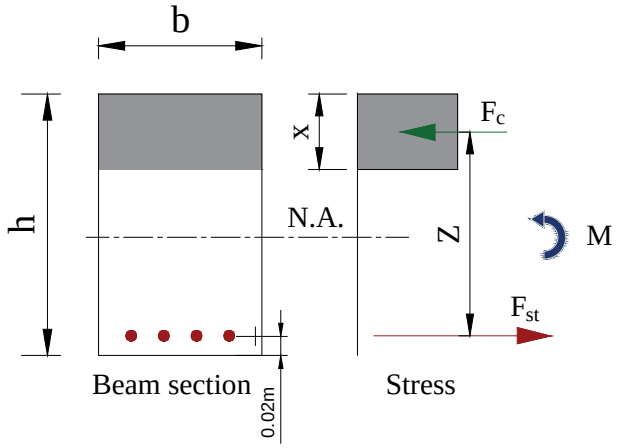


Figure 6.15: *Beam section and stress*

$$x = \frac{A_s.f_y}{0.85bf_c} \tag{6.2}$$

$$z = d - \frac{x}{2} \tag{6.3}$$

$$F_c = f_c.b.0.8.x \tag{6.4}$$

$$F_{st} = A_s.f_y \tag{6.5}$$

$$M = F_c.z \tag{6.6}$$

Notting that, this analytical calculations is a simplified method used fro pre-stressed members, since these equations (Equations 6.2 to 6.6) are usually used for reinforced concrete members. Figure 6.13 shows that the calculated values of the ultimate load are similar to the finite element results for the first year when the corrosion loss is very small (near to zero). As the corrosion increase, the calculated values become smaller and the differences become larger. This difference can be mainly attributed to the simple theory which can not simulate the complete 3D non-linear behaviour. In addition, for finite element analysis the corrosion is assumed to be near the joints only and the remaining parts of tendons did not suffer from corrosion. Therefore, the ultimate loads are higher than those resulting from the assumption in the analytical calculations.

According to Figure 6.13, using L_u equal to 800 and 900 mm results in better convergence between the non-linear model and the analytical solution. Therefore, the tendon element length used in this study was 800 mm and the corrosion is assumed to be within the elements near the joints as shown in Figure 6.14.

6.3.4 Modelling the boundary conditions

According to Woodward and Williams (1988), the bridge was a simply supported segmental post-tensioned deck. Therefore, hinge and roller boundary conditions were applied at the two ends to restrain the beam model and to measure the reaction forces. The pre-stress has been modelled by applying initial stress, using Initial Condition in ABAQUS, to the tendons before any solution step. This is followed by a static analysis step (equilibrium step before any actively load) to simulate the pre-stressing release. The losses of pre-stress have been considered at each element of pre-stressing steel as will be explained in Section 7.2.1. The beam is then tested using four point bending by applying vertical displacement.

6.3.5 Bond-slip model

The bond between steel and concrete in ABAQUS can be represented with various methods such as constraints, contact elements and connector elements. As a type of constraint, the embedded region can be used to simulate the full bond condition, because it assigns the same displacements to the concrete nodes. However, the full bond condition does not represent the actual case because the accumulation of corrosion products around the steel will lead to reduce bond. Moreover, the expansion of corrosion products will lead to stress the concrete which leads to concrete cracks and subsequently bond reduction. Accordingly, the stiffness and strength of concrete will be reduced causing damage to the structure. Therefore, in this study, the bond strength reduction due to corrosion was analysed for the first time in post-tensioned concrete beams.

Han et al. (2007) and Mohammed and Osman (2013) simulate the behaviour of

bond in ABAQUS using surface-to-surface contact element. This element defines the friction between the two surfaces. However, this tool can be used to model contact between two surfaces only such as two blocks moving relative to each other. Therefore, this tool can be used when both steel and concrete are modelled with solid element. In this study, the five tendons were modelled using beam elements which have simple geometry, each element contained two nodes, with one dimensional line element. Therefore, there is no surface generated for tendons and subsequently, surface-to-surface contact element can not be used in this study. Alternatively, for this modelling technique, especial elements must be placed at the interface between the two materials to represent the bond mechanism. Connector elements are available for two, CONN2D2, and three, CONN3D2, dimensional analysis; the connector elements for three dimensional analysis have been used in this study. A connector element can define a connection between two nodes (ABAQUS, 2013). The stiffness of a connector element is based on a force displacement relationship that makes it suitable to simulate bond slip behaviour, which is stress versus displacement as will be explained in Section 7.2.5. Connector elements have a relative displacement and rotation referred to a component of relative motion (CORM). For the three dimensional case, the connector element has six relative motion components: three displacements and three rotations (ABAQUS, 2013).

There are different types of connections that can be used to define a connector element in ABAQUS, axial, hinge, link, beam, rotation etc.. In this study, connector element of type Cartesian-Rotation has been used in which the six relative motion components (U1, U2, U3, UR1, UR2, UR3) are available. The Cartesian connections do not impose kinematic constraints, but define three local directions at node a and measure the change in position of node b along these local coordinate directions as shown in Figure 6.16a. The Rotation connection is a finite rotation connection where the local directions at node b are parameterized relative to the local directions at node a by the rotation vector ϕ as shown in Figure 6.16b.

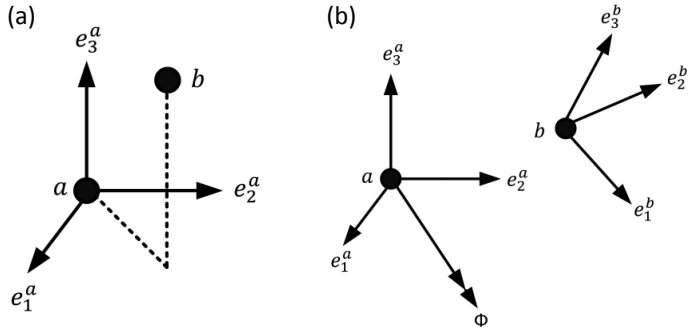


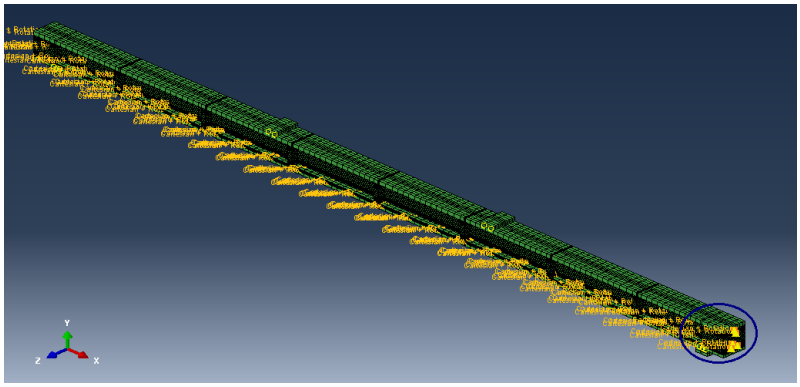
Figure 6.16: *Connector element type: (a) Cartesian and (b) Rotation (ABAQUS, 2013)*

To model connectors, one or more point-to-point wire features on assembly must be defined. In ABAQUS, the wire features were used to connect the node pairs with a straight wire at the interface between concrete and steel along the length of the steel reinforcement, as shown in Figure 6.17. So that, the two materials can have a relative movement in all directions.

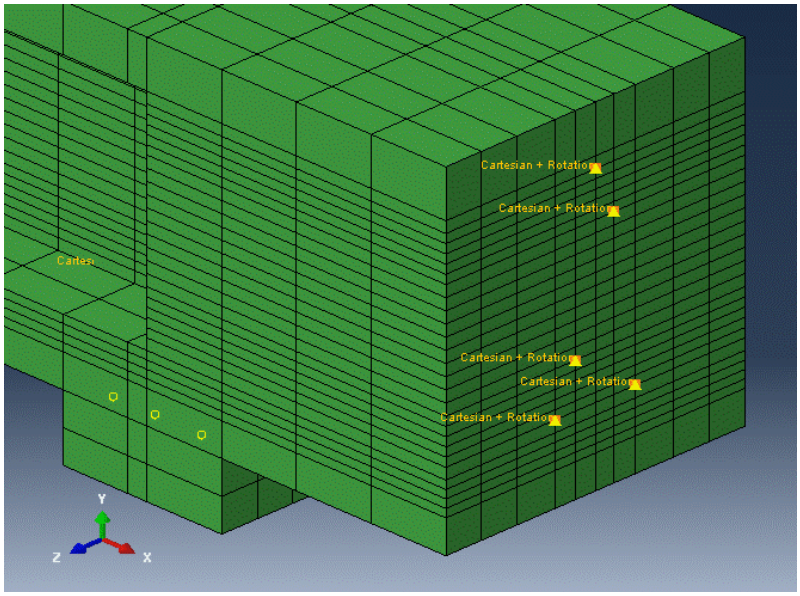
In addition to the connecting capabilities described above, various specific connector behaviours can be defined in connector element in ABAQUS. For instance, according to ABAQUS (2013), the user can define a spring-like elastic behaviour, damping, friction, plasticity, damage and other diverse behaviours associated with the available components of relative motion.

The mathematical bond-slip relationship proposed by Haskett et al. (2008), was used in this study. The plasticity behaviour of connector element has been used in this study to define the bond-slip relationship. The plasticity behaviour can be defined in terms of force (f) and the constitutive motion (u) corresponds to the plastic relative motion (u^{pl}). To define connector plasticity in ABAQUS, the elastic behaviour of the connector need to be defined first by inputting its stiffness. According to that, by defining the elastic and plastic behaviour of connector element, the plastic deformation with the degradation portion can be simulated as will be described in Section 7.2.5.

The simulation of bond deterioration with the time using connector elements can release the model from some convergence problems in ABAQUS, rather than us-



(a)



(b)

Figure 6.17: *Connector elements in the finite element model*

ing an alternative method. The alternative method that have been used (before using connector elements) was the using of the equivalent stress-strain constitutive law for embedded reinforcement (de Terán and Haach, 2017). This method is based on considering the bond-slip behaviour derived from the interpolation of the Model Code (CEB, 1992) bond-slip model, and can be employed using finite element models with embedded reinforcing bars. However, using this method causes some convergence problem in ABAQUS when the corrosion loss increases.

6.4 Summary

This chapter presents the details of Ynys-y-Gwas bridge with regards to its geometry, material properties and the cause of collapse. The chapter also introduces the numerical approach used to simulate the bridge in ABAQUS. The modelling approach depends mainly of what has been explained in Chapter 4 regarding the the consideration of the non-linear behaviour of concrete using concrete damage plasticity model (CDP) in ABAQUS.

Next chapter will focus on applying reliability analysis for the considered bridge depending on the modelling that has been done in this chapter.

Chapter 7

Case study: Reliability analysis and results

In Chapter 6, the numerical model of Ynys-y-Gwas bridge has been developed. This chapter will present the reliability analysis methodology of the considered bridge. Preliminary calculations regarding to the deterioration process of the bridge have been presented first. Then, the procedure of applying time dependent reliability analysis will be explained with the considered limit state function and the relevant random variables. Three cases have been examined and compared: i) assuming no deterioration due to corrosion and bond loss, ii) deterioration due to corrosion only (assuming full bond), iii) deterioration due to corrosion and bond loss. This chapter also presents a parametric study to investigate the impact of increasing corrosion on the reliability of the bridge and the bond degradation. Finally, the results will be presented.

7.1 Introduction

This chapter focuses on applying reliability analysis to Ynys-y-Gwas bridge that has been numerically modelled in Chapter 6. Uncertainties associated with material properties, geometry, loads and corrosion parameters are taken into account.

The probabilistic models of the uncertainties are combined with the non-linear finite element analysis to study the effect of pitting corrosion of the tendons on the post-tensioned concrete bridge. The limit state function considered is flexural strength. The proposed method in Chapter 5 (ABAQUS and MATLAB connection) is used in this chapter to reduce the time required for applying reliability analysis. Monte-Carlo simulation method is used to compute the statistical properties of the moment of resistance. Finally, FORM method has been applied, based on MCS results, to estimate the bridge probability of failure during its service life.

7.2 Preliminary calculations

Before applying reliability analysis, there are some important variables that are need to be prepared first. These variables include e.g. the losses of pre-stressing force ,$\Delta P(x,t)$, time to corrosion initiation, t_i, progress of chloride concentration with the time, $C(x,t)$, pitting factor, R, corrosion level with the time, η, load on bridge and the bond stress-slip relation ship. All these variables are required to simulate the actual behaviour of the bridge. The following subsections include the explanation of these variables preparation.

7.2.1 Prestress losses

The pre-stressing force is the main variable in pre-stressed concrete application and it should be kept throughout the life of the structure. However, the jack gauge reads some drops in the pre-stressing force, which are termed as the losses in pre-stress. The pre-stress force losses can be classified into two categories: immediate and time dependent losses. The immediate losses happen during the pre-stressing of the tendons and force transfer to the concrete at time t_o and vary along the length of the tendon. They represent the difference between the jacking force P_j and the remaining pre-stress force immediately after transfer at distance

x from the active end of the tendon $P_{mo}(x)$. The immediate losses include elastic shortening, friction and drawn in of the anchorage; these losses can be expressed according to Equation 7.1.

$$\Delta P_{immediate} = P_j - P_{mo}(x) \tag{7.1}$$

The time dependent losses occur over time during the service life of the pre-stressed member. They represent the difference between the remaining pre-stress force after immediate losses ($P_{mo}(x)$) and the final pre-stress force ($P_{mt}(x)$) (after all losses) as expressed in Equation 7.2. The time dependent losses include those resulting from creep and shrinkage of concrete and steel relaxation.

$$\Delta P_{time-dependent} = P_{mo}(x) - P_{mt}(x) \tag{7.2}$$

7.2.1.1 Elastic shortening

After the pre-stress force is transferred to a member, the concrete will immediately shorten elastically due to compression stress. In pre-tensioned concrete, the steel will shorten by the same amount as the concrete because all tendons are bonded to the concrete and the tendons are stressed before the casting of concrete. The remaining pre-stress force after elastic shortening losses can be calculated according to Equation 7.3 (Mosley et al., 2012).

$$P' = \frac{P_j}{1 + \alpha_e . \frac{A_p}{A}\left(1 + \frac{e^2 A}{I}\right)} \tag{7.3}$$

where α_e is the modular ratio $\frac{E_{cm}}{E_s}$, E_{cm} and E_s are the modulus of elasticity for concrete and steel respectively, A_p is the area of pre-stressing steel, A is the area of concrete section, e is the eccentricity and I is the second moment of area for the concrete section.

In post-tensioned concrete, if there is one tendon or more tendons stressed simultaneously, the elastic shortening losses will be zero because the applied pre-stress

is recorded in the pre-stress gauge after the elastic shortening has taken place. However, if the tendons are stressed sequentially then all tendons except the last one will lose stress due to elastic shortening of concrete caused by forces in the subsequent tendons.

Therefore, Mosley et al. (2012) suggest to assume 50% of the stresses for the post-tension concrete and in this case the remaining pre-stress force is:

$$P' = \frac{P_j}{1 + \alpha_e.0.5.\frac{A_p}{A}\left(1 + \frac{e^2 A}{I}\right)} \tag{7.4}$$

The elastic shortening loss percentage for the tendons is calculated in this study according to Equation 7.4 since the tendons have been stressed sequentially (Kaylor, 1954). This results in an elastic shortening loss percentage is 0.3%.

7.2.1.2 Friction losses

Friction losses are only relevant for post-tensioned concrete members. Tendons are housed in ducts and when the cable is stressed, it tends to resist this movement as it slides against the duct, which result in a frictional resistance beeing developed. According to Mosley et al. (2012), friction losses are generated from two basic mechanisms:

- **Curvature of the tendon to achieve a desired profile**

  When the duct is curved, and during tensioning, the tendon attempts to straighten and that will generate large friction losses in pre-stress force because of the friction force between tendon and duct.

- **Deviation between the centreline of the tendons and the ducts (wobble effect)**

  The stretching of the tendon has to overcome the wobble of the tendon. The wobble refers to the change in tendon position along the duct.

The losses of pre-stress force due to friction are calculated according to Equation 7.5

$$\Delta P(x) = P_j\Big(1 - e^{(-\mu(\theta+kx)}\Big) \tag{7.5}$$

where P_j is the jacking force (1000 MPa); μ is the coefficient of friction according to Table 7.1 ($\mu = 0.19$ is used in this study); θ is the sum of angular displacement over the distance x (in radian); k is the wobble coefficient in the range of 0.005 to 0.01 radian/metre (0.01 is used in this study); x is the segment length from the jacking end.

Table 7.1: *Friction coefficient (μ) for post-tensioned tendons (Eurocode-2, 2004)*

	Internal tendons	Steel duct/ non-lubricated	HDPE duct/ non-lubricated	Steel duct/ lubricated	HDPE duct/ lubricated
Cold-drawn wire	0.17	0.25	0.14	0.18	0.12
Strand	0.19	0.24	0.12	0.16	0.1
Deformed bar	0.65	-	-	-	-
Smooth round bar	0.33	-	-	-	-

The sum of the angular displacement (θ) over distance x is firstly calculated for each tendon as shown in Figure 7.1. The different tendons have different curvatures (Figure 6.2) therefore, θ increases as the profile of the tendon increased in curvature as shown in Figure 7.1. Consequently, the percentage loss in pre-stress force (according to Equation 7.5) due to friction shows an increase with distance from the jacking ends as shown in Figure 7.2. The greatest percentage losses occur in the middle, as the maximum θ is in the middle of the tendon, 4.3% for tendon 1 and 3.9%, 2.7% and 2.2% for tendon 2, 3, 4 and 5 respectively.

7.2.1.3 Anchorage losses

In post-tensioned members, when the tendons are stressed they should be anchored with a conical wedge. This process will cause pre-stress losses when the

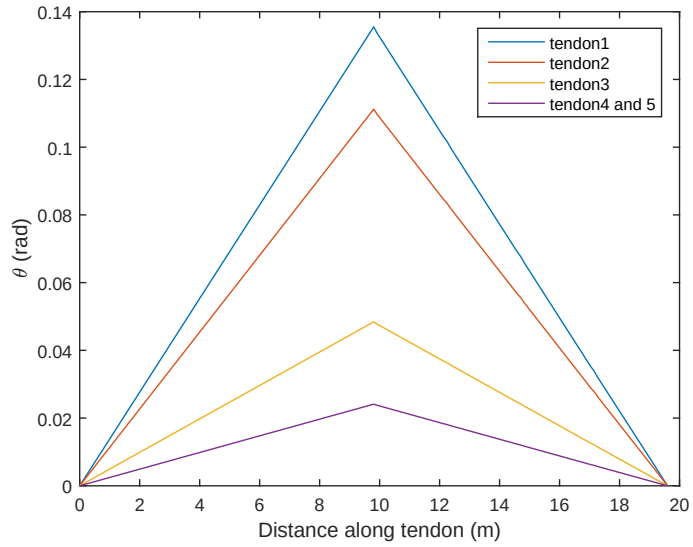


Figure 7.1: *Sum of angular displacement (θ) at each tendon.*

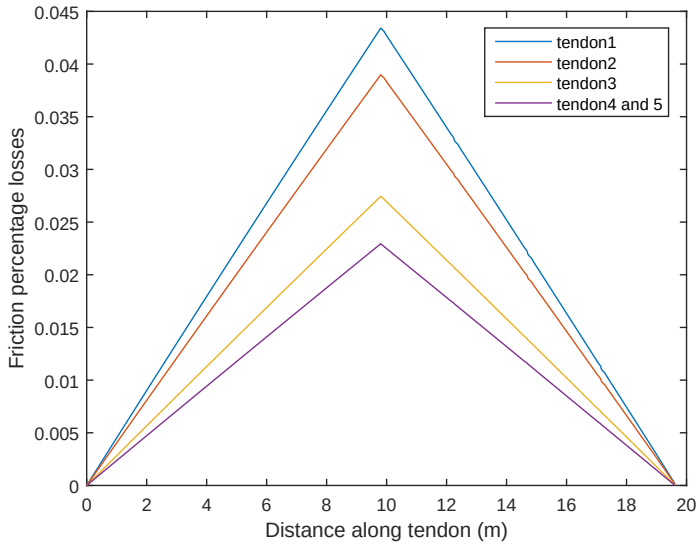


Figure 7.2: *Percentage losses of the prestress force due to friction for the five tendons. Losses are arranged from high to low values according to the profile of the tendon*

slip or draw which occurs as the pre-stress force transfers from jack to the anchorage. For the wedge type anchorage, which is usually used for strands, the slip is $\triangle_{slip} = 6$ mm (Gilbert et al., 2017). The anchorage losses have a much greater effect on short pre-stressed concrete members than long ones.

The anchorage losses $\triangle P_a$ due to the anchorage slip can be calculated according to the general equation:

$$\triangle P_a = 2\beta L_{di} \tag{7.6}$$

where β is the slope of the friction loss line (the friction loss per unit length (see Figure 7.3)); L_{di} is the length of draw in line (see Figure 7.3). L_{di} can be determined by equating the anchorage slip $\triangle_{slip}$ with the integral of the change in strain in the steel tendons over the length of the draw-in line as follows:

$$\triangle_{slip} = \int_0^{L_{di}} \frac{2\beta x}{E_p A_p} dx = \frac{\beta L_{di}^2}{E_p A_p} \tag{7.7}$$

and simplifying gives:

$$\sqrt{\frac{E_p A_p \triangle_{slip}}{\beta}} \tag{7.8}$$

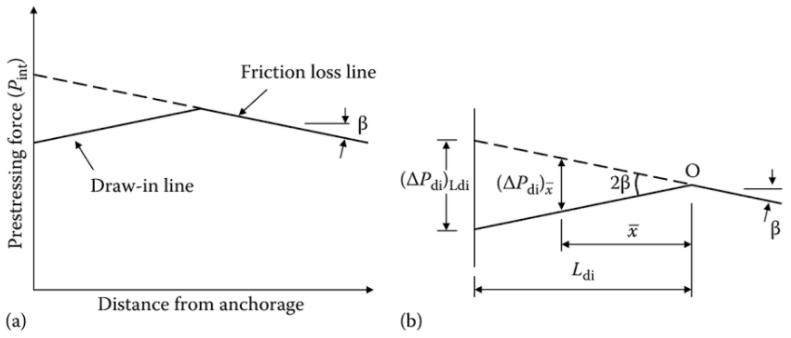


Figure 7.3: *Anchorage losses. (a) Anchorage draw-in effect along distance. (b) pre-stress loss near the anchorage (Gilbert et al., 2017)*

The effect of anchorage losses in this study was large, around 14% near the jacking ends, due to the short length of the bridge beam. Therefore, the effect of anchorage loss is extended along the whole length of the tendons as shown in Figure 7.4. The anchorage losses will be resisted by the friction between steel and concrete and as a result there will be a force drop in the tendons with increasing distance from the jacking ends (see Figure 7.5). The remaining pre-stress force along the length of the tendon, for the five tendons, after the total short term losses are shown in Figure 7.6. The figure shows that the remaining forces in tendons are increasing as the curvature of the tendon decrease. This is due to the reduction of the sum of the angular displacement (θ) as shown in Figure 7.1.

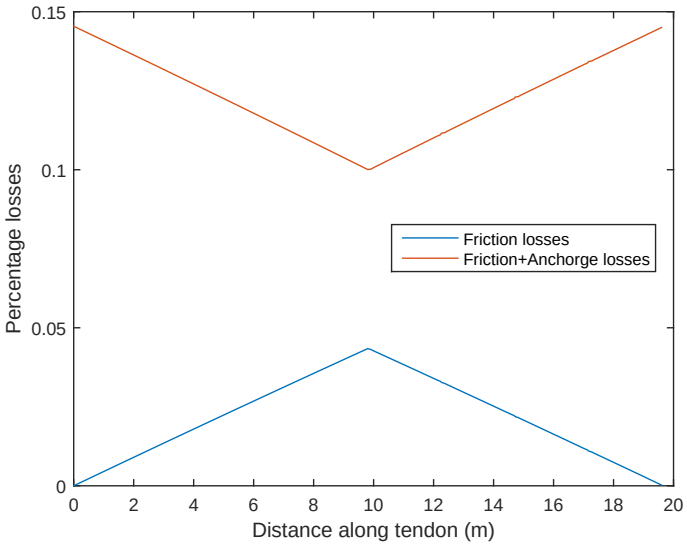


Figure 7.4: *Comparison between losses due to friction effect only and losses due to friction + anchorage draw-in effect.*

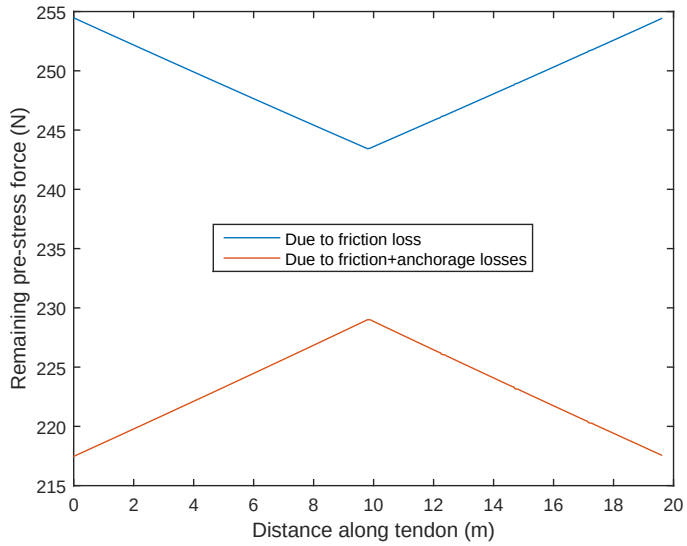


Figure 7.5: *The increase of the drop in the prestressing force with distance from the jacking ends due to the effect of anchorage draw-in.*

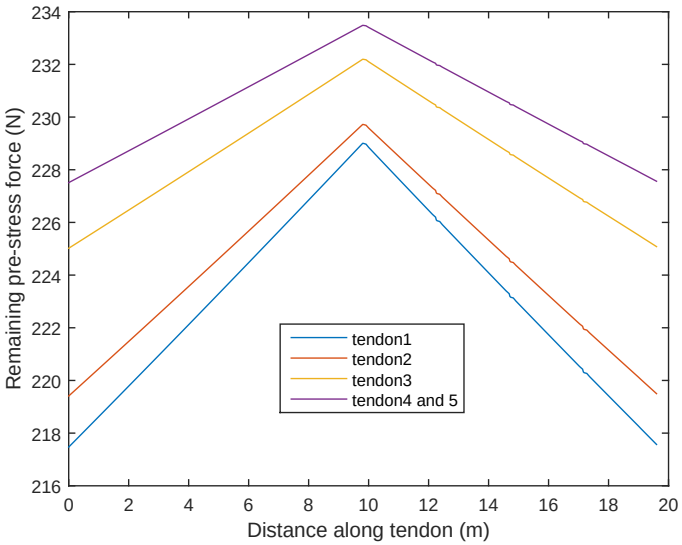


Figure 7.6: *Remaining prestressing force at each tendon.*

7.2.1.4 Creep, shrinkage and steel relaxation

Creep, shrinkage of concrete and steel relaxation affect the long term serviceability of the structure. Creep of concrete is the increase in strain that results from the permanent loads such as the self weight and the sustained compressive stress on concrete induced by post-tensioning. Shrinkage is shortening of concrete due to drying and it is independent of applied loads. Steel relaxation is a loss of stress in the tendon after being held at a constant elongation. The loss of pre-stress force due to creep, shrinkage and steel relaxation are calculated according to equations 7.9, 7.10 (Mosley et al., 2012) and 7.11 respectively:

$$\Delta P_{cr} = \phi(t, t_o)\frac{E_s A_p}{(1.05E_{cm})A}(1 + e^2\frac{A}{I})P' \tag{7.9}$$

where $\phi(t, t_o)$ is the value of creep coefficient for some arbitrary time t. Dujmovic et al. (2015) presents the details of calculating $\phi(t, t_o)$. P' is the remaining prestress force after the short term losses.

$$\Delta P_{sh} = \varepsilon_{cs}(t)E_s A_p \tag{7.10}$$

where ε_{cs} is the shrinkage strain at time t. Dujmovic et al. (2015) presents the details of its calculation.

$$\Delta P_{re} = P^{'} K1 \rho_{1000} e^{K2.\mu} (\frac{t}{1000})^{0.75(1-\mu)} 10^{-3} \tag{7.11}$$

where $K1$ and $K2$ are parameters dependent on the steel class, which has been taken as 0.66 and 9.1 respectively for low relaxation; ρ_{1000} is the relaxation after 1000 hours and it also depends on the steel class, ρ_{1000} has been taken as 2.5% in this study according to Dujmovic et al. (2015); μ is the ratio between the initial pretsress σ_{pi} (remaining prestress after the short term losses) and the characteristic value of the tensile strength of the prestressing steel (f_{py}). More detailed information about prestress losses can be found in Dujmovic et al. (2015), Eurocode-2 (2004), Mosley et al. (2012).

By applying these equations, the percentage losses for creep, shrinkage and steel relaxation are shown in Figures 7.7, 7.8 and 7.9 respectively. The total percentage loss for short and long term losses is shown in Figure 7.10. According to that, the remaining prestress force is calculated at each element of the tendons at each year of the bridge service life. Figure 7.11 shows the final remaining prestress force at each element at each year for tendon 1. In the present study, the prestress is treated as a normal distribution with mean value represented by the nominal prestress and COV 0.075 according to JCSS (2001).

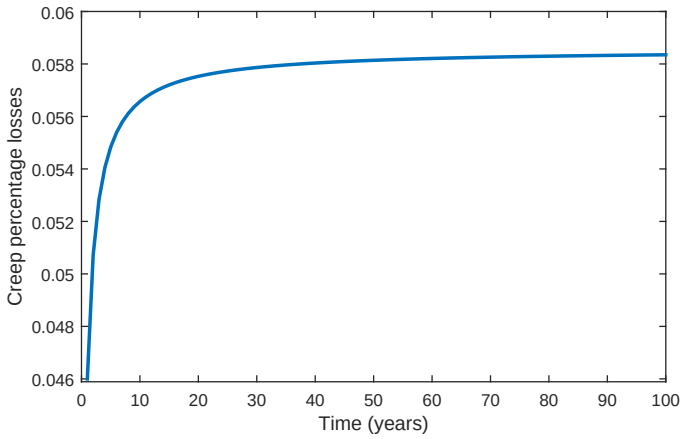


Figure 7.7: *Losses in prestress force due to concrete creep*

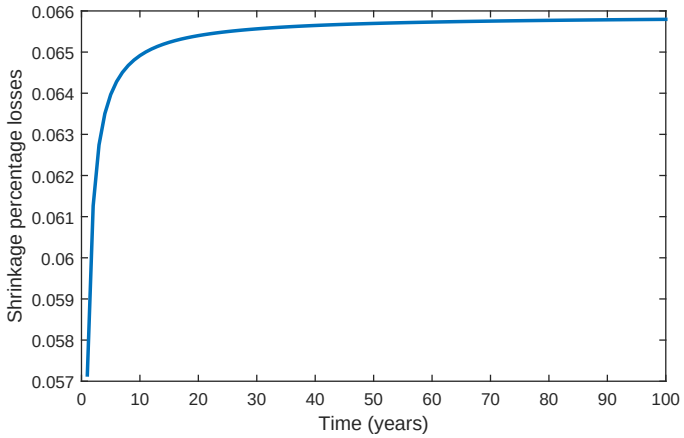


Figure 7.8: *Losses in prestress force due to concrete shrinkage*

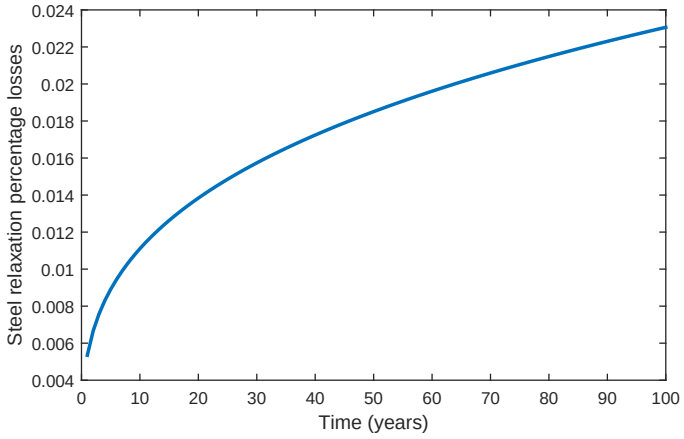


Figure 7.9: *Losses in prestress force due to tendon relaxation*

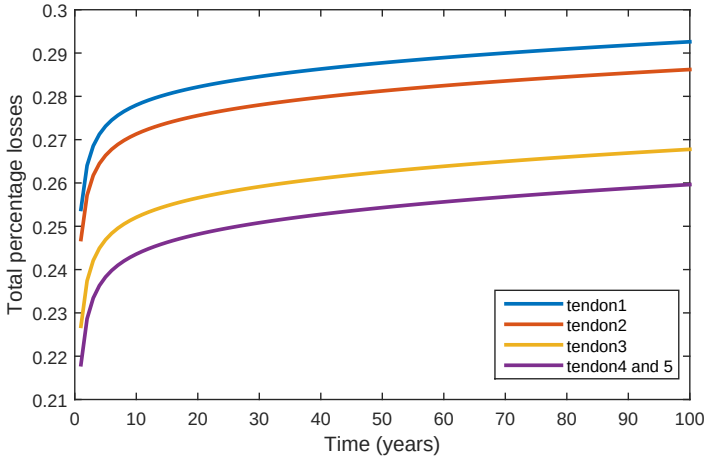


Figure 7.10: *Total pre-stress losses: short term losses + long term losses*

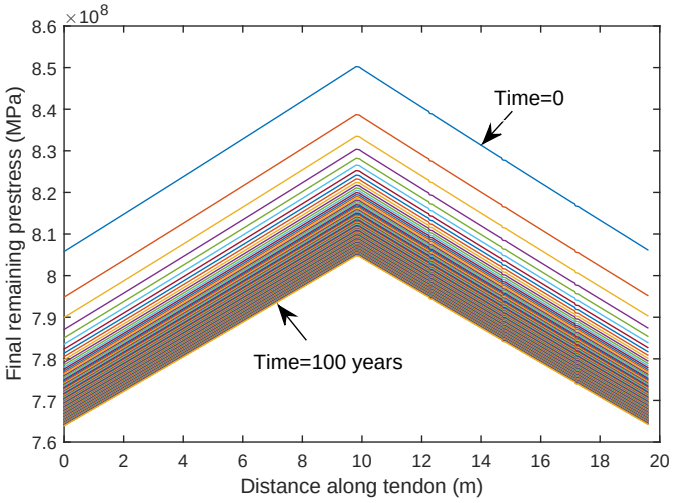


Figure 7.11: *Final remaining prestress along the length of tendon 1 over time*

7.2.2 Corrosion initiation and propagation

7.2.2.1 Corrosion initiation

As mentioned in Chapter 2, corrosion is usually initiated by chloride ion contamination when their concentration at the steel surface exceeds the threshold limit C_{th} (0.6-1.2 Kg/m^3 with mean 0.9 Kg/m^3). The time needed for chloride ions to reach the threshold chloride concentration is called the time to corrosion initiation (t_i) as shown in Figure 7.12. This figure shows the diffusion of chloride ions through the transverse joints. As mentioned in Section 6.2.2, there was no duct around the longitudinal tendons near the transverse joints and alternatively, a cardboard tubes have been used. The absence of duct near the joints accelerate the corrosion process and the initiation of corrosion. To estimate t_i, the progress of chloride concentration with the time should be specified first.

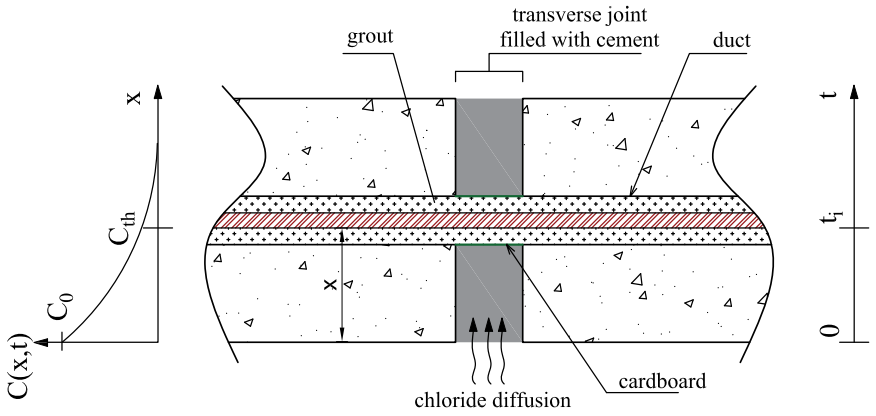


Figure 7.12: *Chloride diffusion process of corrosion initiation through the transverse joint in Ynys-y-Gwas bridge*

The chloride concentration in the bridge at the time of failure (after 32 years) was measured (by the TRRL) in samples that were taken from different positions (deck, flanges, web, diaphragms and soffit) of the TRRL segments. The chlorides were found in the grout near the joints, the concrete surface and the mortar. However, a very small amount of chlorides have been found in the grout within

the segments (see Table 7.2). This indicates that the chlorides have diffused during the bridge service and not during its construction (Woodward and Williams, 1988). The TRRL results also show that there was no decrease in concentration with increasing depth from the surface (see Figure 7.13), which would have been expected if de-icing salts had penetrated from above. The higher concentration of chlorides in joints has been found near the soffit as shown in Figure 7.13 where G and J are represent beam G and beam J respectively as shown in Figure 6.4 while EB is the edge beam.

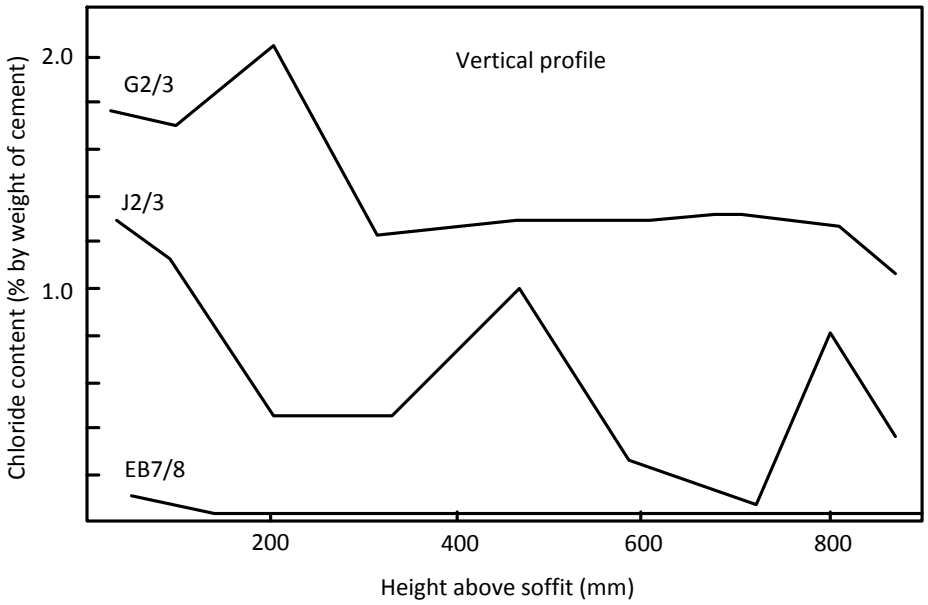


Figure 7.13: *Vertical profile of chloride concentraion in Ynys-y-Gwas bridge at different levels from the soffit (Woodward and Williams, 1988)*

Equation 2.37 can be used to estimate t_i by assuming the chloride concentration ($C(x,t)$) to be equal to the chloride concentration threshold value (C_{th}) over which the steel corrosion is triggered. However, t_i can not be estimated directly since the diffusion coefficient (D_0) is unknown. Therefore, Equation 2.37 is used first to calculate D_0 by using the values of $C(x,t)$ and C_0, at time of failure ($t = 32$).

The surface chloride concentration (C_0), in this study, represents the chloride concentration near the soffit, 0.59% weight by cement according to Table 7.2.

Table 7.2: *Chloride concentrations obtained for different positions of TRRL segments according to Woodward and Williams (1988)*

Element	Chloride concentration: % weight by cement		
	Average	Standard deviation	Maximum
Concrete deck	0.2	0.19	0.73
I-beam			
top flange	0.12	0.08	0.32
web	0.2	0.18	0.64
diaphrams	0.43	0.22	0.78
bottom flange	0.58	0.33	1.15
soffit	0.59	0.33	1.01
Edge beam			
deck	0.09	-	0.09
outer web	0.12	0.03	0.14
inner web	0.4	0.28	0.83
Mortar			
I-beam	0.66	0.63	2.08
edge beam	0.09	0.15	0.96
Grout			
at joint, longitudinal ducts	0.32	0.26	0.81
at joint, transverse ducts	0.22	0.11	0.36
within segments, longitudinal ducts	0.01	0.01	0.03
within segments, transvrese ducts	0.01	0.004	0.02
Aspestos	<0.01	<0.01	0.01

The chloride concentration ($C(x,t)$), in this study, represents the chloride concentration in grout at the joints through the longitudinal duct, 0.32% weight by cement (cement in grout).

According to the mix of concrete and grout, described in Section 6.2.2, the amount of the surface chloride was 2.44 Kg/m^3 and within the joint is 3.2 Kg/m^3. This shows that the chloride concentration $C(x,t)$ within the grout is higher than the surface chloride concentration C_o which is impossible because the chlorides were penetrated from the surface and therefore, chloride concentration should be more higher at the points near the surface. The large standard deviation of chloride concentration might be the cause of that. Therefore, 90% of C_o has been assumed for the chloride in the grout since the bridge was suffered from a very severe corrosion. Accordingly, the surface chloride concentration and the chloride concentration in grout were taken as 2.44 and 2.196 Kg/m^3 respectively. By substituting these two values in Equation 2.37, the diffusion coefficient (D_0) has been found to be 0.0078 m^2/year (2.47×10^{-6} cm^2/sec) which is much higher than

the mean value of the concrete diffusion coefficient (2×10^{-8} cm^2/sec according to Hoffman and Weyers (1994)). This might be due to the higher durability of concrete comparing to grout that make it less permeable to water and hence gives the ability to resist weathering actions.

Equation 2.37 is used again to estimate the progress of chloride concentration with the time as shown in Figure 7.14. Consequently, time to corrosion initiation is estimated as 0.773 years which corresponds to a 0.9 Kg/m^3 chloride concentration. This very early time to corrosion initiation indicated that corrosion was attacked the bridge immediately after construction, due to the damp environment near the surface and the inadequate protection for the tendons near the joints. In this study, time to corrosion initiation is treated as a deterministic value as, being so small, its variability will not impact safety.

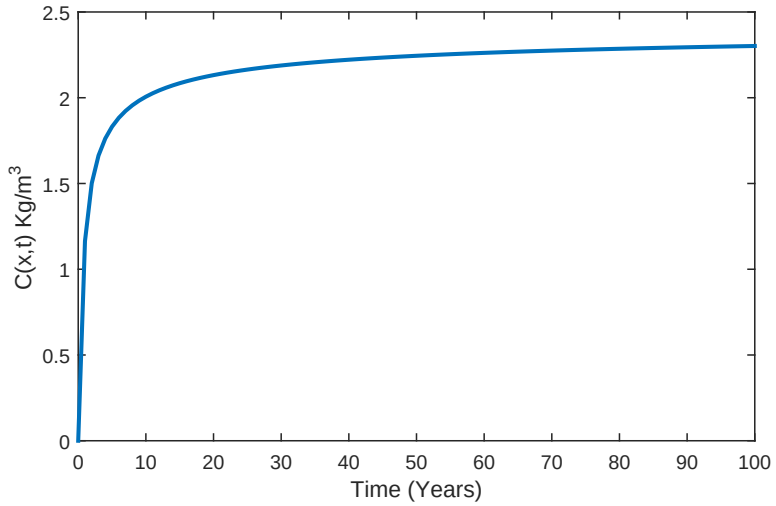


Figure 7.14: *Progress of chloride concentration with the time for Ynys-y-Gwas bridge*

7.2.2.2 Corrosion propagation

Corrosion propagation happens when the reinforcement corrodes, cause metal loss, loss of area and bond, and therefore reducing structural capacity. Corrosion propagation is usually described in terms of corrosion rate (i_{corr}) as described in Chapter 2.

The corrosion rate at the start of corrosion propagation ($i_{corr}(1)$) is calculated according to Equation 2.38, then the reduction of corrosion rate (i_{corr}) with time is estimated according to Equation 2.40. The formation of rust products on the steel surface will reduce the diffusion of iron ions away from the steel surface and therefore, the corrosion rate reduces with the time as shown in Figure 7.15.

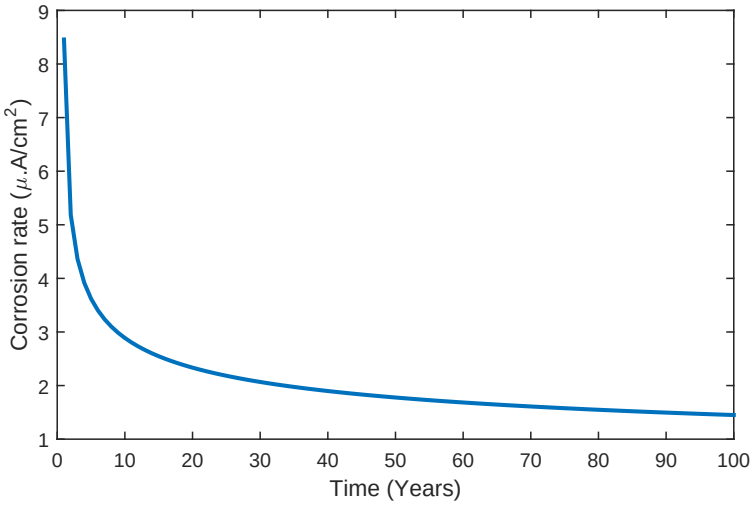


Figure 7.15: *Progress of the corrosion rate with the time for Ynys-y-Gwas bridge*

7.2.3 Pitting factor

The pitting factor represents the ratio between the maximum and average corrosion penetration (Equation 2.44 to Equation 2.46, as shown in Figure 2.14). Stewart (2004) and Stewart and Al-Harthy (2008) proposed a statistical parameter for the pitting factor based on an accelerated corrosion test for 10, 16 and 27 mm diameter and 100 mm length of reinforcement bar. A Gumbel distribution (EV type I) was used to model the maximum pit depth and the proposed statistical parameters are summarized in Table 2.10. For an increased length of bar (L_u), the Gumbel statistical parameters can be computed according to Equation 2.46.

The pitting factor for the bridge is first calculated according to Equation 2.46 where L_u represents the length of the reinforcement bar element considered in ABAQUS. According to this, the Gumbel parameters for the pitting factor were 7.118 and 1.02 for μ and α respectively. However, using this statistical parameter for the pitting factor underestimates the probability of failure by predicting very small values of P_f with time as shown in Figure 7.16. This figure shows that the probability of failure is 3% at the year of bridge failure (32 years) which is very low corresponding to failure. Therefore, in this study the probabilistic model of pitting factor was developed in different way, as described below, to match the degree of corrosion in the bridge.

The statistical parameters of the pitting factor were re-estimated depending on the corrosion assessment for tendons near the joints (Woodward and Williams, 1988). The assessment was done by classifying the degree of corrosion on each wire and giving it a score on a scale of 0 to 4 as shown in Table 7.3 (Woodward and Williams, 1988). The total mark for each tendon was then subdivided into five groups depending on the degree of corrosion: none, mild, moderate, severe and very severe as shown in Table 7.3.

The results of corrosion assessment in the longitudinal tendons near joints, in beams J, H and G and in segments 1, 2 and 3, are shown in Figure 7.17.

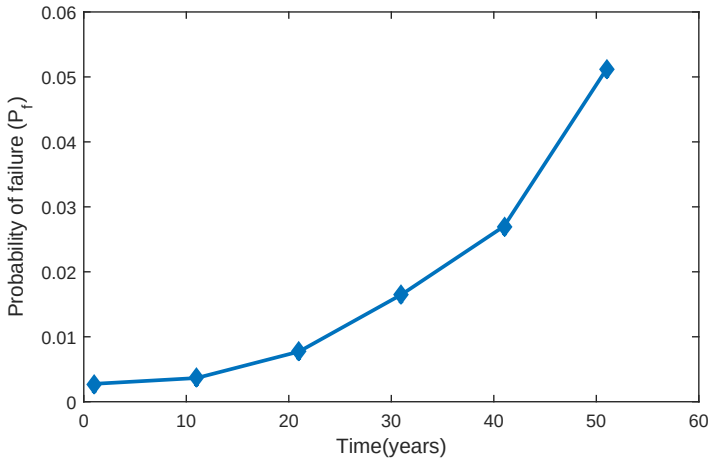


Figure 7.16: *Probability of bridge failure along the years, when the statistical parameters of the pitting factor were considered according to Equation 2.46*

Table 7.3: *Classification of corrosion (Woodward and Williams, 1988)*

Degree of corrosion	Condition of wire	Marking
None	No corrosion	0
Mild	Slight surface corrosion with some scaling and pitting	1
Moderate	Mild corrosion plus up to 25% loss of section	2
Severe	25-50% loss of section	3
Very severe	$>$ 50% loss of section	4

According to Figure 7.17, 45 tendons have been tested. From them: 11 tendons suffered from very severe corrosion ($>$ 50% loss of area); 10 tendons affected by severe corrosion ($>$ 25% and $<$ 50% loss of area); 6 tendons experienced moderate corrosion ($<$ 25% loss of area). That means the probability of getting tendons with a very high corrosion is 24% (11/45) and for the severe corrosion is 22% (10/45). as shown in Figure 7.18. This figure shows a clarification to the expected distribution of the loss of tendon area due to corrosion at the time of bridge failure.

Therefore, a MATLAB code has been written to fit the best statistical parameters for pitting factor using Monte-Carlo simulation. This has been done by assuming an initial mean (μ) and standard deviation (α) for the pitting factor (R). Then,

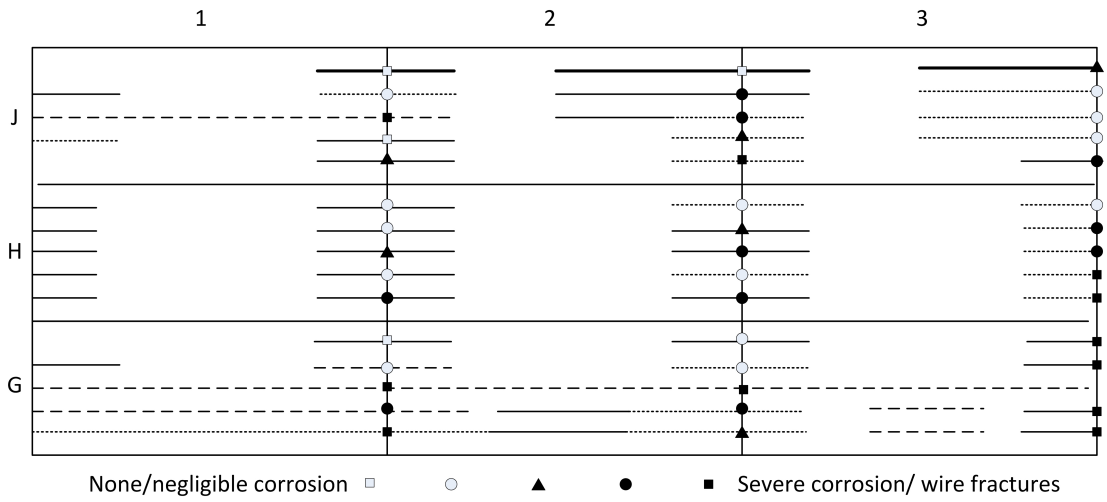


Figure 7.17: *Degree of corrosion in longitudinal tendons near joints for beams J, H and G and segments 1, 2 and 3 (Woodward and Williams, 1988)*

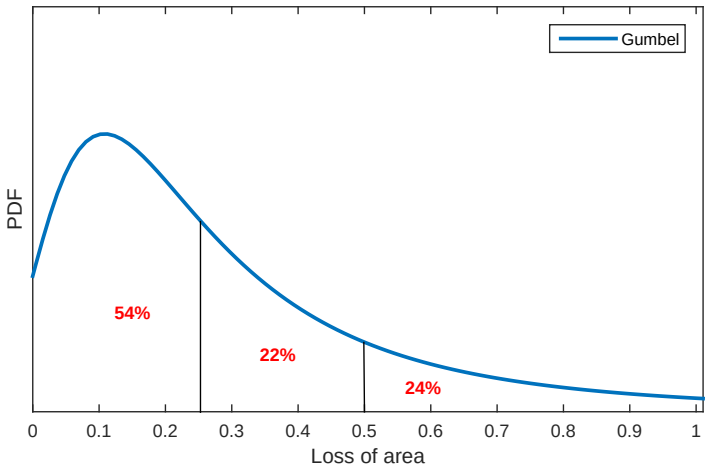


Figure 7.18: *The probability of loss of cross sectional area according to the corrosion assessment of the longitudinal tendons near joints*

10^6 number of samples have been generated for R according to its distribution, μ and α. According to these samples, the pit depth ($P(t)$) and the remaining area of tendons (A_r) were calculated (at the time of bridge failure t = 32 years) according to Equations 2.43, 2.47 and 2.48. Then, the loss of area for each sample of R were calculated according to $(A_{initial} - A_r)/A_{initial}$. According to the values of the loss of area, the percentage of the tendons that have been affected by very sever and sever corrosion were found. Finally, It has been checked that if the loss

of area percentage is close to the loss of area percentage in the tested segments (as described above) then the assumed μ and α are correct, otherwise, they are going to be changed using trial and error method. Accordingly, μ and α for the pitting factor has been specified as 6.7 and 5.2 respectively. The values specified give the same percentages of loss of area corresponding to the percentage of area losses described above. The histogram of cross sectional area losses at each year are shown in Figures 7.19 to 7.24. The figures show that the percentage of area loss $> 50\%$ increased with time due to increasing corrosion as shown in Table 7.4. The histogram of year 31 gives an identical loss percentages to that computed according to the assessed segments.

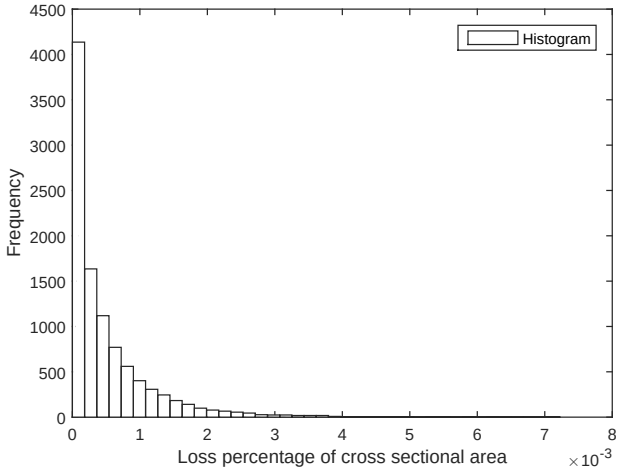


Figure 7.19: *Histogram of loss of cross sectional area at year 1*

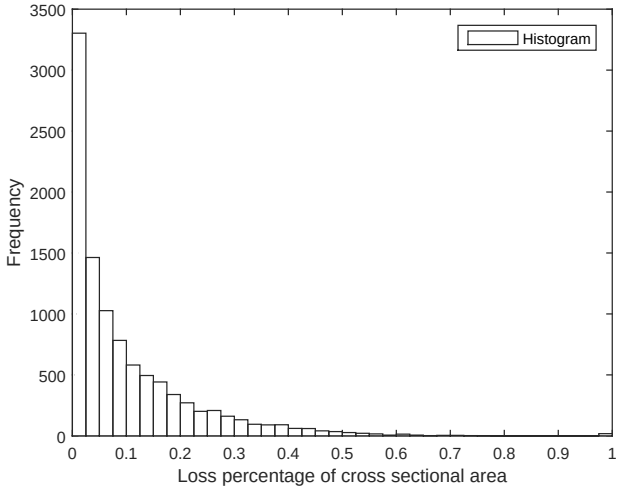


Figure 7.20: *Histogram of loss of cross sectional area at year 11*

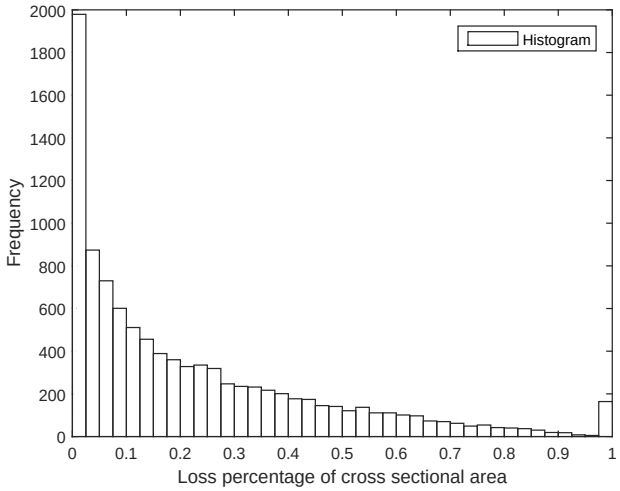


Figure 7.21: *Histogram of loss of cross sectional area at year 21*

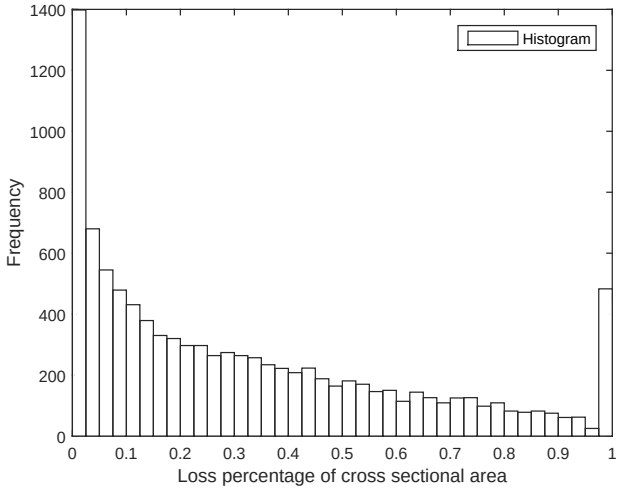


Figure 7.22: *Histogram of loss of cross sectional area at year 31*

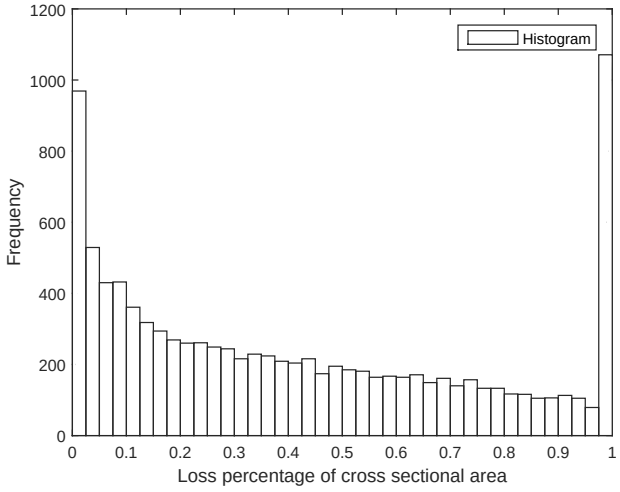


Figure 7.23: *Histogram of loss of cross sectional area at year 41*

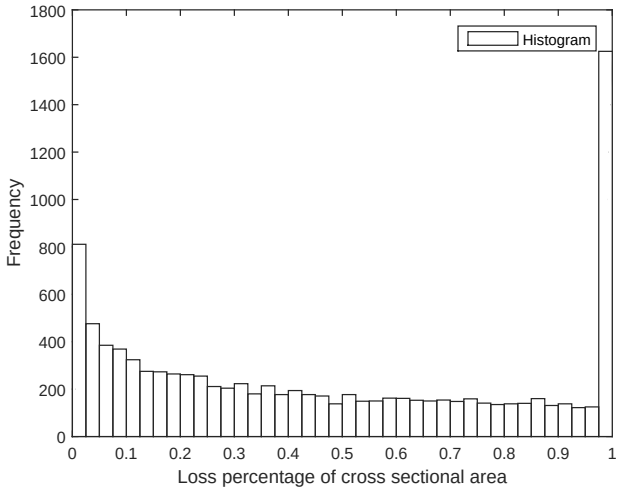


Figure 7.24: *Histogram of loss of cross sectional area at year 51*

Table 7.4: *Loss of tendon area percentage along the years for Ynys-y-Gwas bridge*

Years	loss > 50%	loss > 25%	loss = 100%
1	0	0	0
11	0.0133	0.1142	0.002
21	0.1183	0.3461	0.014
31	0.255	0.4773	0.06
41	0.35	0.5713	0.094
51	0.44	0.6411	0.142

7.2.4 Bridge load

The total bridge load is the sum of the permanent and truck live loads. In section 2.4.3, it has been been mentioned that the dead load is the sum of three components: the weight of pre-cast elements, weight of cast in place and weight of asphalt (Nowak and Collins, 2012). In this case, only two of these components are considered: the weight of precast concrete D_1 (weights of concrete segments and tendons) and 100 mm asphalt overlay D_2 (100 mm thickness according to Figure 6.1). The values of the permanent loads considered for the bridge assessment are the average self weight of the concrete segments - 8.69 kN/m and asphalt wearing surface - 1.411 kN/m.

The live load covers a range of forces produced by vehicles moving on the bridge. According to Woodward and Williams (1988), the axle loadings on the bridge were checked to ensure that they were not in excess of HA loading. Therefore,

the live load of the bridge is calculated according to the specified trucks weight in HA loading.

The HA loading is a formula loading introduced by the British Standard (BS) in 1945, which is intended to represent the vehicle load for highway bridges in the UK. According to Clark (1983), HA loading is represented by a uniformly distributed load (UDL) and a knife edge load (KEL). The UDL of HA loading depends on the loaded length (L) which is the span of the bridge. For up to 30 m loaded length, the UDL is 30 kN/m per notional lane while for longer loaded length, the UDL is given by $151(1/L)^{0.475}$. For the knife edge load, the code value is 120 kN per notional lane positioned perpendicular to the notional lane as shown in Figure 7.25.

The total bridge load is used in this study to evaluate the action moment on the bridge and subsequently the limit state function as will be described in Section 7.3.

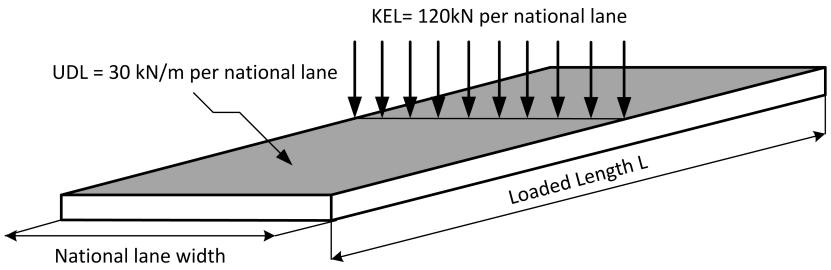


Figure 7.25: *HA loading includes the unifomly distributed load (UDL) and the knife edge load (KEL) on one notional lane*

7.2.5 Bond-slip relationship

Bond between reinforcing steel and concrete is an important characteristic which allows the stresses to transfer from steel to concrete. Considering the bond effect in reliability analysis of corroded RC structures is an important task since corrosion can affect the performance of a structure in the form of cracking of concrete cover due to rust expansion. Once cracks develop, the force transfer between the steel and the concrete will be affected and that will lead to change the

behaviour of the bond. This will decrease the bond strength capacity and subsequently, reduce the resistance capacity of the structure. Therefore, the effect of bond reduction on the bridge capacity will be considered in reliability analysis, for the first time, by modelling the bond slip relationship between concrete and pre-stressing steel using ABAQUS.

According to the literature, the earliest and the simplest way to test the bond behaviour is the pull out test. The bond-slip behaviour has been studied by different researchers such as Azizinamini et al. (1993), Lee et al. (2002) and Haskett et al. (2008). According to the Model Code 90 CEB (1992), the bond-slip relation is shown in Figure 7.26. The bond-slip curve can be divided in four distinct regions. The first region is represented by the ascending segment (over which the peak bond stress τ_{max} is reached) which corresponds to the penetration of steel ribs into concrete materials that leads to micro-cracking near the concrete cover. The second region is represented by the horizontal segment which appears only if the crushing and shearing of concrete between ribs occur. In the third region, the descending segment after the peak bond, the bond resistance reduces as the local slip increases due to splitting cracks along the bars. The final region is represented by the horizontal part which corresponds to the residual bond capacity due to the residual friction force.

There is a difference between the bond slip relationship for ordinary steel bars and that for pre-stress steel strands. This is due to the difference in surfaces, as steel strands have a smooth surface compared with ordinary steel bars. However, as the wires in strands are twisted together, strands have spiral ribs, which is similar to but not the same as the ribs in the deformed bar. The spiral ribs may result in a screwing effect and therefore, the constitutive law of bond-slip is slightly different from the deformed bar.

For both deformed bar and strands, the gear action coming from ribs maintains the bond strength at a high level after cracking. For strands, if the screwing effect is reduced, due to corrosion, then the gear action will increase and lead to higher bond strength within a certain range (less than 6% corrosion loss accord-

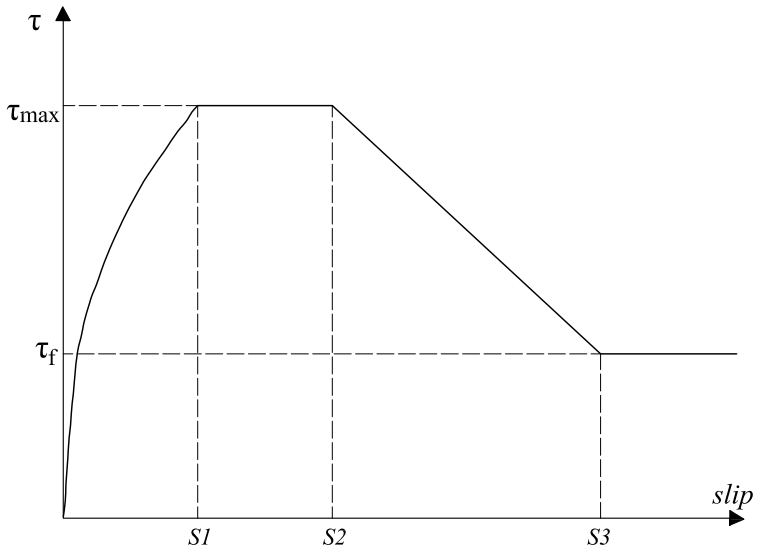


Figure 7.26: *Bond stress-slip relationship according to Model Code (CEB, 1992)*

ing to Wang et al. (2016)). Therefore, Wang et al. (2016) developed an improved constitutive law that can be used to predict the bond slip relationship between corroded strands and concrete, which is used in this study. The improved constitutive law (see Figure 7.27) based on the bond-slip relationship that is suggested by the Model Code CEB (1992) for the deformed bar.

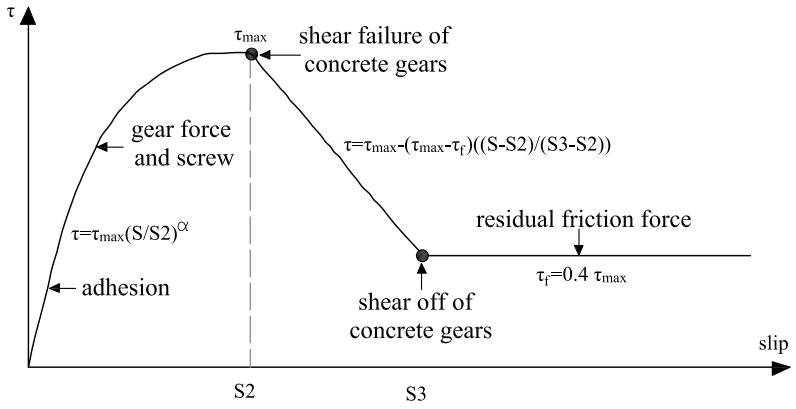


Figure 7.27: *Improved local bond stress-slip relationship between strand and concrete (Wang et al., 2016)*

Figure 7.27 shows that the bond transfer curve can be divided into three regions:

1. ascending non-linear curve. In this region, the initial bond stress depends on the adhesion. Then the adhesion action starts to reduce as the slip increases. This will lead to increase the friction and gear force until the maximum bond stress is reached.

2. Linear decrease region. This region represents the appearance of excessive local slip until the concrete gear shears off.

3. Constant residual strength region due to the remaining friction force

The improved function according to the Model Code (CEB, 1992) is expressed as:

$$\tau = \begin{cases} \tau_{max}(S/S2)^{\alpha} & 0 \leq S \leq S2 \\ \tau_{max} - (\tau_{max} - \tau_f)\left(\dfrac{S - S2}{S3 - S2}\right) & S2 \leq S \leq S3 \\ \tau_f & S3 \leq S \end{cases} \tag{7.12}$$

where τ_{max} is the maximum bond stress taken as $2.5\sqrt{f_{ck}}$, τ_f is the residual friction stress taken as $0.4\tau_{max}$, α and $S2$ are constants taken as 0.4 and 3 mm respectively and $S3$ is the distance between ribs taken as 15 mm according to Haskett et al. (2008). Furthermore, Wang et al. (2016) proposed an empirical model that can be used to predict the residual bond strength between concrete and corroded strands by calculating the normalized maximum bond stress (R_b). The maximum normalized bond stress represents the ratio between the maximum bond strength of the corroded specimen to the maximum bond strength of the intact specimen. Wang et al. (2016) keeps the maximum bond strength constant for slight corrosion loss ($\leq$ 6%) while for larger corrosion loss, the maximum bond stress depends on an exponential function (see Figure 7.28), decreases as the corrosion loss (η) exceeds 6% as follows:

$$R_b = \begin{cases} 1 & \eta \leq 6\% \\ 2.03e^{-0.118\eta} & \eta > 6\% \end{cases} \tag{7.13}$$

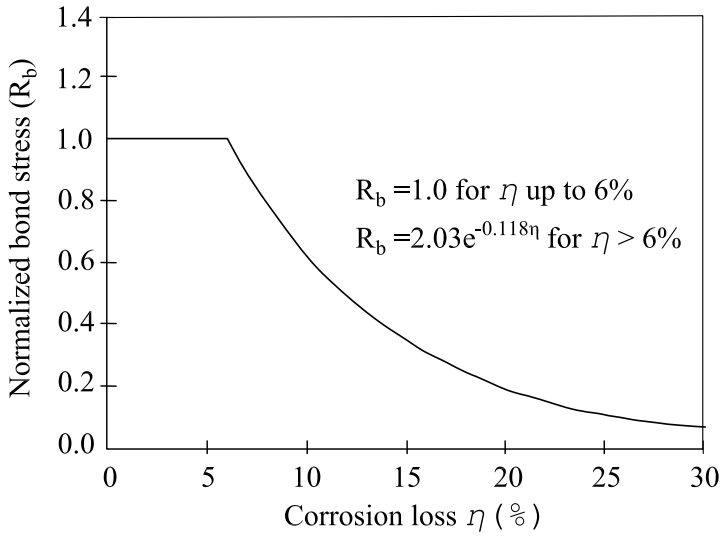


Figure 7.28: *Deterioration of the maximum normalized bond strength (R_b) with increasing corrosion (Wang et al., 2016)*

7.3 Limit state function

As the failure of the bridge occurred due to the severe corrosion at joints, reliability analysis was performed under two conditions. In the first condition, it is assumed that the deterioration of the bridge is concentrated at regions of peak actions at mid joint, which is known as the mid-section analysis. For this condition, the flexural limit state function is determined as a function of time as:

$$g_{mid}(t) = \theta_R M_{R_{mid}}(t) - M_{S_{mid}}\theta_E \tag{7.14}$$

where θ_R and θ_E are, respectively, the resistance and load model uncertainty. $M_{R_{mid}}$ is the resistance moment of the bridge at mid span as a function of time. The resistance moment at mid span is calculated from ABAQUS by calculating the resultant stresses of its cross section. To compute this, the normal stress at each concrete element integration point has been found, then each of these

stresses were multiplied by element area and distance to the neutral axis. $M_{S_{mid}}$ is the action moment of the bridge at mid span and it can be calculated from:

$$M_{S_{mid}} = \frac{wl^2}{8} \tag{7.15}$$

where w is the dead load (D_1 and D_2) plus the truck load (UDL and KEL) as described in Section 7.2.4.

In the second condition, it is assumed that the safety of the bridge depends on the whole seven joints (considering the beam as a series system). The flexural limit state function is determined as a function of time as follows:

$$g_j(t) = \theta_R M_{R_j}(t) - M_{S_j}\theta_E \tag{7.16}$$

where M_{R_j} is the resistance moment of the bridge at each joint as a function of time. To calculate the resistance moment at each joint, the joint ultimate capacity need to be found first by changing the load and support positions as shown in Figure 7.29 and then repeating the analysis. Then, to calculate M_{R_j}, the same procedure described above is used. Due to symmetry, the resistance moments were calculated for joint 1, 2 and 3 only while joint 4 was previously calculated using the mid section analysis. M_{S_j} is the action moment of the bridge

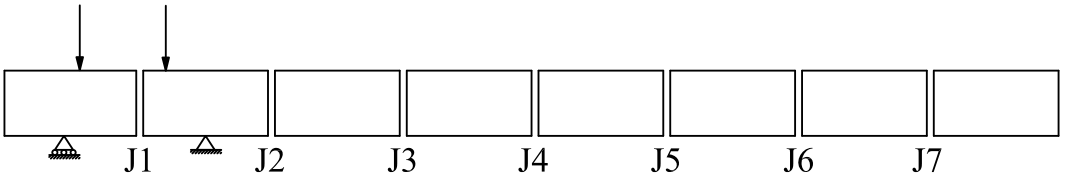


Figure 7.29: *Method of testing joints to find their capacities*

at each joint and it can be calculated according to (see Figure 7.30):

$$M_{S_j} = \frac{w.x}{2}(l - x) \tag{7.17}$$

where x is the distance from support to the joint as shown in Figure 7.30. Ditlevsen (1979) bounds were used to estimate the probability of failure of a

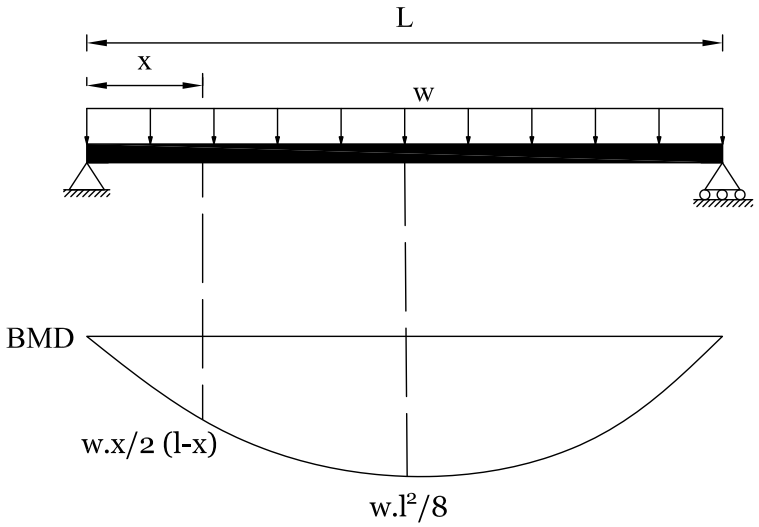


Figure 7.30: *Bending moment diagram of the simply supported beam*

series system, taking into account the correlation between joints according to Equation 2.24.

7.4 Random variables

To reduce the time required for reliability analysis, some of random variables were treated as deterministic values. For example, the dimensions that have a small coefficient of variation, such as the geometry of concrete and steel (length, width, height and diameter). However, there are some dimensions which cannot be easily measured such as concrete cover and asphalt thickness which were treated as random variables. The random variables considered in this study, the considered distributions and the sources used to define these distributions are listed in Table 7.5. The table contains three different variables categories:

- Material properties, which include the concrete compressive strength ,f_{creal}, concrete tensile strength, f_{ct}, concrete modulus of elasticity, E_c, prestressing ultimate strength, f_{pu}, prestressing yield strength, f_{py}, prestressing modulus

of elasticity, E_p, prestressing steel ultimate strain, ε_u and the resistance model uncertainty, θ_R.

- Load variables, which include the dead load (D_1 and D_2), the truck load (UDL and KEL), the remaining prestress force after losses, $P(x,t)$, and the load model uncertainty, θ_E.

- Corrosion variables which include the concrete cover, C, corrosion rate, i_{corr}, the maximum pit depth, $P(t)$, the pitting factor, R, and the model error of corrosion rate and pit depth, $M_{E_{icorr}}$ and $M_{E_{P(t)}}$ respectively.

Table 7.5: *Statistical parameters of random variables used in time dependent reliability analysis*

Variable	Unit	Mean	Standard deviation	COV	Distribution	Source
Concrete compressive strength, f_{creal}	MPa	50	-	0.09	Lognormal	Wiśniewski (2007)
Concrete tensile strength, f_{ct}	MPa	4.07	-	0.2	Normal	Eurocode-2 (2004)
Concrete modulus of elasticity, E_c	MPa	35.65	-	0.08	Normal	Eurocode-2 (2004)
Prestressing steel yeaild strength, f_{py}	MPa	1440	50	-	Normal	Jacinto et al. (2012)
Prestressing steel ultimate strength, f_{pu}	MPa	1665.8	40	-	Normal	Jacinto et al. (2012)
Prestressing steel modulus of elasticity, E_p	Gpa	200	-	0.025	Normal	Jacinto et al. (2012)
Prestressing steel ultimate strain, ε_u	-	0.05	0.004	-	Normal	Jacinto et al. (2012)
Resistance model uncertainties, θ_R	-	1	0.1	-	Lognormal	JCSS (2001)
Dead load precast, D_1	kN/m	8.69	-	0.08	Normal	Nowak (1993)
Dead load asphalt, D_2	mm	100	-	0.25	Normal	Nowak (1993)
Truck load, UDL	kN/m	14.7	-	0.4	Gumbel	Nowak (1993)
Truck load, KEL	kN	58.7	-	0.4	Gumbel	Nowak (1993)
Prestress force	kN	$P(x,t)$ at each element	-	0.075	Normal	JCSS (2001)
Load model uncertainties, θ_E	-	1	0.1	-	Lognormal	JCSS (2001)
Concrete cover, C	cm	8.9	0.79	-	Normal	Mirza and MacGregor (1979)
Corrosion model error, ME_{icorr}		1	-	0.2	Normal	Vu and Stewart (2005)
Pit depth model error, $ME_{P(t)}$		1	-	0.2	Normal	Vu and Stewart (2005)
Pitting factor, R		6.7	5.2	-	Gumbel	-

7.5 Time dependent reliability analysis procedure

In this study, the reliability analysis procedure is applied for three cases:

- Case 1: intact beam (no deterioration due to corrosion and bond).
- Case 2: deteriorated beam due to corrosion only, without considering the bond loss effect, (assuming full bond).
- Case 3: deteriorated beam due to corrosion and bond loss.

For these three cases, the reliability analysis is performed by applying the method described in Chapter 5. An ABAQUS Python script file has been prepared first, which include the model and output database. All random variables were included in the script file as variables. The samples of these variables were generated in MATLAB using MCS. After completing the analysis of each sample, the resistance moment is calculated according to the normal stresses at each element as has been described in Section 7.3.

The corrosion in tendon is modelled through the strand area reduction as a function of time and the spatial randomly generated pit depth over the beam joints. The loss of bond strength and pre-stress force, due to corrosion, at each time interval is calculated in MATLAB and then included in ABAQUS through the connection of the two software which helps to automate the analysis. The file of the reliability model is submitted in HPC to reduce the time required for reliability analysis. After completing the analysis, the statistical parameters of the bridge resistance moment at each time interval have been computed.

The last part of analysis procedure is using FORM to compute the design points and the reliability index. This is done by considering the resistance moment at each time as a random variable, in addition to the random variables that are relevant to the action moment, as has been described in Section 7.2.4. Several iterations have been performed until convergence has been achieved.

The time dependent reliability analysis has been performed according to the mechanical behaviour of tendons. Stewart (2009) mentioned that the mechanical behaviour of reinforcement steel can be changed from ductile to brittle as corrosion loss increases. Therefore, to consider this effect, Stewart (2009) assumed two bounds on structural reliability, namely, (i) all reinforcement in a RC structural component exhibits ductile behaviour or (ii) all reinforcement in a RC structural component exhibits brittle behaviour. As the capacity of a perfectly brittle system is less than that of a perfectly ductile system, it follows that the actual structural reliability (P_f) of the RC structural component will lie somewhere between these structural reliabilities such that:

$$P_{f-ductile} < P_f < P_{f-brittle} \tag{7.18}$$

In this study, time dependent reliability analysis has been carried out considering the two behaviours separately. Which means, the probability of failure is estimated for the brittle behaviour by selecting the ultimate load capacity, for the beam, when the first tendon (at any joint) has reached its yield strength. While, for the ductile behaviour, the ultimate load capacity of the beam is selected when the tendon reaches its ultimate strength.

7.6 Results

The presented results are organized according to the deterministic and reliability analysis.

7.6.1 Deterministic analysis

In this analysis all random variables were defined by their mean values and, the pre-stressing corrosion is considered through strand area reduction as a function of time. Firstly, pitting corrosion is assumed to be distributed uniformly along strands, when the pitting factor has been taken equal to the mean value of 6.

According to that, the corrosion loss, measured as $(A_{pit}(t)/A_{stnom})$ (see Figure 7.31), and the maximum normalized bond strength R_b is obtained at each time interval as shown in Figure 7.32. For this case, the reduction in the beam ultimate load capacity due to corrosion only is shown in Figure 7.33.

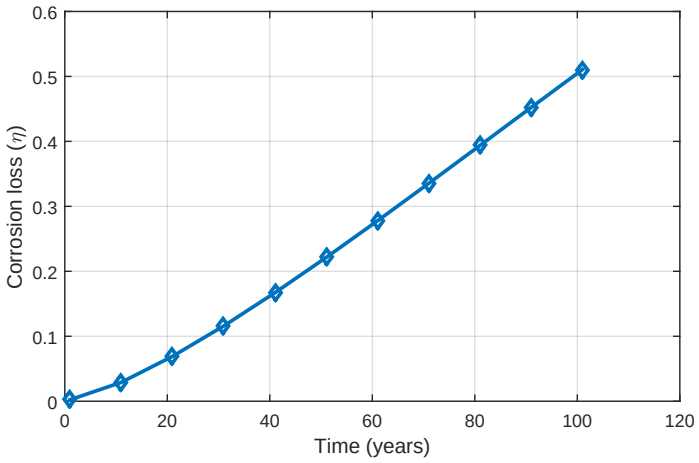


Figure 7.31: *The progress of corrosion level with the time for the deterministic analysis with using pitting factor $R = 6$*

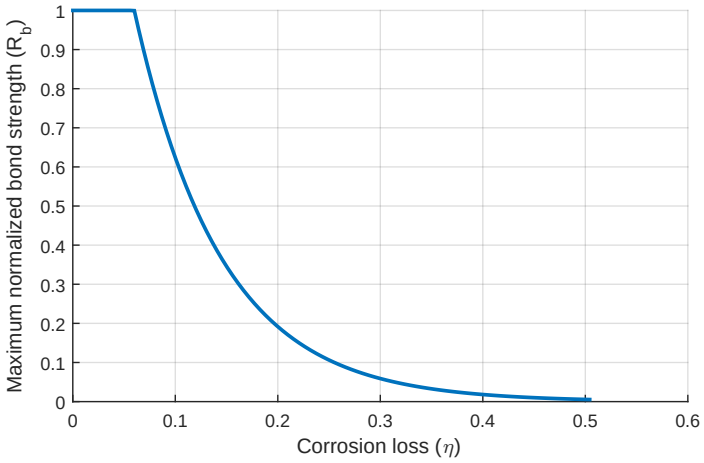


Figure 7.32: *The deterioration of maximum normalized bond strength with increasing corrosion loss, used in this study for determinstic analysis*

The bond-slip relationship is obtained in this study (see Figure 7.34) according to the improved relationship between strands and concrete (Wang et al., 2016). This constitutive law is used in ABAQUS to define the behaviour of connector

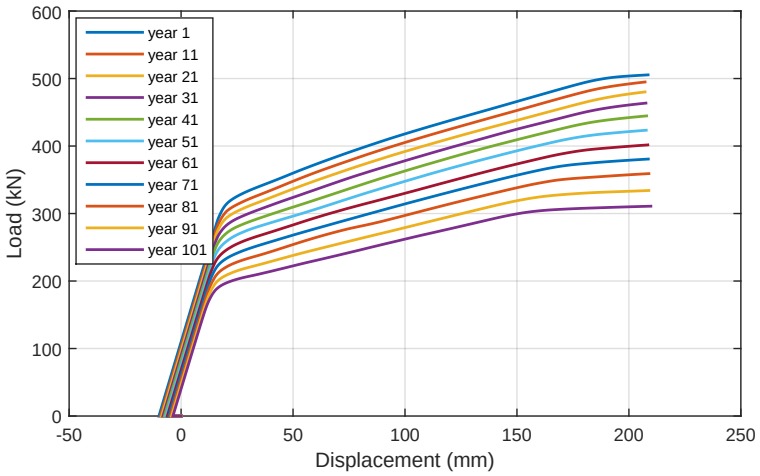


Figure 7.33: *The deterioration of beam capacity due to corrosion only*

element at each time interval. Figures 7.35 to 7.44 show the comparison between the bond behaviour of the model (from ABAQUS) and the bond-slip curves that are input to the model (mathematical bond-slip relationship).

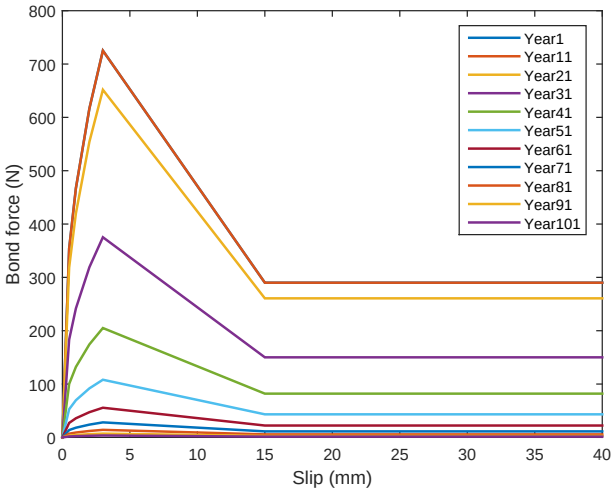


Figure 7.34: *Bond-slip relationshp input to the model*

The figures show that for the first 60 years, there is no damage in bond since the bond-slip curve stays within the elastic region. However, for years 71, 81, 91 and 101, the bond between corroded strands and concrete starts to deteriorate and the relationship reported for the bond-slip relation is mostly the same as what was input. This agreement indicates that the connector element used in this study successfully responded to the bond-slip behaviour that was input. Therefore, the formulation of the connector element was deemed satisfactory.

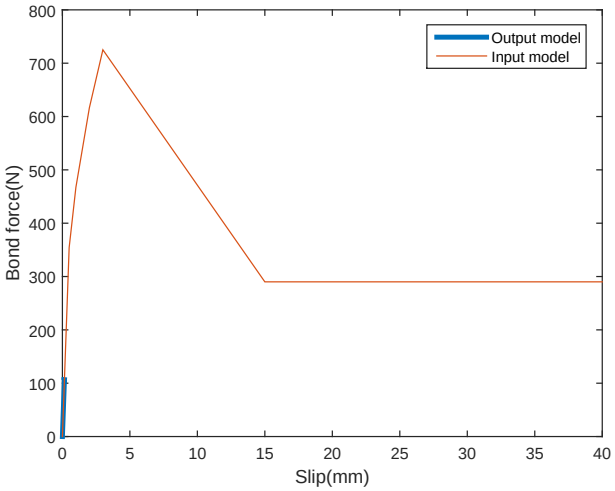


Figure 7.35: *The input and output bond-slip model for years 1 and 11*

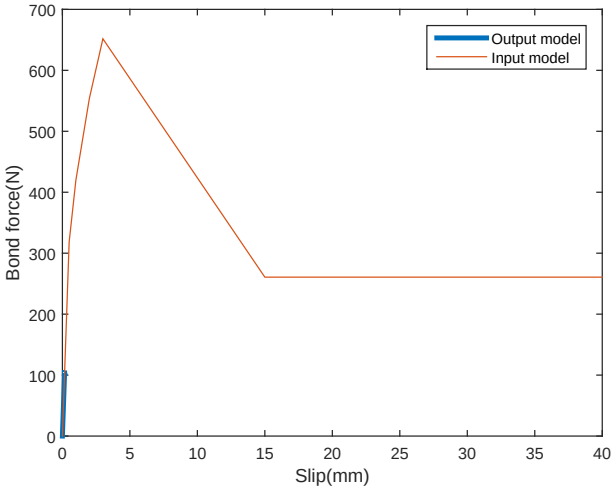


Figure 7.36: *The input and output bond-slip model for year 21*

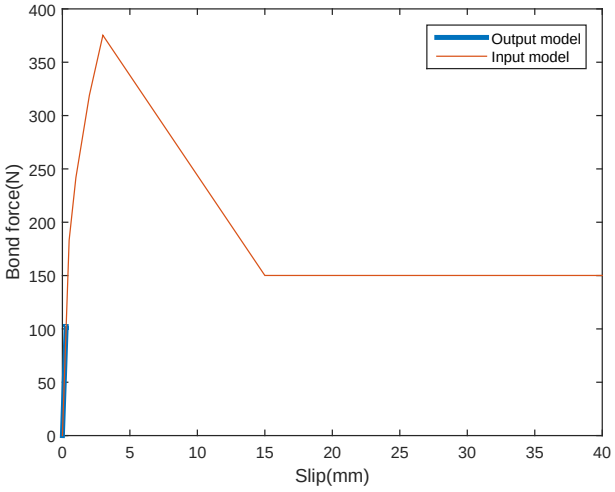


Figure 7.37: *The input and output bond-slip model for year 31*

Figure 7.45 shows the comparison of the beam ultimate load capacity of case

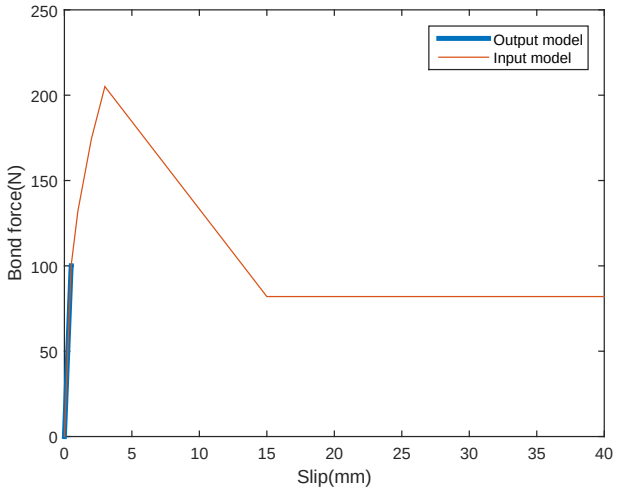


Figure 7.38: *The input and output bond-slip model for year 41*

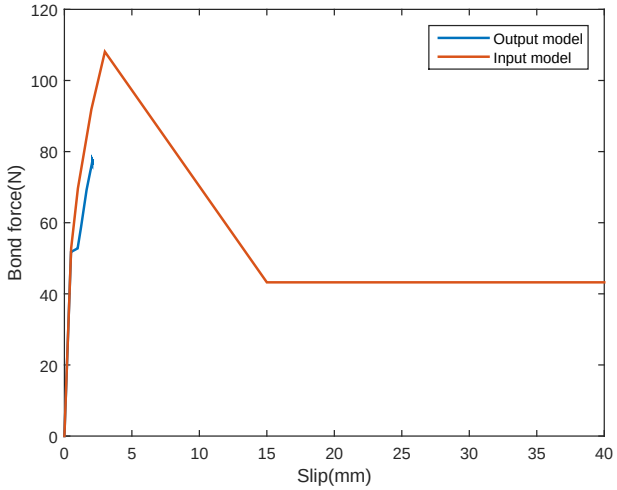


Figure 7.39: *The input and output bond-slip model for year 51*

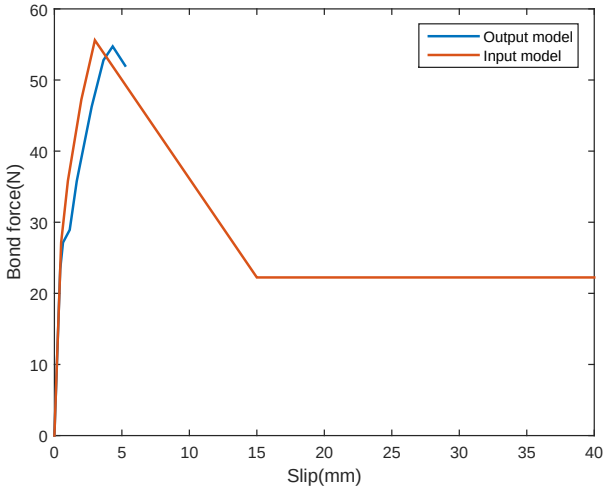


Figure 7.40: *The input and output bond-slip model for year 61*

1, case 2 and case 3 along the years. The figure shows that case 2 and case 3 exhibited similar ultimate load capacity until year 61. However, the ultimate

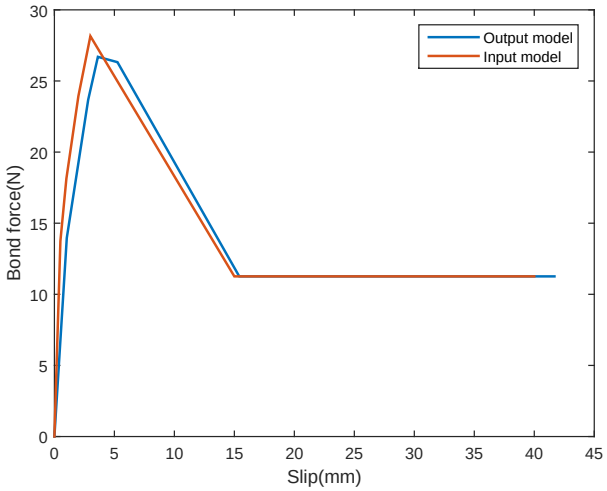


Figure 7.41: *The input and output bond-slip model for year 71*

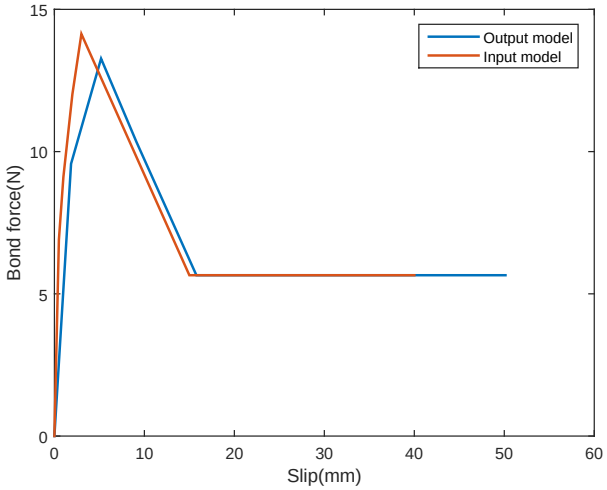


Figure 7.42: *The input and output bond-slip model for year 81*

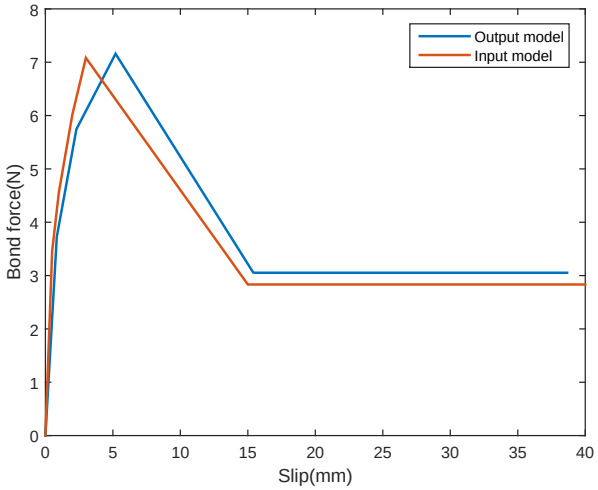


Figure 7.43: *The input and output bond-slip model for year 91*

load capacity of the beam starts to degrade in case 3 at year 71 when the corrosion loss exceed 27%. These results are similar to those obtained by Zhang

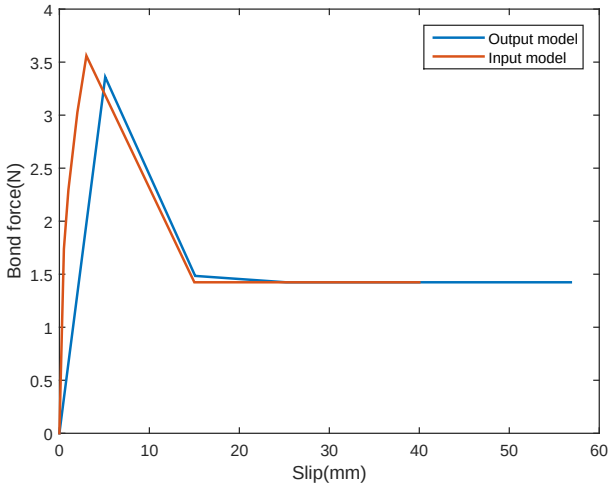


Figure 7.44: *The input and output bond-slip model for year 101*

et al. (2017) when they performed an experimental test of eight PT beams subjected to different level of corrosion in order to investigate the flexural behaviour of bonded posttensioned concrete beams under strand corrosion. Zhang et al. (2017) found that the deterioration of bond due to strands corrosion can affect the strain compatibility between strands and concrete leading to deteriorate the ultimate load capacity of the beam. However, this effect can be neglected for slightly and modestly corrosion level ($0 < \rho < 27\%$), while it has a significant effect when the corrosion loss exceeds 27%. Furthermore, Zhang et al. (2017) concluded that strand corrosion can accelerate the shifting of neutral axis and decreases the compressive concrete reducing markedly the ultimate load capacity of the beam. In this study, a corrosion loss of 22% decreases the ultimate load capacity by 17.5%, which is similar to what have been found by Zhang et al. (2017) who got a 16.7% reduction in beam capacity for 19.5% corrosion loss.

Furthermore, Zhang et al. (2017) found that for beams with slightly and modestly corrosion level, the distribution of cracks is uniform and the depth of the cracks were similar. However, when corrosion loss exceeds 27%, the distribution of cracks becomes irregular and the depth is different (see Figure 7.46). These cracks can cause the formation of main cracks and subsequently reduce the safety of the beam.

In this study, the cracks pattern for the beam with corrosion level 11% and 51%

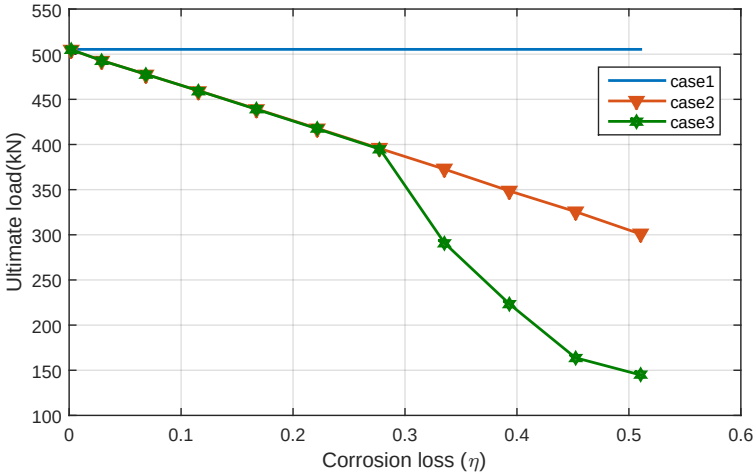
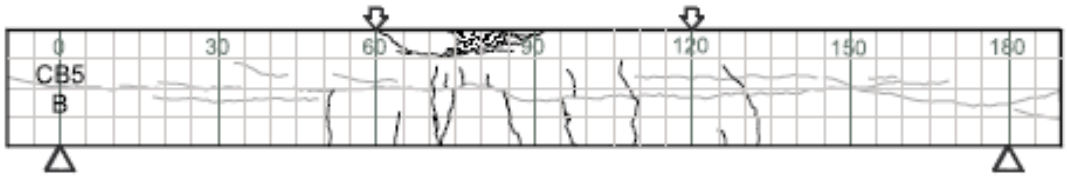
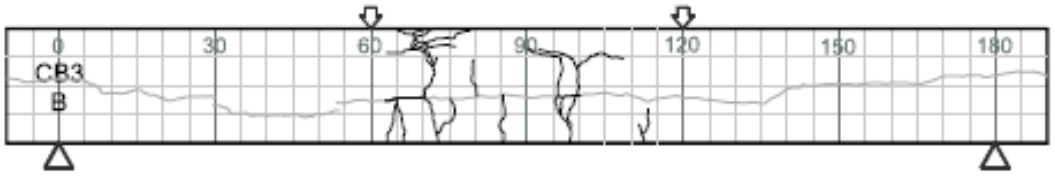


Figure 7.45: *Deterioration of the beam ultimate loads along the years in case of considering general corrosion*



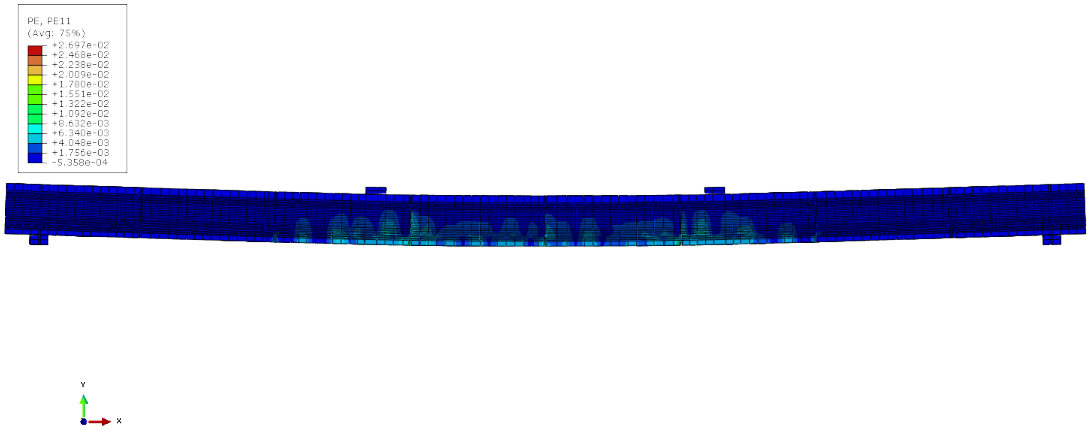
(a) η=12%



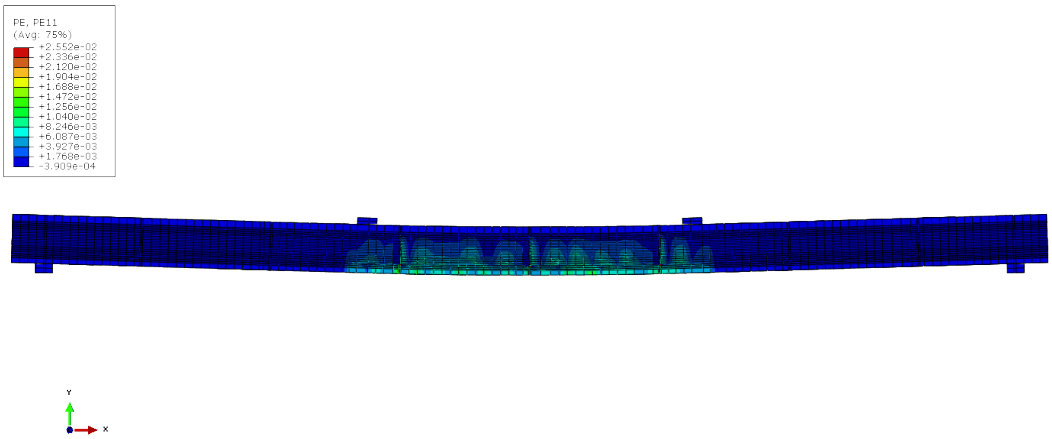
(b) η=60%

Figure 7.46: *Flextural crack distribution according to the experimental test carried out by Zhang et al. (2017) where (a) Crack distribution when η=12% and (b) Crack distribution when η=60%*

are shown in Figure 7.47. The figure shows that, for 51% corrosion level, some cracks were propagated upward to the compression zone which can make it more harmful than cracks of 11% corrosion level. In addition, for 51% corrosion level, the number of cracks are lower but they have a large spacing. These results are consistent to the results of Zhang et al. (2017). This indicates that the method used for modelling the bridge and simulating the bond deterioration using connector element works successfully.



(a) η=11%



(b) η=51%

Figure 7.47: *Flextural crack distribution of the Ynys-y-Gwas bridge according to the finite element analysis, where (a) Crack distribution when η=11% and (b) Crack distribution when η=51%*

The deterministic analysis has been repeated considering localized corrosion near the joints only. For this case, the effect of bond deterioration near joints does not have an effect on beam ultimate capacity as shown in Figure 7.48. In fact, after 45% corrosion level, the effect of bond loss leads to reduce the ultimate load capacity by less than 3% which is insignificant and it can be neglected. This is reasonable since the partial reduction of bond strength around the pitting corrosion has an insignificant effect of structural resistance (Val and Melchers, 1997).

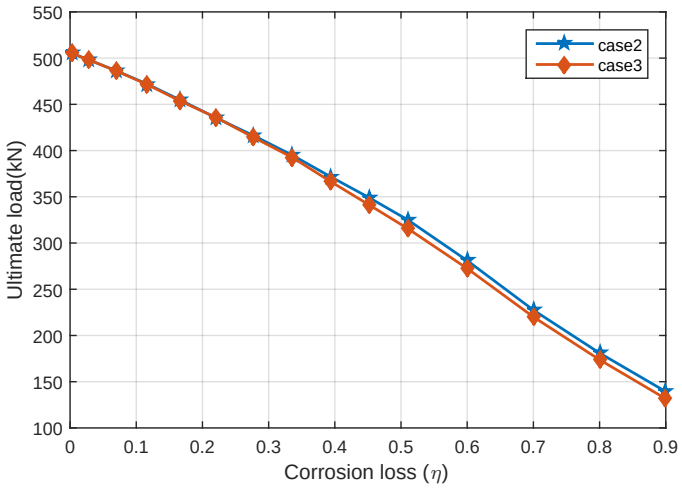


Figure 7.48: *Deterioration of the beam ultimate load, due to localized corrosion, for case 2 (area reduction) and case 3 (area and bond reduction)*

7.6.2 Time dependent reliability analysis

In reliability analysis, all variables are treated as random by including their distribution and statistical parameters (see Table 7.5) to estimate the probability of failure. Figure 7.49 shows the probability of failure and the reliability index, according to mid-section analysis condition, for the three cases considered in this study.

The figure shows the effect of strands mechanical behaviour on the annual probability of failure. The probability of failure is considerably higher (10%) when considering all reinforcement to exhibit brittle behaviour. This is consistent with the results obtained by Stewart (2009) as he found that the mechanical behaviour of reinfoecement steel has a significant effect on structural reliability and the capacity of the beam.

According to Figure 7.49, comparing case 2 and case 3, the effect of bond deterioration due to pitting corrosion can be neglected for the first 30 years, after that the results show that considering bond degradation effect increases the probability of failure by 3%. These results show that the effect of bond deterioration due to pitting corrosion has insignificant impact on the bridge reliability.

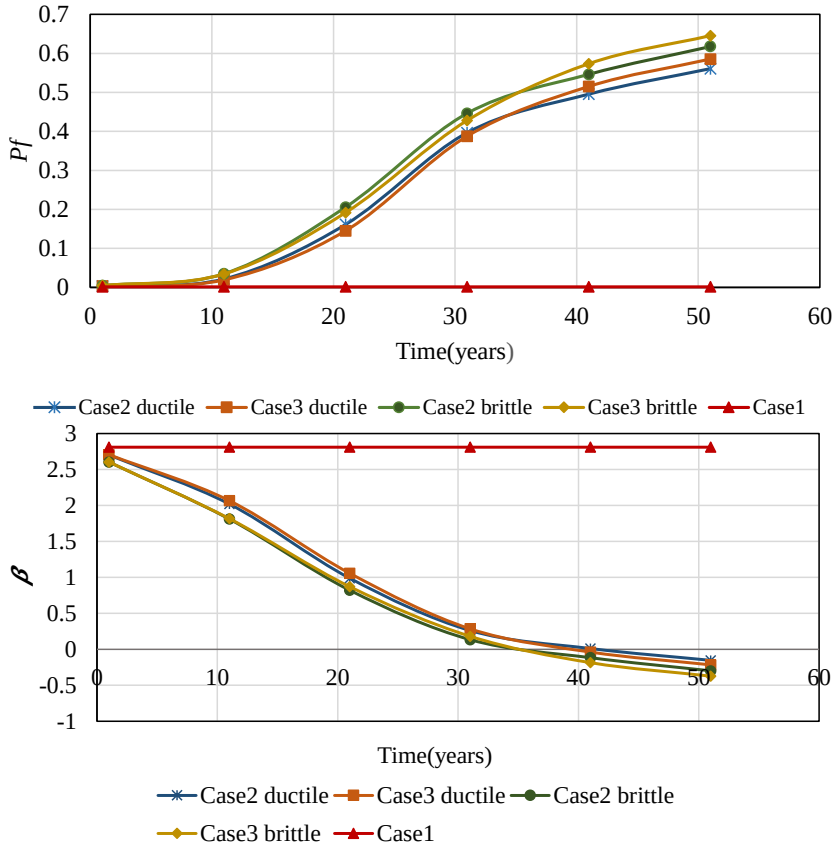


Figure 7.49: *Probability of failure (P_f) and reliability index (β) as a function of time for the three cases considering the exhibition of brittle and ductile behaviour of strands*

The results also show that the bridge reliability index when assuming no deterioration is 2.81. This value is need to be compared with the target reliability index (β_T) of RC bridges. The standard CEN (1990) recommends $\beta_T = 4.7$ for a one year reference period assuming no deterioration. Hence, by comparing the obtained reliability index with the target value, the results show that the bridge did not fulfil the reliability criterion stated in CEN (1990). That means, the bridge didn't achieve the safety requirements immediately after construction. This might be due to the poor design and the poor workmanship (Woodward and Williams, 1988). The probability of failure after 31 years is around 40% (β = 0.25) which is high enough to lead to bridge failure. This result is in accordance with BD54/15 (2015) since this standard classified the simply supported

segmental bridges with longitudinal and transverse joints and pre-stress as high risk bridges.

Figure 7.49 shows that the reliability index decrease sharply as the corrosion increases, from 2.81 in the first year to 2.025, 0.978, 0.27, 0.177 and -0.228 for years 11, 21, 31, 41 and 51 respectively. This reduction is due to the importance of the uncertainty of the resistance moment which depends on the uncertainty of corrosion rate (i_{corr}). The influence of the uncertainty of resistance moment on the bridge reliability is illustrated in Figure 7.50. The figure shows that for the first few years the weight of M_R is small, 0.197 and 0.27 for year 1 and 11 respectively. Therefore, the reliability of the bridge for the first 11 years is relatively high. As corrosion increases, the importance of M_R uncertainty increase and become more significant to reduce the reliability index of the bridge.
After 30 years, the importance of M_R uncertainty become almost constant since most tendons area have been lost and therefore, the corrosion rate has a small influence on M_R. However, the reliability index after 30 years keeps decreasing because other parameters might have an effect. Figure 7.51 shows the direction cosines at the design points of the random variables as a function of time. The figure shows that the uncertainty of θ_E has the highest weight in the analysis reaching a value of -0.73 and exhibiting a small reduction of its importance as the deterioration increase. This is followed by the knife edge load (KEL) and θ_R variables in which have a high weight in the analysis, -0.543 and 0.26 respectively. The influence of the uncertainties associated with the other parameters: permanent load (g), asphalt thickness (t_a) and the uniformly distributed load (UDL) are small since their sensitivity factors are less than 0.2 (Val and Melchers, 1997).

For the spatial analysis, the probability of failure according to the series system has been estimated, at each joint, using Ditlevsen (1979) bounds. The results show that considering the correlation between joints does not have any effect on the probability of failure as shown in Figure 7.52. On the other hand, Stewart

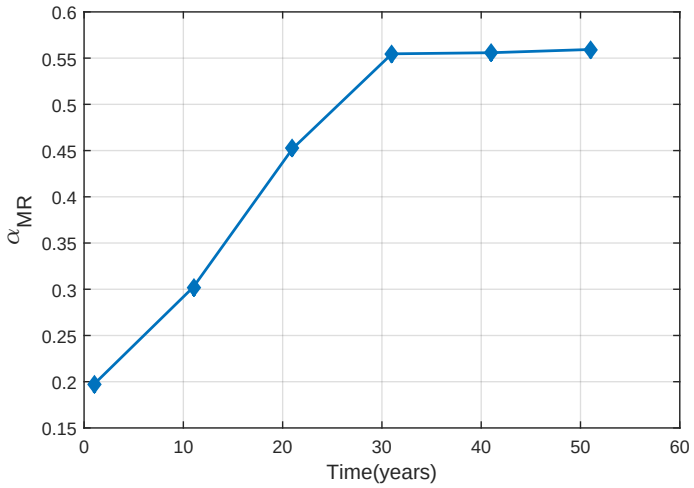


Figure 7.50: *Direction cosine values of M_R with the time for the original case (rate 1)*

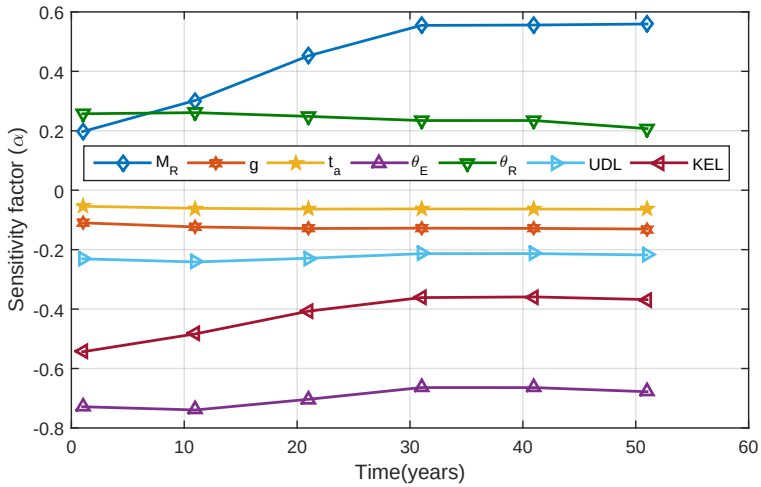


Figure 7.51: *Sensitivity factors α at the design points that give the importance of each random variables for the original case (rate 1)*

(2004) found that considering the correlation between segments due to the spatial variability of pitting corrosion gives a higher probability of failure when compared with mid-section analysis. However, the obtained results are reasonable because the values of P_f in joints 1, 2 and 3 are very low compared with the mid joint (joint 4) as shown in Figure 7.53. This indicates that the failure of the bridge has been happened at the mid segment.

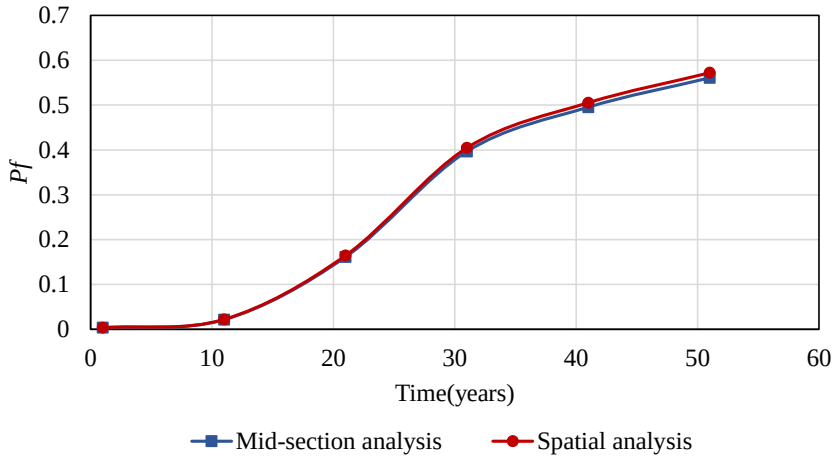


Figure 7.52: *Probability of failure P_f for a spatial and mid-section analysis*

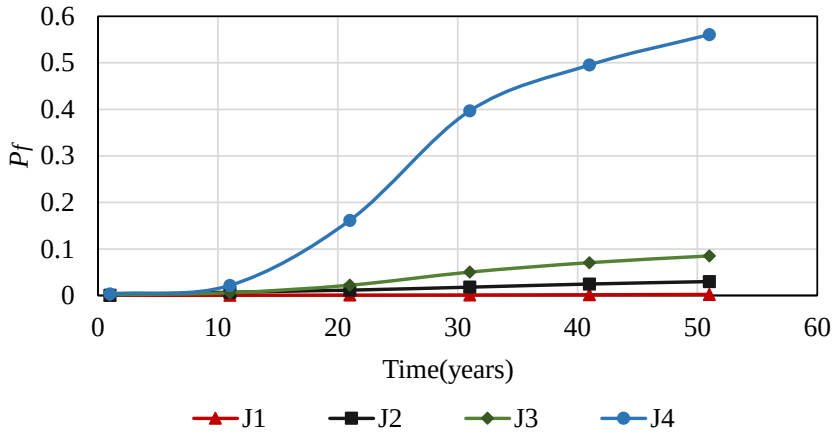


Figure 7.53: *Comparison of the probability of failure P_f of each joint*

7.7 Parametric study

As the degree of corrosion and the reduction in tendons area were estimated based on sparse data, a parametric study regarding the degree of corrosion was conducted in this study. The parameters that are related to corrosion are chloride concentration ($C(x,t)$), and corrosion rate (i_{corr}).

The chloride concentration can be used to estimate the time to corrosion initiation (t_i) as described in Section 7.2.2. In this study, the time to corrosion initiation, t_i, for the bridge was found to be equal to 0.773 year, which means that corrosion starts immediately after construction. Hence, there is no worse case than what has been found to start the corrosion and therefore, chloride concentration was

not considered in the parametric study.

The parametric study was depended on using different values of corrosion rates to study the effect of tendons area reduction on bridge reliability. Firstly, reliability analysis has been repeated with using higher corrosion rate (rate 2) at the three middle joints (3, 4 and 5) and lower corrosion rate (rate 1) (see Figure 7.54) at the remaining joints (1, 2, 6 and 7). This assumption is a result of the data in Figure 7.17 showing that the very severe corrosion condition ($\eta > 0.5$) is concentrated in joint 3 rather than the others. This analysis leads to 46% (7/15) of tendons in joint 3, 4 and 5 suffering very severe corrosion ($\eta > 0.5$) while 20% of tendons have $\eta > 0.25$. The results show that the probability of failure is considerably increased compared with the original analysis, when corrosion rate = rate 1 in all joints, as shown in Figure 7.55. These results might be more represent the actual case since the probability of failure is very high (72%) after 32 years.

The method used in this chapter can be used for any identical bridges to give the decision about the condition of these bridges. Such as, if the bridge need for maintenance, repair or need to be closed. This can be done by comparing the estimated reliability index with the target reliability index (β_T). Bridges can be inspected first to measure how corroded they are, then the probability of failure can be estimated. If the estimated probability of failure is high, then an actions need to be taken to reduce corrosion and keep the bridge safe. For instance, if the considered bridge is under service now, corrosion might be reduced by sealing the joints to reduce the penetration of chlorides. Accordingly, the probability of failure can be reduced to 20% and 3% (as shown in Figure 7.55) when reducing the corrosion rate to rate 3 and rate 4, respectively (Figure 7.54).

The sensitivity analysis shows that the weights of resistance moment increase as the corrosion rate increases and decrease with decreasing corrosion rate (Figure 7.56). This means the importance of M_R, in case of rate 2, is considerably higher than the importance of M_R in case of rate 1, while rate 3 and rate 4 give less importance. The weights of M_R along the time for each corrosion rate are

listed in Table 7.6. Figure 7.56 also shows that the weight of M_R increases with

Table 7.6: *Cosines direction of M_R along time for each corrosion rate considered in this study*

	α_{M_R}					
Years	1	11	21	31	41	51
rate 1	0.197	0.302	0.452	0.554	0.555	0.556
rate 2	0.251	0.354	0.568	0.573	0.576	0.576
rate 3	0.106	0.255	0.377	0.517	0.569	0.576
rate 4	0.09	0.126	0.184	0.267	0.297	0.369

the time as the corrosion increases. However, after a period of time the weights become constant (except for rate 4) since most tendons area has been lost and therefore, the corrosion rate has a small influence. In rate 4, the weights of M_R keeps increasing along the time because this rate is considerably low compared with the others and hence, the reduction in area stay significant after 50 years. M_R weight in rate 2 reaches its upper value (0.568) earlier than in rate 1 and rate 3. This means, in rate 2 the upper value of M_R weight has been reached after 20 years while in rate 1 and rate 3 the upper value is reached after 30 and 40 years, respectively. This is reasonable since rate 2 is higher and subsequently, the area of tendons has been lost earlier. The reduction in P_f for rate 3 and rate 4 was due to the reduction in weight of M_R comparing with rate 1 and rate 2. The remaining parameters have the same influence as they have for rate 1 and rate 2. Therefore, it can be concluded that the uncertainty of resistance moment, which depends mainly on corrosion rate, has a great effect on bridge reliability since its importance increased with the time as the corrosion increase. The results also show that after 32 years, corrosion rate was needed to be less than 1 to keep the bridge safe.

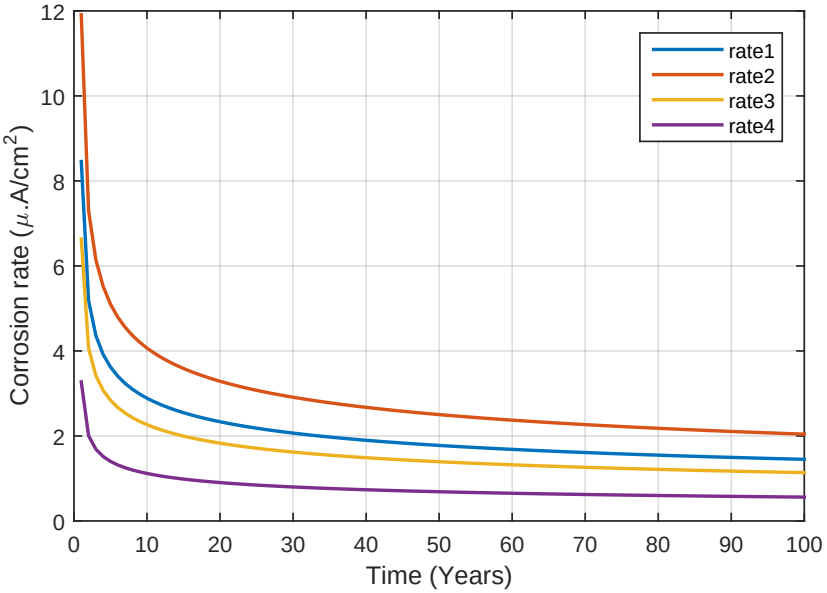


Figure 7.54: *Reduction of corrosion rates with the time used in this study*

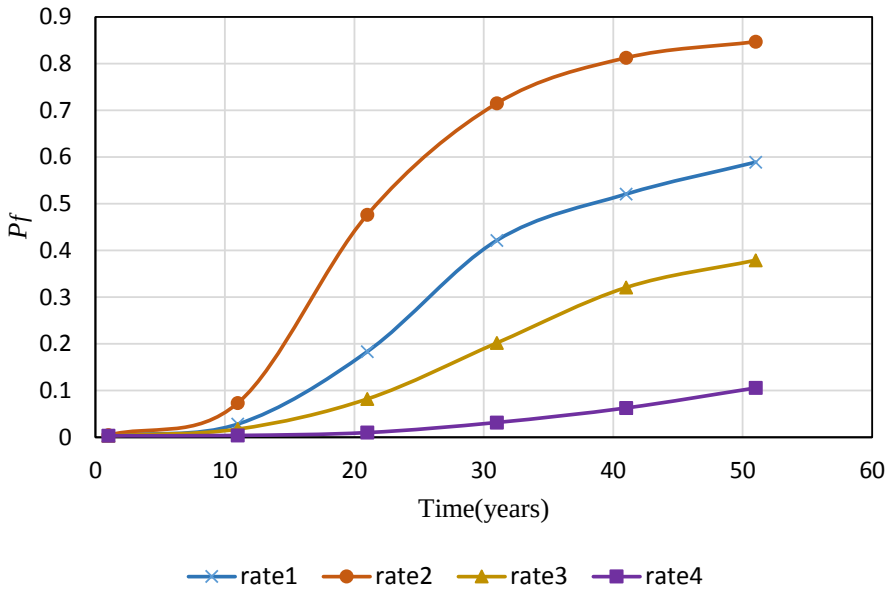


Figure 7.55: *Probability of failure P_f for different corrosion rates*

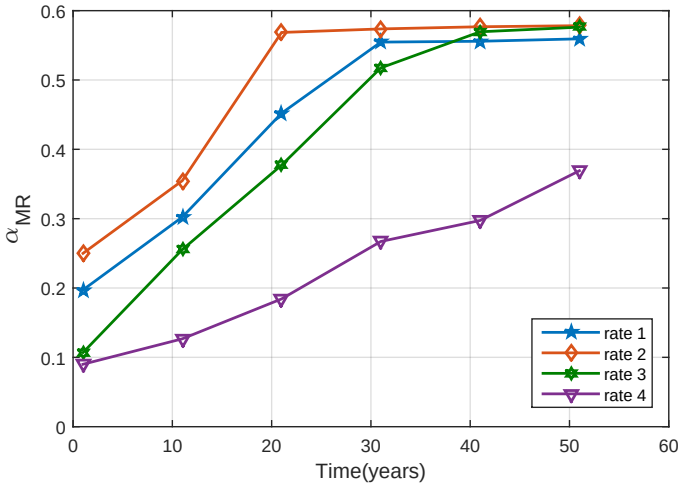


Figure 7.56: *Direction cosine values of M_R with the time for the four rates considered. The figure shows the influence of M_R uncertainty on reliability analysis*

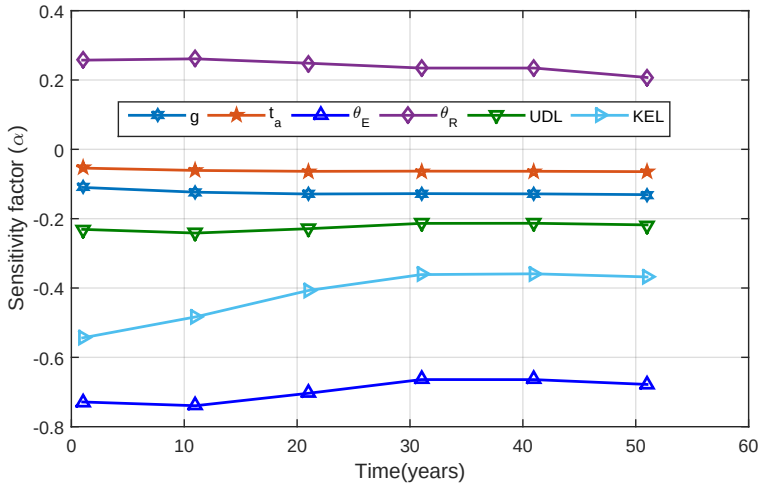


Figure 7.57: *Sensitivity factors α at the design points that gives the importance of each random variables for the four rates considered*

7.8 Summary

This chapter presented a time-dependent reliability analysis of an existing post-tensioned concrete bridge. Three case have been considered and compared: i) assuming no deterioration due to corrosion and bond loss, ii) deterioration due to corrosion only (assuming full bond), iii) deterioration due to corrosion and bond loss. For the first two cases, embedded region has been used to represent the full bond condition while for case 3, connector element with non-linear behaviour has been used to model the bond degradation due to corrosion.

For deterministic analysis, when assuming the pitting corrosion to be uniformly distributed, the effect of bond degradation is very significant when corrosion loss exceeds 27%. However, it has a negligible effect when corrosion level is less than or equal 27%. In the case of localized corrosion, the effect of bond can be neglected, as, when corrosion loss exceeds 40%, the ultimate load capacity reduces by 3% comparing with the full bond condition. These results compared well with experimental works in the literature which indicates that the method applied for bridge modelling and bond simulating were successfully executed. Furthermore, considering bond degradation using connector element, in finite element, for PT concrete beam under flexural load is performed for the first time in this study.

For reliability analysis, the safety margin of the bridge has been assessed in terms of reliability index β which is quiet low when it was compared with target reliability index for a one year reference period. That means the bridge has not been appropriately designed and was not achieved the safety requirements at the time of construction. Therefore, the probability of failure after 31 years was very high that lead to bridge failure. The fully probabilistic non-linear method that is used in this study can be successfully used in the assessment of the existing segmental posttensioned bridges, since they need for a regular inspection due to their risk to corrosion.

Chapter 8

Conclusions and Recommendations

8.1 Summary and main conclusions

In this thesis, the reliability of a deteriorated segmental post-tensioned concrete bridge is studied. The main aim is to establish a framework to assess the reliability of these structures. Post-tensioned concrete bridges are an important element of the traffic network since they offered many benefits to the economy and the construction industry of bridges. This is when they behave well throughout their service life when properly constructed and maintained. However, these structures could be most at risk due to the presence of joints between segments and voids within the ducts in which they can increase chloride penetration through the bridge. Consequently, there is always a need to ensure that these bridges are properly maintained in a safe and serviceable condition. This can be done by a periodic on-site inspections to make a clear decision about the condition of the bridge. However, the results of these inspections are usually poor and have a high degree of uncertainty due to the incomplete information as it is only possible to inspect a small sample of ducts. Hence, decision making regarding the existing segmental post-tensioned concrete bridges is done in UK according BD54/15

(2015). It is a risk based method, mostly qualitative and based on the exposure condition and the definition of critical sections followed by inspection and non-destructive testing. The approach followed in this thesis is similar but tries to quantify risk using reliability analysis method. Reliability analysis methods are increasingly used for the evaluation and assessment of risk of concrete structures.

After a short introduction, in Chapter 2 a literature review on structural reliability, focusing the main issues of this topic is presented. This chapter intends to give the theoretical background about the principles of reliability analysis that served as the basis of this thesis.

Chapter 3 addresses FORM method 2 as the most appropriate method (as a branch of FORM method) used in reliability analysis since it can be used for the complicated performance function (nonlinear limit state function) by using a Newton-type recursive formula. In addition, FORM method 2 can be used for the normal and non-normal variables. However, this method is only applicable for problems with an explicit limit state function. For an implicit limit state function, MCS is an alternative method, which can be used to estimate the reliability of structure. However, this method is not likely to be used in practical problems since a large number of simulations are required to estimate the reliability of structure and that could be take a very long time to complete. For such cases, different methods should be used as it has been explained and used in Chapter 5. In this chapter, the two methods (FORM method 2 and MCS) have been applied on a simple example of RC beam subjected to corrosion. The computed reliability index is reduced sharply with the time due to the aggressive environmental condition considered in this study. The analysis results also show that ignoring the uncertainty of corrosion rate and area of steel can significantly reduce the reliability of the beam. The importance of corrosion rate increases with the increasing of corrosion and consequently increase the probability of failure. The analysis results also show that ignoring the uncertainties of load and

resistance model significantly increases the reliability index by 23%. Therefore, it is very important to consider the load and resistance model uncertainties in reliability analysis. The reliability indices, of the beam, that have been obtained from FORM method are very close to that obtained from MCS which indicates that the two methods have the capability to estimate the reliability of the beam.

In Chapter 4, a numerical models for four RC beams, that were tested experimentally by Barros and Fortes (2005) have been developed. The developed FE models intended to simulate the nonlinear behaviour of the RC beams using CDP model to represent the post-cracking behaviour of concrete. A sensitivity analysis study on the CDP model parameter, viscosity parameter μ, is presented. The numerical results compare well with the published experimental data by giving a small differences (less than 10% for the comparison of the ultimate load and the vertical displacement). These results demonstrate the effectiveness of the CDP model. For the viscosity parameter sensitivity analysis, the results show a value between 10^{-4} and 10^{-5} gives a good agreement with the experimental results. This recommended value of viscosity parameter is in a good agreement with the previous numerical test that has been carried out by Szczecina and Winnicki (2015).

The developed numerical models allow characterising in a more realistic manner the RC beams since they consider the full nonlinear behaviour of the beams. Based on this, a finite element model was used in Chapter 6 to model the actual behaviour of the bridge in time dependent reliability analysis. However, using the numerical model is computationally more expensive especially when it is used with time dependent reliability analysis because of the high number of runs needed for each iteration. Based on this, in Chapter 5, a new method which depends on the connection between MATLAB and ABAQUS Python script file has been exploited to reduce the time required for reliability analysis by automating the processing. This method is used in conjunction with HPC to apply time dependent reliability analysis on a deteriorated simply supported RC beam.

Two methods have been used to estimate the reliability of the beam: i) MCS with FORM and ii) ANN-based FORM. The two methods have been successfully estimated the reliability of the beam and they show a good agreement with a very small difference (0.0029%) between them. The results also show that the effect of corrosion was very significant on the ultimate and flexural capacity of the beam. The percentage reduction in ultimate capacity were in accordance with the findings of Malumbela et al. (2010) in which they found that for every 1% maximum mass loss of steel there was a corresponding 0.7% reduction in the ultimate capacity of the beam.

The most important parameter for the analysis are traffic loads, followed by model uncertainties. This means that a correct definition of traffic load CoV is fundamental since it can drastically impact results. The weight of the resistance moment increased with the time as the corrosion increase.

The method used in this chapter shows its applicability and efficiency to automate the repetitive tasks which can help to simplify the analysis, generate a multiple simulations easily and minimize the time.

In Chapter 7, this method is used to assess the reliability of the Ynys-y-Gwas bridge. The numerical model of the bridge, in Chapter 6, depended on data from the bridge produced when its failure was investigated (Woodward and Williams, 1988) in terms of geometry, material properties and corrosion level. The numerical model considers the tendon corrosion by reducing the area of tendon near the joints. The area reduction with time depended on several parameters: the corrosion rate, time to corrosion initiation and pitting factor. These parameters were calculated according to the bridge chloride concentrations, near the joints, at the time of failure as it has been recorded in Woodward and Williams (1988). The estimated time to corrosion initiation was very small (0.773 years) which means it was likely that corrosion attacked the bridge immediately after construction.

The effect of bond degradation due to corrosion is considered (for the first time in PT bridges under flexural loading) in the numerical model using connector element. The improved constitutive law (Wang et al., 2016) of bond-slip between

concrete and strands has been used to represent the behaviour of connector element.

For deterministic analysis, the results allow the conclusion that the connector element successfully represents deterioration of bond since there was a good agreement between the mathematical input and output behaviour. Furthermore, good agreement between the obtained and experimental results, presented by Zhang et al. (2017) was also found.

The time dependent reliability analysis considers the tendons corrosion by using existing analytical model to account for the temporal variation of tendons area reduction. For reliability analysis, the initial reliability index is lower than the Eurocode 2 (CEN, 1990) requirements. Localized corrosion reduced the reliability index to nearly zero (0.27) in a period of 30 years which represent the time of failure.

The knife edge load and the resistance model uncertainties are the most important variables for this analysis. The importance of the knife edge load reduces with corrosion, whereas resistance moment increases its weight. The sensitivity analysis also shows that the importance of the resistance moment is highly affected by increasing and decreasing the amount of corrosion while the other variables have the same influence. This indicates the influence of corrosion on bridge reliability.

All the above creates a framework to assess the reliability of segmental post-tensioned concrete bridges. This means that the main aim of this thesis has been achieved. The proposed framework can be used by engineers and researchers as a tool to support decision for segmental PT bridges maintenance since they need for a regular inspection due to their risk to corrosion. This can be done by comparing the estimated reliability index with the target reliability index (β_T).

8.2 Recommendations for future work

During the research some areas were identified that required for further study to provide more accurate characterisation manner of the PT concrete bridges. Among those, the most significant ones include the usage of the uniform capacity length which represents the length of steel element in which localized corrosion will have a harmful effect on structural capacity. This length is very important because it can simulate the extent of pitting corrosion along the steel. In this thesis, this length did not represent the actual extent of pitting corrosion along tendons, due to numerical convergence problems. Therefore, addressing this problem is of great interest for future research in reliability analysis.

Moreover, flexural was the only failure mode considered in this study. Nevertheless, the shear failure mode was also has a small contribution to bridge failure. Applying reliability analysis, using numerical model, with this failure mode is of great necessity for further study.

Further numerical work should be conducted considering the effect of voids in post-tensioning ducts on the corrosion of the tendons. The presence of voids inside the ducts can accelerate the corrosion of strands resulting in tendon failure and subsequently the reliability of structures. Additionally, consideration should be given to the effect of the climate change on accelerating the corrosion in segmental post-tensioned concrete bridges. The environmental change is mainly influenced by the climate change caused by the global warming and pollution. Rising temperature will increase the rates of corrosion and subsequently decrease the reliability of structures.

Bibliography

ABAQUS, P. (2013). Documentation, ABAQUS User's Manual Part I-VII. *DS Simulia*.

Andrade, C. & Alonso, C. (1996). Corrosion rate monitoring in the laboratory and on-site. *Construction and Building Materials*, 10(5):315–328.

Attard, M. M. & Stewart, M. G. (1998). A two parameter stress block for high-strength concrete. *Structural Journal*, 95(3):305–317.

Azizinamini, A., Stark, M., Roller, J. J., & Ghosh, S. K. (1993). Bond performance of reinforcing bars embedded in high-strength concrete. *Structural Journal*, 90(5):554–561.

Barbosa, A., Idelsohn, S., Oñate, E., Dvorkin, E., et al. (1998). Analysis of reinforced concrete structures using ansys nonlinear concrete model.

Barros, J. A. & Fortes, A. (2005). Flexural strengthening of concrete beams with CFRP laminates bonded into slits. *Cement and Concrete Composites*, 27(4):471–480.

Bastidas-Arteaga, E., Bressolette, P., Chateauneuf, A., & Sánchez-Silva, M. (2009). Probabilistic lifetime assessment of rc structures under coupled corrosion–fatigue deterioration processes. *Structural safety*, 31(1):84–96.

Bastidas-Arteaga, E., Chateauneuf, A., Sánchez-Silva, M., Bressolette, P., &

Schoefs, F. (2010). Influence of weather and global warming in chloride ingress into concrete: A stochastic approach. *Structural Safety*, 32(4):238–249.

Bathurst, R. J. & Javankhoshdel, S. (2017). Influence of model type, bias and input parameter variability on reliability analysis for simple limit states in soil–structure interaction problems. *Georisk: Assessment and Management of Risk for Engineered Systems and Geohazards*, 11(1):42–54.

BD54/15 (2015). Management of post-tensioned concrete bridges.

Belarbi, A. & Hsu, T. T. (1994). Constitutive laws of concrete in tension and reinforcing bars stiffened by concrete. *Structural Journal*, 91(4):465–474.

Belarbi, A., Zhang, L., & Hsu, T. T. (1996). Constitutive laws of reinforced concrete membrane elements. In: *Sociedad Mexicana de Ingenieria Sismica in World Conference On Earthquake Engineering*, pages 1–8.

Benaissa, K., Abdellatif, K., et al. (2015). Reliability analysis of reinforced concrete buildings: comparison between FORM and ISM. *Procedia Engineering*, 114:650–657.

Broomfield, J. (1994). Corrosion rate measurements in reinforced concrete structures by a linear polarization device. *Special Publication*, 151:163–182.

Buyukozturk, O. & Shareef, S. S. (1985). Constitutive modeling of concrete in finite element analysis. *Computers & structures*, 21(3):581–610.

Cady, P. D. & Weyers, R. E. (1983). Chloride penetration and the deterioration of concrete bridge decks. *Cement, concrete and aggregates*, 5(2):81–87.

Capra, B., Bernard, O., & Gerard, B. (2003). Reliability assessment of a reinforced concrete beam subjected to corrosion. In: *Transactions of the 17th International Conference on Structural Mechanics in Reactor Technology*, pages 1–8.

Cardoso, J. B., de Almeida, J. R., Dias, J. M., & Coelho, P. G. (2008). Structural reliability analysis using monte carlo simulation and neural networks. *Advances in Engineering Software*, 39(6):505–513.

Carstensen, J. V. (2011). *Modelling of Reinforced Concrete at Elevated Temperatures*. PhD thesis, Technical University of Denmark, DTU, DK-2800 Kgs. Lyngby, Denmark.

CEB (1992). CEB-FIP Model Code 1990: Design Code. London. T. Telford.

CEN, E. (1990). Eurocode 2 Basis of Structural Design. European Committee for Standardization, 2002.

Chojaczyk, A., Teixeira, A., Neves, L. C., Cardoso, J., & Soares, C. G. (2015). Review and application of artificial neural networks models in reliability analysis of steel structures. *Structural Safety*, 52:78–89.

Clark, L. A. (1983). *Concrete bridge design to BS 5400*. Number Monograph.

Cornell, C. A. (1969). A probability-based structural code. In: *Journal Proceedings*, volume 66, pages 974–985.

Daily, S. F. (1999). *Understanding corrosion and cathodic protection of reinforced concrete structures*. Corrpro Companies, Incorporated.

Darmawan, M. (2010). Pitting corrosion model for reinforced concrete structures in a chloride environment. *Magazine of Concrete Research*, 62(2):91–101.

Darmawan, M. S. (2009). Pitting corrosion model for partial prestressed concrete (pc) structures in a chloride environment. *IPTEK The Journal for Technology and Science*, 20(3).

Darmawan, M. S. & Stewart, M. G. (2007). Spatial time-dependent reliability analysis of corroding pretensioned prestressed concrete bridge girders. *Structural Safety*, 29(1):16–31.

Das, P. C. & Frangopol, D. M. (2001). *Current and Future Trends in Bridge Design, Construction and Maintenance: Safety, Economy, Sustainability, and Aesthetics*, volume 2. Thomas Telford.

de Terán, J. R. D. & Haach, V. G. (2017). Crack opening prediction at casting joints with a new modified stress-strain law for embedded reinforcement. *Construction and Building Materials*, 157:668–675.

Dhir, R., Jones, M., & McCarthy, M. (1994). PFA concrete: Chloride-induced reinforcement corrosion. *Magazine of Concrete Research*, 46(169):269–277.

Ditlevsen, O. (1979). Narrow reliability bounds for structural systems. *Journal of structural mechanics*, 7(4):453–472.

Du, Y., Clark, L., & Chan, A. (2005). Residual capacity of corroded reinforcing bars. *Magazine of Concrete Research*, 57(3):135–147.

Dujmovic, D., Androic, B., & Lukacevic, I. (2015). *Composite Structures According to Eurocode 4: Worked Examples*. John Wiley & Sons.

Elfergani, H. A., Pullin, R., & Holford, K. M. (2013). Damage assessment of corrosion in prestressed concrete by acoustic emission. *Construction and Building Materials*, 40:925–933.

Elhewy, A. H., Mesbahi, E., & Pu, Y. (2006). Reliability analysis of structures using neural network method. *Probabilistic Engineering Mechanics*, 21(1):44–53.

Ellingwood, B. (1980). *Development of a probability based load criterion for American National Standard A58: Building code requirements for minimum design loads in buildings and other structures*, volume 13. US Department of Commerce, National Bureau of Standards.

Estes, A. C. (1997). *A System Reliability Approach to the Lifetime Optimization of Inspection and Repair of Highway Bridges*. PhD Thesis. Technical report, University of Colorado.

Eurocode-2 (2004). *Eurocode 2: Design of Concrete Structures: Part 1-1: General Rules and Rules for Buildings*. British Standards Institution.

Faber, M. H. (2005). Risk and safety in civil, surveying and environmental engineering. Technical report, Swiss Federal Institute of Technology.

Frangopol, D. M. & Hearn, G. (1996). *Structural Reliability in Bridge Engineering: Design, Inspection, Assessment, Rehabilitation and Management: Proceedings of the Workshop on Structural Reliabity in Bridge Engineering, Organized by the University of Colorado at Boulder, Colorado, Boulder, Colorado, October 2-4, 1996*. MCGraw-Hill.

Frangopol, D. M., Lin, K.-Y., & Estes, A. C. (1997). Reliability of reinforced concrete girders under corrosion attack. *Journal of Structural Engineering*, 123(3):286–297.

Ganji, A. & Jowkarshorijeh, L. (2012). Advance first order second moment (AFOSM) method for single reservoir operation reliability analysis: a case study. *Stochastic Environmental Research and Risk Assessment*, 26(1):33–42.

Gilbert, R. I., Mickleborough, N. C., & Ranzi, G. (2017). *Design of Prestressed Concrete to Eurocode 2*. CRC Press.

Gomes, H. M. & Awruch, A. M. (2004). Comparison of response surface and neural network with other methods for structural reliability analysis. *Structural safety*, 26(1):49–67.

Gonzalez, J., Andrade, C., Alonso, C., & Feliu, S. (1995). Comparison of rates of general corrosion and maximum pitting penetration on concrete embedded steel reinforcement. *Cement and Concrete Research*, 25(2):257–264.

Gumbel, E. (1958). Statistics of extremes. 1958. *Columbia Univ. press, New York*, 247.

Guo, T., Chen, Z., Liu, T., & Han, D. (2016). Time-dependent reliability of strengthened psc box-girder bridge using phased and incremental static analyses. *Engineering structures*, 117:358–371.

Guo, T., Sause, R., Frangopol, D. M., & Li, A. (2010). Time-dependent reliability of psc box-girder bridge considering creep, shrinkage, and corrosion. *Journal of Bridge Engineering*, 16(1):29–43.

Hackl, J. & Kohler, J. (2016). Reliability assessment of deteriorating reinforced concrete structures by representing the coupled effect of corrosion initiation and progression by bayesian networks. *Structural Safety*, 62:12–23.

Hajializadeh, D., Stewart, M. G., Enright, B., & OBrien, E. (2016). Spatial time-dependent reliability analysis of reinforced concrete slab bridges subject to realistic traffic loading. *Structure and Infrastructure Engineering*, 12(9):1137–1152.

Han, L.-H., Yao, G.-H., & Tao, Z. (2007). Performance of concrete-filled thin-walled steel tubes under pure torsion. *Thin-Walled Structures*, 45(1):24–36.

Haskett, M., Oehlers, D. J., & Ali, M. M. (2008). Local and global bond characteristics of steel reinforcing bars. *Engineering Structures*, 30(2):376–383.

Hasofer, A. M. & Lind, N. C. (1974). Exact and invariant second-moment code format. *Journal of the Engineering Mechanics division*, 100(1):111–121.

Hawn, D. (1977). Extreme value prediction of maximum pits on pipelines. *Mater. Performance;(United States)*, 16.

Hewson, N. R. (2003). *Prestressed concrete bridges: design and construction*. Thomas Telford.

Hobbs, D. W. (1998). Minimum requirements for durable concrete: carbonation- and chloride-induced corrosion, freeze-thaw attack and chemical attack. *Crowthorn (UK): British Cement Association*.

Hoffman, P. & Weyers, R. (1994). Predicting critical chloride levels in concrete bridge decks. *Structural safety and reliability: Proceedings of ICOSSAR*, 93:957–959.

Jacinto, L., Pipa, M., Neves, L. A., & Santos, L. O. (2012). Probabilistic models for mechanical properties of prestressing strands. *Construction and Building Materials*, 36:84–89.

JCSS (2001). Probabilistic model code. joint committee on structural safety. *URL: http://www.jcss.byg.dtu.dk/Probabilistic*.

Kaylor, H. (1954). A recently built road bridge in prestressed concrete. *Civ. Engng Publ. Wks Rev.*, 49(580):1061–1063.

Kmiecik, P. & Kamiński, M. (2011). Modelling of reinforced concrete structures and composite structures with concrete strength degradation taken into consideration. *Archives of Civil and Mechanical Engineering*, 11(3):623–636.

Kwak, H.-G. & Filippou, F. C. (1990). *Finite element analysis of reinforced concrete structures under monotonic loads*. Research report of Department of Civil Engineering, University of California Berkeley, CA, USA.

Lee, H.-S., Noguchi, T., & Tomosawa, F. (2002). Evaluation of the bond properties between concrete and reinforcement as a function of the degree of reinforcement corrosion. *Cement and Concrete research*, 32(8):1313–1318.

Lee, J. & Fenves, G. L. (1998). Plastic-damage model for cyclic loading of concrete structures. *Journal of engineering mechanics*, 124(8):892–900.

Leitch, R. D. et al. (1995). Reliability analysis for engineers: an introduction. *OUP Catalogue*.

Li, C., Xu, H., & Yuan, X. (2007). Research on risk in long-term reservoir dynamic probability scheduling. In: *Natural Computation, 2007. ICNC 2007. Third International Conference on*, volume 5, pages 84–87. IEEE.

Li, C.-Q., Melchers, R. E., & Zheng, J.-J. (2006). Analytical model for corrosion-induced crack width in reinforced concrete structures. *ACI Structural Journal*, 103(4).

Liu, T. & Weyers, R. (1998). Modeling the dynamic corrosion process in chloride contaminated concrete structures. *Cement and Concrete Research*, 28(3):365–379.

Lubliner, J., Oliver, J., Oller, S., & Onate, E. (1989). A plastic-damage model for concrete. *International Journal of solids and structures*, 25(3):299–326.

Mahadevan, S. & Haldar, A. (2000). Probability, reliability and statistical method in engineering design.

Malkawi, A. I. H., Hassan, W. F., & Abdulla, F. A. (2000). Uncertainty and reliability analysis applied to slope stability. *Structural safety*, 22(2):161–187.

Malumbela, G., Alexander, M., & Moyo, P. (2010). Variation of steel loss and its effect on the ultimate flexural capacity of rc beams corroded and repaired under load. *Construction and Building Materials*, 24(6):1051–1059.

McCulloch, W. S. & Pitts, W. (1943). A logical calculus of the ideas immanent in nervous activity. *The Bulletin of Mathematical Biophysics*, 5(4):115–133.

Mehta, P. K. (1991). Concrete in the marine environment.

Melchers, R. (1999). Structural Reliability Analysis and Prediction. *Baffins Lane, Chichester, West Sussex, England: Wiley.*

Melchers, R. E. & Beck, A. T. (2017). *Structural reliability analysis and prediction.* John Wiley & Sons.

Middleton, C. & Hogg, V. (1998). Review of deterioration models used to predict corrosion in reinforced concrete structures. Cambridge University.

Mirza, S. A., Kikuchi, D. K., & MacGregor, J. G. (1980). Flexural strength reduction factor for bonded prestressed concrete beams. In: *Journal Proceedings*, volume 77, pages 237–246.

Mirza, S. A. & MacGregor, J. G. (1979). Variations in dimensions of reinforced concrete members. *Journal of the Structural Division*, 105(4):751–766.

Mirza, S. A., MacGregor, J. G., & Hatzinikolas, M. (1979). Statistical descriptions of strength of concrete. *Journal of the Structural Division*, 105(6):1021–1037.

Mohammed, A. & Osman, A. (2013). *Assessment of bonded post-tensioned concrete with ruptured tendons*. PhD thesis, University of Nottingham.

Mosley, W. H., Hulse, R., & Bungey, J. H. (2012). *Reinforced Concrete Design: to Eurocode 2*. Palgrave macmillan.

Nguyen, V.-S., Jeong, M. C., Han, T. S., & Kong, J. S. (2013). Reliability-based optimisation design of post-tensioned concrete box girder bridges considering pitting corrosion attack. *Structure and Infrastructure Engineering*, 9(1):78–96.

Nowak, A. S. (1993). Live load model for highway bridges. *Structural safety*, 13(1):53–66.

Nowak, A. S. (1995). Calibration of LRFD bridge code. *Journal of Structural Engineering*, 121(8):1245–1251.

Nowak, A. S. & Collins, K. R. (2012). *Reliability of structures*. CRC Press.

Nowak, A. S. & Szerszen, M. M. (1998). Bridge load and resistance models. *Engineering structures*, 20(11):985–990.

Otieno, M., Beushausen, H., & Alexander, M. (2011). Prediction of corrosion rate in RC structures-a critical review. In: *Modelling of Corroding Concrete Structures*, pages 15–37. Springer.

Ožbolt, J., Oršanić, F., Balabanić, G., & Kušter, M. (2012). Modeling damage in concrete caused by corrosion of reinforcement: coupled 3D FE model. *International journal of fracture*, 178(1-2):233–244.

Pankaj (1990). *Finite element analysis in strain softening and localisation problems*. PhD thesis, University College of Swansea.

Papadakis, V., Roumeliotis, A., Fardis, M., & Vagenas, C. (1996). Mathematical modelling of chloride effect on concrete durability and protection measures. *Concrete repair, rehabilitation and protection*, pages 165–174.

Pearson-Kirk, D. (2014). Managing post-tensioned bridges–better than before. *Concrete Solutions 2014*, page 29.

Pham, L. (1985). Reliability analyses of reinforced concrete and composite column sections under concentric loads. *Institution of Engineers (Australia) Civ Eng Trans*, (1).

Pillai, R., Hueste, M., Gardoni, P., Trejo, D., & Reinschmidt, K. (2010). Time-variant service reliability of post-tensioned, segmental, concrete bridges exposed to corrosive environments. *Engineering Structures*, 32(9):2596–2605.

Pillai, R., Trejo, D., Gardoni, P., Reinschmidt, K., & Hueste, M. (2012). A reliability-based service-life design approach for segmental concrete bridges subject to corrosive conditions.

Pillai, R. G., Trejo, D., Gardoni, P., D. Hueste, M. B., & Reinschmidt, K. (2014). Time-variant flexural reliability of posttensioned, segmental concrete bridges exposed to corrosive environments. *Journal of Structural Engineering*, 140(8):A4014018.

Rackwitz, R. & Fiessler, B. (1978). Non-normal vectors in structural reliability. *Technical University of Munich, SFB*, 96:1–22.

Ren, W., Sneed, L. H., Yang, Y., & He, R. (2015). Numerical simulation of prestressed precast concrete bridge deck panels using damage plasticity model. *International Journal of Concrete Structures and Materials*, 9(1):45–54.

Rodriguez, J., Ortega, L., & Casal, J. (1997). Load carrying capacity of concrete structures with corroded reinforcement. *Construction and building materials*, 11(4):239–248.

Rots, J. G., Nauta, P., Kuster, G., & Blaauwendraad, J. (1985). Smeared crack approach and fracture localization in concrete. *HERON, 30 (1), 1985.*

Schneider, J. (2006). *Introduction to safety and reliability of structures*, volume 5. Iabse.

Scholten, C. v., Enevoldsen, I., Arnbjerg-Nielsen, T., Randrup-Thomsen, S., Sloth, M., & Engelund, S. (2004). Reliability-based classification of the load carrying capacity of existing bridges. *Road directorate—ministry of transport Denmark. ISBN*, pages 87–7923.

Sheikh, A., Boah, J., & Hansen, D. (1990). Statistical modeling of pitting corrosion and pipeline reliability. *Corrosion*, 46(3):190–197.

Stewart, M. G. (1995). Workmanship and its influence on probabilistic models of concrete compressive strength. *ACI Materials Journal*, 92(4):361–372.

Stewart, M. G. (2001). Reliability-based assessment of ageing bridges using risk ranking and life cycle cost decision analyses. *Reliability Engineering & System Safety*, 74(3):263–273.

Stewart, M. G. (2004). Spatial variability of pitting corrosion and its influence on structural fragility and reliability of rc beams in flexure. *Structural Safety*, 26(4):453–470.

Stewart, M. G. (2009). Mechanical behaviour of pitting corrosion of flexural and shear reinforcement and its effect on structural reliability of corroding rc beams. *Structural safety*, 31(1):19–30.

Stewart, M. G. (2010). Reliability safety assessment of corroding reinforced concrete structures based on visual inspection information. *ACI Structural Journal*, 107(6):671.

Stewart, M. G. (2012). Spatial and time-dependent reliability modelling of corrosion damage, safety and maintenance for reinforced concrete structures. *Structure and Infrastructure Engineering*, 8(6):607–619.

Stewart, M. G. & Al-Harthy, A. (2008). Pitting corrosion and structural reliability of corroding rc structures: Experimental data and probabilistic analysis. *Reliability Engineering & System Safety*, 93(3):373–382.

Stewart, M. G. & Mullard, J. A. (2007). Spatial time-dependent reliability analysis of corrosion damage and the timing of first repair for rc structures. *Engineering Structures*, 29(7):1457–1464.

Stewart, M. G. & Rosowsky, D. V. (1998). Time-dependent reliability of deteriorating reinforced concrete bridge decks. *Structural Safety*, 20(1):91–109.

Strauss, A., Wendner, R., Bergmeister, K., & Costa, C. (2012). Numerically and experimentally based reliability assessment of a concrete bridge subjected to chloride-induced deterioration. *Journal of Infrastructure Systems*, 19(2):166–175.

Szczecina, M. & Winnicki, A. (2015). Calibration of the CDP model parameters in Abaqus. *Incheon: World Congress on Advances in Structural Engineering and Mechanics*.

Tarefder, R. A. & Zaman, M. (2005). Design of neural networks for pavement rutting. In: *Applied Research in Uncertainty Modeling and Analysis*, pages 193–213. Springer.

Thoft-Christensen, P. & Hansen, HI, . (1993). Optimal strategy for maintenance of concrete bridges using expert systems. In: *Optimal Strategy for Maintenance of Concrete Bridges using Expert Systems*, pages 939–946.

Tu, B., Fang, Z., Dong, Y., & Frangopol, D. M. (2017). Time-variant reliability analysis of widened deteriorating prestressed concrete bridges considering shrinkage and creep. *Engineering Structures*, 153:1–16.

Tuutti, K. (1982). Corrosion of steel in concrete. *Swedish Cement and Concrete Research Institute Stockholm*.

Val, D. V. & Melchers, R. E. (1997). Reliability of deteriorating rc slab bridges. *Journal of structural engineering*, 123(12):1638–1644.

Vu, K. A. & Stewart, M. G. (2005). Predicting the likelihood and extent of reinforced concrete corrosion-induced cracking. *Journal of structural engineering*, 131(11):1681–1689.

Vu, K. A. T. & Stewart, M. G. (2000). Structural reliability of concrete bridges including improved chloride-induced corrosion models. *Structural safety*, 22(4):313–333.

Wang, L., Zhang, X., Zhang, J., Yi, J., & Liu, Y. (2016). Simplified model for corrosion-induced bond degradation between steel strand and concrete. *Journal of Materials in Civil Engineering*, 29(4):04016257.

Willam, K. J. (1975). Constitutive model for the triaxial behaviour of concrete. *Proc. Intl. Assoc. Bridge Structl. Engrs*, 19:1–30.

William, K. & Warnke, E. (1975). Constitutive model for the triaxial behavior of concrete. *International Associaion for Bridge and Structural Engineering Proceedings*.

Wiśniewski, D. F. (2007). *Safety Formats for the Assessment of Concrete Bridges*. PhD thesis, Universidade do Minho, Portugal.

Woodward, R. (2001). Durability of post-tensioned tendons on road bridges in the UK. In: *Durability of Post-tensioning Tendons, Technical Report, Proceedings of a workshop held at Ghent University on 15-16 November 2001*.

Woodward, R. & Williams, F. (1988). Collapse of yns-y-gwas bridge, glamorgan. *Proceedings of the Institution of Civil Engineers*, 84(4):635–669.

Xiaogang, H. (1999). *Constitutive modelling of reinforced concrete for nonlinear finite element analysis*. PhD thesis, University of Hong Kong.

Yalcyn, H. & Ergun, M. (1996). The prediction of corrosion rates of reinforcing steels in concrete. *Cement and concrete research*, 26(10):1593–1599.

Zhang, W., Zhou, B., Gu, X., & Dai, H. (2013). Probability distribution model for cross-sectional area of corroded reinforcing steel bars. *Journal of Materials in Civil Engineering*, 26(5):822–832.

Zhang, X., Wang, L., Zhang, J., Ma, Y., & Liu, Y. (2017). Flexural behavior of bonded post-tensioned concrete beams under strand corrosion. *Nuclear Engineering and Design*, 313:414–424.

Zhu, X., Zi, G., Lee, W., Kim, S., & Kong, J. (2016). Probabilistic analysis of reinforcement corrosion due to the combined action of carbonation and chloride ingress in concrete. *Construction and Building Materials*, 124:667–680.

.1 Appendix A

ABAQUS Python script file consists from two parts: the model database mdb.py and output database.

```
################################  MDB FILE ################################
from part import *
from material import *
from section import *
from assembly import *
from step import *
from interaction import *
from load import *
from mesh import *
from optimization import *
from job import *
from sketch import *
from visualization import *
from connectorBehavior import *
execfile('E_c.py')
execfile('V_LOAD.py')
#CREATE THE SKETCH AND PARTS
mdb.models['Model-1'].ConstrainedSketch(name='__profile__', sheetSize=10.0)
mdb.models['Model-1'].sketches['__profile__'].rectangle(point1=(0.0, 0.0),
    point2=(-0.4, 0.8))
mdb.models['Model-1'].Part(dimensionality=THREE_D, name='Part-1', type=
    DEFORMABLE_BODY)
mdb.models['Model-1'].parts['Part-1'].BaseSolidExtrude(depth=5.0, sketch=
    mdb.models['Model-1'].sketches['__profile__'])
del mdb.models['Model-1'].sketches['__profile__']
#MATERIAL, SECTION AND SECTION ASSIGNMENT
mdb.models['Model-1'].Material(name='concrete')
mdb.models['Model-1'].materials['concrete'].Elastic(table=((E_c,  # This is the first variable (concrete modulus of elasticity)
    0.2), ))
mdb.models['Model-1'].HomogeneousSolidSection(material='concrete', name=
    'Concrete_Sec', thickness=None)
```

```
mdb.models['Model-1'].parts['Part-1'].Set(cells=
    mdb.models['Model-1'].parts['Part-1'].cells.getSequenceFromMask(('[#1 ]',
    ), ), name='Set-1')
mdb.models['Model-1'].parts['Part-1'].SectionAssignment(offset=0.0,
    offsetField='', offsetType=MIDDLE_SURFACE, region=
    mdb.models['Model-1'].parts['Part-1'].sets['Set-1'], sectionName=
    'Concrete_Sec', thicknessAssignment=FROM_SECTION)
#ELEMENT TYPE AND MESH
mdb.models['Model-1'].parts['Part-1'].setElementType(elemTypes=(ElemType(
    elemCode=C3D8R, elemLibrary=STANDARD, secondOrderAccuracy=OFF,
    kinematicSplit=AVERAGE_STRAIN, hourglassControl=DEFAULT,
    distortionControl=DEFAULT), ElemType(elemCode=C3D6, elemLibrary=STANDARD),
    ElemType(elemCode=C3D4, elemLibrary=STANDARD)), regions=(
    mdb.models['Model-1'].parts['Part-1'].cells.getSequenceFromMask(('[#1 ]',
    ), ), ))
mdb.models['Model-1'].parts['Part-1'].seedPart(deviationFactor=0.1,
    minSizeFactor=0.1, size=0.4)
mdb.models['Model-1'].parts['Part-1'].generateMesh()
mdb.models['Model-1'].rootAssembly.DatumCsysByDefault(CARTESIAN)
mdb.models['Model-1'].rootAssembly.Instance(dependent=ON, name='Part-1-1',
    part=mdb.models['Model-1'].parts['Part-1'])
#BOUNDARY CONDITIONS AND LOAD
mdb.models['Model-1'].StaticStep(name='Step-1', previous='Initial')
mdb.models['Model-1'].rootAssembly.Set(faces=
    mdb.models['Model-1'].rootAssembly.instances['Part-1-1'].faces.getSequenceFromMask(
    ('[#10 ]', ), ), name='Set-1')
mdb.models['Model-1'].EncastreBC(createStepName='Initial', localCsys=None,
    name='BC-1', region=mdb.models['Model-1'].rootAssembly.sets['Set-1'])
mdb.models['Model-1'].rootAssembly.Set(name='Set-2', vertices=
    mdb.models['Model-1'].rootAssembly.instances['Part-1-1'].vertices.getSequenceFromMask(
    ('[#24 ]', ), ))
```

```
mdb.models['Model-1'].ConcentratedForce(cf2=V_LOAD, createStepName='Step-1',  #This is the second variable (the vertical load)
    distributionType=UNIFORM, field='', localCsys=None, name='Load-1', region=
    mdb.models['Model-1'].rootAssembly.sets['Set-2'])
mdb.models['Model-1'].rootAssembly.Set(name='reactions', nodes=
    mdb.models['Model-1'].rootAssembly.instances['Part-1-1'].nodes.getSequenceFromMask(
    mask=('[#7 #1c00 ]', ), ))
mdb.models['Model-1'].HistoryOutputRequest(createStepName='Step-1', name=
    'reactions', rebar=EXCLUDE, region=
    mdb.models['Model-1'].rootAssembly.sets['reactions'], sectionPoints=DEFAULT
    , variables=('RF2', ))
#SUBMIT JOB
mdb.Job(atTime=None, contactPrint=OFF, description='', echoPrint=OFF,
    explicitPrecision=SINGLE, getMemoryFromAnalysis=True, historyPrint=OFF,
    memory=90, memoryUnits=PERCENTAGE, model='Model-1', modelPrint=OFF,
    multiprocessingMode=DEFAULT, name='RC_beam', nodalOutputPrecision=SINGLE,
    numCpus=1, numGPUs=0, queue=None, resultsFormat=ODB, scratch='', type=
    ANALYSIS, userSubroutine='', waitHours=0, waitMinutes=0)
mdb.jobs['RC_beam'].submit(consistencyChecking=OFF)
mdb.jobs['RC_beam']._Message(STARTED, {'phase': BATCHPRE_PHASE,
    'clientHost': 'PEZP62124', 'handle': 0, 'jobName': 'RC_beam'})
mdb.jobs['RC_beam']._Message(ODB_FILE, {'phase': BATCHPRE_PHASE,
    'file': 'D:\\RC_beam\\RC_beam.odb', 'jobName': 'RC_beam'})
mdb.jobs['RC_beam']._Message(COMPLETED, {'phase': BATCHPRE_PHASE,
    'message': 'Analysis phase complete', 'jobName': 'RC_beam'})
mdb.jobs['RC_beam']._Message(STARTED, {'phase': STANDARD_PHASE,
    'clientHost': 'PEZP62124', 'handle': 5172, 'jobName': 'RC_beam'})
mdb.jobs['RC_beam']._Message(STEP, {'phase': STANDARD_PHASE, 'stepId': 1,
    'jobName': 'RC_beam'})
mdb.jobs['RC_beam']._Message(ODB_FRAME, {'phase': STANDARD_PHASE, 'step': 0,
    'frame': 0, 'jobName': 'RC_beam'})
```

```
mdb.jobs['RC_beam']._Message(STATUS, {'totalTime': 0.0, 'attempts': 0,
    'timeIncrement': 1.0, 'increment': 0, 'stepTime': 0.0, 'step': 1,
    'jobName': 'RC_beam', 'severe': 0, 'iterations': 0,
    'phase': STANDARD_PHASE, 'equilibrium': 0})
mdb.jobs['RC_beam']._Message(MEMORY_ESTIMATE, {'phase': STANDARD_PHASE,
    'jobName': 'RC_beam', 'memory': 24.0})
mdb.jobs['RC_beam']._Message(ODB_FRAME, {'phase': STANDARD_PHASE, 'step': 0,
    'frame': 1, 'jobName': 'RC_beam'})
mdb.jobs['RC_beam']._Message(STATUS, {'totalTime': 1.0, 'attempts': 1,
    'timeIncrement': 1.0, 'increment': 1, 'stepTime': 1.0, 'step': 1,
    'jobName': 'RC_beam', 'severe': 0, 'iterations': 1,
    'phase': STANDARD_PHASE, 'equilibrium': 1})
mdb.jobs['RC_beam']._Message(END_STEP, {'phase': STANDARD_PHASE, 'stepId': 1,
    'jobName': 'RC_beam'})
mdb.jobs['RC_beam']._Message(COMPLETED, {'phase': STANDARD_PHASE,
    'message': 'Analysis phase complete', 'jobName': 'RC_beam'})
mdb.jobs['RC_beam']._Message(JOB_COMPLETED, {
    'time': 'Tue Aug 02 11:56:19 2016', 'jobName': 'RC_beam'})
# -*- coding: mbcs -*-
#
# Abaqus/Viewer Release 6.14-1 replay file
# Internal Version: 2014_06_04-23.11.02 134264
# Run by evxda9 on Tue Aug 02 12:02:25 2016
#

# from driverUtils import executeOnCaeGraphicsStartup
# executeOnCaeGraphicsStartup()
#: Executing "onCaeGraphicsStartup()" in the site directory ...
#: Abaqus Error:
#: This error may have occurred due to a change to the Abaqus Scripting
```

```
#: Interface. Please see the Abaqus Scripting Manual for the details of
#: these changes. Also see the "Example environment files" section of
#: the Abaqus Site Guide for up-to-date examples of common tasks in the
#: environment file.
#: Execution of "onCaeGraphicsStartup()" in the site directory failed.
###################################  ODB FILE ###################################
from abaqus import *
from abaqusConstants import *
session.Viewport(name='Viewport: 1', origin=(0.0, 0.0), width=286.737518310547,
    height=141.3681640625)
session.viewports['Viewport: 1'].makeCurrent()
session.viewports['Viewport: 1'].maximize()
from viewerModules import *
from driverUtils import executeOnCaeStartup
executeOnCaeStartup()
o2 = session.openOdb(name='RC_beam.odb')
#: Model: D:/RC_beam/RC_beam.odb
#: Number of Assemblies:         1
#: Number of Assembly instances: 0
#: Number of Part instances:     1
#: Number of Meshes:             1
#: Number of Element Sets:       3
#: Number of Node Sets:          5
#: Number of Steps:              1
session.viewports['Viewport: 1'].setValues(displayedObject=o2)
session.viewports['Viewport: 1'].view.setValues(nearPlane=8.90131,
    farPlane=13.378, width=4.19381, height=3.29313, viewOffsetX=0.118442,
    viewOffsetY=0.0733604)
session.viewports['Viewport: 1'].view.setValues(nearPlane=8.87551,
    farPlane=13.4038, width=4.18165, height=3.28358, viewOffsetX=0.311572,
```

```
    viewOffsetY=-0.22097)
odb = session.odbs['D:/RC_beam/RC_beam.odb']
xy0 = xyPlot.XYDataFromHistory(odb=odb,
    outputVariableName='Reaction force: RF2 at Node 1 in NSET REACTIONS',
    steps=('Step-1', ), suppressQuery=True)
xy1 = xyPlot.XYDataFromHistory(odb=odb,
    outputVariableName='Reaction force: RF2 at Node 2 in NSET REACTIONS',
    steps=('Step-1', ), suppressQuery=True)
xy2 = xyPlot.XYDataFromHistory(odb=odb,
    outputVariableName='Reaction force: RF2 at Node 3 in NSET REACTIONS',
    steps=('Step-1', ), suppressQuery=True)
xy3 = xyPlot.XYDataFromHistory(odb=odb,
    outputVariableName='Reaction force: RF2 at Node 43 in NSET REACTIONS',
    steps=('Step-1', ), suppressQuery=True)
xy4 = xyPlot.XYDataFromHistory(odb=odb,
    outputVariableName='Reaction force: RF2 at Node 44 in NSET REACTIONS',
    steps=('Step-1', ), suppressQuery=True)
xy5 = xyPlot.XYDataFromHistory(odb=odb,
    outputVariableName='Reaction force: RF2 at Node 45 in NSET REACTIONS',
    steps=('Step-1', ), suppressQuery=True)
xy6 = sum((xy0, xy1, xy2, xy3, xy4, xy5, ), )
xy_result = session.XYData(name='XYData-1', objectToCopy=xy6,
    sourceDescription='sum((Reaction force: RF2 at Node 1 in NSET REACTIONS, Reaction force: RF2 at Node 2 in NSET REACTIONS, Reaction force:
c1 = session.Curve(xyData=xy_result)
xyp = session.XYPlot('XYPlot-1')
chartName = xyp.charts.keys()[0]
chart = xyp.charts[chartName]
chart.setValues(curvesToPlot=(c1, ), )
session.viewports['Viewport: 1'].setValues(displayedObject=xyp)
x0 = session.xyDataObjects['XYData-1']
```